

Mastering Electro-Mechanical Dynamics of Large Off-Shore Direct-Drive Wind Turbine Generators

Proefschrift

ter verkrijging van de graad van doctor
aan de Technische Universiteit Delft,
op gezag van de Rector Magnificus prof. ir. K. C. A. M. Luyben,
voorzitter van het College voor Promoties,
in het openbaar te verdedigen op donderdag 31 maart 2016 om 12:30 uur

door

Michael Kirschneck

Diplom Ingenieur
geboren te Hamburg, Duitsland.

Dit proefschrift is goedgekeurd door de promotor:

Prof. dr. D.J. Rixen

Copromotors: Dr. ir. H. Polinder and dr. ir. R.A.J. van Ostayen

Samenstelling promotiecommissie:

Rector Magnificus,	voorzitter
Prof. dr. D.J. Rixen,	Technische Universiteit Delft/ TU München, promotor
Dr. ir. H. Polinder,	Technische Universiteit Delft, copromotor
Dr. ir. R.A.J. van Ostayen	Technische Universiteit Delft, copromotor

Onafhankelijke leden:

Prof. dr. C. Vuik	Technische Universiteit Delft
Prof. dr. A. de Boer	Universiteit Twente
Prof. dr. G. van Bussel	Technische Universiteit Delft
Prof. Dr.-Ing. K. Hameyer	Rheinisch-Westfälische Technische Hochschule Aachen



Printed by: Ridderprint BV

Front & Back: Michael Kirschneck

Copyright © 2016 by Michael Kirschneck

ISBN 978-94-6299-323-5

An electronic version of this dissertation is available at
<http://repository.tudelft.nl/>.

Abstract

The ever growing population of human beings on earth introduces the challenge of providing affordable, sustainable energy for everyone. Emerging markets, such as China, India or Brazil, quench their thirst for cheap energy by fossil fuels and nuclear power. At the same time researchers from all over the globe warn the public of the advent of a new, civilisation threatening disaster: climate change.

Over the last two centuries mankind has gotten used to cheap but polluting energy provided by burning coal, gas and oil. The challenge arises in the form of the transition of our current economy towards a sustainable way of living. Renewable energy sources such as wind, tidal currents, the sun and geothermal heat have seen enormous growth rates since the early nineties, as they are seen as the best approach to overcome this challenge.

Of these renewable energy sources, wind energy is one that has received major attention. In the quest for expanding wind energy capacity, focus has shifted towards the sea in recent years. The potential energy yield is higher off-shore caused by higher average wind speeds. Maintenance and availability are key issues off-shore, due to the more complex logistics. In recent years, the price of on-shore wind energy has decreased to a level that is competitive with prices for energy from some types of fossil fuel. However, the prices for off-shore wind energy remain above the ones of fossil fuels. It is, thus, not surprising that the reduction of off-shore wind energy costs is one of the main innovation drivers within the wind industry.

With the advent of off-shore wind energy more and more companies started investigating a new turbine topology called direct-drive wind turbines. This turbine type eliminates the gearbox found in other types of wind turbines, as this might lead to increased availability and lower maintenance costs.

In the search for the best design of direct-drive wind turbines, every part of the turbine is investigated, analysed, measured and optimised to improve the functionality of that part. At the heart of the turbine, where the mechanical is transformed into electrical energy, is the generator. Also this component needs to be optimised with respect to weight and efficiency.

This thesis aims to find the structural design that optimally utilises the mass of the generator structure to minimise deformation. This is done for the dynamic loads encountered in the generator. Special focus is given to the interaction between the structural dynamics and the magnetic field. This is important as the interaction

between these two physical domains can lead to unexpected dynamic behaviour of the system.

In *Part I* of this thesis, the modelling techniques that accurately include the interaction between the structural part of the turbine and the magnetic field in the generator are introduced. These techniques can, for the first time, predict the modal parameter changes, including damping changes, due to the interaction by forming a monolithic eigenvalue problem of the coupled system. The model neglects certain nonlinear influences on the dynamics, such as hysteresis and saturation. Its ability to predict changes of the modal parameters is validated by vibration measurements of a magneto-mechanical coupled system.

Furthermore, this part develops new methods to handle huge magneto-mechanical coupled models that emerge when magnetic fields and structural dynamics of a direct-drive wind turbine are modelled. The bottleneck is the memory requirements of the monolithic formulation that makes it necessary to solve for all degrees of freedom simultaneously.

Part II applies the techniques developed in Part I to the generator of the XD-115, a 5 MW direct-drive wind turbine and conducts the first two-way coupled analysis of such a generator type. The detailed dynamic analysis of the generator gives new insights in the dynamic behaviour of the generator. Furthermore, the eigenfrequencies, modes and possible causes for excitation are identified.

An experimental validation of the XD-115 models was conducted using in-situ experimental and operation modal analyses. Various techniques are compared for the challenging task of exciting the rotor structure.

In the second part of Part II, the loads identified during the dynamic analysis are used as load case for a structural optimisation. Topology and shape optimisation were used to identify the optimal mass distribution for the rotor structure that minimises the deformation in the air gap. This way, the weight of the structure could be reduced significantly without compromising the static and dynamic performance of the generator structure. During the optimisation the suitability and potential of topology optimisation for direct-drive wind turbines was evaluated.

Although the introduced methodology can be applied to any electric machine, the implications for direct-drive wind turbine generators are most significant, as for these machines the ratio between produced torque and weight is especially high. Important influences on and encountered challenges for improving the design are collected to improve future turbine designs.

Samenvatting

De groeiende bevolking op aarde werpt de kwestie op, hoe de mensheid toegang krijgt tot goedkope, duurzame energie. Groeimarkten zoals China, India of Brazilië stillen deze dorst met goedkopere fossielen brandstoffen of kernenergie. Tegelijkertijd waarschuwen wetenschappers overal ter wereld voor een nieuwe wereldwijde ramp: de klimaatverandering.

Tijdens de afgelopen twee eeuwen is de mensheid gewend geraakt aan goedkope maar vervuilende energie. De toekomstige uitdaging schuilt in de transitie van een economie gebaseerd op fossiele energie naar een duurzame. Duurzame energie zoals windenergie, zonne-energie, aardwarmte of getijdenenergie kennen een enorme groei sinds de jaren negentig, omdat zij als beste alternatief worden gezien om de fossiele uitdaging aan te gaan.

Van de genoemde duurzame energiebronnen heeft windkracht verreweg de meeste aandacht ontvangen. De zoektocht naar nieuwe locaties voor windturbines werd in de afgelopen jaren naar zee uitgebreid. De mogelijke energieopbrengsten zijn hoger op zee vanwege de gemiddeld hogere windsnelheden. Onderhoud en beschikbaarheid van windturbines zijn essentiële aspecten op zee, omdat de logistiek op deze locaties ingewikkelder is. In de afgelopen jaren is de prijs van windenergie op land gedaald tot een niveau dat kan concurreren met olie- of kolengestookte energieproductie. Daarentegen zijn de kosten van windenergie op zee nog steeds hoger dan die van energie uit fossiele energiebronnen. Daarom zijn de stroomkosten een van de hoofdredenen voor innovatie in offshore windenergie.

Met de introductie van offshore windenergie overwegen steeds meer bedrijven een nieuwe turbinesoort, namelijk de direct-drive windturbine. Direct-drive windturbines hebben geen versnellingsbak tussen generator en wieken/wiekennaaf zoals in andere turbinesoorten. Dit zou mogelijk kunnen leiden tot hogere beschikbaarheid en lagere onderhouds- en energiekosten.

Voor de optimalisatie van het design van direct-drive windturbines is een analyse van elk onderdeel op mogelijke verbeteringen noodzakelijk. Een essentieel deel van elke windturbine is de generator, waar de mechanische energie in elektrische energie wordt omgezet. Zoals elk ander onderdeel wordt ook de generator kritisch beschouwd. Vooral de optimalisatie ten aanzien van efficiëntie en gewicht zijn belangrijk.

Dit proefschrift heeft de doelstelling om de generatorstructuur van windturbines, met optimaal gebruik van massa, te minimaliseren voor de deformatie ten gevolgen van dynamische belastingen. De

wisselwerking tussen magnetisch veld en structuurdynamica krijgt daarbij bijzondere aandacht, vanwege het onverwachte gedrag als gevolg van deze afhankelijkheden tussen deze twee aspecten.

In *Deel I* van dit proefschrift worden modelleringstechnieken geïntroduceerd, die een nauwkeurig berekening van de interactie tussen structuur dynamica en het magnetisch veld mogelijk maken. Met behulp van een monolithisch eigenwaardeprobleem kan men voor het eerst de verandering van de modale parameters van het gekoppelde systeem ten opzichte van het ongekoppelde systeem berekenen. De modeleringstechnieken laten de niet-lineaire effecten, zoals magnetische verzadiging en hysteresis buiten beschouwing. De methoden zijn gevalideerd aan de hand van metingen aan een gekoppeld magneto-mechanisch systeem.

Vervolgens ontwikkelt *Deel I* nieuwe methoden voor de modelreductie van grote magnetische en magnetisch-mechanisch gekoppelde eindige element modellen. Het grote aantal elementen is nodig voor een nauwkeurige beschrijving van de interactie tussen de structuurdynamica en het magnetisch veld. De uitdaging is de grote behoefte aan geheugencapaciteit voor het monolithisch eigenwaardeprobleem.

Deel II past de methoden, die in *Deel I* ontwikkeld zijn, toe op de generator van de XD-115, een 5 megawatt windturbine. Een gedetailleerde analyse van de generator heeft nieuwe inzichten in de dynamica van dit onderdeel geleverd. Daarnaast zijn de resonantiefrequenties, modale vormen en mogelijke excitatie bronnen geïdentificeerd. De experimentele validatie van de modellen is door middel van trillingsmetingen ter plaatse gedaan. Verschillende technieken voor de excitatie van de generator zijn getest en geëvalueerd.

Vervolgens worden in *Deel II* de magnetisch krachten, die tijdens de metingen en simulaties zijn geïdentificeerd, gebruikt voor een optimalisatie van de generatorstructuur. Topologie- en vormoptimalisatie zijn toegepast om de optimale massaverdeling te vinden voor het minimaliseren van de vervormingen in de luchtspleet. Op deze manier is het gewicht van de generator aanzienlijk verminderd zonder daarbij de functionaliteit te beïnvloeden. Tijdens de optimalisatie werd de geschiktheid van topologieoptimalisatie voor de verbetering van het design van generatoren in windturbines geëvalueerd.

Hoewel de methoden op elke elektrische machine kunnen worden toegepast, hebben zij in het bijzonder een grote implicatie voor direct-drive generatoren, omdat de verhouding tussen aandrijfmoment en massa zeer hoog is. Belangrijke invloeden op de dynamica van generatoren en andere geïdentificeerde uitdagingen zijn verzameld voor de verbetering van toekomstige windturbines.

Zusammenfassung

Die wachsende Erbevölkerung wirft die Frage auf, wie die Menschheit mit günstiger und erneuerbarer Energie versorgt werden kann. Wachstumsmärkte, wie China, Indien oder Brasilien, decken ihren Bedarf an Energie mit fossilen Energieträgern oder durch Kernenergie. Gleichzeitig warnen Wissenschaftler auf der ganzen Welt vor einem neuen, weltumspannenden Desaster: dem Klimawandel.

In den letzten zwei Jahrhunderten hat sich die Menschheit an billige, aber Umweltbelastende Energiequellen gewöhnt. Die Herausforderung ist der Übergang von dieser auf fossilen Quellen basierten hin zu einer nachhaltigen Wirtschaft. Erneuerbare Energien, aus Sonne, Wind, Gezeiten oder Geothermie, haben enorme Zuwächse erreicht seit Anfang der Neunziger, da sie als bestes Mittel zur Bewältigung der fossilen Herausforderung gesehen werden.

Von den genannten erneuerbaren Energien hat Windkraft große Aufmerksamkeit erhalten. Die Suche nach neuen Standorten für Windräder wurde in den letzten Jahren auf die Meere ausgeweitet. Die möglichen Energieerträge sind auf See höher wegen der höheren Windgeschwindigkeiten. Wartung und Verfügbarkeit der Windkraftanlagen sind wichtige Aspekte auf See, weil die Logistik an diesen Standorten komplexer ist. In den vergangenen Jahren ist der Preis von on-shore Windenergie stark gesunken auf ein Niveau das mit fossilen Energieträgern wettbewerbsfähig ist. Im Gegensatz dazu ist der Preis von off-shore Windenergie immer noch höher als konkurrierende öl- oder kohlebasierte Energieproduktion. Daher sind die Energiekosten einer der Hauptgründe für Innovationen bei off-shore Windenergie.

Mit dem Aufkommen von off-shore Windenergie haben sich immer mehr Turbinenhersteller einer neuen Turbinenart zugewandt. Direkt getriebene Windräder verzichten auf das Getriebe zwischen Generator und Flügelhuben, um die Verfügbarkeit zu erhöhen und so die Wartungs- und Energiekosten zu senken.

Die Verbesserung des Designs von direkt getriebenen Windrädern macht eine Überprüfung jedes Bauteils auf mögliche Verbesserungen notwendig. Zentrales Bauteil eines jeden Windrades ist der Generator, in dem die mechanische in elektrische Energie umgesetzt wird. Insbesondere die Optimierung des Generators hinsichtlich der Effizienz und des Gewichtes sind interessant.

Diese Dissertation befasst sich mit der Optimierung der Generatorstruktur hinsichtlich der optimalen Nutzung der Masse, um Verformungen durch dynamische Lasten so weit wie möglich zu vermeiden. Die Wechselwirkung zwischen dem magnetischem Feld im Generator und der Strukturmechanik findet dabei besondere Be-

achtung, da diese unerwartetes Verhalten des Systems zur Folge haben kann.

In *Teil I* werden die Modellierungstechniken, die die präzise Berechnung der Wechselwirkung zwischen magnetischem Feld und Strukturmechanik ermöglichen, eingeführt. Diese Techniken können erstmalig die Veränderungen der modalen Parameter, inklusive Veränderung der Dämpfung, des gekoppelten Systems gegenüber ungekoppelten Systemen berechnen. Die Modellierungsmethoden vernachlässigen nichtlineare Effekte, wie magnetische Sättigung und Hysterese. Die Genauigkeit der Methode wird anschließend durch Labormessungen bestätigt.

Des Weiteren entwickelt *Teil I* neue Methoden zur Modellreduktion von großen magnetischen und magnetisch-mechanisch gekoppelten Finiten Elemente Modellen. Diese Modelle entstehen, wenn die Interaktion zwischen der Strukturmechanik und dem magnetischen Feld berechnet wird. Die Herausforderung bei diesen Modellen besteht im großen Speicherbedarf bei der monolithischen Formulierung des Eigenwertproblems.

Teil II wendet die in *Teil I* eingeführten Methoden auf die XD-115, eine 5 MW direkt getriebene Windkraftanlage, an und führt erstmalig eine Analyse der gekoppelten Dynamik eines solchen Generators durch. Eine detaillierte dynamische Analyse des Generators gab neue Einsichten in die Dynamik des Generators. Des Weiteren werden die Resonanzfrequenzen, Eigenschwingformen und mögliche Anregungsquellen identifiziert. Eine experimentelle Validierung der Modelle wurde durch Schwingungsmessungen vor Ort erreicht. Verschiedene Anregungstechniken für den Generator wurden getestet und evaluiert.

Weiterhin werden in *Teil II* die während der Messungen und Simulation identifizierten magnetischen Kräfte für eine Optimierung der Generatorstruktur genutzt. Topologie- und Parameteroptimierung wurden verwendet, um die optimale Massenverteilung zur Minimierung der Luftspaltverformung zu finden. Auf diese Weise konnte das Gewicht des Generators erheblich reduziert werden, ohne die Funktionalität des Generators zu beeinflussen. Dabei wurde das Potential von Topologieoptimierung für die Verbesserung des Designs von Generatoren von Windkraftanlagen evaluiert.

Obwohl die Methoden auf jede elektrische Maschine anwendbar sind, haben sie die größte Auswirkung auf direkt getriebene Windkraftanlagen, da hier das Verhältnis zwischen Drehmoment und Masse besonders hoch ist. Wichtige Einflüsse auf die Dynamik von Generator von Windkraftanlagen und identifizierte Herausforderungen wurde zusammen getragen für die Verbesserung zukünftiger Turbinen.

Acknowledgement

When I started studying in 2005, I would have contradicted anyone strongly who told me I would end up doing a PhD. The idea was planted into my head by Prof. Mark A. Shannon, my supervisor during a summer internship at the University of Illinois, who sadly passed away in 2012. At that time I discovered that I have a liking for the working style that is required for Master and PhD theses.

Besides Marc Shannon, there are several individuals whose input were crucial for finishing this thesis. These person I would like to thank at this place.

First, I would like to thank my supervisors Daniel Rixen, Henk Polinder and Ron van Ostayen, for all their support and the good ideas. Thank you for the quick answers to my questions from where ever you were in the work at that moment and for asking all the question during our meetings that always made me rethink my argumentation, in particular the parts that seemed clear to me but turned out not to be.

I would like to thank all my colleagues at the TU Delft for their support and technical knowledge they provided for this thesis. I will never forget the various activities at conferences, in the weekends and the many fun nights in Delft for which I stayed out longer than I should have.

In addition, I would like to thank the staff of XEMC-Darwind for their support during the measurements in the turbine and the help organising them. In particular, I would like to thank Jan Kastelijn who helped me conduct the measurements in the turbine, carried the equipment to the nacelle and was even willing to stay until 10 pm to finish my measurements.

Furthermore, I would like to thank my master students, Anoop and Didier, I had the honour to supervise during the last 4 years.

Finally, I would like to thank my parents, Christa and Erich Kirschneck, and my sister, Katharina Kirschneck, who have supported me during the last four years. Sorry, that you mainly experienced the bad times when things were not going as planned. Thank you for your support especially in those hours when I wondered why I started doing a PhD and I was on the phone again complaining.

Michael Kirschneck
Delft, September 2015

Abstract	iii
Samenvatting	v
Zusammenfassung	vii
Acknowledgement	ix
Nomenclature	xii

I Modelling Magneto-Mechanical Coupled Dynamics

1	Introduction	1	2	Modelling Techniques	21
1.1	Bigger, Higher, Further Off-shore – Trends in Wind Turbines	2	2.1	Introduction	22
1.2	Generators in Wind Turbines	6	2.2	Basic Magnetic Field Modelling	23
1.3	Magneto-Mechanical Coupling and Vibrations in Electric Machines	10	2.3	Lumped Magneto-Mechanical Systems	30
1.4	Problem Definition	14	2.4	Continuous Modelling of Magneto-Mechanical Coupling	36
1.5	Thesis Outline	15	2.5	Discrete Modelling of Magneto-Mechanical Coupling	58
1.6	Scientific Contributions	18	2.6	Linearized Coupled Eigenvalue Problem	83
			2.7	Summary	84
			3	Experimental Validation	85
			3.1	Introduction	86
			3.2	The Test Set Up	86
			3.3	Verification Measurements	92
			3.4	3D Finite Element Model	96
			3.5	Results	97
			3.6	Summary	97
			4	Model Reduction	99
			4.1	Introduction	100
			4.2	Modal Analysis for Quasi-Static Magnetic Fields	102
			4.3	Introduction to Model Order Reduction and Dynamic Substructuring	107
			4.4	Linear Reduction Methods Based on Modal Analysis	114
			4.5	Application to the 600 W Ampair Wind Turbine	121
			4.6	Reduction of Magneto-Mechanical Coupled Systems	125
			4.7	Discussion	130
			4.8	Summary	131

II Application to Large Off-Shore Wind Turbine Generators

5	Application to the XD-115	135
5.1	Introduction	136
5.2	The XD-115 Wind Turbine	137
5.3	The Coupled Dynamics of the XD-115 Generator	139
5.4	Experimental Validation	161
5.5	Conclusion	185
5.6	Summary	187
6	Optimisation	189
6.1	Introduction	190
6.2	The Dynamic Optimisation Problem	192
6.3	Optimisation of Single Bearing Topologies	204
6.4	Double Bearing Configurations	216
6.5	Conclusions & Summary	219

III Discussion and Conclusions

7	Design Considerations	225
7.1	Introduction	226
7.2	The Influence of Bearings	227
7.3	The Influence of the Static Magnetic Field	229
7.4	Excitation by Magnetic Forces	231
7.5	Cyclic Symmetry	233
7.6	Summary	234
8	Conclusions and Outlook	235
8.1	Conclusions	236
8.2	Research Outlook	239

Appendix A - Magnetic Energy in Deformable Structure	245
Appendix B - Measurements	257
Appendix C - Magnetic Torque Harmonics	261
Curriculum Vitae	267
References	268

Nomenclature

Notation Convention

In this thesis, a lot of algebra is used to explain the mathematical methods used. In this thesis, scalars are denoted by regular letters. Small letters stand for a value per cubic meter or square meter, i.e. a density, whereas capitalised letters denote the total quantity. For example, f stands for a force density whereas F denotes a force.

Because the theory is first explained in a continuous analytical way and then in a numerical way, this thesis distinguishes between numerical vectors, which denote a set of nodal values, and analytical vectors, which denote a direction at a certain point of a vector field. Bold roman letters, \mathbf{F} , denote the numerical vectors, whereas \vec{f} denotes the vector of a vector field.

Matrices are denoted by a bold capital letter \mathbf{M} , whereas tensors are denoted by a double underlined letter, $\underline{\underline{T}}$. Block diagonal matrices are indicated by $\text{diag}(\bullet, \bullet)$. For instance

$$\text{diag}(X, Y) = \begin{bmatrix} X & \mathbf{0} \\ \mathbf{0} & Y \end{bmatrix} \quad \text{diag}(m_m) = \begin{bmatrix} m_1 & & \\ & \ddots & \\ & & m_m \end{bmatrix}$$

The transposed of a matrix is indicated by the superscript T:

$$\begin{bmatrix} \mathbf{0} & X \\ Y & \mathbf{0} \end{bmatrix}^T = \begin{bmatrix} \mathbf{0} & Y^T \\ X^T & \mathbf{0} \end{bmatrix}$$

In some equations the Einstein notation or index notation is used. This notation sums over an index if that index appears twice in a term. The inner product of the two vectors \vec{x} and \vec{y} is thus given by

$$\sum_i x_i y_i = x_i y_i$$

The integral sign is used only once even when the integration domain is two dimensional or three dimensional. The domain is indicated below the integration sign and its dimension becomes clear from the context.

$\text{tr}(\bullet)$ denotes the trace of a tensor or matrix, defined as

$$\text{tr} \left(\begin{bmatrix} x_{11} & x_{12} \\ x_{21} & x_{22} \end{bmatrix} \right) = x_{11} + x_{22}$$

The imaginary number is denoted by i .

A variation of a quantity is denote by δ . When a certain other quantity, x , is constant under the variation δ , this is indicated by

$$\delta(\bullet)|_{\delta x=0}$$

General meaning of sub- and superscripts, unless otherwise noted in context

$(\bullet)^{(s)}$	Belonging to substructure s	\bullet_i	Internal
\bullet_b	Boundary	\bullet_{ii}	Structural
\bullet_A	Magnetic	$\tilde{\bullet}$	Reduced
$\hat{\bullet}$	Amplitude, especially of sinusoidal functions	\bullet	Block diagonal form
\bullet_s	quantity on side s of an interface	$[\bullet]_x$	skew symmetric matrix for cross product

Often Used Abbreviations

ACB	Augmented Craig Bampton Method	FEM	Finite Element Method
CB	Craig Bampton Method	LCOE	Levelised Cost of Energy
CMS	Component Mode Synthesis	LDV	Laser Doppler Vibrometer
CVA	Canonical Variate Analysis	MMF	Magneto Motive Force
DCB	Dual-Crag-Bampton Method	MOR	Model Order Reduction
DFIG	Doubly Fed Induction Generator	MTA	Mode Truncation Augmentation
DOF	Degrees of Freedom	OMA	Operational Modal Analysis
DS	Dynamic Substructuring	PM	Permanent Magnet
EFDD	Enhanced Frequency Domain Decomposition	POD	Proper Orthogonal Decomposition
FDD	Frequency Domain Decomposition	POM	Proper Orthogonal Modes
FRF	Frequency Response Function	POV	Proper Orthogonal Value
EM	Electro-Magnetic	SSI	Stochastic Subspace Identification
EMA	Experimental Modal Analysis	SVD	Singular Value Decomposition
DAQ	Data Acquisition System	TF	Transfer Function
FE	Finite Element		

List of Symbols

n_b	Discrete normal vector of raceway	5.8	$\vec{f}_{mag,stat}$	Static magnetic force applied to rotor	5.16
A_b	Surface of bearing raceway	5.7	\vec{f}_{rel}	radial - tangential relation vector	5.16
E^*	Equivalent Young's modulus	5.1	f_{pos}	Position of Magnets	5.16
$F_{bearing}$	Total bearing force	5.5	k_{elem}	Stiffness of bearing element	5.3
F_{elem}	Force per bearing element	5.1	l_{blade}	Length of turbine blade	1.1
P_{nom}	Nominal power of turbine	1.1	l_{elem}	Length of bearing element	5.1
T_{nom}	Nominal turbine torque	1.3	n_b	Normal vector on bearing raceway	5.7
δ	Indentation of bearing element	5.1	n_{poles}	Number of poles	5.9
$k_{bearing}$	Bearing stiffness matrix	5.8	n_{slots}	Number of slots	5.9
ω_{ref}	Reference frequency for normalisation	5.20	n_{sym}	number of cyclo-symmetric parts	5.11
$\vec{f}_{b,rad}$	Bearing force density, radial on race way	5.7	n_{sym}	number of cyclo-symmetric parts	5.17
$\vec{f}_{mag,dyn}$	Dynamic magnetic force applied to rotor	5.17	$r_{r,out}$	Outer radius of rotor	5.15

Magneto Mechanical Coupling

Γ	Boundary with mechanical b.c.	2.36	Φ_B	Total magnetic flux	2.14
γ	Conductivity	2.38	Ψ_{elt}	Electric enthalpy	2.113
γ	Electric conductivity	2.4b	Ψ_{mag}	Magnetic enthalpy	2.114
Γ_c	Cross section of coil core	2.50	ρ	Density	2.35
Γ_w	Cross section of coil	2.52	$\underline{\underline{\epsilon}}$	Strain tensor	2.34
Γ_w	Cross section of coil	2.53	$\underline{\underline{\sigma}}$	Stress Tensor	2.34
λ	Eigenvalue of the dynamic system	2.171	$\underline{\underline{\tau}}$	Shear Stress	2.34
λ_c	Flux linkage of a coil	2.16	$\underline{\underline{\Xi}}$	Material Stiffness Tensor	2.34
\mathcal{D}	Dissipation function	2.118	$\underline{\underline{T}}$	Maxwell's stress tensor	2.98
\mathcal{D}_{mag}	Dissipation function of eddy currents	2.81	$\underline{\underline{A}}$	Magnetic Vector Potential	2.38
\mathcal{F}_{coil}	Magneto motive force of a coil	2.12	$\underline{\underline{B}}$	Magnetic Flux Density	2.3d
\mathcal{F}_{pm}	Magneto motive force of a magnet	2.13	$\underline{\underline{B}}_r$	Remanent flux density	2.6
\mathcal{R}	Reluctance	2.14	$\underline{\underline{D}}$	Displacement Field	2.3d
\mathcal{T}	Kinetic energy	2.59	$\underline{\underline{E}}$	Electric Field	2.3d
\mathcal{T}_{mag}	Kinetic energy	2.106	$\underline{\underline{E}}'$	Electric field in structure reference frame	2.4b
\mathcal{V}_{elt}	Electric potential energy	2.113	$\underline{\underline{E}}_i$	Irrotational electric field	2.2
\mathcal{V}_{ext}	Total external energy potential	2.64	$\underline{\underline{E}}_s$	Solenoidal electric field eddy currents	2.4b
\mathcal{V}_{int}	Potential internal energy	2.59	$\underline{\underline{F}}_{mag}$	Total force on an object	2.101
$\underline{\underline{\Xi}}$	Material Stiffness Matrix	2.129	$\underline{\underline{H}}$	Magnetic Field	2.1
$\underline{\underline{B}}_u$	Matrix of shape fun. spatial derivatives	2.128	$\underline{\underline{j}}$	Current Density	2.1
$\underline{\underline{D}}_k$	Matrix of mech. damping coefficients	2.133	$\underline{\underline{j}}_i$	Eddy current density	2.46
N	Shape function	2.104	$\underline{\underline{j}}_{source}$	Source term for magnetic field	2.4b
μ	Permeability of a lin. magnetic material	2.5	$\underline{\underline{j}}_{surface}$	Current sheet on interface	2.48
$\underline{\underline{C}}$	The damping Matrix	2.126	$\underline{\underline{n}}$	Normal vector of an interface	2.48
$\underline{\underline{K}}$	The tangent stiffness Matrix	2.126	$\underline{\underline{v}}$	Velocity field of a structure	2.4b
$\underline{\underline{M}}$	The mass Matrix	2.126	dW_{eddy}	Energy change due to eddy currents	2.60
γ	Conductivity matrix	2.140	dW_{fric}	Energy change due to friction	2.62
$\underline{\underline{\Phi}}$	Matrix of eigenvectors	2.171	f_{mag}	Scalar magnetic force	2.17
$\underline{\underline{B}}_A$	Derivatives of magnetic shape functions	2.135	H_{pm}	Magnetic field within a magnet	2.13
$\underline{\underline{B}}_{2u}$	Derivative of mechanical shape function	2.155	i_c	Current in a coil	2.12
$\underline{\underline{F}}_2$	Derivatives of magnetic shape functions	2.158	N_c	Winding number of a coil	2.50
$\underline{\underline{F}}_3$	Derivatives of magnetic shape functions	2.159	q	Electric Charge Density	2.2
$\underline{\underline{K}}_{uu}^{mag}$	Magnetic structural stiffness	2.130	R_c	Resistance of coil	2.49
$\underline{\underline{f}}_{ext}$	Nodal values of forces applied externally	2.132	u	Scalar displacement	2.16
$N_{u,s}$	shape function to discretise Γ_{sigma}	2.132	V	Electric Potential	2.40
$\underline{\underline{q}}$	DoFs of discrete system	2.104	V	Volume of domain	2.92
$\underline{\underline{q}}_c$	Discrete values of coil current	2.146	v_{ext}	External voltage applied to coil	2.49
Ω_c	Coil Domain	2.52	v_{ind}	Induced voltage in coil	2.49
Ω_c	Coil Domain	2.53	W_{coil}	External energy of a coil	2.60

$W_{ex,m}$	Exchanged energy	2.28	w_{mag}	Specific magnetic energy	2.8
$W'_{ex,m}$	Exchanged co-energy	2.30	W'_{mag}	Total magnetic co-energy	2.22
$W_{ext,m}$	External mechanical energy	2.62	W_{mech}	Internal mechanical energy	2.59
W_{int}	Internal energy	2.59	$w_{pm,o}$	Internal specific energy of PM	2.10
$W_{mag,lin}$	Energy of linear magnetic field	2.66	w_{pm}	Specific magnetic energy of a PM	2.10
$W_{mag,pm}$	Total energy within a permanent magnet	2.33	W_{strain}	Strain energy	2.59
W_{mag}	Total magnetic energy	2.20	W_{tot}	Total energy of the system	2.63

Model Reduction

Φ	Column matrix of modes	4.2	g_y	Unique interface forces/currents	4.26
η_m	Modal DoF	4.1	J	Nodal Values of external current Density	4.2
η_r	Participation factor of the r^{th} mode	4.49	$J_{eddy,m}$	Eddy Currents of m^{th} mode	4.10
K_{cpl}	Multi-physical damping coupling matrix	4.44	q	DoFs of the system	4.1
K'_{cpl}	Multi-physical stiffness coupling matrix	4.44	q_{hom}	Homogenous solution	4.5
Φ_f	Free vibration modes	4.36	u_y	Unique interface DoFs	4.19
Φ_r	Rigid body modes	4.36	ω_r	eigenfrequency of the r^{th} mode	4.51
Φ_{CB}	Fixed interface used for CB reduction	4.31	ω_{ext}	Excitation frequency	4.6
Φ_M	Column matrix of MTAs	4.32	$\omega_{r,cpl}$	Coupled eigenfrequency of the r^{th} mode	4.55
Ψ_r	Residual attachment modes	4.36	Φ_r	Participationfactor of the r^{th} mode	4.50
Ψ_s	Static condensation matrix	4.30	\tilde{C}	Reduced Damping Matrix	4.16
B_b	Signed Boolean assembly matrix	4.26	\tilde{f}	Reduced external forces	4.17
D	Collocation Matrix	4.29	\tilde{g}	Reduced interface forces	4.17
F	Column matrix of applied Forces	4.32	\tilde{K}	Reduced Stiffness Matrix	4.16
$K_{A\Phi}$	Coupling Matrix for spectral expansion	4.51	\tilde{M}	Reduced Mass Matrix	4.16
L_b	Boolean assembly matrix	4.19	c_m	Modal magnetic damping factor	4.6
R	Reduction Matrix	4.15	k_m	Modal magnetic stiffness	4.6
q_b	Boundary DoFs	4.14	k_r	Modal structural stiffness	4.6
q_i	Internal DoFs	4.14	k_r	modal stiffness of the r^{th} mode	4.52
q_r	Non reduced DoFs	4.14	m_r	Modal structural mass	4.6
q_r	Reduced DoFs	4.14	m_r	modal mass of the r^{th} mode	4.49
ϕ_m	m^{th} Mode	4.1	$W_{ex,m,r}$	Exchange energy for r^{th} mode	4.53
Ψ_m	m^{th} eigen value	4.3	W_r	Energy for r^{th} mode	4.54
g_b	Forces/Currents between substructures	4.14			

Optimisation

χ	Indicator function	6.12	ρ_n	Density associated with a node	6.35
λ	Adjoint Variable	6.19	g_{constr}	Constraint function	6.12
ξ	Adjoint Variable	6.25	g_{obj}	Objective Function	6.6
ζ	Adjoint Variable	6.25	v_n	Volume associated with a node	6.35
$q_{u,o}$	Static Solution	6.37	W_{dyn}	Dynamic mechanical energy	6.9
ρ_f	Density design parameters	6.13			

Introduction

'Of all the forces of nature, I should think the wind contains the largest amount of motive power.'

Abraham Lincoln 1860

1.1

Bigger, Higher, Further Off-shore – Trends in Wind Turbines

Since the beginning of the utilisation of wind as a power source back in the first millennium, the technology employed has undergone quite some significant improvements. The rate of change has increased over the last 40 years since the technology became a focus of the renewable energies development.

1.1.1

A Short History of Wind Energy

When looking at recent developments in and the ongoing discussion about wind energy, one can easily be misled to think that wind energy has been developed only recently. In fact, windmills and the concept of harvesting the wind for work is much older. There are speculations about the existence of wind mills 3000 years ago [78]. The first reliable information about windmills dates back to 644 A.D. [49].

The horizontal axis wind mills, the one which is most commonly used even today, is probably a European invention [58]. The first reliable information dates back to 1180 about a windmill in Normandy. Another source points to Brabant where a post windmill was supposedly built as early as 1119 [58]. These early European post windmills were made entirely of wood. The tower windmill, which made its appearances about two centuries later, consists of a stone tower, on which the wind wheel rests. According to [58], this windmill spread across Europe starting in the south of France.

In the 16th century, the "Dutch windmill" was developed in the Netherlands. This windmill consisted of a fixed mill house. Only the wooden top of the house and the wind wheel were rotated into the wind for operation. This system was improved until the middle of the 19th century and they can still be seen throughout the Netherlands today.

At the end of the 19th and the beginning of the 20th century the development of windmills slowed. Steam engines and combustion engines took over power production and energy production at that time, eliminating the necessity to harvest the wind for power. However, the development of the first wind mill producing electricity falls into this time span, which was done by Poul La Cour in 1891 [58].

The idea of wind mills gained popularity again in the 70s after the first oil crisis. Consequently, development of new types of wind turbines picked up again. In Denmark, due to the idea of decentralized power production in rural areas, there was a tradition of

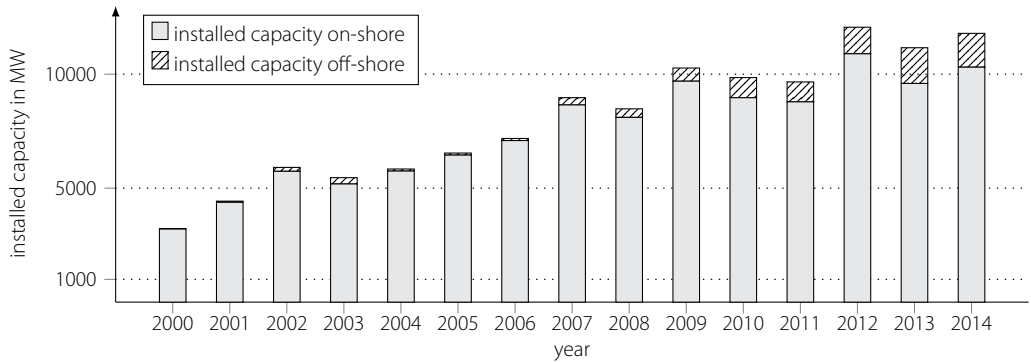


Figure 1.1

Annual total Installed wind turbine capacity in Europe. [42, 54]

building small three bladed wind turbines for farms. Small companies that were producing these turbines throughout the whole 20th century (e.g. Vestas) started to increase their business in the 70s [58]. Since then the installed capacity of wind turbines has increased enormously. Fig. 1.1 shows the development of the installed wind turbines in Europe since 2000. Together with the installed capacity in total, the rated power of each turbine increased over the years as well.

The first off-shore wind farm was inaugurated in 1991 [43]. Until 2001 the major share of installed capacity was contributed by near shore projects in Denmark and the Netherlands. In 2001 the first "utility scale" off-shore wind farm went on-line. Since then, the installed annual capacity has increased tremendously. In 2014 a capacity of 1483 MW was installed in Europe. For the future, predictions state that the installed capacity will increase further, reaching a total European capacity of 40 GW and an annual energy production of 148.2 TWh by 2020 [43]. The largest part of the off-shore capacity will be installed in Germany and the UK.

cost reduction – the driving force behind innovation in wind energy

1.1.2

Since the first wind park in 1980 [154], wind energy had a reputation of being an expensive alternative to energy production based on fossil fuels and nuclear energy. While this might have been the case in the beginnings of wind energy, the prices of on-shore wind energy have dropped to a level which is very much competitive with energy prices of coal and gas [80]. Off-shore wind energy is still more expensive than the energy produced by on-shore wind turbines. The outlook into the future, according to [80], sees an increase in prices for coal and gas combined with a decrease of prices

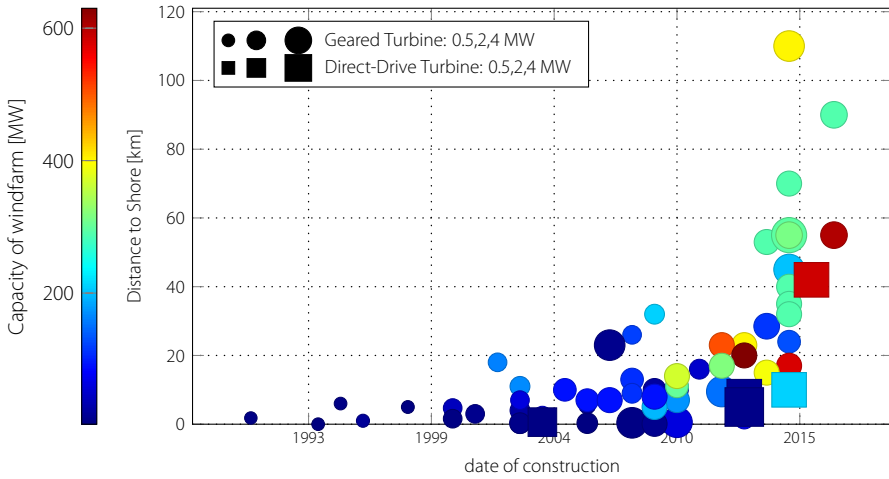


Figure 1.2

Capacity of windfarms, individual turbine size, water depth and date of construction of off-shore wind farms in the UK, Germany, Denmark, The Netherlands and Sweden. The size of the marker indicates the individual turbine size. Data from [172]

for wind energy. Nonetheless off-shore energy will remain more expensive than coal power in the near future. The incentive to invest in off-shore wind energy does thus not originate from a decreased levelised cost of energy (LCOE) but from the large amount of possible turbine sites. Additionally, off-shore wind turbines do not face opposition by local residents, which leads to discussion and rejection of on-shore turbine projects.

Analysing the LCOE only gives a distorted picture of the real cost of energy, as it does not include additional costs, so called external costs. For each energy source there are certain additional costs that have to be taken into account for the total cost of energy. For fossil fuel based power sources this includes the environmental cost as well as transporting the fuel to the power plant. However, the energy can be produced close to the customer decreasing the cost for electrical transmission lines. For wind energy, the source of the energy, i.e. wind, is free, but the energy is not readily available at all times and needs under certain circumstances be transported from the location where it is produced to the customer (This triggered a nation wide discussion in Germany, where an extension of the power grid is strongly opposed by some parts of the population and politicians, mainly in Bavaria [7]). [121] is a report for the European commission quantifying the external costs of various sources of energy. It lists the external cost for coal and oil at 4 and 5 Euro cent per kWh, while the external cost for wind energy are listed at around 0.1 - 0.2 Euro cent per kWh.

The external costs of nuclear power are difficult to calculate. Estimates for decommissioning range widely and costs for long-term waste storage are unknown [25]. Furthermore, no insurance for

nuclear power plants is available, as the possible liabilities in case of a worst scenario are too high to be insured. Therefore, the government insures these kinds of accidents indirectly by helping victims of nuclear disasters, as happened in Fukushima, Japan. It can be argued that these are hidden costs that do not appear on the bill for nuclear energy and, hence, distort the picture that LCOE give about the prices of nuclear energy.

Although the cost of wind energy has already decreased by a factor of 5 since the 1980s [83], there is still a strong incentive for wind turbine manufacturers to decrease the cost of energy. Utility companies strive to maximise their profit. A reduction of production cost is only beneficial for that goal. Because wind turbines and wind turbine technology has received little attention at the beginning of the 20th century, its technology is less developed than the one of fossil fuel based power production. The potential for cost reduction in wind turbines is thus considered to be larger compared to conservative power production methods.

In off-shore wind energy, there are two trends visible to reach this goal.

1. The wind parks tend to locations further away from shore in deeper waters (see Fig. 1.2 for the trend towards larger distances to shore). At those locations the average wind speeds are higher than at locations closer to shore [35]. Higher average wind speed amounts to more kinetic energy in the wind. More energy can, therefore, be harvested from the same rotor diameter, leading to generators with a higher nominal power.
2. Larger wind turbines entail decreasing maintenance costs, because less individual turbines need to be maintained in a wind farm of the same capacity. This trend can be seen in Fig. 1.2 by an increasing size of marker towards the right of the plot and also in Fig. 1.3, which shows the average individual turbine capacity over the years.

Another idea that is currently debated in the industry is a transition towards direct-drive wind turbines. This topology has the advantage that there is no gear box present in the turbine. [45] shows that although the occurrence of gear box failures of wind turbines is not the most common failure, it leads to the longest down time of all failure types recorded. For off-shore turbines maintenance is especially expensive. Waiting times are longer, logistics more complex and the weather plays a major role when planning repairs. Direct-drive turbines are intended for off-shore use, as they promise to decrease downtime and maintenance cost by eliminating gear box failures.

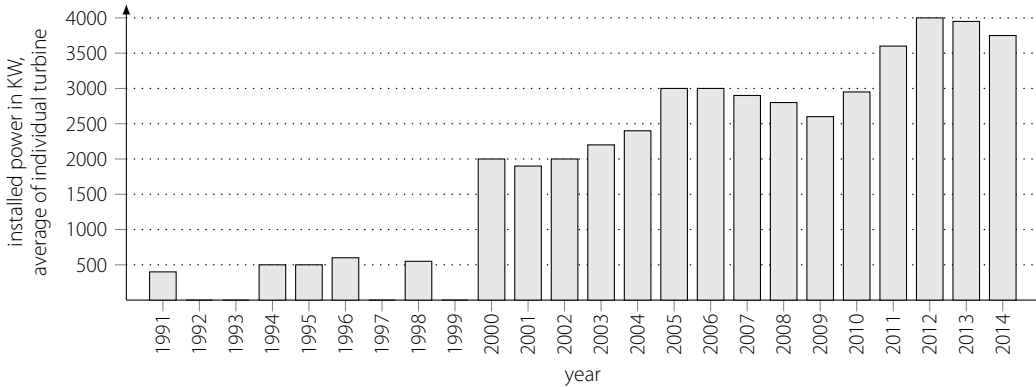


Figure 1.3

Average individual turbine capacity of off-shore wind turbines for Europe. Data from [42]

Fig. 1.2 shows that there are hardly any direct-drive wind turbine off-shore wind farms at the moment. However, some manufacturers have developed direct-drive wind turbines mainly for their off-shore business (Siemens, Alstom, XEMC-Darwind). Other manufacturers believe that geared topologies have an advantage even for off-shore applications (Vestas, RePower, Gamesa). Enercon is a special case, as they have been exclusively producing on-shore direct-drive turbines since the early 90s. [76] gives an overview of current direct-drive designs in use by the major wind turbine manufacturers.

1.2

Generators in Wind Turbines

The topology used for the drive train in a wind turbine determines the type of the generator. It is, therefore, impossible to describe developments and trends in wind turbine generator design without looking at the wind turbine as a whole.

[9, 116, 117] give an overview over all generator topologies currently in use as well as their advantages and drawbacks. The most important topologies at the moment are

- A fixed speed squirrel cage induction motor with a gear box. No frequency converter is needed
- A variable speed doubly fed induction machine with a gear box and a partly rated converter
- A variable speed direct-drive synchronous generator without gear box and a full converter
- A variable speed turbine with gear box, a generator and a full converter

The first topology in this list is an outdated topology that is no longer used for new commercial scale multi-megawatt wind turbines.

As mentioned above, the direct-drive generator is currently debated among the off-shore turbine manufacturers. In this topology, the generator rotor rotates at the same speed as the blades. The speed is determined by the tip speed ratio which is maintained at a certain level to extract the most energy from the wind [58]. The resulting low generator rotation speed requires a large torque in order to achieve the nominal power of the turbine. The generators for direct-drive wind turbines are, therefore, very special machines as these need to produce a very large torque at low rotation speeds. The torque per unit surface in the air gap depends on the magnetic flux density in the air gap. In order to produce this large torque a large air gap surface is needed. This can be achieved by increasing the axial length and the diameter of the machine.

Considering the trend towards larger turbines further off-shore, the direct-drive topology might not be feasible any longer for larger turbines. Assuming a linear relation between the mass of the drive train and the torque, the mass would increase more than linearly with an increase in nominal power. This can be shown with a short calculation.

The nominal power of a turbine is determined by the surface that the blades cover

$$P_{nom} \propto l_{blade}^2 \quad (1.1)$$

The rotation speed of the rotor is determined by the tip speed ratio which is as close to an ideal figure as possible. The rotation speed decreases thus with an increasing blade length

$$\omega \propto \frac{1}{l_{blade}} \quad (1.2)$$

The torque of the turbine is given by

$$T_{nom} = \frac{P_{nom}}{\omega} \quad (1.3)$$

Now it is possible to deduce that the torque will increase with the exponent of $\frac{3}{2}$ when the nominal power increases.

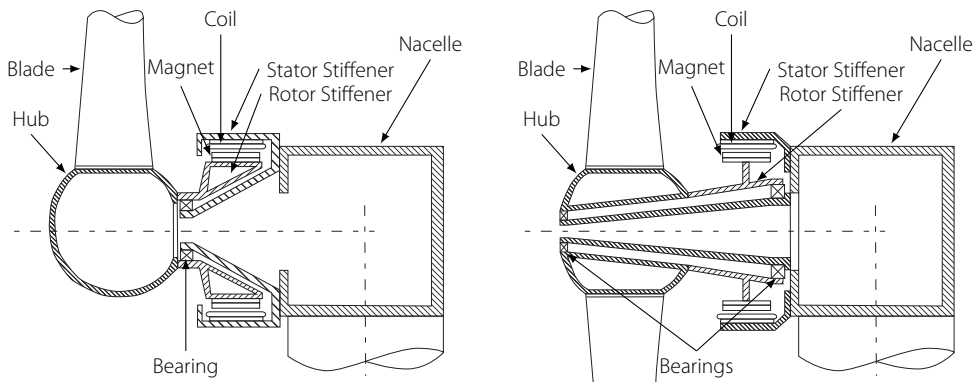
$$T_{nom} \propto P_{nom}^{\frac{3}{2}} \quad (1.4)$$

The increased torque will lead to heavier constructions, as more material is needed to transmit this torque. In order to ensure the feasibility of direct-drive wind turbines for larger machines in the future, the mass of the generator needs to be reduced dramatically. [137] deduces the scaling laws in more detail of direct-drive generators for static forces and yields even larger exponents than above.

1.2.1

Double vs. Single Bearing Topologies

There are various bearing topologies that are discussed for direct-drive generators. Because of the size of the generator, distances between parts where forces are applied and support structures, i.e. bearings, can be larger than in generators with a higher rotation speed. Various designs have been proposed for bearing placements. [145] gives an overview of the various bearing placements and topologies, including designs with one, two, or even three bearings.



a) Schematic of a direct-drive single bearing wind turbine b) Schematic of a direct-drive kingpin design wind turbine

Figure 1.4

Various bearing topologies for wind turbines

The two most used designs, the single bearing design and the kingpin design, will be discussed in more detail here.

The single bearing topology incorporates a single bearing that consequently supports the rotor in all three directions. Fig. 1.4a shows a direct-drive generator that is supported by a single-bearing. This bearing usually features a large diameter as this increases the leverage of the bearing elements while supporting the rotor against wind induced torque and consequently reduces loads on the bearing elements.

The advantages of a single bearing design are its compactness in axial direction and an easy access to the hub and thus to the blades, which need to be accessed regularly for maintenance purposes. The drawbacks are a highly complex bearing, due to its diameter. Slipping of bearing elements is difficult to avoid, because the diameter difference between the inner and outer edge of the axial raceway is large. This will likely increase the wear of the bearing elements.

The kingpin design features one bearing at the very front of the hub that is supported by a long cone extending all the way on the inside of the hub to its front. The other bearing is located within the generator. In Fig. 1.4b such a design is shown. The location

of the bearings maximise the distance between the two bearings, giving them more leverage while supporting the rotor against wind induced torques. The smaller diameter of the bearings make each of them simpler. The drawback is the more difficult access to the blades that has to be done on the outside of the turbine.

Weight Reduction of Direct-Drive Wind Turbine Generators

1.2.2

In the past several approaches were suggested to reduce the weight of direct-drive generators. The first step was to use a permanent magnet generator instead of electrical excited generators which has been done by Enercon since the early nineties [116].

Besides this method, which is widely used in the industry by now, there exist a couple of methods that can be split up in four categories according to [136]:

Load or load path reduction: This approach aims to reduce the amount of mass by decreasing the load on the structure by changing the design of the support structure. This involves either using iron less generators [143] or keeping the distance between the air gap and the bearing of the rotor as small as possible. [41, 136]

Size reduction: This method proposes to increase the current or the flux in the air gap to produce the same amount of torque at a smaller diameter and/or axial length of the generator. Various ways to accomplish this increase in flux density have been proposed. The methods include using superconducting generators [1, 81, 101], better cooling by either forced air or water cooling or transverse flux machines [37, 168]

Use of lighter materials: This approach uses light weight materials (mainly aluminium, carbon fibre) to reduce the weight of the support structure. However, the price of these materials are significantly higher than the more commonly used structural steel. The life cycle cost need therefore be carefully analysed. [100]

Flexibility: This method was proposed in [136] and [138]. The idea is to use designed flexibility to reduce weight of the support structure of the generator. The method can be applied to the rotor as well as the stator side. [136] investigated the feasibility of this method taking static forces in the generator into account

Besides the approaches above, there were several investigations on optimising the support structure of direct-drive wind turbines. [145]

gives an overview of all possible topologies for the support structure of direct-drive turbines, including topologies with one two and three bearings. [104, 175, 176] covers structural optimisation for direct-drive wind turbine generators and [118] developed a slip-synchronous permanent magnet generator.

1.2.3

Functions of the Generator Rotor Support Structure

The structure in the rotor of a direct-drive wind turbine generator has to fulfil the following functions. The performance of a certain design can thus be measured by how well these functions are fulfilled.

1. Hold the electro-magnetic active material in place relative to other electro magnetic active parts on the rotor. This ensures that all electro-magnetic active parts move synchronously. The placement of the electro-magnetic active parts on the rotor is crucial, because a displacement relative to each other will influence the performance of the generator.
2. Transmit the torque generated by the blades from the hub to the electro-magnetic active parts on the rotor, where the electro-magnetic torque is applied to the structure.
3. Hold the electro-magnetic active parts in place relative to the electro-magnetic parts on the stator, i.e. maintain the air gap length between stator and rotor. To do this any attractive forces between stator and rotor need to be transferred to the supporting element that connects the rotor and the stator, i.e. the bearing.

Another factor that influences the performance of the structure is its weight and its cost. The three functions mentioned above should be fulfilled with as little weight as necessary.

1.3

Magneto-Mechanical Coupling and Vibrations in Electric Machines

The coupling between magnetic fields and the mechanical world has been at the interest of research endeavours for as long as Maxwell's Equations have been around. In fact, one of the original equations that Maxwell wrote down in 1865 was the Lorentz force equation [66, p. 22].

Since electric machines depend heavily on this interaction, it was always at the heart of electric power generation as well as electric motors. In that sense, the development and research on electric

machines was always also partial the research on magneto-mechanical coupling.

According to [148, p. 145], the derivation of the magnetic and electro static forces from an energy principle has first been proposed by the Dutch mathematician Korteweg in 1880 [79]. It was further developed by Helmholtz in [61]. Heaviside, who also brought Maxwell's equations into the form we still use today, picked up the idea and formed stress tensors from the idea in his work '*On the Forces, Stresses, and Fluxes of Energy in the Electromagnetic Field*' [60].

In the beginning, the coupling could only be accounted for on a global variable scale. The research on magneto-mechanical coupling changed radically when the finite element method was introduced both for electro magnetic fields and elastic deformations. Now, it was possible to calculate local displacements and magnetic fluxes and the magneto-mechanical coupling could be analysed on a local level rather than a global level.

Computation of Magnetic Forces in Finite Elements

1.3.1

The first paper to exploit the finite element method to calculate magnetic forces were J. Coulomb and G. Meunier in their papers from 1983 and 1984 [27, 28]. They discuss the calculation of the magnetic force acting on a body. For that, the principle of virtual work is used. They already discuss the problems arising using Maxwell's Stress Tensor and proposes most of the techniques introduced in Sec. 2.5.8. Further, the moving mesh associated with a distorted body is mentioned. This method has been vastly implemented and is seen as the standard for calculating magnetic force in either edge elements [17, 125] and other finite elements [107]. Various papers address the problem of comparing various formulas of calculating forces [77, 105, 123]

[62] picks up the topic and includes the underlying material and its deformation into his considerations. This is done for various magnetic materials including permanent magnets. It addresses a problem at the heart of the principle of virtual work which assumes a virtual displacement. However, this displacement will have an influence on the magnetic field. This opens up the discussion about energy and co-energy and how the magnetisation of permanent magnets behaves under deformation.

[135] gives a detailed outline over surface forces between arbitrary linear materials and permanent magnets.

1.3.2

Modelling the Magneto-Mechanical Coupling

Besides [62], no-one of the above mentioned publications took into account the effects of the displacement on the magnetic field formulation. [31, 32] formulates a linear coupling in both directions for the static case. Although, it takes magnetostriction into account, the dynamic coupling terms are neglected. However, the modal analysis done on the stator of an electric machine includes modal participation factors, to describe which modes are excited by a certain distribution of magnetic forces. It is, however, not a coupled eigenvalue analysis.

[124] derives a fully coupled monolithic formulation for the interaction between mechanical deformation and magnetic fields. It is applied to a simple system consisting of a yoke, a coil and a moving armature. Belahcen extends this approach and uses it to analyse electric machines [11–13, 48]. This formulation is used to calculate extensive time dependent problems of vibrational behaviour of electric machines.

[36] and [120] derive the system equations for magneto-mechanical coupled systems, starting from the Lagrange equations. The variational formulation for electro-mechanical coupled dynamics is also covered in [2, 131] and [146]. The derivation for magnetic fields is almost analog.

1.3.3

Vibrations of Electric Machines

The investigation of vibrational behaviour of electric machines is almost as old as the machines themselves. In the past, there were mainly two reasons to look into vibrational behaviour of electric machines. The first interest is the torsional vibrational behaviour for electric machines. This is mainly caused by torque ripple and consequently the aim of the research was the reduction of torque ripple [97, 112, 134]. The methods to reduce vibrations mainly focus on changing the current input of the machine to counteract the torque ripple created by either the supply harmonics or the torque ripple created by torque cogging and space harmonics. Other techniques to reduce torque cogging incorporate skewed rotors [70] or changing the magnet layout of the rotor using unsymmetrical rotors. [15] describes various design techniques for reducing cogging torque in permanent magnet drives.

The other area of interest is noise generation of electric machines. This is mainly caused by the oscillations of the stator [51, 86, 153]. The topic has also relevance for wind turbines as noise annoyance is a problem for on-shore wind turbines [111]. The generator is one

of the main sources of noise in such a turbine.

The dynamic modelling of the structural parts of the turbine are complex because the stator lamination stack shows nonlinear behaviour. How to approximate this nonlinear behaviour has been the topic of many research projects [55, 95, 114, 140, 141, 161, 162, 166, 169]. All approaches model the stator lamination as an orthotropic material. The macro-mechanical parameters for this material are either determined by vibration measurements [95, 169] or by modelling a part of the stator lamination in great detail to extract the parameters from that model [114]. However, all above mentioned papers discuss stator laminations which are not separated. As far as the author is aware there is no research on the dynamics of interlinked and segmented stator laminations.

Approximating the nonlinear behaviour by a linear model using orthotropic material models, makes it possible to include the dynamic behaviour of lamination in a modal analysis to estimate resonance frequencies. Nonlinear dynamics decreases the accuracy of vibration behaviour that is approximated using these modes.

Reducing the vibrations of permanent magnet (PM) direct-drive generators has been the focus of previous research. Valavi et al. [155–157] identifies which design parameters in such a generator are of importance for the harmonic excitation forces. They neglect the two-way coupling that is analysed in this thesis.

Model Reduction for Electric Machines

1.3.4

Model order reduction methods for large linear time invariant dynamic systems can be split in three categories [3]: Singular value decomposition (SVD) based, Krylov-based and the Singular Value Decomposition Krylov based method. These methods project the system onto a subspace which is of much smaller dimension. The three methods mentioned above have various approaches to find the smaller subspace, which should contain the dominant dynamics of the system in order to yield an accurate approximation.

The methods introduced in [3] approach the system that is reduced in state space configuration. Reduction for finite element models work differently, as here no input and output is given. Instead all DoFs of the model can be input and output.

The methods used in structural dynamics [8, 130, 132] are singular value decomposition based methods. Because the matrices encountered in a structural FE model are square, the SVD becomes an eigenvalue problem. For structural systems, the eigenvalues and modes identified this way correspond to the physical properties of resonance frequencies and mode shapes.

Although SVD-based methods have been around for a while and are commonly applied in structural dynamics, no survey on the practicality of these methods for magnetic fields in electric machines has been conducted. In the case of electric machines, the singular value decomposition does not yield physical quantities as it does in structural dynamics. The application to electric machines facilitates the identification of a dominant subspace the system is projected on.

Another advantage of this approach is its easy integration into existing structural model order reduction techniques when reducing magneto-mechanical coupled systems.

1.3.5

Topology Optimisation of Electric Machines

Using topology optimisation to reduce the deformation caused by magnetic forces, has been around for a couple of years. [72] uses topology optimisation to reduce the vibrations caused by a harmonic magnetic force. [63] uses the same method to optimise a static magneto-mechanical coupled system. [88] uses topology optimisation to not only minimise the compliance of the structure, but simultaneously maximise the magnetic force.

The systems used in these studies are all not generators or motors but simple actuators. Nonetheless the developed methods can be used in electric machines too. [69] uses topology optimisation in combination with a genetic algorithm, to maximise the torque of the machine. Manufacturability was specifically taken into account in a second optimisation step.

All of these methods however do not look at the dynamic behaviour of the systems at hand or do not look at rotating electric machines.

1.4

Problem Definition

The project aims at developing the needed knowhow and methodology to properly model the magneto-mechanical coupling, determining the dynamic behaviour and the electro-magnetic performance of the generator/drive-train of a direct-drive wind turbine. Modelling the electro-dynamics between the rotor and the stator will enable designers and engineers to converge to the best design for future generators by properly balancing cost, performance and lifetime.

In particular, the project was planned to reach the following objectives:

- Modelling:
 - Determine the appropriate modelling approach for the magneto-mechanical dynamics in generators in order to design for the lowest weight of the structure, which facilitates a lower cost of energy.
 - Build a model that can describe the electromagnetic and structural phenomenon determining the dynamical behaviour and the electromagnetic performance of the generator, taking into account the strong two-way magneto-mechanical coupling. Such a model must be validated in such a way that it accurately describes the phenomenon most relevant for performance, fatigue and wear.
 - Identify modelling techniques and calculation methods, that make the modelling of coupled dynamics possible in the future for larger generator size and more complex geometries.
- Design:
 - Clarify the role of the magneto-mechanical behaviour of the generator/drive-train in determining the design trade-offs of the overall turbine design.
 - Identify methods to optimise the design of direct-drive wind turbine generators.
 - Develop innovative ideas for the design of future drive-train/generator systems.

Thesis Outline

1.5

According to the problem definition in Sec. 1.4 the thesis is structured in three parts. The first part will cover the modelling techniques appropriate to simulate the magneto-mechanical coupling in wind turbine generators. The second part will cover the application of the previously introduced modelling techniques to large direct-drive wind turbine generators and the optimisation of them. The last part draws the conclusions and gives an extensive overview over possible research topics in the future.

Fig. 1.5 shows an overview how the various topics of the thesis are related to each other.

1.5.1

Part I – Modelling Magneto-Mechanical Coupled Dynamics

Part I covers the modelling of magneto-mechanical coupling in wind turbine generators, the validation of the models and model reduction techniques. It consists of the chapters 2, 3 and 4.

The *second chapter* of the thesis starts with the basics of magnetic fields modelling and continuum mechanics. As most of the modelling theory has been done in the past, this introduction is rather short. On the contrary, the chapter is rather specific on how the two physics are coupled. Furthermore, the coupled eigenvalue problem is introduced in detail.

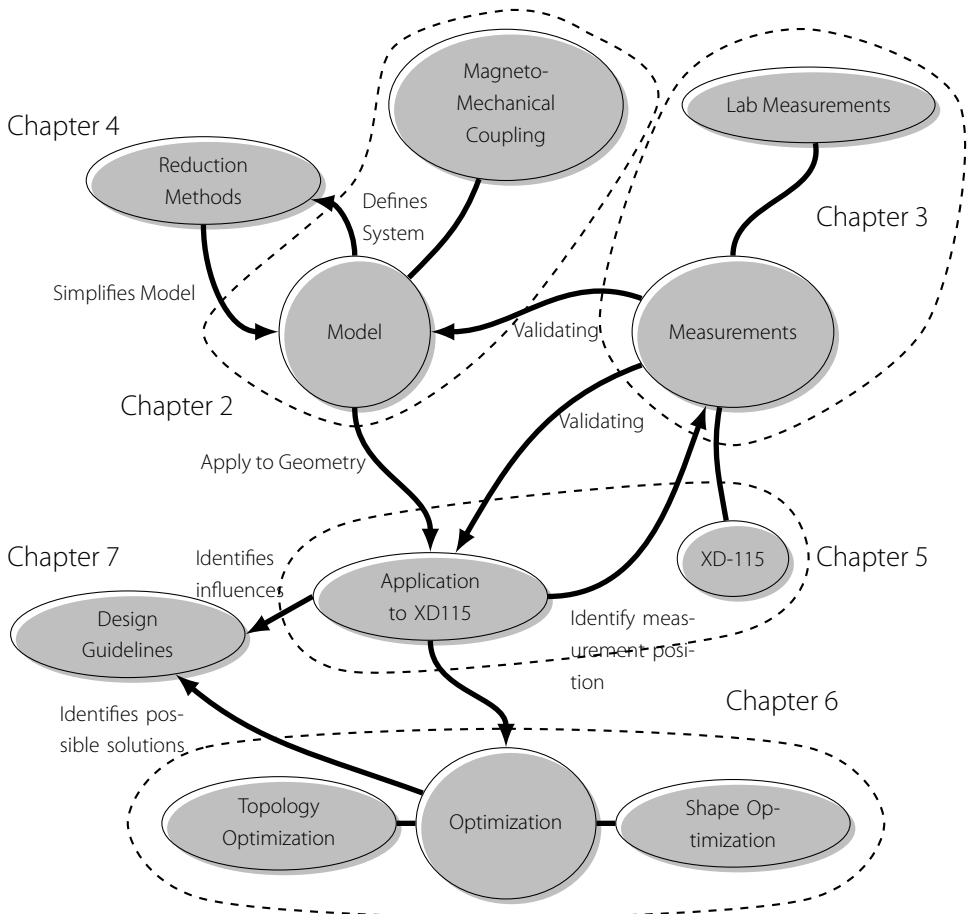


Figure 1.5

Various topics of the thesis and how they are interlinked

The *third chapter* covers validation measurements for the magnetic coupling introduced in Chapter 2. These measurements are necessary to insure that the techniques introduced previously reflect

reality and indeed can be used for the optimisation of wind turbine generators. For the validation a test set up consisting of two permanent magnets and a flexible beam was used.

The *fourth chapter* covers reduction methods for quasi-static magnetic field problems. These problems are discovered when magnetic forces have to be calculated in the time domain. The methods introduced are based on a modal analysis of quasi-static magnetic fields which will be introduced shortly. In the linear case various reduction methods known from structural dynamics can be used. It will be shown that these reduction methods are also applicable to magnetic field problems. Further, the chapter introduces some ideas how to reduce magneto-mechanical coupled systems.

Part II – Application to Large Off-Shore Wind Turbine Generators

1.5.2

In the second part of the thesis the focus shifts from methods towards application. It consists of the chapters 5 and 6.

In the *fifth chapter* the methods developed in Chapter 2 are applied to the XD-115, yielding an accurate analysis of the excitation forces and system dynamics of the generator. The models are validated with in-situ vibration measurements of the turbine.

In *Chapter six* the models developed in chapter five are used to explore design improvements for the current design. For this shape optimisation as well as topology optimisation is used. Further, a short look at topologies including two bearings and their optimal design was taken.

Part III – Conclusion and Outlook

1.5.3

The last part contains the conclusion and the outlook into the future.

In the *seventh chapter* the various effects and influences identified during the research leading up to this thesis are summarised. Their influence is mentioned and possible solutions and changes to the current design are discussed.

The *eighth chapter* draws the conclusions for the thesis and identifies opportunities and challenges future research can concentrate on.

1.6

Scientific Contributions

This thesis makes scientific contributions to the field of magneto-mechanical coupling, design of wind turbine generators and model reduction for quasi-static magnetic fields:

- A consistent set of equations for modelling magneto-mechanical coupled vibrations in electric machines is formed. For that all relevant modelling techniques and equations needed to be collected from various sources in literature. It is differentiated carefully between effects that are important for electric machines and effects that play a minor role. (Chapter 2).
- The damping terms for a monolithic formulation resulting from the magneto-mechanical coupling are added to the formulation for monolithic magneto-mechanical coupling formulation found in literature. (Chapter 2).
- This formulation is cast in a monolithically coupled eigenvalue formulation which makes it possible to see the effects of the magnetic field on the modal parameters. (Chapter 2).
- The modelling technique introduced is experimentally verified (Chapter 3).
- It is investigated to what extent the concept of modes of magnetic fields can be used for model order reduction of time depend analysis and eigenvalue problems (Chapter 4).
- The importance of the two-way magneto-mechanical coupling is investigated for direct-drive wind turbine generators (Chapter 5).
- A dynamic analysis of the XD-115 wind turbine generator is conducted, establishing structural excitation sources and how they interact with the resonance frequencies (Chapter 5).
- Optimised generator rotor designs for the XD-115 are presented, minimising the amount of structural material used while retaining the same compliance (Chapter 6).
- Topologies incorporating the king pin design are analysed by employing the same method. This way optimal bearing placement and density distributions for this type of topology can be identified (Chapter 6).
- An overview is given of the parameters which influence the dynamic behaviour of the structural part of the generator and its excitation. Recommendations are given how to avoid unwanted vibrations (Chapter 7).



PART I

Modelling Magneto-Mechanical
Coupled Dynamics

This Chapter is based on the papers:

Kirschneck, M., Rixen, D.J., Polinder, H., van Ostayen, R.A.J.
Electro-Magneto-Mechanical Coupled Vibration Analysis
of a Direct-Drive Off-Shore Wind Turbine Generator.
Journal of Computational and Nonlinear Dynamics. 2014

Abstract:

The dynamic behaviour of wind turbine generators is influenced by the coupling between the structural dynamics and the magnetic field in the generator. Multi-physical modelling necessitates specialised approaches to accurately capture the dynamics and, especially, the influence of the magnetic field. This chapter introduces an approach for a multi-physical modal analysis that makes it possible to predict the dynamics of strongly coupled magneto-mechanical systems.

2.1

Introduction

This chapter will introduce the necessary theoretical background for modelling magneto-mechanical coupled systems including permanent magnets (PMs) and coils in 3D. Although in theory the method can be used for all applications where structural deformation and quasi-static magnetic fields interact, the introduced formulation will concentrate on describing vibrations in electric machines. With that in mind, certain simplifications, such as neglecting hysteresis of the magnetic field and magnetostriction or using orthotropic materials to simulate the lamination, will be applied to the formulation. It might be possible, therefore, that for other applications some of the introduced simplifications cannot be applied and in fact will yield wrong results for those systems.

As this is a multi disciplinary thesis, the basics of both physics will be explained in detail. Therefore, depending if the reader has a mechanical or a electrical engineering background, some of the parts of this chapter might seem trivial and can be skipped. This chapter will start with a general introduction to magneto-mechanical couplings and will include more details with every section. Several aspects are, thus, revisited in successive sections, increasing the detail and complexity of the model.

The chapter starts with a general description of magnetic fields in Sec. 2.2. That subsection will cover the basics of modelling magnetic fields. It can be skipped by the reader, when he/she is familiar with Maxwell's equations and modelling of magnetic fields. Next, the modelling of magnetic fields and mechanical systems is introduced in Sec. 2.3. The section follows the structure in [173], which introduces lumped coupled models. It is intended to give a better insight into the concepts of magneto-mechanical coupling such as the relation between co-energy and energy, but the content will hardly be used in the rest of the thesis. Readers that are already familiar with these concepts can skip Sec. 2.3. In Sec. 2.4, the continuous version of the coupled magneto-mechanical formulas will be introduced. This section is fundamental to understand Sec. 2.5, where the equations from Sec. 2.4 will be discretised. However, for the rest of the thesis, mainly the discretised formulas from Sec. 2.5 will be used. Sec. 2.6 will finally introduce the monolithic eigenvalue problem used for analysing the magneto-mechanical coupled dynamics in electric machines.

2.1.1

Strong Coupling vs. Weak Coupling

In literature, there is some ambiguity about the terms strong coupling and weak coupling. For clarity, the terminology used in this

thesis will be explained briefly. It should be noted that the definition differs to some definitions found in literature, e.g. [53].

One-way coupling: A one-way coupled system takes the coupling in only one direction into account. This can either be the dependency of the magnetic field on the deformation of the structure or the magnetic force affecting the structural deformation. Usually, the effect of the magnetic field on the mechanical system, i.e. the magnetic forces, are accounted for. From a dynamic point of view, the magnetic forces in a one-way coupled system can be treated as excitation forces for the mechanical system, as they do not depend on the mechanical system itself.

Two-way coupling: For two-way coupled systems, the magnetic field affects the structural dynamics as well as the displacement affects the magnetic field.

Strong coupling: A strong coupling is a coupling that has a large influence on the system. The system should be analysed taking both physics into account.

Weak coupling: Contrary to a strongly coupled system, a weakly coupled system is a system where the effects of one physical domain hardly affects the other physically domain. An analysis of two physical domains separately yields a good approximation of the system.

The modelling techniques covered in this chapter are suited to describe any of the system types above. Depending on the type of coupling, certain parts of the introduced equations and terms can be omitted.

Basic Magnetic Field Modelling

2.2

This section will introduce the basics of modelling magnetic fields and the electric circuits generating them. It will cover energy in magnetic systems and lumped modelling to give a general overview of the interactions between magnetic fields and mechanical forces and displacements.

Maxwell's Equations

2.2.1

By adding the displacement term in his publication 'A *Dynamical Theory of the Electromagnetic Field*' [99] to the set of equations describing the dynamics of electro-magnetic fields, James Clerk Maxwell completed our understanding of electro-magnetic dynamics.

Before that, various laws describing certain aspects of the electromagnetic field were previously discovered by Ampere, Gauß and Faraday.

Ampere formulated the law that bears his name in 1826. It describes the relation between magnetic fields and currents. It reads as

$$\oint_{\partial S} \vec{H} \cdot d\vec{l} = \iint_S \vec{j} \cdot d\vec{S} \quad (2.1)$$

where \vec{H} denotes the magnetic field, \vec{j} the electric current density and $d\vec{l}$ an infinitesimal small part of the closed path ∂S , which encloses the surface S . Ampere's law makes it possible to calculate the field strength of magnetic fields depending on the path of a field line and the material. It is, therefore, directly used in analytical models of magnetic circuits and electric machines to estimate the magnetic field at a certain point.

Faraday's law describes the interaction of a closed loop of a conductor and a changing magnetic field.

'The induced electromotive force in any closed circuit is equal to the negative of the time rate of change of the magnetic flux through the circuit.'

from [59]

When Faraday published his experimental work in 1831 the law was only formulated in words [30]. Maxwell later casted the ideas of Faraday in mathematics which yielded the formulation (2.3a).

The third important law that made its way into Maxwell's formulation is Gauß's law. It was formulated in 1835 by Carl Friedrich Gauß. The law describes the relation between a distribution of electric charges and the resulting electric field for media with constant permittivity ϵ_0 .

$$\nabla \cdot \vec{E}_i = \frac{q}{\epsilon_0} \quad (2.2)$$

where \vec{E}_i is the electric field that is created by a charge density, q the electric charge density and ϵ_0 the vacuum permittivity.

The last of the four equations that constitute Maxwell's equation is Gauß's law for magnetics, which is named so because of its resemblance to the electric Gauß law in (2.2).

At the time when Maxwell published his 'A Dynamical Theory of the Electromagnetic Field' [99], the three laws above were already known. Maxwell assembled these equations to a complete set of equations describing electro-magnetic dynamics. Some of the equations needed to be extended or adapted. Faraday's law needed to be formulated in mathematical terms all together. This way, Maxwell compiled his theory to comprise of 20 equations. The final set of

equations, the one that is still used today, was not formulated before 1884 when Oliver Heaviside used vector notation to rewrite the equation from 1864. (2.3) shows Maxwell's four equations as formulated by Heaviside.

$$\nabla \times \vec{E} = -\frac{\partial \vec{B}}{\partial t} \quad (2.3a)$$

$$\nabla \times \vec{H} = \vec{j} + \frac{\partial \vec{D}}{\partial t} \quad (2.3b)$$

$$\nabla \cdot \vec{D} = q \quad (2.3c)$$

$$\nabla \cdot \vec{B} = 0 \quad (2.3d)$$

where \vec{B} denotes the magnetic flux density, \vec{E} the electric field and \vec{D} the electric displacement. Assembling these equations using the constitutive modelling introduced in Sec. 2.2.2 will result in a 2nd order partial differential equation in space and time. The resonance frequencies of this equation for systems of the size of electric machines are so high that they play no role for magnetic fields in electric machines. Therefore, the so called displacement term $\frac{\partial \vec{D}}{\partial t}$ can be dropped from (2.3b) leaving a first order system of partial differential equations. This set of equations is called the quasi-static Maxwell's equations.

Constitutive Modelling

2.2.2

To be able to solve Maxwell's equations (2.3), it is necessary to do some constitutive modelling of the materials. For the conductivity of materials, a linear material law is assumed with a constant conductivity.

$$\vec{j} = \gamma \underbrace{(\vec{E}_s + \vec{E}_i + \vec{v} \times \vec{B})}_{\vec{E}'} + \vec{j}_{source} \quad (2.4a)$$

$$\vec{D} = \epsilon \vec{E} \quad (2.4b)$$

where γ denotes the conductivity of the material and \vec{v} the velocity of the conducting structure. (2.4b) is given here for completeness, as it is needed to solve all parts of Maxwell's equations. It is not used for the rest of the thesis.

\vec{E} can be split up in two parts, a solenoidal part, \vec{E}_s , which is induced by changing magnetic fields and a rotation free part, \vec{E}_i , which is created by potential gradients. \vec{j}_{source} denotes an additional source term for magnetic fields, which accounts for all sources of magnetic fields that are not created by electric potential gradients or the Lorentz' force.

For moving structures the Lorentz force, \vec{E}' in (2.4), instead of Faraday's law (2.3a) needs to be used to compute the electro motive force (EMF). For fixed structures, the second term of \vec{E}' is zero.

For the relation between the magnetic field and the magnetic flux density, the constitutive modelling is more complex, as several different materials are included in the models presented here. Most materials, such as air or copper or plastic, are linear magnetic materials. That means, a linear relation between the magnetic flux density and the magnetic field is sufficient to describe the material behaviour

$$\vec{B} = \mu \vec{H} \quad (2.5)$$

where μ denotes the permeability of the material. Permanent magnets are special, as they have a remanent flux density \vec{B}_r that is still present when there is no external magnetic field is applied to the magnet. Their relation can be expressed by

$$\vec{B} = \vec{B}_r + \mu \vec{H} \quad (2.6)$$

Because of this remanent flux, the permanent magnet can act as a source of magnetic fields.

The last types of material are ferromagnetic materials where the relation between the flux density and the magnetic field is expressed as nonlinear function that includes hysteresis and saturation.

$$\vec{B} = \vec{B}(\vec{H}) \quad (2.7)$$

Usually, the nonlinear material law is expressed in terms of the norm of the magnetic field and the magnetic flux density. The direction of both fields is the same. Therefore, only the magnitudes of the fields need to be related to each other.

Nonlinear material behaviour can usually be encountered in ferromagnetic materials such as iron or cobalt. These materials exhibit saturation, which leads to a flattening H-B curve at strong magnetic fields. Saturation is an important effect in electric machines, because most machines are designed to operate in or close to saturation. It affects the coupling between the magnetic domain and the mechanical domain. An accurate magneto-mechanical model will, thus, need to account for this effect.

Another important effect for ferromagnetic materials is hysteresis. This effect is not easily incorporated into a linear magneto-mechanical model. In this thesis, we develop our understanding-modelling of the electromagnetic-structural coupling without considering hysteresis.

Energy in Magnetic Fields

2.2.3

Energy of magnetic fields, and how to calculate it, is fundamental for the discretisation of the magnetic field and the coupling with the mechanical system. While the calculation in nonlinear and linear magnetisable materials is rather straight forward, the calculation of energy in permanent magnets is still a topic that is being debated [23, 50, 92, 147].

The energy in permanent magnets has a fundamentally different character as in magnetisable media, such as air or iron. In general, the specific magnetic energy for a domain can be calculated by

$$w_{mag} = \int_{\vec{B}_0}^{\vec{B}} \vec{H}(\vec{B}) \, d\vec{B} \quad (2.8)$$

B_0 denotes the value of the magnetic flux density for which the energy w_{mag} is equal to zero. For magnetisable media, this point is easily identified at $\vec{B} = 0$, $\vec{H} = 0$. This yields the following expression for the specific energy for linear magnetic materials

$$w_{mag} = \int_0^{\vec{B}} \frac{\vec{B}}{\mu} \, d\vec{B} = \frac{\vec{B}^T \vec{B}}{2\mu} \quad (2.9)$$

In (2.9), \vec{B} denotes an integration variable. This lower integration limit holds even for nonlinear materials that are not permanently magnetised.

For permanent magnets, $\vec{B} = 0$ and $\vec{H} = 0$ do not coincide at the same point as (2.6) applies. This is shown in Fig. 2.1. Instead, the BH-curve passes the abscissa at $H = H_c$ and the ordinate at $B = B_r$. H_c is the value of H for which $B = 0$ within the permanent magnet. It is called the coercivity.

[147] explains thoroughly that for permanent magnets the distinction between recoverable energy and non-recoverable energy needs to be made. Recoverable energy, is the energy stored in a permanent magnet that can be used for generating magnetic fields outside the permanent magnet. Non-recoverable energy is energy that cannot be used for this purpose. It was stored in the magnet when it was magnetised and will be transformed to heat by hysteresis losses in the magnet.

According to [147], the recoverable energy for a permanent magnet is zero at $\vec{B} = \vec{B}_r$ and $\vec{H} = 0$. Setting $B_0 = B_r$ and inserting (2.6) into

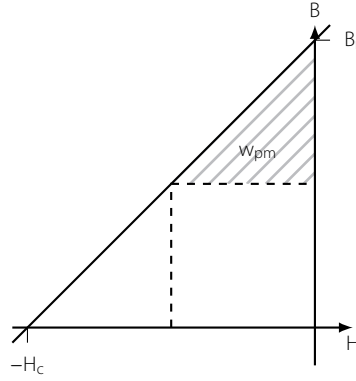


Figure 2.1
magnetisation curve of a
permanent magnet and its
recoverable energy

(2.8) yields

$$\begin{aligned}
 w_{pm} &= \int_{B_r}^B \frac{\overset{\circ}{\vec{B}} - \vec{B}_r}{\mu} d\overset{\circ}{\vec{B}} = \frac{\overset{\circ}{\vec{B}}^T \overset{\circ}{\vec{B}}}{2\mu} - \frac{\vec{B}_r^T \overset{\circ}{\vec{B}}}{\mu} \Big|_{B_r}^B \\
 &= \frac{\vec{B}^T \vec{B}}{2\mu} + \underbrace{\frac{\vec{B}_r^T \vec{B}_r}{2\mu}}_{w_{pm,o}} - \frac{\vec{B}_r^T \vec{B}}{\mu} = \frac{\vec{H}^T \vec{H}}{2} \mu
 \end{aligned} \tag{2.10}$$

for permanent magnets. $w_{pm,o}$ denotes the maximal recoverable energy in the magnet, represented by the whole triangle formed by the axes and the magnetisation line.

2.2.4

1D Magnetic Circuit

This subsection introduces the equations for 1D magnetic circuits. Although not used extensively afterwards in this thesis, these equations will illustrate the basic relations between fundamental quantities of magnetic and electric fields. Furthermore, they can explain certain effects of magneto-mechanical coupling, which will be discussed in Sec. 3.2.2.

Maxwell's equations can be simplified to a set of linear equations, when certain assumptions are made. Using Ampere's law in integral form (2.1) and assuming that the magnetic field is constant within each material, a 1D magnetic circuit equation can be established [46].

$$\sum_n H_n l_n = I \tag{2.11}$$

(2.11) can be derived from (2.1) by dividing the path of a magnetic flux line in n sections. Within each section the magnetic field is constant over the length l_n . l_n denotes the length of the flux line

that is followed in the n^{th} section and H_n the according magnetic field magnitude. Adding the magnetic flux over all sections of the flux line yields the total current I that particular flux line encloses.

Applying (2.11) results in a formulation for magnetic flux lines that is similar to electric circuits. Each of the n elements can be seen as a component of a magnetic circuit. Such a circuit comprises of magnetic reluctance, magnetic fluxes and magneto motive forces (MMF). These elements corresponds to an Ohmic resistance, a current, and the electro motive force in electric circuits, respectively. More complex concepts, such as saturation or fringe effects, cannot be taken into account with this model. However, the magnetic circuit makes it possible to estimate the magnetic flux density of more complicated magnetic devices such as electric motors or transformers without solving partial differential equations first.

The magnetic circuit is governed by a handful of equations. The MMF drives the magnetic flux through the magnetic circuit. It can be seen as a potential difference within the circuit similar to the voltage in an electric circuit. The MMF which is generated by a coil can be computed by

$$\mathcal{F}_{coil} = Ni_c \quad (2.12)$$

where i_c denotes the current in the coil and N the number of turns. This law is derived from Ampere's law (2.1), which relates the magnetic field to the total current it encircles. For permanent magnets, the MMF can be calculated by

$$\mathcal{F}_{pm} = \frac{H_{pm}l_{pm}}{\mu_{r,pm}} \quad (2.13)$$

where \mathcal{F}_{pm} denotes the MMF created by the permanent magnet, H_{pm} the magnetic field within, l_{pm} the length of and $\mu_{r,pm}$ the relative permeability of the permanent magnet.

The total magnetic flux of the circuit can be calculated by dividing the MMF by the magnetic 'resistance', called reluctance

$$\Phi_B = \frac{\mathcal{F}}{\mathcal{R}} \quad (2.14)$$

where \mathcal{R} denotes the reluctance. It can be calculated by

$$\mathcal{R} = \frac{l}{\mu A} \quad (2.15)$$

where l denotes the length of the material within the magnetic circuit with the permeability μ and A the cross section of the material perpendicular to the field line. It is, thus, assumed that the cross

section of the material is constant within one section. This formula can be used for any magnetic material that shows linear magnetisation behaviour. For more complicated systems several reluctances can be placed in series or parallel. The laws for calculating the total reluctance are identical to the calculations of Ohmic resistances in series or parallel.

2.3

Lumped Magneto-Mechanical Systems



Figure 2.2
The three different parts of the coupled system and how they interact with each other

In Sec. 2.2.1, the focus was laid on basic magnetic modelling. In this section, the focus shifts towards the interaction between the magnetic field and the mechanical system.

To get a fundamental understanding of how magneto-mechanical coupled systems work, we will start examining lumped systems. Analysing these systems can explain many phenomena of magneto-mechanical coupled systems. For that, the interface between the three subsystems depicted in Fig. 2.2 are considered. The inside of the three systems will be considered later in Sec. 2.4 and are treated as black boxes for now.

There are some fundamental differences for magneto-mechanical interaction between systems in which the magnetic field is created by a permanent magnet and systems with a magnetic field generated by a coil. In this section, both types of systems will be analysed to show the difference and give a deeper understanding of magneto-mechanical coupling.

2.3.1

Systems Including Coils

Fig. 2.3 shows a magneto-mechanical coupled system, in which the magnetic field is created by a coil. This system contains an electric circuit as well as a mechanical system. The two physics are coupled in one or two directions by means of a magnetic force and/or a dependency of the magnetic field on the geometry and, thus, on the displacement of the mechanical system.

As mentioned above, the magnetic field is considered to be a black

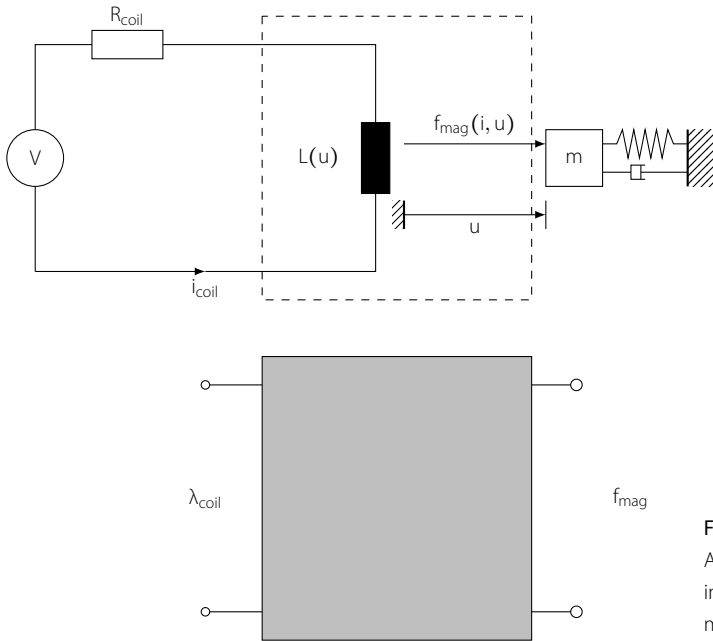


Figure 2.3
A mechanical and an electric system interacting by means of a magnetic field

box with energy entering and leaving the system. It creates forces acting on the mechanical system and is created by a current flowing through a coil. This approach yields a black box with two terminals. The mechanical terminal consists of the magnetic force and the displacement, whereas the circuit terminal consists of the two variables, coil current and flux linkage. The flux linkage of a coil λ_c is the total magnetic flux that flows through the coil, which is denoted by Φ_c . The flux linkage of the coil depends on the displacement u as well as on the current in the coil i_c

$$\lambda_c = \lambda_c(u, i_c) \tag{2.16}$$

where λ_c is the flux linkage of the coil. From this relation, it can be concluded that the flux linkage of the coil will change, when the mechanical system deforms.

A similar relation can be established for the magnetic force

$$f_{mag} = f_{mag}(i_c, u) \tag{2.17}$$

When the current increases the magnetic force increases. It can also be determined that the displacement has an effect on the force.

Energy and Co-energy Considerations

Applying the principle of energy conservation, it is possible to make some fundamental statements about the coupled system in Fig. 2.3.

The black box in that figure contains a magnetic field, which is considered to be lossless. The only way for exchanging energy with another system is either by means of an electric power applied to the coil or by a mechanical power. The relation for the energy change in the dashed box can, therefore, be written as

$$\frac{dW_{mag}}{dt} = i_c \frac{d\lambda_c}{dt} - f_{mag} \frac{du}{dt} \quad (2.18)$$

In (2.18), W_{mag} denotes the total energy stored in the magnetic field. This energy is not known, but some statements about the energy change can be made. The first term on the right hand side of (2.18) is the power input through the electric circuit, which is determined by the change of the total flux multiplied with the coil current. The second term denotes the power input through the mechanical system. The minus sign in front of the second term results from the definition that the force acts on the mechanical system and, thus, introduces energy into the mechanical system, while, reducing the energy of the magnetic system, when the magnetic force and the displacement it causes point in the same direction.

Multiplying (2.18) with dt yields the conservation of energy for a magnetic field:

$$dW_{mag} = i_c d\lambda_c - f_{mag} du \quad (2.19)$$

Because the system at hand is a conservative system, the energy for a certain set of variables is unique. It does, thus, not depend on the way how the system got into its current state [46, 173]. The energy for a certain configuration can thus be computed by

$$W_{mag}(\lambda_c, u_o) = \int_0^{\lambda_c} i_c(\lambda_c, u_o) d\lambda_c \quad (2.20)$$

where λ_c denotes an integration variable and u_o an arbitrary system displacement.

(2.16) and (2.17) show that only two of the four variables introduced so far can be set independently. Therefore, two of the variables describe the total energy sufficiently and the energy can be expressed by:

$$W_{mag} = W_{mag}(u, \lambda_c) \quad (2.21)$$

In fact, any two of the four variables u, i, λ_c and f_{mag} are sufficient to describe the energy stored in the magnetic field distinctively. This is because they can be expressed by one another. It is possible to use a Legendre transformation to express the energy by any of the four variables, identical to thermodynamics where this can be done for the state functions [22]. Using such a transformation, it is possible to substitute λ_c for the current i_c in (2.21) resulting in the co-energy

$$W'_{mag} = W'_{mag}(u, i_c) \quad (2.22)$$

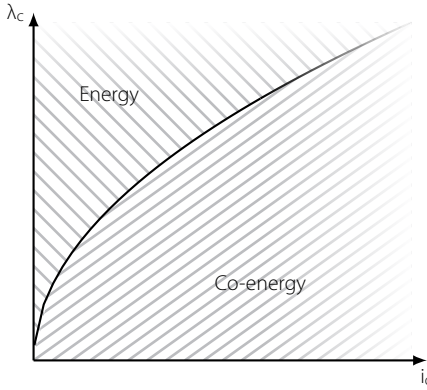


Figure 2.4

Illustration of energy and co-energy for a system with a nonlinear relation between λ_c and i_c

and

$$dW'_{mag} = \lambda_c di_c + f_{mag} du \quad (2.23)$$

for the co-energy change of the system. As stated in [46], the integration path does not matter, because the co-energy is a state function, of which the value do not depend on the history of the system. An integration analog to the energy yields

$$W'_{mag}(i, u_0) = \int_0^{i_c} \lambda_c(i) di \quad (2.24)$$

where i denotes an integration variable. Fig. 2.4 shows the relation between energy and co-energy in a magnetic field excited by coils. Using the co-energy simplifies calculations in systems, in which the current in coils is known.

Force-Energy Relations

Assuming a conservative system, the energy in the magnetic field is fully determined by the independent variables u and λ_c . It is possible to take the total derivative of (2.21) yielding

$$dW_{mag} = \frac{\partial W_{mag}}{\partial \lambda_c} d\lambda_c + \frac{\partial W_{mag}}{\partial u} du \quad (2.25)$$

Subtracting (2.25) from (2.19) yields

$$0 = \left(i_c - \frac{\partial W_{mag}}{\partial \lambda_c} \right) d\lambda_c - \left(f_{mag} + \frac{\partial W_{mag}}{\partial u} \right) du \quad (2.26)$$

Because the variables u and λ_c are independent, (2.26) must be true for any combination of du and $d\lambda_c$, resulting in

$$\begin{aligned} i_c &= \left. \frac{\partial W_{mag}(\lambda_c, u)}{\partial \lambda_c} \right|_{u=const.} \\ f_{mag} &= - \left. \frac{\partial W_{mag}(\lambda_c, u)}{\partial u} \right|_{\lambda_c=const.} \end{aligned} \quad (2.27)$$

(2.27) shows that the principle of virtual work can be used to calculate the forces acting on the mechanical part of the system. Furthermore, it is now possible to calculate the exchanged energy between the magnetic field and the mechanical system, which depends on u and λ_c . (2.25) shows that the energy exchanged with the magnetic field can be calculated by:

$$dW_{ex,m} = f_{mag} du \Big|_{\lambda_c=const.} \quad (2.28)$$

assuming that u is the independent variable. In (2.28), $dW_{ex,m}$ denotes the total energy exchanged between the mechanical domain and the magnetic domain. It is positive for energy that leaves the magnetic systems and enters the mechanical system.

Co-energy-Force Relation

For certain systems, it is beneficial to use the current instead of the flux linkage as an independent variable. This is especially true for electric machines, where the current is controlled and, hence, can be considered constant for the force computation. Using the magnetic energy for force calculations in systems, in which the currents are constant, is quite complicated. To clarify this consider the system in Fig. 2.3 again.

(2.16) shows that the flux linkage will change when the displacement changes and the currents in the system are held constant. Because λ_c as well as u change, the force calculation in (2.27) is no longer valid. In this case, energy enters through the coil because $d\lambda_c i_c$ is not longer constant. This energy change has to be taken into account when calculating the magnetic force.

The calculation can be simplified by using the current in the coil as the independent variable. Starting from (2.23) and following the same reasoning as for the energy yields

$$\begin{aligned} \lambda_c &= \left. \frac{\partial W'_{mag}(i, u)}{\partial i} \right|_{u=const.} \\ f_{mag} &= \left. \frac{\partial W'_{mag}(i, u)}{\partial u} \right|_{i=const.} \end{aligned} \quad (2.29)$$

for the magnetic force and the flux linkage. Note that now the force is calculated for a constant current. Analog to the exchanged energy between the magnetic field and the mechanical system, it is possible to define an exchanged co-energy:

$$dW'_{ex,m} = -f_{mag} du \Big|_{i=const.} \quad (2.30)$$

Note that the change of the co-energy is opposed to the change of the magnetic energy for the same force and movement.

It is possible to calculate the force that is associated with a displacement at constant current using the magnetic energy. In that case, an additional term needs to be introduced that accounts for the energy that enters the system during the movement. Using (2.19) we can express the force as

$$f_{mag}(u) = -\frac{dW_{mag}(u, \lambda_c)}{du} + i_c \frac{d\lambda_c}{du} \quad (2.31)$$

Compared to (2.27) we get a correction term that takes the change of the flux density into account. Expressing the energy in terms of the co-energy yields

$$\begin{aligned} f_{mag}(u) &= \frac{d}{du} (\lambda_c i_c - W'_{mag}(u, i)) - i_c \frac{d\lambda_c}{du} \\ f_{mag}(u) &= \frac{d\lambda_c i_c}{du} - \frac{dW'_{mag}(u, i)}{du} - i_c \frac{d\lambda_c}{du} \end{aligned} \quad (2.32)$$

As i_c is constant during the deformation, it can be moved in front of the derivation in the first term and the total derivative can be substituted for a partial derivative in the second term. Multiplication with du yields the same expression as in (2.30) for the magnetic force. In some circumstances, using the co-energy is more convenient from an algebraic point of view. In that case, the current needs to be used as independent variable which might cause some challenges.

The equations for systems including PMs and coils hardly differ from the equations of systems which include coils only. A permanent magnet will introduce an additional energy source for the system. The equations for the energy and co-energy change (2.19) and (2.23), respectively, will not change. Therefore, the force computation will also stay the same.

Systems with Permanent Magnets

2.3.2

Let us now consider a system where the magnetic field is created by a permanent magnet. In this case, the electric circuit that was

present in the system in Fig. 2.3 disappears. The system has, therefore, no terminal at the left side of the black box. As there is no electric circuit, there is also no flux linkage and inductance. The only two variables present are the magnetic force and the displacement

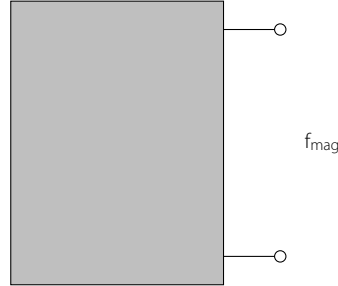


Figure 2.5

Black box of a coupled system in which the magnetic field is created by a permanent magnet

Energy and Co-energy Considerations

Systems in which the magnetic field is created by a permanent magnet show a different energy behaviour. Now, the energy depends only on the displacement u or force f_{mag} , depending which variable is chosen to describe the system. There is a certain amount of energy stored in the system, which is concentrated in the PM. When work is done on the system the recoverable energy of the PM changes.

Using (2.19) without the circuit part of the equation yields

$$dW_{mag,pm} = -f_{mag}(u) du \quad (2.33)$$

where $dW_{mag,pm}$ denotes the energy change of the magnetic field which is only created by a permanent magnet. (2.33) shows that the energy of the system decreases, when the force and displacement are aligned.

Co-energy is a concept that was specifically introduced for the system including coils and electric circuits. The concept is pointless to introduce to systems where the magnetic field is excited by permanent magnets only, as the two variables λ_c and i_c do not exist in those systems.

2.4

Continuous Modelling of Magneto-Mechanical Coupling

In the last section, only the energy entering and leaving a magnetic field were analysed. This way of viewing a coupled system

can already tell much about energy fluxes and the state of the system. However, it is not possible to make statements about the inner state of the system, because only the interface variables are known. This chapter extends the model introduced in Sec. 2.2.1 and Sec. 2.3 by a formulation that describes the spatial distribution of the magnetic field, $\vec{A}(t, \vec{x})$, and the displacement $\vec{u}(t, \vec{x})$. For that the variables i_c , λ_c , u and f_{mag} will be expressed by the new vector fields introduced above.

Consider the domains depicted in Fig. 2.6, to get an understanding of the spatial relations in magneto-mechanical coupled systems. It depicts the domains for the magnetic field and the mechanical system. The model consists of a mechanical domain that overlaps partly with the magnetic domain.

In electric machines, the magnetic field of interest is located in the electro-magnetic active part of the stator and rotor as well as the air gap between them. The air gap has no structure and does not need to be included in the structural model. That is why, a part of the magnetic domain is not part of the mechanical domain in Fig. 2.6. The support structure of the generator has no influence on the magnetic behaviour of the machine. It does not need to be included in the magnetic field calculation. This explains the part of the mechanical domain that is not included in the magnetic domain.

The magnetic domain Ω_{mag} consists of a large part of linear materials (depicted in white), a part that shows nonlinear material behaviour (Ω_{nl}), a part that are permanent magnets (Ω_{pm}) and a part where external currents can be applied (Ω_c). The boundary conditions for the magnetic domain are either a magnetic insulation, i.e. no magnetic flux crosses that boundary, or a periodic condition where the vector potential at one boundary is the same as at another one. The mechanical model is not separated in various

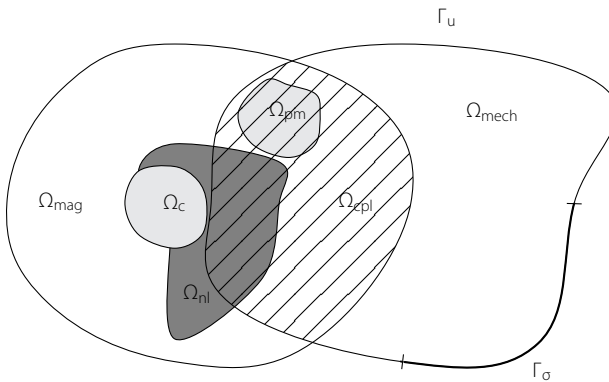


Figure 2.6
Magnetic and mechanical domain

material sub-sections. All parts of the model are assumed to behave linearly. The boundary can be separated in two sections. On the first section the displacement of the material is set to a certain value. This section is denoted by Γ_u . On the second boundary section a surface force is applied. This section is denoted by Γ_σ . A free boundary is realised by a surface force of zero.

The description of the modelling techniques in this thesis will concentrate on Ω_{cpl} , the coupled part of the system, which is depicted by the hatched domain in Fig. 2.6. In that part, the magneto-mechanical coupling takes place as it is part of both physical domains.

2.4.1

The Governing Equations of the Elastic Field

The formulas for continuous elastic fields can be found in any book for continuum mechanics. For a more detailed description of continuum mechanics refer to [73] or [65].

The material is assumed to be linear elastic. The stress tensor $\underline{\underline{\sigma}}$ can therefore be calculated from the strain tensor $\underline{\underline{\varepsilon}}$ by multiplication with a constant stiffness tensor $\underline{\underline{\Xi}}$

$$\underline{\underline{\sigma}} = \underline{\underline{\Xi}} \underline{\underline{\varepsilon}} \quad (2.34)$$

The stress tensor $\underline{\underline{\sigma}}$ is symmetric, because the shear stresses $\tau_{xy} = \tau_{yx}$ are equal. The PDE describing the structural displacement $\bar{\mathbf{u}}$ can therefore be described as

$$\frac{\partial \sigma_{ij}}{\partial x_j} + f_{i\text{ext}} = \frac{\partial}{\partial x_j} (\Xi_{ijkl} \varepsilon_{kl}(u_i)) + f_{i\text{ext}} = \rho \frac{\partial^2 u_i}{\partial t^2} \quad (2.35)$$

in Einstein's index notation (see notation section in preamble for explanation), where $f_{i\text{ext}}$ denotes all the external body forces acting on the structure. ρ denotes the density of the structure.

This PDE is subject to Dirichlet and Neuman boundary conditions on the boundaries Γ_u and Γ_σ

$$\begin{aligned} \bar{\mathbf{u}} &= \bar{\mathbf{u}}_e \quad \text{on} \quad \Gamma_u \\ \underline{\underline{\sigma}}^T \bar{\mathbf{n}} &= \bar{\mathbf{t}}_e \quad \text{on} \quad \Gamma_\sigma \end{aligned} \quad (2.36)$$

where $(\bullet)^T$ denotes the transpose, $\bar{\mathbf{t}}_e$ denotes surface forces imposed on Γ_σ . In some cases the external force $\bar{\mathbf{t}}_e$ can depend on the displacement of the boundary. This is the case when an external spring support is modelled.

2.4.2

The Governing Equations of Continuous Magnetic Fields

The fundamental equations for describing a magnetic field were already introduced in Sec. 2.2.1. The equations consist of Maxwell's

equation (2.3), the material modelling for the conductivity and the relation between the magnetic field and the magnetic flux density (2.6), (2.5) and (2.7). The basic equations were adapted to describe magnetic circuits in Sec. 2.2.4. In this section, the focus is laid on the continuous magnetic field equations and how they can be used to describe magnetic fields in two and three dimensions.

The magnetic field can be described by a spatial distribution of the magnetic flux density $\vec{B}(\vec{x})$. Just like the formulation for elastic fields, the spatial distribution of the magnetic field is governed by a set of partial differential equations. These partial differential equations can be derived from the quasi static maxwell equations (2.3). Starting from (2.3 b) without the displacement term $\frac{\partial \vec{D}}{\partial t}$, inserting (2.4 a) yields

$$\nabla \times \vec{H} = \vec{j}_{source} + \gamma(\vec{E}_s + \vec{E}_i + \vec{v} \times \vec{B}) \quad (2.37)$$

Introducing the magnetic vector potential

$$\vec{B} = \nabla \times \vec{A} \quad (2.38)$$

(2.3 a) can be written as

$$\nabla \times \left(\vec{E}_s + \vec{E}_i + \frac{\partial \vec{A}}{\partial t} \right) = 0 \quad (2.39)$$

Introducing the electric potential, \vec{E}_i can be expressed by

$$\nabla V = -\vec{E}_i \quad (2.40)$$

Using the identity $\nabla \times \nabla(\bullet) = 0$, (2.39) becomes

$$\frac{\partial \vec{A}}{\partial t} = -\vec{E}_s \quad (2.41)$$

Inserting (2.40) and (2.41) into (2.37) yields

$$\nabla \times \vec{H} = \vec{j}_{source} + \gamma \left(-\frac{\partial \vec{A}}{\partial t} + \nabla V + \vec{v} \times \nabla \times \vec{A} \right) \quad (2.42)$$

For electric machines, it is usually assumed that there are no electric charges present, besides the moving charges of the coil currents self. Therefore, the imposed electric potential is zero except in the coil domains. The electric potential applied to the coils is substituted by an imposed current density \vec{j}_e . For the rest of the model the electric field is purely solenoidal. This yields for (2.42)

$$\nabla \times \vec{H} = \vec{j}_{source} + \vec{j}_e + \gamma \left(-\frac{\partial \vec{A}}{\partial t} + \vec{v} \times \nabla \times \vec{A} \right) \quad (2.43)$$

The introduction of the magnetic vector potential made the solution to (2.42) non-unique. This can be proven by adding an arbitrary gradient of a scalar potential to \vec{A} . Since the curl of any gradient is zero ($\nabla \times \nabla(\bullet) = 0$), this will not affect the magnetic flux density \vec{B} .

Several divergence conditions have been proposed to overcome this non-uniqueness [16]. For the static and time dependent solutions of magnetic fields, the non-uniqueness is no problem as the magnetic flux density \vec{B} is of interest, which is unique. Care needs to be taken for eigenvalue problems of quasi-static magnetic fields as will be explained in Chapter 4.

The set of partial differential equations in (2.45) governs the dynamic behaviour of magnetic fields. The solution is subject to the boundary conditions applied to Γ_{mag} . For an electric machine usually no Neumann boundary condition is applied on the boundary of the magnetic domain Ω_{mag} . A Dirichlet boundary condition is often used to impose magnetic insulation $\vec{A} = 0$ on the outer boundary of the magnetic system.

For electric machines, the only source of magnetic fields, besides electric currents in coils, are permanent magnets. Therefore, the additional source term \vec{j}_{source} only contains the excitation of these magnets

$$\vec{j}_{source} = \vec{j}_{pm} = \frac{1}{\mu} \nabla \times \vec{B}_r \quad (2.44)$$

This yields for the magnetic PDE

$$\nabla \times \vec{H} + \gamma \left(\frac{\partial \vec{A}}{\partial t} - \vec{v} \times \nabla \times \vec{A} \right) = \vec{j}_{pm} + \vec{j}_e \quad (2.45)$$

In (2.45), the left hand side consists of internal current terms that determine the static and dynamic behaviour of the magnetic field, whereas the right hand side consists of the source terms that create the magnetic field. The internal currents that are generated by a physical effect within the system and, thus, depend on the system are on the left hand side. The internal currents and external currents have to be in equilibrium everywhere in the system.

The terms $\gamma \frac{\partial \vec{A}}{\partial t}$ and $\gamma \vec{v} \times \nabla \times \vec{A}$ describe the eddy currents induced in conducting materials.

$$\vec{j}_{eddy} = -\gamma \frac{\partial \vec{A}}{\partial t} + \gamma \vec{v} \times \nabla \times \vec{A} \quad (2.46)$$

In (2.45), the relation between the magnetic field \vec{H} and the magnetic flux density \vec{B} is not defined. For nonlinear magnetic materials, the relation between the magnetic field and the internal currents is governed by a general relation between $|\vec{H}|$ and $|\vec{B}|$. For a

linear magnetic material, for which (2.5) holds, (2.45) can be further simplified to

$$\gamma \frac{\partial \vec{A}}{\partial t} - \gamma (\vec{v} \times \nabla \times \vec{A}) + \frac{1}{\mu} \nabla \times \nabla \times \vec{A} = \vec{j}_e + \vec{j}_{pm} \quad (2.47)$$

At interfaces between materials with varying permeability, the interface conditions apply (see for instance [73, p. 110]).

$$\begin{aligned} \vec{n} \cdot (\vec{B}_1 - \vec{B}_2) &= 0 \\ \vec{n} \times (\vec{H}_1 - \vec{H}_2) &= \vec{j}_{surface} \end{aligned} \quad (2.48)$$

These can be derived directly from Maxwell's equations. For non-magnetised materials, i.e. for non-permanent magnets, the surface current $\vec{j}_{surface}$ is zero. The interface conditions state that the component normal to the interface of the magnetic flux density is continuous across the interface. The same is true for the tangential component of the magnetic field.

Electric Circuit Coupling

(2.45) and (2.47) make it possible to calculate the magnetic field distribution when the currents generating that field and properties of the permanent magnets are known. Currents, in general, cannot be controlled directly. They are created as result of a electric potential difference. In electric machines, this is done within a conductor. Usually, that conductor is wound to form a coil to maximise the magnetic field generated with a certain current. It is, therefore, convenient to express the external current densities in the equations (2.45) and (2.47) as function of the lumped variables $i_c(t)$ used in Sec. 2.3.

The circuit equation for a coil is

$$v_{ext} = R_c i_c(t) + \underbrace{\frac{\partial \lambda_c}{\partial t}}_{v_{ind}} \quad (2.49)$$

where λ_c represents the flux linkage of the coil, v_{ind} the induced voltage in the coil, R_c the Ohmic resistance of the coil and v_{ext} the external voltage applied to the coil.

To understand the relation between the external current density, \vec{j}_e , in (2.47) and the lumped current variable, $i_c(t)$, consider Fig. 2.7. It depicts a coil domain in a 3D model. In Fig. 2.7, the coil domain is modelled as a hollow cylinder with the cross section Γ_w . This hollow cylinder is the coil domain that is denoted as Ω_c in Fig. 2.6.

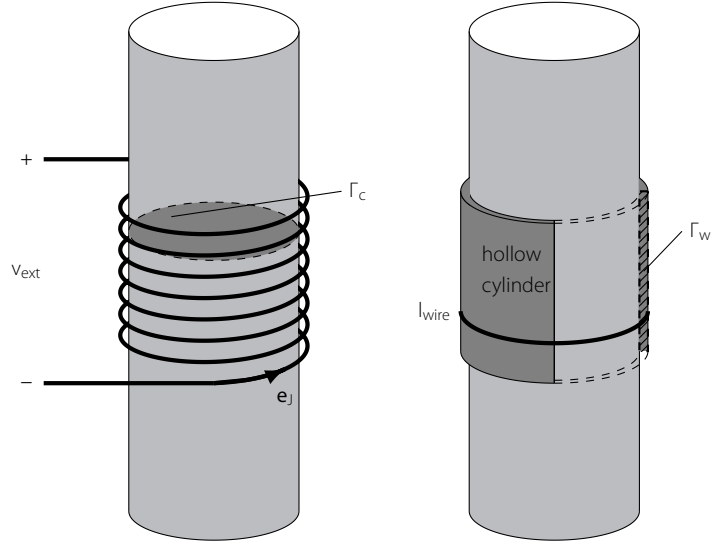


Figure 2.7
A coil and its simplified
representation as domain

The derivation of the coil equations is done in 3D. The derivation for a 2D domain is analog. It can be looked up in [73].

For non-deforming, non-moving coil, the flux linkage is the same as the total flux that flows through the coils cross section Γ_c . Therefore λ_c depends on the magnetic field that interacts with the coil and can be described by Faraday's equation. The total induced potential difference is equal to the integral of the changing magnetic field in the direction of the wires over the coil domain.

Faradays law can be used to calculate the induced voltage of a coil. Assuming that the axial length of the coil is negligible, Faraday's law for a coil can be simplified to

$$\frac{\partial \lambda_c}{\partial t} = v_{ind}(t) \approx N_c \iint_{\Gamma_c} \frac{\partial \vec{B}}{\partial t} \cdot \vec{n}_\Gamma d\Gamma_c \quad (2.50)$$

where Γ_c represents the surface that the coil encloses and \vec{n}_Γ denotes its normal direction. (2.50) can be rewritten in terms of the vector potential. Applying Stoke's theorem yields:

$$\frac{\partial \lambda_c}{\partial t} = N_c \oint_{\partial \Gamma_c} \frac{\partial \vec{A}}{\partial t} \cdot \vec{e}_\Gamma d\partial \Gamma_c \quad (2.51)$$

where $\partial \Gamma_c$ denotes the contour of the surface Γ_c and \vec{e}_Γ the tangential direction of the contour line $\partial \Gamma_c$. In the case of Fig. 2.7, the coil is modelled as a volume and the contour $\partial \Gamma_c$ as a hollow cylinder. The integral in (2.51) becomes then an integral over the whole volume of the simplified coil, i.e. the hollow cylinder. To

make sure that only the current density change in the direction of the conductors is taken into account, a vector \vec{e}_j is introduced that is tangential to the conductors of the coil. (2.51) becomes then

$$\frac{\partial \lambda_c}{\partial t} = v_{ind} \left(\frac{\partial \vec{A}}{\partial t} \right) = \frac{N_c}{\Gamma_w} \int_{\Omega_c} \frac{\partial \vec{A}}{\partial t} \cdot \vec{e}_j \, d\Omega_c \quad (2.52)$$

where Γ_w denotes the cross section of the hollow cylinder.

Note that (2.52) only holds for non-deforming, non-moving coils. For moving or deforming coils Faraday's law in (2.3a) can no longer be used. Instead, the Lorentz force, \vec{E}' , needs to be used for the calculation of the EMF in the coil. In that case, (2.52) becomes

$$\frac{\partial \lambda_c}{\partial t} = v_{ind} \left(\frac{\partial \vec{A}}{\partial t} \right) = \frac{N_c}{\Gamma_w} \int_{\Omega_c} \left(-\frac{\partial \vec{A}}{\partial t} + \vec{v} \times \nabla \times \vec{A} \right) \cdot \vec{e}_j \, d\Omega_c \quad (2.53)$$

For the rest of the thesis, coil domains are assumed to be rigid and stationary, so that (2.52) will be used.

The coil current, i_c , in (2.49) can be expressed by the current density in the coil domain

$$i_c(t) = \frac{1}{N} \int_{\Omega_c} \vec{j}_e \cdot \vec{e}_j \, d\Omega_c \quad (2.54)$$

Assuming that the external current is equally distributed over the coil domain, the external current density can be calculated from the coil current by

$$\vec{j}_e = \vec{e}_j \cdot J = \vec{e}_j \frac{i_c(t) N}{\Gamma_w} \quad (2.55)$$

(2.55) and (2.52) establish a coupling between the continuous magnetic field and the lumped variables v_{ind} and i_c .

Coupling the Physics

2.4.3

With the equations introduced in Sec. 2.4.1 and 2.4.2, the magnetic and elastic field can be modelled separately. However, the aim is to model magneto-mechanical coupled systems. This section will explain how the two governing equations (2.45) or (2.47) and (2.35) can be coupled.

In (2.35), the internal and external forces have to be equal to the dynamic forces. As mentioned, f_i , the external body forces, are all forces that are not linked to a displacement or movement of the structure. When the structure is exposed to a magnetic field, which is the case for magneto-mechanical coupled systems, this external

force includes forces resulting from the magnetic field acting on the structure. (2.35) can be rewritten as

$$\frac{\partial \sigma_{ij}}{\partial \xi_j} + f_i + f_{i\text{mag}}(\vec{A}) = \rho \frac{\partial^2 u_i}{\partial t^2} \quad (2.56)$$

where $f_{i\text{mag}}$ represents the components of the magnetic force vector. In (2.56) the material coordinate, ξ_j , is used compared to (2.35) to indicate, that the elastic field is described in an Eulerian coordinate frame.

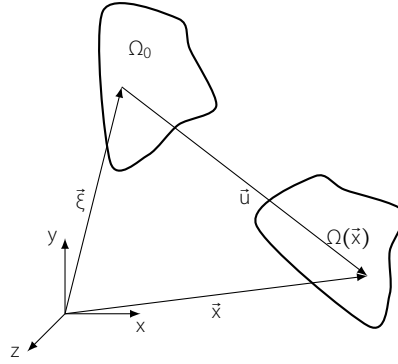


Figure 2.8

The deformation of the structure and the associated reference frames

The governing equation for the magnetic field on the other side, (2.45) or (2.47), is described in Lagrangian coordinates. This means that the magnetic field moves with the underlying structure and is, thus, affected by the displacement field. The magnetic vector potential, \vec{A} , is thus dependent on the spatial coordinates, \vec{x} , whereas the displacement field depends on the material coordinates $\vec{\xi}$. The spatial coordinate, \vec{x} , can be described by

$$\vec{x} = \vec{\xi} + \vec{u}(t, \vec{\xi}) \quad (2.57)$$

Therefore, all boundaries and all domains of the magnetic domains move and deform with the structure. Thus, all spatial derivatives and integrals in the formulation of the magnetic field depend on \vec{u} .

The coupled system can be written as a set of three equations

$$\frac{\partial \sigma_{ij}}{\partial \xi_j} + f_i + f_{i\text{mag}}(A_i) = \rho \frac{\partial^2 u_i}{\partial t^2} \quad (2.58a)$$

$$\gamma(\vec{x}) \frac{\partial \vec{A}(\vec{x})}{\partial t} - \gamma(\vec{x}) \left(\frac{\partial \vec{u}}{\partial t} \times \nabla_{\vec{x}} \times \vec{A}(\vec{x}) \right) + \nabla_{\vec{x}} \times \vec{H}(\vec{A}(\vec{x})) = \vec{j}_e(\vec{x}, i_c(t)) + \vec{j}_{pm}(\vec{x}) \quad (2.58b)$$

$$R_c i_c(t) + \frac{\partial \lambda_c(\vec{A}, \vec{u})}{\partial t} = v_{ext} \quad (2.58c)$$

where $\nabla_{\bar{x}}$ denotes the del operator in the spatial coordinate frame and $\frac{\partial(\bullet)}{\partial \bar{x}_i}$ a spatial derivative with respect to the material coordinates.

How the magnetic force can be calculated will be covered in Sec. 2.4.5. The dependency of the magnetic field on the displacement will be covered in Sec. 2.5.10.

Energy Considerations

2.4.4

In Sec. 2.2.3, the equations to calculate the specific energy of various magnetic materials were introduced. In Sec. 2.3.1, the energy balances of a control volume were investigated. The system within the control volume was seen as a black box. Based on the equation in Sec. 2.2.3, the equations to calculate the energy within the control volume are introduced in this section. Furthermore, for each of the sub-systems, i.e. the mechanical and the magnetic system, the power balance from Sec. 2.3.1 will be extended by energy that is dissipated and thus leaves the system. Additionally, the model will be extended by losses such as eddy currents and friction losses.

The magnetic as well as the elastic field can store energy. The elastic field stores potential energy in the strain of the structure. Therefore, this energy is also called strain energy. The mechanical system can also store energy kinetically as movement of masses. The magnetic field stores energy wherever there is a magnetic field. The internal energy of the system can, therefore, be calculated by adding up all the above energies.

$$W_{int} = \mathcal{V}_{int} + \mathcal{T} = W_{mag} + W_{strain} + \mathcal{T} = W_{mag} + W_{mech} \quad (2.59)$$

where \mathcal{V}_{int} denotes the total potential internal energy of the system, W_{strain} describes the strain energy of the deformation of a structure and \mathcal{T} the kinetic energy of the movement of a structure and W_{mag} the magnetic energy. These are internal energies, W_{int} , as they are internally stored in the system. Besides these internal energies, there are potential energies of external loads, also called external energies, which describe the amount of energy external forces or currents introduce into the system.

Besides the two mechanisms to exchange energy, that were already introduced in Sec. 2.3.1, the magnetic domain can dissipate energy due to eddy currents. The extended energy balance for the magnetic field, which includes this energy, reads as

$$dW_{mag} = dW_{coil} - dW_{ex,m} - dW_{eddy} \quad (2.60)$$

dW_{coil} denotes the energy that enters the magnetic field by means of the current in the coils, $dW_{ex,m}$ the energy that is exchanged with

the mechanical system by applying a magnetic force to a moving object, as established in Sec. 2.3.1, and dW_{eddy} the energy that is dissipated by eddy currents.

The currents in the coils and magnetic forces represent methods how energy can enter and leave the magnetic system without losses. Therefore, these types of energy are recoverable and the loads they create are conservative. They can be expressed as a potential of external loads $W_{mag,ext}$, which means that their instantaneous values does not depend on the history of the system and it can be computed from the vector fields \vec{u} and \vec{A} and the external currents/forces.

$$W_{mag,ext} = W_{coil} - W_{ex,m} \quad (2.61)$$

For dW_{eddy} , this is not the case. Energy always leaves the system due to eddy currents and is, thus, not recoverable. Furthermore, the total amount of dissipated energy can only be computed by taking the history of the system into account and integrating the friction energy change over time. It is, thus, fundamentally different from the other two exchange mechanisms.

The energy of the mechanical system can change due to three mechanisms. Friction within the mechanical system can dissipate energy, energy can be transferred from the magnetic field and the system can exchange energy by means of external forces applied to the system. The total energy change of the mechanical system can be written as

$$dW_{mech} = dW_{ex,m} + dW_{ext,m} - dW_{fric} \quad (2.62)$$

where $dW_{ext,m}$ denotes the energy change due to external forces acting on the system and dW_{fric} the energy change due to friction. Like the energy change due to eddy currents, dW_{eddy} always decreases the energy of the system and cannot be derived from a potential.

Adding the power balances (2.62) and (2.60) for the separate systems yields the power balance for the coupled system of magnetic and elastic field

$$dW_{tot} = dW_{coil} + dW_{ext,m} - dW_{eddy} - dW_{fric} \quad (2.63)$$

where dW_{tot} denotes the total energy change of the coupled system. The energy exchanged between the mechanical and magnetic domain cancels out as the energy that is exchanged between the mechanical system and the magnetic system does not leave the total system. The sum of all external energies, the total external energy, can be written as

$$\mathcal{V}_{ext} = W_{coil} + W_{ext,m} \quad (2.64)$$

Energy in continuous Magnetic Fields

The various terms for the internal and external energies need to be expressed in terms of the field variables $\vec{A}(\vec{x})$ and $\vec{u}(\vec{\xi})$, to be able to calculate them within the control volume in Fig. 2.3. Using (2.9), the total energy of a linear magnetic domain Ω_{mag} can be calculated, yielding.

$$\begin{aligned} W_{mag} &= \int_{\Omega_{mag}} w_{mag} d\Omega_{mag} \\ &= \int_{\Omega_{mag}} \int_0^{\vec{B}} \vec{H}(\vec{B}) d\vec{B} d\Omega_{mag} \end{aligned} \quad (2.65)$$

For linear magnetic materials, (2.65) can be further simplified to

$$W_{mag,lin} = \int_{\Omega_{mag}} \frac{\vec{B}^2}{2\mu} d\Omega_{mag} \quad (2.66)$$

The co-energy can be derived from the energy by

$$W'_{mag} = \int_{\Omega_{mag}} \vec{B}^T \vec{H} d\Omega_{mag} - W_{mag} = \int_{\Omega_{mag}} \int_0^{\vec{H}} \vec{B}(\vec{H}) d\vec{H} d\Omega_{mag} \quad (2.67)$$

For linear magnetic materials, the term for the energy can be substituted by (2.66) yielding

$$W'_{mag} = \int_{\Omega_{mag}} \vec{B}^T \vec{H} - \frac{\vec{B}^2}{2\mu} d\Omega_{mag} = \int_{\Omega_{mag}} \mu \frac{\vec{H}^2}{2} d\Omega_{mag} = \int_{\Omega_{mag}} \frac{\vec{H}^T \vec{B}}{2} d\Omega_{mag} \quad (2.68)$$

Energy and co-energy are, thus, identical for linear magnetic materials.

For nonlinear materials, (2.68) no longer holds. In that case, the complicated relation between \vec{B} and \vec{H} makes it impossible to express the two magnetic fields by one another. Fig. 2.4 shows the energy and co-energy in a λ i - coordinate system. [148, p. 122 - 124] shows that

$$\int_0^{\lambda_c} i_c d\hat{\lambda} = \int_{\Omega_{mag}} \int_0^{\vec{B}} \vec{H} \cdot d\vec{B} d\Omega_{mag} \quad (2.69)$$

where \vec{B} and $\hat{\lambda}$ denote integration variables, so that

$$W_{mag} - i_c \lambda = W_{mag} - \int_{\Omega_{mag}} \vec{B} \vec{H} d\Omega_{mag} \quad (2.70)$$

for singly excited systems. Therefore, for nonlinear materials the same diagram can be drawn with the magnetic field on the x-axis and the magnetic flux density on the y-axis.

Energy and Co-energy in Permanent Magnets

The formula for the specific magnetic energy in permanent magnets has been introduced in (2.10). For the discretisation, it is more convenient to separate the intrinsically stored energy of a permanent magnet and the energy associated to magnetisation.

$$\begin{aligned}
 W_{pm,source} &= \int_{\Omega_{pm}} \frac{\vec{B}_r^2}{2\mu} - \frac{\vec{B}_r^T \vec{B}}{\mu} d\Omega_{pm} \\
 W_{mag} &= \int_{\Omega_{pm}} \frac{\vec{B}^2}{2\mu} d\Omega_{pm}
 \end{aligned}
 \tag{2.71}$$

where Ω_{pm} denotes the sub domain of Ω_{mag} , in which describe permanent magnets, $W_{pm,source}$ denotes the intrinsically stored energy of the magnet and W_{mag} the energy that is associated with a varying magnetic flux. The the total magnetic energy W_{pm} can be expressed as the sum of the two.

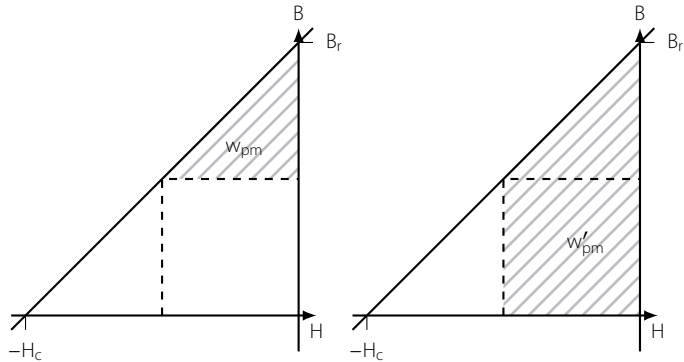


Figure 2.9
energy and co-energy of a linear permanent magnet

Using again the convention described in Sec. 2.2.1, the co-energy for permanent magnets with constant permeability can be computed by

$$\begin{aligned}
 w'_{pm} &= \int_0^{\vec{H}} \vec{B}(\vec{H}) d\vec{H} = \int_0^{\vec{H}} \vec{B}_r + \mu \vec{H} d\vec{H} = \left[\vec{B}_r^T \vec{H} + \mu \frac{\vec{H}^2}{2} \right]_0^{\vec{H}} \\
 &= \vec{B}_r^T \vec{H} + \mu \frac{\vec{H}^2}{2}
 \end{aligned}
 \tag{2.72}$$

This will be negative, as permanent magnets operate in the second quadrant of the B-H coordinate system, where \vec{H} and \vec{B}_r point in

opposite directions rendering the scalar product $\vec{B}_r \cdot \vec{H}$ negative. This is denoted in the B-H coordinate system by negative values for H . Fig. 2.9 shows the energy and co-energy as defined in (2.10) and (2.72) in the magnetisation curve of a linear permanent magnet in a B-H coordinate system.

Energy Exchange by Means of a Coil

Now that the internal energy is defined in terms of \vec{B} and \vec{H} and, thus, in terms of \vec{A} , the same can be done for the energy changes introduced in (2.60).

The energy change due to an external current density, dW_e , can be expressed by

$$dW_e = \int_{\Omega_{mag}} \vec{j}_e \cdot d\vec{A} \, d\Omega_{mag} \quad (2.73)$$

(2.73) can be derived by applying the Ampere's law (2.3 a) and applying the vector identity $\vec{A} \cdot (\vec{B} \times \vec{A}) = (\nabla \times \vec{A}) \cdot \vec{B} - \vec{A} \cdot (\nabla \times \vec{B})$ as shown in [148]. Applying the divergence theorem afterwards yields

$$\int_{\Omega_{mag}} \vec{j}_e \cdot d\vec{A} \, d\Omega_{mag} = \int_{\Omega_{mag}} \vec{H} \cdot d\vec{B} \, d\Omega_{mag} + \int_{\partial\Omega_{mag}} (\vec{H} \times d\vec{A}) \, d\partial\Omega_{mag} \quad (2.74)$$

where $\partial\Omega_{mag}$ denotes the boundary of Ω_{mag} . Assuming that the magnetic vector potential is zero on the boundary of Ω_{mag} , as usually done for electric machines, eliminates the second term and leaves only the magnetic energy in Ω_{mag} .

Assuming that the current density is constant yields

$$W_e = \int_{\Omega_{mag}} \vec{j}_e \cdot \vec{A} \, d\Omega_{mag} \quad (2.75)$$

The energy exchange of a coil is more complicated than that, because the current of a coil is linked to the voltage drop over the coil. Assuming that the external voltage is set, so that the current in the coil $i_c(t)$ is constant, the energy introduced into the system by a coil is, indeed, equal to (2.75). Inserting (2.55) into (2.75) yields

$$W_{coil} = \frac{i_c(t)N}{\Gamma_w} \int_{\Omega_{mag}} \vec{e}_j \cdot \vec{A} \, d\Omega_{mag} \quad (2.76)$$

The change of the magnetic co-energy due to currents in a coil can be calculated by

$$dW'_{coil} = \int_{\Omega_{mag}} \vec{A}(\vec{j}_e) \cdot d\vec{j}_e \, d\Omega_{mag} \quad (2.77)$$

However, (2.16) shows that the flux linkage and, thus, the magnetic vector potential cannot be considered constant when the current changes.

Energy Exchanged with Mechanical Systems

The energy exchanged between the mechanical domain and the magnetic domain in the continuous case can be derived from the second term in (2.60)

$$dW_{ex,m} = \int_{\Omega_{cpl}} \vec{f}_{mag} \cdot d\vec{u} d\Omega_{cpl} \quad (2.78)$$

For the continuous equation, the force density is used instead of the total force, because the displacement varies over \vec{x} . Sec. 2.4.5 is dedicated to calculating the magnetic force in more detail as it is a crucial part of the coupling.

Dissipated Energy by Eddy Currents

The last term in (2.60) is the energy dissipated by eddy currents. This effect is caused by Joule heating in the structure. The instantaneous power that is lost can be expressed by multiplying the current density with the Lorentz force

$$\frac{dw_{eddy}}{dt} = \vec{j}_{eddy} \cdot \vec{E}' \quad (2.79)$$

It is possible to define a dissipation function analog to Rayleigh's dissipation function for mechanical systems. [102, p. 403] defines this dissipation function for Ohmic resistances in electric circuits as

$$\mathcal{D}_{mag} = \frac{1}{2} RI^2 \quad (2.80)$$

where R denotes the resistance and I the current in a conductor. The continuous equivalent to (2.80) can be written as

$$\mathcal{D}_{mag} = \int_{\Omega_{mag}} \frac{\gamma}{2} \vec{j}_{eddy} \cdot \vec{j}_{eddy} d\Omega_{mag} \quad (2.81)$$

Inserting the definition of the eddy currents (2.46) into (2.81) yields

$$\mathcal{D}_{mag} = \int_{\Omega_{mag}} \frac{\gamma}{2} \left[\left(\frac{\partial \vec{A}}{\partial t} \right)^2 - 2 \frac{\partial \vec{A}}{\partial t} \cdot (\vec{v} \times \nabla \times \vec{A}) + (\vec{v} \times \nabla \times \vec{A})^2 \right] d\Omega_{mag} \quad (2.82)$$

The eddy current losses depend, thus, on the velocity of the displacement of the structure as well as the magnetic vector potential and its time derivative. The forces and currents acting on the

system, caused by the dissipation, can be calculated from (2.82) by expressing the velocity \vec{v} as the time derivative of the displacement $\dot{\vec{u}}$ and taking the derivative of the dissipation function density (the part under the integral in (2.82)) with respect to the vector fields $\dot{\vec{u}}$ and $\dot{\vec{A}}$.

$$\begin{aligned} \begin{bmatrix} \vec{f}_{eddy} \\ \vec{j}_{eddy} \end{bmatrix} &= \frac{1}{2} \begin{bmatrix} -\frac{\partial}{\partial \dot{\vec{u}}} \\ \frac{\partial}{\partial \dot{\vec{A}}} \end{bmatrix} \left[\gamma \left(\left(\frac{\partial \vec{A}}{\partial t} \right)^2 - 2 \frac{\partial \vec{A}}{\partial t} \cdot (\dot{\vec{u}} \times \nabla \times \vec{A}) + (\dot{\vec{u}} \times \nabla \times \vec{A})^2 \right) \right] \\ &= \gamma \begin{bmatrix} -[\nabla \times \vec{A}]_{\times} \frac{\partial \vec{A}}{\partial t} + [\nabla \times \vec{A}]_{\times} [\dot{\vec{u}}]_{\times} [\nabla]_{\times} \vec{A} \\ \frac{\partial \vec{A}}{\partial t} - [\dot{\vec{u}}]_{\times} [\nabla]_{\times} \vec{A} \end{bmatrix} \end{aligned} \quad (2.83)$$

where $[\dot{\vec{u}}]_{\times} [\nabla]_{\times} \vec{A} = \dot{\vec{u}} \times \nabla \times \vec{A}$ and $[\bullet]_{\times}$ is the matrix operator form of the cross product defined as the skew symmetric matrix:

$$[\vec{a}]_{\times} = \begin{bmatrix} 0 & -a_3 & a_2 \\ a_3 & 0 & -a_1 \\ -a_2 & a_1 & 0 \end{bmatrix} \quad (2.84)$$

Energy of the Elastic Field

For the mechanical system the potential energy stored in the strain of the material can be calculated by:

$$W_{strain} = \int_{\Omega_{mech}} \frac{1}{2} \underline{\underline{\boldsymbol{\varepsilon}}}^T \underline{\underline{\boldsymbol{\sigma}}} d\Omega_{mech} \quad (2.85)$$

where $\underline{\underline{\boldsymbol{\sigma}}}$ denotes the stress tensor and $\underline{\underline{\boldsymbol{\varepsilon}}}$ the strain tensor. The kinetic energy can be expressed by

$$\mathcal{T} = \int_{\Omega_{mech}} \frac{1}{2} \rho \dot{\vec{u}}^2 d\Omega_{mech} \quad (2.86)$$

The energy changes for the mechanical domain are stated in (2.62). The external mechanical energy \mathcal{V}_{ext} can be expressed in terms of \vec{u} by

$$W_{ext,m} = \int_{\Omega_{mech}} \vec{u} \cdot \vec{f}_{ext} d\Omega_{mech} + \int_{\Gamma_{\sigma}} \vec{u} \cdot \vec{t}_e d\Gamma_{\sigma} \quad (2.87)$$

where \vec{t}_e denotes the surface forces imposed on the boundary Γ_e as defined by (2.36) and \vec{f}_{ext} the body forces imposed on the mechanical domain Ω_{mech} . The exchange energy was already defined in

(2.78). The energy loss by friction $d\mathcal{D}_{mech}$ can be calculated by

$$dW_{fric} = \int_{\Omega_{mech}} \vec{f}_{fric}(\dot{\vec{u}}) \cdot d\vec{u} d\Omega_{mech} = \int_{\Omega_{mech}} -c\dot{\vec{u}} \cdot d\vec{u} d\Omega_{mech} \quad (2.88)$$

where \vec{f}_{fric} denotes the friction forces that are always directed in the opposite direction of the displacement change $d\vec{u}$ and d_k the friction coefficient which relates the force to displacement change $\dot{\vec{u}}$.

Now, a dissipation function can be defined as done in [52]

$$\mathcal{D}_{mech} = \int_{\Omega_{mech}} \int_0^{\dot{\vec{u}}} \vec{f}_{fric}(\dot{\vec{u}}) \cdot d\dot{\vec{u}} d\Omega_{mech} \quad (2.89)$$

where $\dot{\vec{u}}$ is an integration variable. From \mathcal{D}_{mech} the friction force can, thus, be derived by

$$\vec{f}_{fric} = -\frac{\partial \mathcal{D}_{mech}}{\partial \dot{\vec{u}}} \quad (2.90)$$

2.4.5

Magnetic Force Calculation

(2.28) states that the magnetic force acting on a structure can be calculated from the magnetic energy. For the continuous case the magnetic domain Ω_{mag} depends on the displacement $\vec{u}(\vec{x}\xi)$. Furthermore, for computing the total magnetic force of a structure, integrating over the total magnetic domain is necessary. Thus (2.28) becomes

$$\begin{aligned} dW_{mag} &= \frac{\partial W_{mag}}{\partial \vec{u}} d\vec{u}(\vec{x}) = \frac{\partial}{\partial \vec{u}} \int_{\Omega_{mag}(\vec{u}(\vec{x}))} w_{mag} d\Omega_{mag} d\vec{u}(\vec{x}) \\ \Rightarrow \vec{f}_{mag} &= -\frac{\partial}{\partial \vec{u}} \int_{\Omega_{mag}(\vec{u}(\vec{x}))} w_{mag}(\vec{u}(\vec{x})) d\Omega_{mag} \end{aligned} \quad (2.91)$$

So when applying the principle of virtual work, as in (2.91), the dependency of the domain on the displacement must be taken into account.

Energy and Co-energy for Moving Domain Boundaries

To evaluate the energy change in (2.91), it is important to evaluate the energy change on an arbitrary magnetic domain, Ω_{mag} , which depends on a virtual displacement $\delta\vec{u}$. For the various magnetic energy definitions given in (2.10), (2.66) and (2.65), the change of energy under a virtual displacement can be expressed in terms of a

change of the magnetic flux density or magnetic field. As explained in [62], the behaviour of the magnetic flux density and the magnetic field are very different under deformation.

This is caused by the various independent variables for the magnetic flux and the magnetic field (see Sec. 2.3). The magnetic flux density has as independent variables the total magnetic flux Φ_c and the displacement \bar{u} . Consequently, the magnetic flux should be constant under deformation. As the same needs to be true for the magnetic energy, which also has the fluxes and the displacement as independent variables, the magnetic flux density should be used to compute changes to the magnetic energy under deformation.

On the other side, for the computation of the co-energy change, which has the displacements and system's currents as independent variables, the magnetic field should be used as it has the same independent variables.

Assuming a linear magnetic domain, for which the energy is described by (2.66), the change of that energy with respect to a virtual deformation can be split up in a change of the volume and a change of the energy density

$$\delta W_{mag,lin}|_{\delta\Phi_B=0} = V\delta w_{mag,lin}|_{\delta\Phi_B=0} + \delta V w_{mag,lin} \quad (2.92)$$

where $\delta(\bullet)|_{\delta x=0}$ indicates that for the variation δ , x is constant. V denotes the volume of the domain. (2.28) shows that the magnetic forces are calculated by evaluating the change of the magnetic energy within the domain under a deformation, while holding the flux linkage constant. For an arbitrary domain, a constant flux linkage is equivalent to a constant total magnetic flux on any of the boundaries of the domain. As shown in [62], assuming constant flux in and out of the magnetic domain under deformation yields

$$\delta\bar{\mathbf{B}}|_{\delta\Phi_B=0} = \nabla\delta\bar{\mathbf{u}}\bar{\mathbf{B}} - \bar{\mathbf{B}}\text{tr}(\nabla\delta\bar{\mathbf{u}}) \quad (2.93)$$

(2.93) defines the change of the magnetic flux for an arbitrary displacement $\delta\bar{\mathbf{u}}$ when the total flux through all surface of that domain stays constant over the deformation.

To get a better understanding of the implications of (2.93) let us analyse the specific energy of a magnetic field under deformation. With (2.93), it can be shown that the specific energy of a magnetic domain is always constant under a scaling deformation, i.e. a deformation that only scales the domain but does not contain any further displacements, when the total magnetic flux is held constant.

Using the definition of the specific magnetic energy for linear materials, (2.66), and (2.93), the change of the specific magnetic energy

can be described by:

$$\begin{aligned}\delta w_{mag,lin}|_{\delta\Phi_B=0} &= \frac{1}{\mu} \vec{B}^T \nabla \delta \vec{u} \vec{B} - \frac{\vec{B}^2}{\mu} \text{tr}(\nabla \delta \vec{u}) \\ &= \frac{1}{\mu} \vec{B}^T (\nabla \delta \vec{u})_{rot} \vec{B}\end{aligned}\quad (2.94)$$

where $(\nabla \delta \vec{u})_{rot}$ describes the part of $(\nabla \delta \vec{u})$ without the diagonal. (2.94) shows that the specific energy under deformation does not depend on the volume change but only on the rotation of the deformation $\delta \vec{u}$. A scaling of the domain will, thus, lead to no change of the specific energy. It will, of course, lead to a change of the total energy as the second term in (2.92) will change.

For the magnetic co-energy, the same relation as in (2.92) can be derived

$$\delta W'_{mag,lin}|_{\delta I=0} = V \delta w'_{mag,lin}|_{\delta I=0} + \delta V w'_{mag,lin} \quad (2.95)$$

(2.29) states that the magnetic force can be computed by analysing the change of the magnetic co-energy of a domain under deformation, while the currents in the domain are held constant. [62] derives for this case the following relation

$$\delta \vec{H}|_{\delta I=0} = -\nabla \delta \vec{u} \vec{H} \quad (2.96)$$

Following the same derivation as for the energy, it can be shown that the specific co-energy is not constant under a deformation which only scales the domain.

$$\begin{aligned}\delta w'_{mag,lin}|_{\delta I=0} &= -\mu \vec{H}^T \nabla \delta \vec{u} \vec{H} \\ &= -\mu \vec{H}^T (\nabla \delta \vec{u})_{rot} \vec{H} - \mu \vec{H}^2 \text{tr}(\nabla \delta \vec{u})\end{aligned}\quad (2.97)$$

The specific co-energy will, thus, diminish when the volume of the domain is increased.

Maxwell's stress tensor

Maxwell's stress tensor is an approach to define the magnetic stress on a material in the same ways as it is done in continuum mechanics. Like the stress tensor $\underline{\underline{\sigma}}$ in (2.35), it collects all shear and normal stresses of an infinitesimal small cube. The tensor only depends on the state of the material and magnetic field at its location. It can be calculated directly from the magnetic flux density and magnetic field values.

Maxwell's stress tensor is derived from the principle of virtual work in (2.91) (The derivation is a bit lengthy. See Appendix A for it). As

Description	rel. betw. \vec{H} and \vec{B}	spec. mag. energy	Maxwell's stress tensor
linear magnet material	$\vec{B} = \mu\vec{H}$	$w_{\text{mag}} = \frac{\vec{B}^T\vec{H}}{2}$	$\underline{\underline{T}} = \vec{H}\vec{B}^T - I\frac{\vec{B}^T\vec{H}}{2}$
Permanent Magnet magnetisation behaves like \vec{H} under deformation	$\vec{B} = \mu(\vec{M} + \vec{H})$	$w_{\text{mag}} = \frac{\vec{B}^T\vec{B}}{2\mu} - \vec{B}^T\vec{M}$	$\underline{\underline{T}} = \frac{\vec{B}\vec{B}^T}{\mu} - \frac{\vec{B}_r\vec{B}_r^T}{\mu} - I\frac{\vec{B}^2 - \vec{B}_r^2}{2\mu}$
Permanent Magnet remanence flux density behaves like \vec{B} under deformation	$\vec{B} = \mu\vec{H} + \vec{B}_r$	$w_{\text{mag}} = \frac{(\vec{B} - \vec{B}_r)^2}{2\mu}$	$\underline{\underline{T}} = \frac{\vec{B}\vec{B}^T}{\mu} + \frac{\vec{B}_r\vec{B}_r^T}{\mu} - 2\frac{\vec{B}\vec{B}_r^T}{\mu} - I\left(\frac{(\vec{B} - \vec{B}_r)^2}{2\mu}\right)$

Table 2.1

Different formulation of Maxwell's stress tensor for different materials. I denotes the identity matrix

it is derived from the magnetic energy of a material, the formulation changes with the various sorts of magnetic materials introduced in Sec. 2.2.2. Tab. 2.1 shows the formulations of Maxwell's stress tensor for various materials (See the derivation either in Appendix A or [62]). As explained in the previous section, \vec{H} and \vec{B} behave differently under deformation. For permanent magnets, it is not known how the magnetisation/remanence flux density behaves in that case. Tab. 2.1 shows the resulting expressions for Maxwell's stress tensor for the various assumptions. In Tab. 2.1, the symbol for the magnetisation \vec{M} is used to indicate that the permanent magnetisation of a permanent magnet behaves as the magnetic field, which was described in (2.96), and the symbol for remanence flux density, \vec{B}_r , when (2.93) is used.

Maxwell's stress tensor can be used like other stress tensors known from continuum mechanics. Therefore, the magnetic force density it generates in a structure can be computed by:

$$\vec{f}_{\text{mag}} = -\nabla \cdot \underline{\underline{T}} \tag{2.98}$$

The operator \cdot denotes a divergence operation on a second order tensor. The operation can be written in index notation as

$$f_{\text{mag}i} = -\frac{\partial T_{ij}}{\partial x_j} \tag{2.99}$$

The total force on an object can then be calculated by integrating over the whole volume of that object

$$\vec{F}_{\text{mag}} = -\int_{\Omega_{cpl}} \nabla \cdot \underline{\underline{T}} d\Omega_{cpl} \tag{2.100}$$

Local Force Concentrations

For the coupling between the elastic and the magnetic field, local forces are of interest as the deformation depends on them. (2.98)

implies that the magnetic force depends on the gradient of the magnetic field and the magnetic flux density. The larger those gradients the larger are the resulting forces.

For the static case, gradients are highest at locations where the permeability changes abruptly. This is usually the case at the surface of materials with a high relative permeability, such as the surface of the stator teeth. (2.48) states that an abrupt change in permeability results in an abrupt change of magnetic flux density. For an object that has a significantly different permeability than its surrounding, the main part of the applied magnetic forces is located at the surface of that object.

For the dynamic case, the second term in (2.46) can create eddy currents within a structure that contribute significantly to the total force acting on the structure. Eddy current brakes are based on this principle.

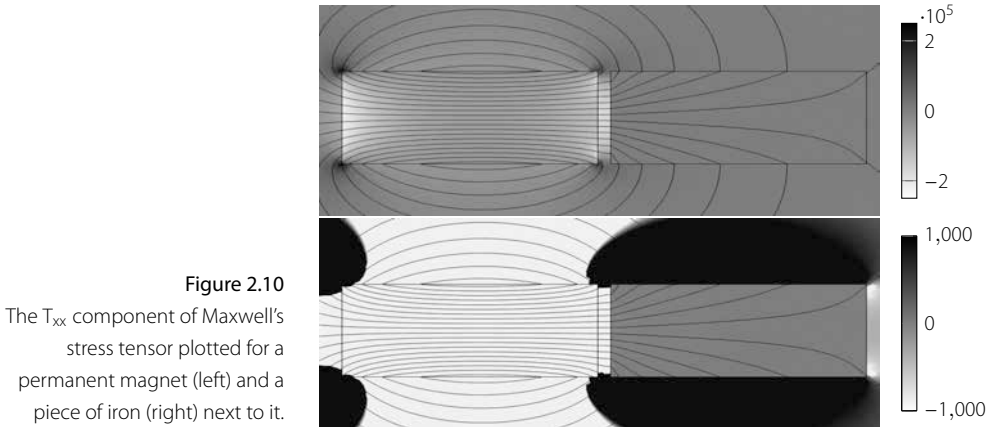


Figure 2.10
The T_{xx} component of Maxwell's stress tensor plotted for a permanent magnet (left) and a piece of iron (right) next to it.

Fig. 2.10 shows the normal x component of Maxwell's stress tensor for the static case, in which a permanent magnet and a piece of iron attract each other due to the magnetic field.

From Fig. 2.10, two things can be deduced. Firstly, Fig. 2.10 shows that around corners of permanent magnets, or its enclosing iron structure, singularities in the magnetic field appear. These singularities contribute strongly to the total force acting on the permanent magnets. They pose a problem for the discrete calculation of the magnetic force as it can lead to major inaccuracies depending on which method is used (see Sec. 2.5.8).

Secondly, the lower part of Fig. 2.10 shows for the static case that the change of the x component of Maxwell's stress tensor across the boundary between the iron and the air is significantly larger than the gradient within the piece of iron. Therefore, the larger

part of the magnetic force in the static case is generated by the discontinuity of the specific magnetic energy at its interface as seen in Fig. 2.10. This is also the case for nonlinear materials. These materials are mainly ferromagnetic materials and store less energy than non-magnetic materials such as copper or air for the same magnetic field magnitude. For permanent magnets, which have a permeability slightly higher than the one of air, this approximation does not hold, as the gradients within the permanent magnet are significant. This can be seen in the first part of Fig. 2.10.

Approximating Total Forces by Surface Forces

(2.100) states how to calculate the total force acting on a domain from Maxwell's stress tensor within that domain. Using Stoke's theorem, the total force acting on a domain can be calculated by

$$\vec{F}_{mag} = - \oint_{\partial\Omega} \vec{n}^T \underline{\underline{T}} d\partial\Omega \quad (2.101)$$

(2.101) has to be used with caution and is used wrongly in some FE packages. The term under the integral sign in (2.101), $\vec{n} \cdot \underline{\underline{T}}$, does not compute the local forces on the surface of the domain $\partial\Omega$. The actual local forces on the surface are computed by taking the gradient of Maxwell's stress tensor over that surface.

The approximation that the term $\vec{n}^T \underline{\underline{T}}$ denotes the local forces on the boundary only holds when the \vec{f} forces within the domain, i.e. the term $\nabla^T \underline{\underline{T}}$ in Ω but not on $\partial\Omega$ in (2.100), hardly contribute to the total force. This is true for the computation of static forces on ferromagnetic materials, where the gradients within the material are relatively low compared to the surface forces and no eddy currents exist.

In most finite element packages, the contribution of the gradient of the magnetic field and magnetic flux density within ferro-magnetic materials is neglected. Using Maxwell's stress tensor simplifies the force calculation at boundaries. Numerically, it is less complex to calculate the change of the magnetic field and flux density across an interface than the gradient within a domain.

Fig. 2.11 shows an interface of two materials over which the force acting on material I should be calculated. The gradient of the Maxwell's stress tensor over an interface can be calculated discretely by taking the difference of each element of the tensor.

$$\vec{f}_{mag} = -\vec{x}(\vec{u})^T (\underline{\underline{T}}_{-II}(\vec{A}) - \underline{\underline{T}}_{-I}(\vec{A})) \quad (2.102)$$

where $\vec{n}(\vec{u})$ describes the normal vector of the interface. Because the magnetic force is evaluated in the spatial coordinate frame, the normal vector depends on the displacement of the structure.

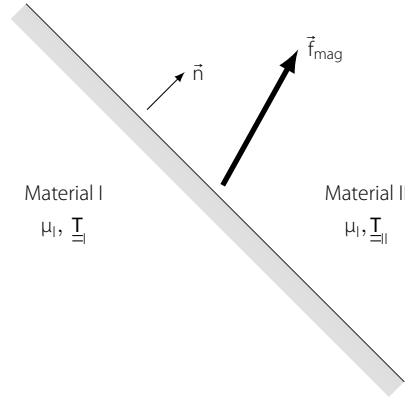


Figure 2.11
Interface between two materials
with different permeability

For the case that one side has a much lower permeability than the other side, the contribution of the side with the higher permeability can be neglected. This is usually the case at an interface between a ferromagnetic and a non-magnetic material

For the case that $\mu_I \gg \mu_{II}$, (2.102) simplifies to

$$\vec{f}_{mag} = -\vec{n}(\vec{x})^T \underline{\underline{T}}_{II}(\vec{A}) \quad (2.103)$$

This method makes it possible to estimate local forces on nonlinear materials without the evaluation of Maxwell's stress tensor within them.

2.5

Discrete Modelling of Magneto-Mechanical Coupling

Solving coupled problems of complex geometry requires sophisticated discretisation techniques. In this thesis, the finite element method (FEM) is used. For an extensive explanation see, for instance, [177]. Additionally, the multi-physical coupling requires special solution approaches. This section covers these solution approaches and shows how the continuous expressions from Sec. 2.4 can be discretised using the FEM.

In this section, matrices for the finite element method are evaluated. All these matrices are element matrices. The domains over which is integrated is the volume or surface of one element. The assembly process that follows the evaluation of the element matrices is not included in this elaboration, as it is analogue to the matrix assembly for non-coupled systems and can thus be found in literature [177].

Discretisation Using the Finite Element Method

2.5.1

For the discretisation of the coupled equations, the FEM is used. This method approximates the values of the vector fields for the displacement $\vec{u}(\vec{\xi})$ and the magnetic vector potential $\vec{A}(\vec{x})$ by discretising the domain of the vector fields by a set of nodes. Nodal values represent the value of the vector fields $\vec{u}(\vec{\xi})$ and $\vec{A}(\vec{x})$ at the location of the associated node. The values between the nodes are approximated by so called shape functions.

$$\begin{aligned}\vec{u}(\vec{\xi}) &\approx \mathbf{N}_u(\xi)\mathbf{q}_u(t) \\ \vec{A}(\vec{x}) &\approx \mathbf{N}_A(\mathbf{x})\mathbf{q}_A(t)\end{aligned}\quad (2.104)$$

In (2.104), \mathbf{N}_u and \mathbf{N}_A denote the shape function of the elastic and magnetic field, respectively. The *generalised coordinates*, \mathbf{q}_u and \mathbf{q}_A , denote the nodal values of the elastic and magnetic field, respectively. Note that the spatial and time information is separated now in two variables. This simplifies finding a solution for the coupled equations, (2.58). The magnetic field and the elastic field depend on different systems of representation. While the elastic field is described in Lagrangian coordinates, the magnetic field depends on Eulerian coordinates. This is denoted in (2.104) by the different coordinate vectors ξ and \mathbf{x} for Lagrangian and Eulerian coordinates frames, respectively. Note that the magnetic field depends on the spatial coordinates and thus implicitly on the displacement of the system as $\vec{x} = \vec{\xi} + \vec{u}(\vec{\xi}, t)$. This leads to the dependency of \mathbf{N}_A on \mathbf{q}_u , and subsequently all magnetic matrices depend on it too. This will play a major role for the coupling terms between the two domains.

Additionally to the above set of coordinates, the currents for the coils are collected in the current vector \mathbf{q}_c . In an electric machine, there are usually three phases and, thus, three different currents. Therefore, \mathbf{q}_c consists of three entries.

$$\mathbf{q}_c = \begin{bmatrix} i_{c,a} \\ i_{c,b} \\ i_{c,c} \end{bmatrix}\quad (2.105)$$

where $i_{c,a}$, $i_{c,b}$ and $i_{c,c}$ denote the currents in the coils of phase a, b and c, respectively. As the currents are lumped variables, they have no spatial distribution and no shape functions are necessary.

Staggered vs. Monolithic Approach

2.5.2

Solving multi-physical coupled problems requires a more sophisticated algorithm than non-coupled problems. Combining the two

physics can create dependencies between the physics that are non-linear. This way, a coupled system consisting of two linear physical domains that are each for itself linear can become nonlinear when the relation between the two physics is nonlinear. Most coupled problems are, thus, nonlinear and require an iterative solution approach compared to a system governed by only one physics, which can be solved in one step when the system is linear.

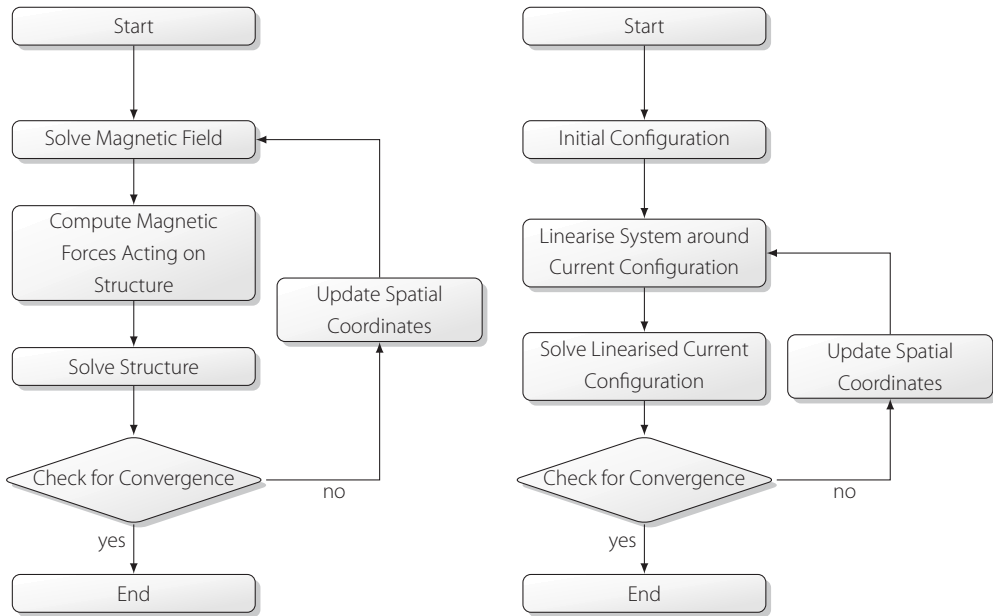


Figure 2.12

Flow charts of staggered (left) and monolithic (right) approaches for solving two way coupled magneto-mechanical systems

There are two possible approaches to solving coupled problems. The *staggered approach* solves both physics separately of each other. The values that depend on the other domain are fixed while one domain is solved. The algorithm goes back and forth between the physics, updates the values that depend on the other physics and iterates this way to a solution of the coupled problem.

For magneto-mechanical coupled problems, the magnetic system is solved first. From that solution, the magnetic forces acting on the structure can be computed. The elastic field can be solved using the magnetic forces as given boundary conditions. The algorithm checks if the two solution fit together, i.e. if the error norm for each domain is smaller than the tolerance. If that is not the case, the spatial coordinates that depend on the displacement of the structure are updated and the magnetic field is solved again. The algorithm iteratively converges towards a solution, in which the errors of both physics are smaller than the tolerance.

The alternative is the *monolithic approach*, which solves the various physical systems simultaneously. For that, the equations need to be combined in a single system of equations. This complicates the discretisation process, but it simplifies the iteration process, because now a genuine Newton-Raphson algorithm can be used to solve the coupled problem. Fig. 2.12 shows the flow charts of the two approaches next to each other.

Both approaches have their advantages and drawbacks. The monolithic approach requires more memory during the solution process as now one large system of equations needs to be solved rather than two smaller ones. It does need less iterations than the staggered approach. Usually, the monolithic approach is chosen for smaller systems where memory issues are not common. The staggered approach is used for large systems.

The monolithic approach for solving magneto-mechanical problems is introduced here, because only this approach facilitates a coupled eigenvalue problem, which can compute the changes of the system's dynamics due to the coupling.

A Variational Approach to Magneto-Mechanical Coupled Systems

2.5.3

Using a variational formulation, as done in [131], for the derivation of the system equations leads to a consistent way to derive the monolithic coupled finite element formulation.

Sec. 2.4 derives two methods to calculate magnetic forces. The type of system determines which method is used. Closed systems, i.e. systems in which the total magnetic energy can only be changed by magnetic forces, use the magnetic energy to determine magnetic forces. Open systems, i.e. systems in which the magnetic energy can change due to mechanisms besides magnetic forces, use the co-energy. Therefore, distinguishing between the type of system is fundamental for the derivation of the coupled system of equation.

Hamilton's Principle for Closed Magneto-Mechanical Systems

According to *Hamilton's principle*, the system follows a trajectory so that the integral

$$\int_{t_1}^{t_2} \mathcal{T} - \mathcal{V} dt \quad (2.106)$$

is stationary with respect to any arbitrary virtual variation of the displacement that is zero at t_1 and t_2 . [52]. \mathcal{T} is the kinetic energy of the mechanical system and \mathcal{V} the potential energy of the

system. For scleronomic kinematic constraints and no dissipative effects (2.106) can be reformulated to

$$\frac{d}{dt} (\mathcal{T}(\bar{\mathbf{u}}, \dot{\bar{\mathbf{u}}}) + \mathcal{V}(\bar{\mathbf{u}}, \bar{\mathbf{A}})) = 0 \quad (2.107)$$

(2.107) states that the total energy stays constant, for systems with only scleronomic constraints and no dissipative effects. For electric machines there are only scleronomic constraints when the rotor stands still. In operation, however, a rheonomic constraint is applied to the magnetic field of the rotor, which depends on the rotor's rotation angle and thus time. However, the magnetic field has no kinematic energy and, thus, the above transformation can be done for magneto-mechanical coupled systems describing electric machines. (2.107) differs from variational principles of systems that include only the structure by inclusion of the magnetic energy (see for instance in [177]).

Assuming that the displacements are small, the kinetic energy depends only on the time derivative of the displacement $\mathcal{T}(\dot{\bar{\mathbf{u}}})$. The Lagrange equations in that case reads as

$$\left[\begin{array}{c} -\frac{d}{dt} \left(\frac{\partial \mathcal{T}}{\partial \dot{\bar{\mathbf{u}}}} \right) + \frac{\partial \mathcal{T}}{\partial \bar{\mathbf{u}}} - \frac{\partial \mathcal{V}}{\partial \bar{\mathbf{u}}} \\ -\frac{\partial \mathcal{V}}{\partial \bar{\mathbf{A}}} \end{array} \right] = 0 \quad (2.108)$$

where $\vec{\mathbf{j}} = -\frac{\partial \mathcal{V}}{\partial \bar{\mathbf{A}}}$ and $\vec{\mathbf{f}} = -\frac{\partial \mathcal{V}}{\partial \bar{\mathbf{u}}}$ are the currents and forces, that follow directly from the principle of virtual work.

\mathcal{V} can be separated in an external potential, \mathcal{V}_{ext} , and an internal potential, \mathcal{V}_{int} . The internal potential describes all energy that is stored within the domain, it is defined by (2.59). When external forces are conservative, they can be described by a potential energy, as was done in (2.64). The external potentials are defined in such a way that they are positive when they have introduced energy into the system so that

$$\mathcal{V} = \mathcal{V}_{int} - \mathcal{V}_{ext} \quad (2.109)$$

In the same way, the currents and forces can be separated into internal and external ones. They can be derived by applying the principle of virtual work to the potential energy \mathcal{V} . That leads to

$$\left[\begin{array}{c} \vec{\mathbf{f}}_{int} \\ \vec{\mathbf{j}}_{int} \end{array} \right] - \left[\begin{array}{c} \vec{\mathbf{f}}_{ext} \\ \vec{\mathbf{j}}_{ext} \end{array} \right] = \left[\begin{array}{c} -\frac{\partial \mathcal{V}}{\partial \bar{\mathbf{u}}} \\ -\frac{\partial \mathcal{V}}{\partial \bar{\mathbf{A}}} \end{array} \right] \quad (2.110)$$

where $\vec{\mathbf{f}}_{int}$ denotes the internal forces and $\vec{\mathbf{j}}_{int}$ the internal currents, whereas $\vec{\mathbf{f}}_{ext}$ and $\vec{\mathbf{j}}_{ext}$ denote the external forces and currents, respectively.

Inserting the various energy terms from (2.64) and (2.59) and inserting (2.86) for the kinetic energy term in (2.108) yields

$$\begin{bmatrix} \vec{f}_{kin}(\ddot{\vec{u}}) + \vec{f}_{strain}(\vec{u}) - \vec{f}_{mag}(\vec{u}, \vec{A}) \\ \vec{j}_{int}(\vec{u}, \vec{A}) \end{bmatrix} = \begin{bmatrix} \vec{f}_{ext,mech}(\vec{u}) \\ \vec{j}_{pm}(\vec{u}) \end{bmatrix} \quad (2.111)$$

where \vec{f}_{kin} is the inertia force computed by

$$\vec{f}_{kin} = -\rho\ddot{\vec{u}} \quad (2.112)$$

$\vec{f}_{strain}(\vec{u})$ the elastic forces caused by the deformation of the system, \vec{j}_{int} the internal currents of the magnetic field, $\vec{f}_{mag}(\vec{u}, \vec{A})$ the magnetic forces defined in (2.91), $\vec{f}_{ext,mech}(\vec{u})$ the external forces acting on the system and $\vec{j}_{pm}(\vec{u})$ the currents representing the excitation of the permanent magnets. The coil energy and coil currents are not included here, as in closed magnetic systems no coils are present.

In (2.111), it becomes apparent, why the energy of permanent magnets was split in a source part and a linear part in (2.71). The currents that are computed by deriving $W_{pm,source}$ are denoted by \vec{j}_{pm} in (2.111) and are written on the right hand side. The currents represent a source for the magnetic field and are constant over \vec{A} . The currents computed from the other energy in (2.71), W_{mag} , are denoted by \vec{j}_{int} , as these currents are created by the change of the magnetic field within the magnet and change with \vec{A} .

(2.111) can be used to simulate the dynamic behaviour of a lossless mechanical system under influence of a magnetic field that reacts instantaneously. The eddy currents that introduce a delay into the behaviour of the magnetic field and the influence of friction losses will be introduced in Sec. 2.5.3.

Hamilton's Principle for Open Magneto-Mechanical Systems

For open magnetic systems, i.e. magnetic systems including coils, the magnetic co-energy instead of the magnetic energy is used to calculate magnetic forces, as explained in Sec. 2.3. Hamilton's principle includes the magnetic enthalpy instead of the magnetic energy in such a case.

The idea for the magnetic enthalpy was taken from the analysis of electro-static mechanical coupled systems. These system's equations resemble the equations of magneto-mechanical coupled systems [113, 131, 151]. They also can be categorised in open and closed systems and according to the system type different state functions are used to calculate the force. Electro-static mechanical coupled systems have been receiving more attention than magneto-mechanical systems, because they describe the vibration behaviour of

piezo electric transducers and microsystems. [151] introduces the electric enthalpy for open electro-static mechanical systems.

$$\Psi_{elt} = \mathcal{V}_{elt} - \vec{E}^T \vec{D} \quad (2.113)$$

where \mathcal{V}_{elt} denotes the total potential energy of the electric and mechanical systems combined and Ψ_{elt} the electric enthalpy. For magneto-mechanical systems, a magnetic enthalpy can be introduced for open systems

$$\Psi_{mag} = \mathcal{V} - \vec{B}^T \vec{H} \quad (2.114)$$

where Ψ_{mag} denotes the magnetic enthalpy and \mathcal{V} the potential energy of the elastic and the magnetic field combined as defined in (2.109). Splitting up the potential energy in its mechanical part and magnetic part and using the definition for the magnetic co-energy, (2.67), (2.114) can be written as

$$\begin{aligned} \Psi_{mag} &= W_{strain} + W_{mag} - \vec{B} \cdot \vec{H} \\ &= W_{strain} - W'_{mag} + \vec{B}^T \vec{H} - \vec{B}^T \vec{H} \\ &= W_{strain} - W'_{mag} \end{aligned} \quad (2.115)$$

Using the magnetic enthalpy changes the set of variables used to describe the system. Instead of the magnetic vector potential, the current densities are used as independent variables. As explained in Sec. 2.3.1, this makes it possible to calculate the force of the magnetic field acting on the structure for a known coil current.

Consequently, the forces and vector potential can be calculated by

$$\begin{bmatrix} \vec{f}_{int} \\ \vec{A}_{int} \end{bmatrix} - \begin{bmatrix} \vec{f}_{ext} \\ \vec{A}_{ext} \end{bmatrix} = \begin{bmatrix} -\frac{\partial \Psi_{mag}}{\partial \vec{u}} \\ \frac{\partial \Psi_{mag}}{\partial \vec{j}} \end{bmatrix} \quad (2.116)$$

which are the open magnetic system's equivalents to mechanical forces and currents in the closed magnetic system. Inserting again the various definitions of energy in (2.59), (2.86) and (2.64) yields

$$\begin{bmatrix} \vec{f}_{kin}(\vec{u}) + \vec{f}_{strain}(\vec{u}) - \vec{f}_{mag}(\vec{u}, \vec{j}) \\ \vec{A}_{int}(\vec{u}, \vec{j}) \end{bmatrix} = \begin{bmatrix} \vec{f}_{ext}(\vec{u}) \\ \vec{A}_{coil}(\vec{u}, \vec{j}) + \vec{A}_{pm}(\vec{u}) \end{bmatrix} \quad (2.117)$$

Since the currents are the independent variable now, the magnetic field needs to be described in terms of them, rather than in terms of the magnetic vector potential. It is possible to rewrite the finite element formulation in terms of the currents, but this will deviate from the FE formulation of magnetic fields in literature. Using the

current density as independent variable is convenient for calculating the magnetic force of an open system but it complicates the calculation of the magnetic field.

Mixing the formulations of energy and co-energy in one system facilitates the monolithic description of the open coupled system. The force terms are evaluated on an element level in the discrete model. Most of the elements, found in the FE model of an electric machine will not include a mechanism by which energy can enter or leave the system, i.e. will not be part of a coil domain. For these elements, the magnetic energy is used as a basis to compute the magnetic forces. For elements, which are part of a coil, i.e. are within Ω_c in Fig. 2.6, are considered open systems and the magnetic enthalpy is used to compute the force term.

On an element level, the above considerations lead to the formulation in Sec. 2.4.5, where the change of co-energy and consequently the force for deformation under constant currents is considered which eventually leads to (2.96).

The Variational Approach including Dissipation Energies

For a system containing dissipation (2.107) can be extended by a dissipation function \mathcal{D} that contains the energy associated with friction losses in the mechanical system and eddy current losses in the magnetic field

$$\mathcal{D} = \mathcal{D}_{mech} + \mathcal{D}_{mag} \quad (2.118)$$

where \mathcal{D}_{mech} and \mathcal{D}_{mag} are the dissipation energies defined in (2.89) and (2.82), respectively. (2.107) becomes

$$\delta(\mathcal{T} + \mathcal{V}) = -m\mathcal{D} \quad (2.119)$$

as stated in [52, p. 26]. m is a factor that depends on the sort of dissipation. $m = 2$, for viscous damping, when the general damping force is proportional to the first derivative of the DoFs. In this case, the equation of motion can be derived by the Lagrange equations

$$\left[\begin{array}{c} -\frac{d}{dt} \left(\frac{\partial \mathcal{T}}{\partial \dot{\bar{\mathbf{u}}}} \right) + \frac{\partial \mathcal{T}}{\partial \bar{\mathbf{u}}} - \frac{\partial \mathcal{V}}{\partial \bar{\mathbf{u}}} - \frac{\partial \mathcal{D}}{\partial \dot{\bar{\mathbf{u}}}} \\ -\frac{\partial \mathcal{V}}{\partial \bar{\mathbf{A}}} - \frac{\partial \mathcal{D}}{\partial \left(\frac{\partial \bar{\mathbf{A}}}{\partial t} \right)} \end{array} \right] = \mathbf{0} \quad (2.120)$$

where only the two terms including the dissipation function, \mathcal{D} , distinguishes (2.120) from (2.108). Inserting the energy terms from (2.64) and (2.59) and the dissipation function from (2.118) yields for closed systems:

$$\begin{bmatrix} \vec{f}_{kin}(\ddot{\mathbf{u}}) + \vec{f}_{mag}(\vec{\mathbf{A}}, \vec{\mathbf{u}}) + \vec{f}_{strain}(\vec{\mathbf{u}}) + \vec{f}_{fric}(\dot{\mathbf{u}}) + \vec{f}_{eddy}(\frac{\partial \vec{\mathbf{A}}}{\partial t}, \vec{\mathbf{A}}, \dot{\mathbf{u}}) \\ \vec{j}_{int}(\vec{\mathbf{A}}, \vec{\mathbf{u}}) + \vec{j}_{eddy}(\frac{\partial \vec{\mathbf{A}}}{\partial t}) \end{bmatrix} = \begin{bmatrix} \vec{f}_{ext}(\vec{\mathbf{u}}) \\ \vec{j}_{pm} \end{bmatrix} \quad (2.121)$$

For open systems, the external current term \vec{j}_e is added to (2.121), yielding

$$\begin{bmatrix} \vec{f}_{kin}(\ddot{\mathbf{u}}) - \vec{f}_{mag}(\vec{\mathbf{A}}, \vec{\mathbf{u}}) + \vec{f}_{strain}(\vec{\mathbf{u}}) + \vec{f}_{fric}(\dot{\mathbf{u}}) + \vec{f}_{eddy}(\frac{\partial \vec{\mathbf{A}}}{\partial t}, \vec{\mathbf{A}}, \dot{\mathbf{u}}) \\ \vec{j}_{int}(\vec{\mathbf{A}}, \vec{\mathbf{u}}) + \vec{j}_{eddy}(\frac{\partial \vec{\mathbf{A}}}{\partial t}) \end{bmatrix} = \begin{bmatrix} \vec{f}_{ext}(\vec{\mathbf{u}}) \\ \vec{j}_{pm} + \vec{j}_e \end{bmatrix} \quad (2.122)$$

Introducing Circuit Equations

To better analyse the effects of the magneto-mechanical coupling on the currents in coils, the circuit equation (2.49) can be added to the set of equations in (2.122). This addition to (2.122) cannot be achieved in a consistent way, i.e. deriving it from a potential energy, without going deeper into modelling of electric fields and charge densities. This is beyond the scope of this thesis.

The addition of (2.49) changes (2.122) in two ways. First, the external current density \vec{j}_e is no longer constant, because it depends on the current in the coils, which are now included in the system. \vec{j}_e , therefore, no longer represents an external current density but an internal one. It is moved to the left side of the equation.

The second change concerns the eddy currents in the coil domains of the FE model. The circuit equations collect all electric potential differences and currents in the coils. The potential difference that a changing magnetic field has and the resulting eddy currents are part of that. Therefore, the potential difference created by a changing magnetic field needs to be collected and added to the circuit equation. This is done by (2.52), which is part of the circuit equation. To ensure that these potential differences and resulting currents are not accounted for twice, the eddy current term in (2.122) needs to be omitted in coil domains.

The coupled equations for a domain where the external current is determined by an extra circuit equation reads as

$$\begin{bmatrix} \vec{f}_{kin}(\ddot{\mathbf{u}}) - \vec{f}_{mag}(\vec{\mathbf{A}}, \vec{\mathbf{u}}) + \vec{f}_{strain}(\vec{\mathbf{u}}) + \vec{f}_{fric}(\dot{\mathbf{u}}) \\ \vec{j}_{int}(\vec{\mathbf{A}}, \vec{\mathbf{u}}) - \vec{j}_e(i_c) \\ v_{ind}(\frac{\partial \vec{\mathbf{A}}}{\partial t}) + v_{ohmic}(i_c) \end{bmatrix} = \begin{bmatrix} \vec{f}_{ext}(\vec{\mathbf{u}}) \\ \vec{j}_{pm} \\ v_{ext} \end{bmatrix} \quad (2.123)$$

Discretisation of the Equations

2.5.4

The set of nonlinear equations, (2.123), are the same coupled partial differential equations that were already stated in (2.58). In Sec. 2.4.3 the physics were coupled by the use of physical understanding. In Sec. 2.5.3 on the other hand, the derivation started from the Hamiltonian of the coupled system and used a variational principle. The equations are so complex that they cannot be solved analytically. Therefore, a discretisation is necessary, in order to solve them numerically. After discretisation, a nonlinear solver such as the Newton-Raphson algorithm can be employed to solve the system of coupled equations (2.123).

Because all nonlinear solving algorithms use an iterative scheme, in which linear systems at a certain system state are evaluated, it is convenient to write the coupled nonlinear system of equations (2.123) in matrix form, in which the entries of the matrices depend on the nodal values \mathbf{q}_A and \mathbf{q}_u . After applying the discretisation in (2.104) and (2.105), (2.123) becomes

$$\mathbf{M} \begin{bmatrix} \ddot{\mathbf{q}}_u \\ \ddot{\mathbf{q}}_A \\ \ddot{\mathbf{q}}_c \end{bmatrix} + \mathbf{C}(\mathbf{q}_A, \mathbf{q}_u) \begin{bmatrix} \dot{\mathbf{q}}_u \\ \dot{\mathbf{q}}_A \\ \dot{\mathbf{q}}_c \end{bmatrix} + \mathbf{K}(\mathbf{q}_A, \mathbf{q}_u) \begin{bmatrix} \mathbf{q}_u \\ \mathbf{q}_A \\ \mathbf{q}_c \end{bmatrix} = \begin{bmatrix} \mathbf{F}_{ext}(\mathbf{q}_u) \\ \mathbf{J}_{pm} \\ \mathbf{v}_{ext} \end{bmatrix} \quad (2.124)$$

with

$$\mathbf{K} = \begin{bmatrix} \mathbf{K}_{uu} & \mathbf{K}_{uA} & \mathbf{0} \\ \mathbf{K}_{Au} & \mathbf{K}_{AA} & \mathbf{K}_{Ac} \\ \mathbf{0} & \mathbf{0} & \mathbf{K}_{cc} \end{bmatrix} = \begin{bmatrix} \frac{\partial^2 \mathcal{V}_{int}}{\partial \mathbf{q}_u^2} & \frac{\partial^2 \mathcal{V}_{int}}{\partial \mathbf{q}_u \partial \mathbf{q}_A} & \mathbf{0} \\ \frac{\partial^2 \mathcal{V}_{int}}{\partial \mathbf{q}_u \partial \mathbf{q}_A} & \frac{\partial^2 \mathcal{V}_{int}}{\partial \mathbf{q}_A^2} & -\frac{\partial^2 W_{coil}}{\partial \mathbf{q}_A \partial \mathbf{q}_c} \\ \mathbf{0} & \mathbf{0} & \frac{\partial v_{ohmic}}{\partial \mathbf{q}_c} \end{bmatrix} = \left(\begin{bmatrix} \frac{\partial}{\partial \mathbf{q}_u} \\ \frac{\partial}{\partial \mathbf{q}_A} \\ \frac{\partial}{\partial \mathbf{q}_c} \end{bmatrix} \begin{bmatrix} \mathbf{F}_{int}(\mathbf{q}) \\ \mathbf{J}_{int}(\mathbf{q}_A) - \mathbf{J}_e(\mathbf{q}_c) \\ \mathbf{v}_{ohmic}(\mathbf{q}_c) \end{bmatrix} \right)^T \quad (2.125)$$

$$\mathbf{M} = \begin{bmatrix} \mathbf{M}_{uu} & \mathbf{0} & \mathbf{0} \\ \mathbf{0} & \mathbf{0} & \mathbf{0} \\ \mathbf{0} & \mathbf{0} & \mathbf{0} \end{bmatrix} = \begin{bmatrix} \frac{\partial}{\partial \dot{\mathbf{q}}_u} \left(\frac{d}{dt} \left(\frac{\partial \mathcal{T}}{\partial \dot{\mathbf{q}}_u} \right) \right) & \mathbf{0} & \mathbf{0} \\ \mathbf{0} & \mathbf{0} & \mathbf{0} \\ \mathbf{0} & \mathbf{0} & \mathbf{0} \end{bmatrix} \quad (2.126)$$

and

$$\mathbf{C} = \begin{bmatrix} \mathbf{C}_{uu} & \mathbf{C}_{uA} & \mathbf{0} \\ \mathbf{C}_{Au} & \mathbf{C}_{AA} & \mathbf{0} \\ \mathbf{0} & \mathbf{C}_{cA} & \mathbf{0} \end{bmatrix} = \begin{bmatrix} \frac{\partial^2 \mathcal{D}}{\partial \dot{\mathbf{q}}_u^2} & \frac{\partial^2 \mathcal{D}}{\partial \dot{\mathbf{q}}_u \partial \dot{\mathbf{q}}_A} & \mathbf{0} \\ \frac{\partial^2 \mathcal{D}}{\partial \dot{\mathbf{q}}_u \partial \dot{\mathbf{q}}_A} & \frac{\partial^2 \mathcal{D}}{\partial \dot{\mathbf{q}}_A^2} & \mathbf{0} \\ \mathbf{0} & \frac{\partial v_{ind}}{\partial \dot{\mathbf{q}}_A} & \mathbf{0} \end{bmatrix} = \left(\begin{bmatrix} \frac{\partial}{\partial \dot{\mathbf{q}}_u} \\ \frac{\partial}{\partial \dot{\mathbf{q}}_A} \\ \frac{\partial}{\partial \dot{\mathbf{q}}_c} \end{bmatrix} \begin{bmatrix} \mathbf{F}_{fric}(\dot{\mathbf{q}}_u) + \mathbf{F}_{eddy}(\dot{\mathbf{q}}) \\ \mathbf{J}_{eddy}(\dot{\mathbf{q}}) \\ \mathbf{v}_{ind}(\dot{\mathbf{q}}_A) \end{bmatrix} \right)^T \quad (2.127)$$

where \mathbf{K} denotes the tangent stiffness matrix, \mathbf{M} the mass matrix of the system and \mathbf{C} the damping matrix.

The following sections (Sec. 2.5.5 - Sec. 2.5.10) will show derive the various terms in (2.125), (2.126) and (2.127), using the equations derived in Sec. 2.4. To do so, the various energies introduced in

Sec. 2.4.4 need to be expressed discretely in terms of the nodal values of the two variable fields and then differentiated with respect to them. Once that is done, a nonlinear solver can be used to solve the discretised equations as described in Sec. 2.5.2.

In this section, the introduced matrices are element matrices. Depending on which physics are present in a certain element, various formulations have to be used and certain matrices can be neglected.

2.5.5

Discretisation of the Elastic Field

The internal mechanical energy of the system can be calculated according to (2.86) and (2.85). Using the discretisation introduced in (2.104), it is now possible to express the strain tensor $\underline{\underline{\epsilon}}$ in a discretised way.

$$\underline{\underline{\epsilon}} \approx \mathbf{B}_u \mathbf{q}_u \quad (2.128)$$

where \mathbf{B}_u is a matrix containing the spatial derivatives of the shape functions N_u . For the finite element formulation the strain tensor is usually written in Voigt notation [163], i.e. as a vector, listing all elements of the strain tensor in a predefined order. Using the Voigt notation, (2.34) can be expressed as a multiplication of matrices. In this notation, the mechanical energy can be written as

$$W_{mech} = \int_{\Omega} \frac{1}{2} \mathbf{q}_u^T \mathbf{B}_u^T \underline{\underline{\Xi}} \mathbf{B}_u \mathbf{q}_u + \frac{1}{2} \dot{\mathbf{q}}_u^T \mathbf{N}_u^T \rho \mathbf{N}_u \dot{\mathbf{q}}_u d\Omega \quad (2.129)$$

$\underline{\underline{\Xi}}$ denotes the material stiffness matrix, introduced in (2.34). In Voigt notation, it can be represented by a matrix instead of a fourth order tensor. For an isotropic linear material, $\underline{\underline{\Xi}}$ is constant over time and for a domain of the same material. It can be calculated from the material properties, Young's modulus and Poisson ratio. Differentiating twice with respect to the displacement yields the structural stiffness matrix. It consists of a part that is derived from the mechanical energy, \mathbf{K}_{uu}^{mech} , and one that is derived from the magnetic energy, \mathbf{K}_{uu}^{mag} . For a linear elastic material, which was assumed in (2.129), the structural part of the tangent stiffness matrix \mathbf{K}_{uu}^{mech} is constant.

$$\mathbf{K}_{uu} = \frac{\partial^2 W_{tot}}{\partial \mathbf{q}_u^2} = \int_{\Omega} \mathbf{B}_u^T \underline{\underline{\Xi}} \mathbf{B}_u d\Omega + \underbrace{\frac{\partial^2 W_{mag}}{\partial \mathbf{q}_u^2}}_{\mathbf{K}_{uu}^{mag}} \quad (2.130)$$

The second term in (2.130) is a coupling term. It will be discretised in Sec. 2.5.8 together with the other coupling terms.

Differentiating the kinetic energy twice with respect to the time derivative of the displacement yields the structural mass matrix

$$\mathbf{M}_{uu} = \int_{\Omega} \mathbf{N}_u^T \rho \mathbf{N}_u \, d\Omega \quad (2.131)$$

External force distributions can be derived by discretising the external mechanical energy (2.87) and differentiating it with respect to the mechanical degrees of freedom \mathbf{q}_u . That yields:

$$\mathbf{F}_{ext} = \int_{\Omega} \mathbf{N}_u^T \mathbf{f}_{ext} \, d\Omega + \int_{\Gamma_{\sigma}} \mathbf{N}_{u,\sigma}^T \mathbf{t}_e \, d\Gamma_{\sigma} \quad (2.132)$$

where \mathbf{F}_{ext} denotes a vector of nodal values for the external forces, \mathbf{f}_{ext} a vector of the external body force density evaluated at the coordinates of the nodes, \mathbf{t}_e a vector of external force density applied to the boundary Γ_{σ} , evaluated at the nodal points and $\mathbf{N}_{u,\sigma}$ 2D shape functions of the finite element discretisation of Γ_{σ} .

The damping matrix can be derived differentiating \mathcal{D} , as defined in (2.118), twice with respect to the nodal values of the velocity. The structural damping matrix consists, like the structural stiffness matrix, of two components. The first component is derived from the mechanical dissipation function, whereas the other component is derived from the magnetic dissipation function. The structural damping matrix reads as

$$\mathbf{C}_{uu} = \frac{\partial^2 \mathcal{D}}{\partial \dot{\mathbf{q}}_u^2} = \int_{\Omega} \mathbf{N}_u^T \mathbf{D}_k \mathbf{N}_u \, d\Omega + \underbrace{\frac{\partial^2 \mathcal{D}_{mecmagh}}{\partial \dot{\mathbf{q}}_u^2}}_{\mathbf{C}_{uu}^{mag}} \quad (2.133)$$

where \mathbf{D}_k denotes a diagonal matrix containing the viscous damping coefficients d_k . The second term in (2.133) is a coupling term and will be derived in Sec. 2.5.10. Now the PDE (2.35) can be written in its discrete uncoupled form as a system of linear equations.

$$\mathbf{M}_{uu} \ddot{\mathbf{q}}_u + \mathbf{C}_{uu} \dot{\mathbf{q}}_u + \mathbf{K}_{uu} \mathbf{q}_u = \mathbf{F}_{ext} \quad (2.134)$$

Discretisation of the Magnetic Field

2.5.6

In (2.104), the discretisation for the magnetic vector potential was introduced.

The magnetic field – magnetic flux density relation is used for the energy equations introduced in Sec. 2.4.4. The magnetic flux density can be numerically expressed in terms of the nodal values of the magnetic vector potential by

$$\vec{\mathbf{B}} \approx \mathbf{B}_A \mathbf{q}_A \quad (2.135)$$

where \mathbf{B}_A represents a matrix containing the spatial derivatives of the shape functions N_A . The curl operator that is used to calculate the magnetic flux density (see (2.38)) is included in the matrix \mathbf{B}_A .

Linear Materials and Permanent Magnets

Starting from the magnetic energy, the linear approximation of the PDEs can be derived. Every magnetic material has a different numerical formulation. The magnetic energy in linear magnetic materials and permanent magnets can be expressed by (2.71), assuming that the magnetisation characteristic of permanent magnets is also linear, as has been done in (2.6). Discretising this equation, using the relation in (2.104), and the definition for the magnetic vector potential, (2.38), yields

$$w_{pm} \approx \frac{1}{2\mu} \mathbf{q}_A^T \mathbf{B}_A^T \mathbf{B}_A \mathbf{q}_A + w_{pm,o} - \frac{\mathbf{B}_r^T \mathbf{B}_A \mathbf{q}_A}{\mu} \quad (2.136)$$

where $w_{pm,o}$ is a constant depending on the magnetic properties of the permanent magnet defined in (2.10). For materials that are no permanent magnets the last two terms in (2.136) are zero.

The stiffness matrix is derived by taking the second derivative of (2.136) with respect to the degrees of freedoms of the system, i.e. \mathbf{q}_A .

$$\mathbf{K}_{AA} = \int_{\Omega_{mag}} \frac{1}{\mu} \mathbf{B}_A^T \mathbf{B}_A d\Omega_{mag} \quad (2.137)$$

The magnetic stiffness matrix is the same for permanent magnets and linear magnetisable materials. The two extra terms for permanent magnets in (2.136) depend only linearly on the nodal values of the magnetic field, \mathbf{q}_A . They can be discretise as source terms \mathbf{J}_{pm} . This term can be derived by taking the first derivative of the third term in (2.136)

$$\mathbf{J}_{pm} = - \frac{\partial}{\partial \mathbf{q}_A} \int_{\Omega_{pm}} \frac{\mathbf{q}_A^T \mathbf{B}_A^T \mathbf{B}_r}{\mu} + w_{pm,o} d\Omega_{pm} = - \int_{\Omega_{pm}} \frac{\mathbf{B}_A^T \mathbf{B}_r}{\mu} d\Omega \quad (2.138)$$

As a source term, (2.138) should be written on the right hand side of the PDE.

Discretising the dissipation function defined by (2.82) yields

$$\begin{aligned} \mathcal{D}_{mag} = \int_{\Omega_{mag}} & \left(\frac{1}{2} \dot{\mathbf{q}}_A^T \mathbf{N}_A^T \boldsymbol{\gamma} \mathbf{N}_A \dot{\mathbf{q}}_A + \dot{\mathbf{q}}_u^T \mathbf{N}_u^T [\mathbf{B}_A \mathbf{q}_A]_{\times} \boldsymbol{\gamma} \mathbf{N}_A \dot{\mathbf{q}}_A \right) \\ & + \dot{\mathbf{q}}_u^T \mathbf{N}_u^T [\mathbf{B}_A \mathbf{q}_a]_{\times} \boldsymbol{\gamma} [\mathbf{B}_A \mathbf{q}_a]_{\times}^T \mathbf{N}_u \dot{\mathbf{q}}_u d\Omega_{mag} \end{aligned} \quad (2.139)$$

where $[\mathbf{B}_A \mathbf{q}_A]_{\times}$ is the skew symmetric matrix that defines the vector product. The operator $[\bullet]_{\times}$ is defined by (2.84).

For now, no movement is assumed and the second and third terms in (2.139) are neglected as they are zero in that case. The dependency on the first derivative of the the displacement DoFs, $\dot{\mathbf{q}}_u$, will create a coupling term depending on the velocity of the structural displacement. The second and third terms will be covered later in Sec. 2.5.10. Without movement the discretised energy of the eddy currents can be differentiated twice with respect to the nodal values of the magnetic field to yield

$$\mathbf{C}_{AA} = \frac{\partial^2 \mathcal{D}_{mag}}{\partial \dot{\mathbf{q}}_A^2} = \int_{\Omega_{mag}} \mathbf{N}_A^T \boldsymbol{\gamma} \mathbf{N}_A d\Omega_{mag} \quad (2.140)$$

where $\boldsymbol{\gamma}$ denotes a diagonal matrix which contains the conductivities in the various directions on its diagonal. For an isotropic material, this matrix can be substituted by a scalar, because in that case the conductivities for all directions are the same.

The magnetic mass matrix is also called magnetic damping matrix. It results from a dissipated energy and, thus, decreases the energy of the systems just like a damping matrix. Accordingly, \mathbf{M}_{AA} as well as \mathbf{C}_{AA} are used for the magnetic mass matrix in literature. In this thesis, the symbol \mathbf{C}_{AA} is used.

The magnetic mass matrix, \mathbf{C}_{AA} , is the same for the linear and non-linear case, because the induced currents stay the same for the linear and nonlinear case. Laminated structures are usually modelled as orthotropic materials. The conductivity normal on the lamination sheets is usually set to a lower values than the real conductivity of the lamination material, to account for the effects of the lamination.

Nonlinear Materials

For a nonlinear relation between $\vec{\mathbf{B}}$ and $\vec{\mathbf{H}}$, the procedure for solving the equation differs to the linear case, as now the tangent stiffness matrix depends on the values of the magnetic vector potential \mathbf{q}_A .

As shown in (2.125), the tangent stiffness matrix for the magnetic field can be derived by

$$\mathbf{K}_{AA}^{mech} = \frac{\partial \mathbf{J}_{int}}{\partial \mathbf{q}_A} = \frac{\partial^2 W_{mag}}{\partial \mathbf{q}_A^2} \quad (2.141)$$

The definition of the BH-curve plays a major role in computing this term. When the relation between $\vec{\mathbf{H}}$ and $\vec{\mathbf{B}}$ is defined as an analytic function, then (2.141) can be expressed analytically too. If the relation is only defined as a set of points then the term can only be evaluated numerically.

Discretised Magnetic System Equations

For a closed system, without any external currents, the derivation of the magnetic field formulation is complete at this point. The system can be written in its discrete form as

$$\mathbf{C}_{AA}\dot{\mathbf{q}}_A + \mathbf{K}_{AA}\mathbf{q}_A = \mathbf{J}_{pm} \quad (2.142)$$

2.5.7

Discretising Open Magnetic Systems

Systems that include coils, considered open magnetic systems, need to include the extra terms resulting from the coils in the discrete formulation. The additional terms result from the additional term in the external energy for open systems and the circuit equation that was added to (2.123).

Discretising Coils

The discrete coupling terms for the interaction between the electric circuit and the magnetic field can be derived from the voltage that a changing magnetic field creates in the coil, v_{ind} , and the energy that enters the magnetic field through a coil, W_{coil} . Discretising (2.52) yields

$$\mathbf{v}_{ind} = \frac{N_c}{\Gamma_w} \int_{\Omega_c} \dot{\mathbf{q}}_A^T \mathbf{N}_A^T \mathbf{e}_j d\Omega_c \quad (2.143)$$

where \mathbf{v}_{ind} collects the induced voltages for all coils. For a three phase coil system in electric machines it consists, thus, of three components, one for each phase. \mathbf{e}_j denotes a matrix that defines the direction of each phase current, i.e. for each component of \mathbf{q}_c , in an element.

$$\mathbf{J}_e = \mathbf{e}_j \mathbf{q}_c = \mathbf{q}_c \quad (2.144)$$

The coupling term in the damping matrix can then be computed to by

$$\begin{aligned} \mathbf{C}_{cA} &= \frac{\partial \mathbf{v}_{ind}}{\partial \dot{\mathbf{q}}_A} = \frac{\partial}{\partial \dot{\mathbf{q}}_A} \left(\frac{N_c}{\Gamma_w} \int_{\Omega_c} \dot{\mathbf{q}}_A^T \mathbf{N}_A^T \mathbf{e}_j d\Omega_c \right) \\ &= \frac{N_c}{\Gamma_w} \int_{\Omega_c} \mathbf{N}_A^T \mathbf{e}_j d\Omega_c \end{aligned} \quad (2.145)$$

The term resulting from W_{coil} is derived by taking the derivative of the discretised version of the term with respect to \mathbf{q}_A and \mathbf{q}_c . W_{coil}

in the continuous system is given by (2.76). Discretising it yields

$$\begin{aligned} \mathbf{K}_{Ac} &= \frac{\partial^2 W_{coil}}{\partial \mathbf{q}_A \partial \mathbf{q}_c} = \frac{\partial^2}{\partial \mathbf{q}_A \partial \mathbf{q}_c} \int_{\Omega_c} \frac{N_c}{\Gamma_w} \mathbf{q}_A^T \mathbf{B}_A^T \mathbf{e}_j \mathbf{q}_c \, d\Omega_c \\ &= \int_{\Omega_c} \frac{N_c}{\Gamma_w} \mathbf{B}_A^T \mathbf{e}_j \, d\Omega_c \end{aligned} \quad (2.146)$$

Finally, the resistance of the coil needs to be modelled. For this, a 'stiffness' matrix \mathbf{K}_{cc} is introduced, which contains the resistances of the various coils. For electric machines, \mathbf{K}_{cc} consists of three values.

$$\mathbf{K}_{cc} = \begin{bmatrix} R_a & 0 & 0 \\ 0 & R_b & 0 \\ 0 & 0 & R_c \end{bmatrix} \quad (2.147)$$

where R_a , R_b , and R_c represent the resistances of phase a,b and c, respectively.

The Discrete Magnetic Field Equation for Open Systems

Bringing the various equations for the open magnetic system together, yields the coupled discrete equations for open magnetic systems.

$$\begin{bmatrix} 0 & 0 \\ \mathbf{C}_{cA} & 0 \end{bmatrix} \begin{bmatrix} \dot{\mathbf{q}}_A \\ \dot{\mathbf{q}}_c \end{bmatrix} + \begin{bmatrix} \mathbf{K}_{AA} & \mathbf{K}_{Ac} \\ 0 & \mathbf{K}_{cc} \end{bmatrix} \begin{bmatrix} \mathbf{q}_A \\ \mathbf{q}_c \end{bmatrix} = \begin{bmatrix} \mathbf{J}_{pm} \\ \mathbf{v}_{ext} \end{bmatrix} \quad (2.148)$$

For coil elements, there is no dissipating term in the magnetic mass matrix, because the electric potential differences created by a changing magnetic field are collected in the coil inductance. The dissipation is modelled by the resistance of the coil circuit and is computed by the \mathbf{K}_{cc} term.

Discrete Calculation of Magnetic Forces

2.5.8

So far, the elastic and the magnetic field have been discretised separately. For the coupling of the two physics, it is necessary to discretise the mechanisms that couple the physics. One of these mechanisms is the magnetic force acting on the structure, denoted by \mathbf{F}_{mag} . This force will depend on the magnetic field and the displacement and influences the mechanical displacement.

The continuous formulation of the magnetic force was introduced in Sec. 2.4.5. In this section, the continuous formulation is discretised and adapted for the finite element method.

There are three methods to calculate the force on mechanical structures. All are based on the principle of virtual work. The methods differ how the quantities are discretised. All three methods were discussed in the past. Since [79], the magnetic energy and its change under deformation were in the focus of magnetic force calculation. Maxwell's stress tensor was introduced shortly after. The implementation for the FEM was done by [28], in which the nodal method is introduced deriving the magnetic forces on the nodes of a finite element mesh.

The system in Fig. 2.13 will be used to explain the drawbacks and advantages of the various methods.

Using the Principle of Virtual Work Globally

The most accurate method for calculating forces on the whole domain is to use the principle of virtual work on a global level. That means that the global energy of the magnetic field is calculated and its sensitivity with respect to a defined displacement $\mathbf{q}_{u\,def}$ is computed.

$$\mathbf{F}_{mag} = - \frac{\partial W_{mag}}{\partial \mathbf{q}_{u\,def}} \quad (2.149)$$

where \mathbf{F}_{mag} denotes the nodal force values for all nodes that are included in the defined displacement $\mathbf{q}_{u\,def}$. Usually, this defined displacement is a rigid motion of a body within the magnetic field such as the rigid rotation of a rotor in an electric machine. For a defined rotation, it is possible to numerically differentiate the energy by the defined displacement after the simulation is done. With this method, it is not possible to calculate local forces on individual nodes.

Using Maxwell's Stress Tensor

Maxwell stress tensor, which was introduced in Sec. 2.4.5, can also be discretised and expressed by the variables introduced in (2.104). For a linear magnetic material, such as air, the first line in Tab. 2.1 is applicable yielding for Maxwell's stress tensor

$$\begin{aligned} \underline{\underline{\mathbf{T}}}(\mathbf{q}_u, \mathbf{q}_A) &= \int_{\Omega} \vec{\mathbf{H}} \vec{\mathbf{B}}^T - \mathbf{I} \frac{\vec{\mathbf{B}}^T \vec{\mathbf{H}}}{2} d\Omega \\ &\approx \int_{\Omega} \mathbf{q}_A \mathbf{B}_A \frac{1}{\mu} \mathbf{B}_A^T \mathbf{q}_A^T - \mathbf{I} \left(\mathbf{q}_A^T \mathbf{B}_A^T \frac{1}{2\mu} \mathbf{B}_A \mathbf{q}_A \right) d\Omega \end{aligned} \quad (2.150)$$

The force on a surface can then be approximated by (2.103). The

discrete form of (2.103) reads as follows:

$$\underline{\mathbf{f}}_{mag} = \mathbf{n}^T(\mathbf{q}_u) \underline{\mathbf{T}}(\mathbf{q}_u, \mathbf{q}_A) \tag{2.151}$$

The coupled part of the tangent stiffness matrix \mathbf{K}_{uA} can be derived by taking the derivative of the magnetic force (2.103) with respect to the nodal values of the magnetic vector potential. This yields

$$\mathbf{K}_{uA} = \mathbf{n}^T(\mathbf{q}_u) \frac{\partial \underline{\mathbf{T}}(\mathbf{q}_u, \mathbf{q}_A)}{\partial \mathbf{q}_A} \tag{2.152}$$

$\frac{\partial \underline{\mathbf{T}}(\mathbf{q}_u, \mathbf{q}_A)}{\partial \mathbf{q}_A}$ is a 3rd order tensor. Multiplying it with a vector yields a matrix.

As can be seen from (2.152), only elements that share an interface with the structure create a magnetic force. In Fig. 2.13 only the elements IV and VI have this common interface. The force created by the other elements is, thus, neglected.

The magnetic contribution to the structural stiffness matrix can be derived by

$$\mathbf{K}_{uu}^{mag} = \mathbf{n}^T(\mathbf{q}_u) \frac{\partial \underline{\mathbf{T}}(\mathbf{q}_u, \mathbf{q}_A)}{\partial \mathbf{q}_u} + \frac{\partial \mathbf{n}^T(\mathbf{q}_u)}{\partial \mathbf{q}_u} \underline{\mathbf{T}}(\mathbf{q}_u, \mathbf{q}_A) \tag{2.153}$$

Using the Principle of Virtual Work Locally

The method using Maxwell’s stress tensor has the disadvantage that it does not compute forces within the structural domain. For that, the gradient of Maxwell’s stress tensor needs to be evaluated numerically. Furthermore, for the force computation around corners, it neglects elements that do not share a surface with the structure, as showed in the previous section.

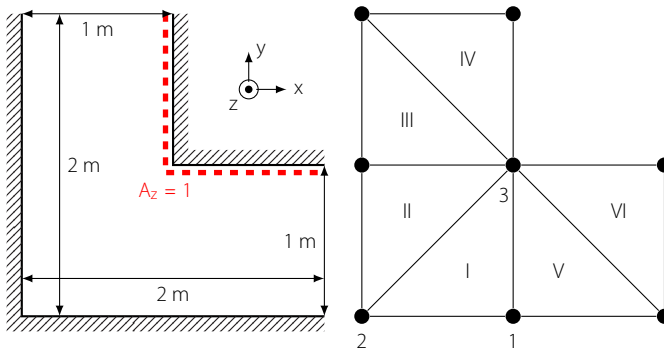


Figure 2.13
Example system including a singularity at the centre point of the system

There is another technique of calculating the magnetic forces. Instead of multiplying the tensor with the surface of the interface it

calculates the change of magnetic energy associated with a change of displacement of each node. This method was first discussed in [28], where it was called nodal method. Although Maxwell's stress tensor is also derived from the principle of virtual work, using it introduces some inaccuracies in the calculation of the magnetic force that the nodal method does not introduce.

Starting from the magnetic energy, w_{mag} , the magnetic force can be calculated by deriving the magnetic energy with respect to the displacement field $\bar{\mathbf{u}}$. As shown in Appendix A this approach leads to

$$\delta W_{mag} = V \frac{\bar{\mathbf{B}}^T (\nabla \delta \bar{\mathbf{u}}) \bar{\mathbf{B}}}{\mu} - \text{tr}(\nabla \delta \bar{\mathbf{u}}) \frac{\bar{\mathbf{B}}^T \bar{\mathbf{B}}}{2\mu} \quad (2.154)$$

which is the same as (A.7), for a virtual displacement, $\delta \bar{\mathbf{u}}$, in a linear magnetic material. In (2.154), V denotes the volume of the element and $\text{tr}(\nabla \delta \bar{\mathbf{u}})$ denotes the traces of the tensor $\nabla \delta \bar{\mathbf{u}}$. Instead of using this formula to derive Maxwell's stress tensor, it can be used to calculate the magnetic force directly. Discretising $\nabla \delta \bar{\mathbf{u}}$, using the finite element method (2.104), yields a matrix, \mathbf{B}_{2u} , containing derivatives of the shape function N_u , which is define by

$$\nabla \bar{\mathbf{u}} = \begin{bmatrix} \frac{\partial u}{\partial x} & \frac{\partial u}{\partial y} & \frac{\partial v}{\partial x} & \frac{\partial v}{\partial y} \end{bmatrix}^T \approx \mathbf{B}_{2u} \mathbf{q}_u \quad (2.155)$$

for a 2D mesh. Because the tensor $\nabla \bar{\mathbf{u}}$ is not symmetric, all elements need to be written out.

Using the approximation in (2.155), the magnetic force vector can be written as

$$\mathbf{F}_{mag} = - \frac{\partial W_{mag}}{\partial \mathbf{q}_u} = - \frac{1}{2\mu} \int_{\Omega} \mathbf{B}_{2u}^T \mathbf{F}(\mathbf{q}_A) d\Omega \quad (2.156)$$

where \mathbf{F} denotes a matrix that contains various products of magnetic flux density components.

$$\mathbf{F} = \begin{bmatrix} B_x^2 - B_y^2 & 2B_x B_y & 2B_y B_x & B_y^2 - B_x^2 \end{bmatrix} \quad (2.157)$$

See Appendix A for a detailed derivation of this formula.

The submatrix of the tangent stiffness matrix denoting the coupling between the magnetic field and the structural mechanics, \mathbf{K}_{uA} , can be derived by taking the derivative of the magnetic force with respect to the nodal value of the magnetic vector potential, as seen in (2.125). The derivation, which leads to

$$\mathbf{K}_{uA}(\mathbf{q}_A) = \frac{1}{2\mu} \int_{\Omega} \mathbf{B}_{2u}^T \mathbf{F}_2(\mathbf{q}_A) \mathbf{B}_A d\Omega \quad (2.158)$$

with

$$\mathbf{F}_2 = \begin{bmatrix} B_x & B_y & B_y & -B_x \\ -B_y & B_x & B_x & B_y \end{bmatrix}^T$$

is written out in Appendix A.

The last term of the stiffness matrix is the mechanical stiffness that is created by the magnetic field. It can be computed by deriving the magnetic energy with respect to a mechanical displacement. This is shown in Appendix A

$$\mathbf{K}_{uu}^{mag} = \frac{1}{2\mu} \int_{\Omega} \mathbf{B}_{2u}^T \mathbf{F}_3(\mathbf{q}_A) \mathbf{B}_{2u} d\Omega \quad (2.159)$$

with

$$\mathbf{F}_3 = \begin{bmatrix} 2H_x B_x & 0 & 2H_y B_x & -(B_x H_x + H_y B_y) \\ 0 & 2H_x B_x & (B_x H_x + H_y B_y) & 2H_x B_y \\ 2H_y B_x & (B_x H_x + H_y B_y) & 2B_y H_y & 0 \\ -(B_x H_x + H_y B_y) & 2B_y H_x & 0 & 2B_x H_x \end{bmatrix} \quad (2.160)$$

The Local Virtual Work Method applied to Permanent Magnets

As shown in [62], the energy and co-energy change of permanent magnets under deformation depends on the behaviour of the magnetisation of the PM. In Sec. 2.4.5 it was shown that the magnetic flux density and the magnetic field behave differently under deformation. This results from the dependence of the magnetic flux on the flux linkage and, thus, on the total flux of the system, whereas the magnetic field depends on the currents of the system. It is unclear how the magnetisation of a permanent magnet behaves under deformation and if the magnetic fluxes or the 'imaginary' currents of the permanent magnet are constant. Therefore, both cases are presented here.

The derivation for the two cases presented in this subsection can be found in Appendix A.

For the first case the magnetic remanence changes like the magnetic flux density under deformation: $\delta \vec{B}_r = \delta \vec{B}_r|_{\delta \Phi_B=0} = \nabla \delta \vec{u} \vec{B}_r - \text{tr}(\nabla \delta \vec{u}) \vec{B}_r$. For this case the force acting on a permanent magnet can be written as

$$\begin{aligned} F_{mag} &= -\frac{1}{2\mu} \int_{\Omega} \mathbf{B}_{2u}^T \mathbf{F}(\mathbf{q}_A) d\Omega \\ &\quad - \frac{1}{2\mu} \int_{\Omega} \mathbf{B}_{2u}^T \mathbf{F}_{PM}(\mathbf{q}_A) d\Omega \\ &\quad + \frac{1}{\mu} \int_{\Omega} \mathbf{B}_{2u}^T \mathbf{F}_{PM2}(\mathbf{q}_A) d\Omega \end{aligned} \quad (2.161)$$

in its discretised form with

$$\mathbf{F}_{PM}(\mathbf{q}_A) = \begin{bmatrix} B_{rx}^2 - B_{ry}^2 & 2B_{rx}B_{ry} & 2B_{rx}B_{ry} & B_{ry}^2 - B_{rx}^2 \end{bmatrix}^T \quad (2.162)$$

$$\mathbf{F}_{PM2}(\mathbf{q}_A) = \begin{bmatrix} B_{rx}B_x & B_{rx}B_y + B_{ry}B_x & B_xB_{ry} + B_{rx}B_y & B_{ry}B_y \end{bmatrix}^T \quad (2.163)$$

For the second case, the remanence flux density behaves like the magnetic field, and the 'imaginary' currents in the permanent magnet are held constant: $\delta\vec{\mathbf{B}}_r = \delta\vec{\mathbf{B}}_r|_{\delta I=0} = -\nabla\delta\tilde{u}\vec{\mathbf{B}}_r$. The discretised form of magnetic force reads as

$$\begin{aligned} \mathbf{F}_{mag} = & -\frac{1}{2\mu} \int_{\Omega} \mathbf{B}_{2u} \mathbf{F}(\mathbf{q}_A) d\Omega \\ & - \frac{1}{2\mu} \int_{\Omega} \mathbf{B}_{2u} \mathbf{F}_{PM}(\mathbf{q}_A) d\Omega \end{aligned} \quad (2.164)$$

The coupling matrices for permanent magnet materials can be derived analog to the derivation for the linear magnetic material in Appendix A, starting from (A.21) and (A.23).

Nonlinear Materials

For nonlinear materials, i.e. where the magnetic flux density and the magnetic field are not linked by a constant scalar, it can be assumed that (2.96) and (2.93) are still valid because the intensity of the magnetic field is assumed constant for their derivation. Therefore, the coupling matrices can be derived in the same way as in Appendix A. However [62] claims that further research on the thermodynamic relations of ferromagnetic materials is necessary to ensure (2.96) and (2.93) are indeed valid for this type of material.

2.5.9

Comparing Different Methods of Calculating Magnetic Forces

To illustrate the difference between the two methods of calculating magnetic forces, consider the simple example depicted in Fig. 2.13, of which the solutions is shown in Fig. 2.14. The magnetic field in vacuum was simulated around a magnetically non-conducting piece of structure. The singularity that is generated in such a system is clearly visible in the right part of Fig. 2.14.

The system's solution can be calculated analytically using conformal mappings. This type of analysis has been done in [146] for an electric field. Conformal mappings and their applications to magnetic fields are thoroughly explained in [16]. The computed solution for this problem can be seen in the right part of Fig. 2.14, which shows

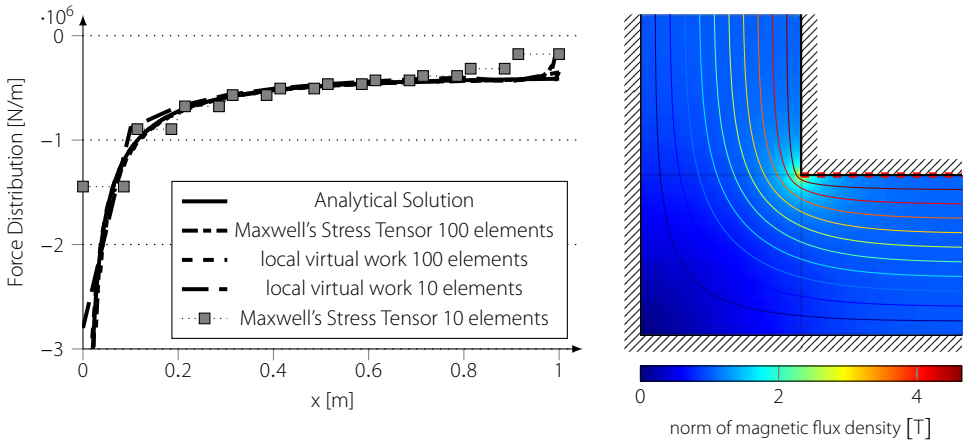


Figure 2.14 Magnetic field around corner including singularity. The dashed red line indicates the surface for which the force is computed.

the magnetic field lines and the magnetic flux norm of the solution. Tab. 2.2 presents the computed forces in y direction for the three methods described above and for the analytic solution. In the left part of Fig. 2.14 the force density in y-direction is depicted over the horizontal boundary of the system at $y = 1$, indicated by the red dashed line in the right part of Fig. 2.14.

Method	Calculated Force in y direction 100 elements		Calculated Force in y direction 10 elements	
	absolute value of force	rel. error	absolute value of force	rel. error
Analytic Solution	-791 153 N	0%	-791 153 N	0%
Globally applied virtual work	-795 630 N	0.6%	-766 050 N	3.2%
Maxwell's stress tensor	-721 158 N	8.8%	-586 236 N	25.9%
Locally applied virtual work	-793 659 N	0.3%	-766 050 N	3.2%

Table 2.2 Comparison of the various methods to calculate magnetic forces

The singularity at the corner results in an increased magnetic force at the corner. This increase is not properly accounted for in the force calculation method using Maxwell's stress tensor. This can be seen by the bad match of the force distribution between the analytical solution and the method using Maxwell's stress tensor on the left part of Fig. 2.14. From Tab. 2.2, it becomes clear that for coarse meshes the method using the method of virtual work (globally and locally) yields more accurate results for the total force than the forces computed by Maxwell's stress tensor. The error that is associated with Maxwell's stress tensor will decrease with increasing numbers of elements in the model.

2.5.10

The Moving Mesh

Magneto-mechanical coupled systems of electric machines necessitate the distinction between two mechanisms that require a moving mesh. The first mechanism is the rotation of the machine's rotor. This rotation depends on the rotor position and can easily be computed from the rotation angle. The other mechanism is the deformation of the structure.

In the past, various methods for handling deformation and movement of the underlying structure of the magnetic field have been proposed. The two most common ones are the method employing Lagrange multipliers [56, 96] and the method using a moving mesh [96, 126, 133]. The first one is mainly used to simulate the rotation of the machine. The second method mainly for the simulation of deformation of a structure.

In this thesis, only the moving mesh method will be discussed in detail, because the method using Lagrange multipliers is rather well known and is used in magnetic finite element models or structural finite element models that include rotation or movement.

For a structural object in a magnetic field, the PDEs (2.47) or (2.45) and (2.35) need to be solved for Ω_{cpl} in Fig. 2.6. The magnetic field is based on Eulerian coordinates, whereas the structural PDE is based on Lagrangian coordinates. Implementing an Eulerian coordinate system in the FE formulation means that each node of the mesh of the magnetic field needs to move with the displacement of that node \mathbf{q}_u . It is therefore necessary that a moving mesh is implemented in the finite element formulation for the magnetic field.

Because the PDEs of the magnetic field are based on the spatial coordinates, the integrals for the magnetic stiffness and mass matrix (2.140) and (2.137) depend on the displacement of the structure.

The exact position of each node within the domain is arbitrary, when solving the magnetic PDE (2.142) without mechanical interaction. It is, however, required that the distance between the nodes is small enough so that the mesh can describe the gradients of the magnetic field. Otherwise, the partial differential equation cannot be solved accurately. The position of the boundary of a domain at which the material properties change is important. The boundary conditions in (2.48) depend on it and it has, therefore, an influence on the solution of the magnetic PDE (2.142).

When deformation is introduced into the system, the above statement is no longer true. In that case, a distinction between domains with a structure and fluids or gaseous domains has to be made.

For magnetic materials that have no structure, e.g. air, the position

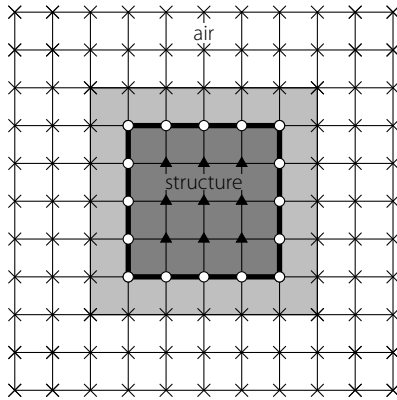


Figure 2.15
Moving Mesh around Structure

of the nodes of the mesh of the magnetic field is still not important. Important is that the position of the boundaries of the air domain follows the displacement of any adjacent structural domain. The position of the magnetic nodes on the boundary have to change according to the displacement of that boundary. The position of the other nodes can be chosen freely, and thus, can be fixed. The various categories of nodes and elements are depicted in Fig. 2.15. The moving boundary, represented by the thick line, only has an influence on the grey elements. Because the nodal placement within the domain is arbitrary, the other nodes, depicted by crosses, can be fixed.

For domains that have a structure, however, the nodal position is very much of importance. Firstly, the force computed in (2.98) needs to be applied to the nodes of the elastic field. It is therefore convenient to evaluate (2.98) at the position of the nodes of the elastic field. Secondly, the movement of the structure can induce eddy currents. These eddy currents, need to be applied to the magnetic PDE at the location of their generation. In order for the magnetic nodes to follow the deformed structure, the magnetic nodes have to follow the displacement of the structure and thus depend on the deformation.

Influence of the Moving Mesh on the Magnetic Field

The moving mesh, introduced in the previous section, is a tool to simulate the influence of the displacement of the structure onto the magnetic field. Because the moving mesh follows the displacement of the structure, the resulting changes on the magnetic field are actually the influences of the deforming and moving structure.

To discretise the effect, the moving boundary has on the magnetic field in the air domain, the magnetic stiffness matrices of the elements directly adjacent to the structure (in Fig. 2.15 the light grey-

ish elements) need to be expressed in terms of the displacement \mathbf{q}_u . Starting from the total energy W_{total} , the internal currents \mathbf{J}_{int} can be derived by taking the partial derivative of the energy with respect to the magnetic displacement. The influence of the displacement on these internal current can be expressed in the coupling matrix \mathbf{K}_{Au}

$$\mathbf{K}_{Au}(\mathbf{q}_A, \mathbf{q}_u) = -\frac{\partial \mathbf{J}_{int}}{\partial \mathbf{q}_u} = \frac{\partial^2 \mathcal{V}_{int}}{\partial \mathbf{q}_u \partial \mathbf{q}_A} \quad (2.165)$$

\mathcal{V}_{int} can be substituted by W_{mag} , because of all energies in (2.59) only the magnetic energy, W_{mag} , depends on both types of nodal values, the displacement and the magnetic field. All other energies will yield zero when derived with respect to the nodal values of the displacement and the magnetic field.

For a potential, the order of taking derivatives does not matter. It is therefore possible to write

$$\begin{aligned} \mathbf{K}_{Au} &= \frac{\partial}{\partial \mathbf{q}_u} \left(\frac{\partial}{\partial \mathbf{q}_A} W_{mag} \right) \\ &= \frac{\partial}{\partial \mathbf{q}_A} \left(\frac{\partial}{\partial \mathbf{q}_u} W_{mag} \right) = -\frac{\partial}{\partial \mathbf{q}_A} \mathbf{F}_{mag} = \mathbf{K}_{uA}^T \end{aligned} \quad (2.166)$$

And indeed, when the correct method is chosen for the calculation of the coupling matrix \mathbf{K}_{uA} , the method using the local principle work, the top left part of the coupled stiffness matrix \mathbf{K} in (2.125) becomes symmetric.

Eddy currents represent the other effect, how the magnetic field is influenced by the mechanical deformation. In (2.46), it was stated that the eddy currents depend on the time derivative of the magnetic conductor's deformation. For the derivation of the magnetic mass matrix in (2.139), this dependency was neglected. This term is especially important for the simulation of rotating machinery. Taking the derivative of the eddy current's energy with respect to the nodal values of the change of the magnetic vector potential and the nodal velocities yields the coupling term

$$\begin{aligned} \mathbf{C}_{uA}(\mathbf{q}) &= \mathbf{C}_{Au}(\mathbf{q})^T = \frac{\partial^2 \mathcal{D}_{mag}}{\partial \dot{\mathbf{q}}_u \partial \dot{\mathbf{q}}_A} \\ &= \int_{\Omega_{mag}} \mathbf{N}_u^T \underbrace{[\mathbf{B}_A \mathbf{q}_A]_{\times}}_{\mathbf{F}_c(\mathbf{q}_A)} \boldsymbol{\gamma} \mathbf{N}_A \, d\Omega_{mag} \end{aligned} \quad (2.167)$$

where $[\mathbf{B}_A \mathbf{q}_A]_{\times}$ is again the matrix representing the cross product defined in (2.84) and already used in (2.139). The third and second term of (2.139) does not contribute to this term as they do not depend on $\dot{\mathbf{q}}_u$ and $\dot{\mathbf{q}}_A$.

For a 2D model with triangular elements, $F_c(\mathbf{q}_A)$ can be evaluated to read as

$$\mathbf{F}_c(\mathbf{q}_A) = \begin{bmatrix} B_y N_{A,A} & B_y N_{A,B} & B_y N_{A,C} \\ -B_x N_{A,A} & -B_x N_{A,B} & -B_x N_{A,C} \end{bmatrix} \quad (2.168)$$

Like the coupling matrices \mathbf{K}_{uA} and \mathbf{K}_{Au} , \mathbf{C}_{uA} and \mathbf{C}_{Au} depend on the magnetic vector potential itself.

The last term of the coupled damping matrix can be derived by deriving the dissipation function of the eddy currents, \mathcal{D}_{mag} in (2.139), twice by the displacement velocity.

$$\mathbf{C}_{uu}^{mag}(\mathbf{q}) = \frac{\partial^2 \mathcal{D}_{mag}}{\partial \dot{\mathbf{q}}_u^2} = \int_{\Omega} 2\mathbf{N}_u^T [\mathbf{B}_A \mathbf{q}_A]_{\times} \gamma [\mathbf{B}_A \mathbf{q}_A]_{\times}^T \mathbf{N}_u d\Omega \quad (2.169)$$

Again, two terms in (2.139) do not contribute due to their missing dependency on $\dot{\mathbf{q}}_u$.

The Discretised Coupled System

2.5.11

With the matrices introduced in Sec. 2.5, the nonlinear system of equation (2.58) can be written as a linear discretised system that depends on the nodal values of the magnetic field and the displacement field.

$$\underbrace{\begin{bmatrix} \mathbf{M}_{uu} & \mathbf{0} & \mathbf{0} \\ \mathbf{0} & \mathbf{0} & \mathbf{0} \\ \mathbf{0} & \mathbf{0} & \mathbf{0} \end{bmatrix}}_M \underbrace{\begin{bmatrix} \ddot{\mathbf{q}}_u \\ \ddot{\mathbf{q}}_A \\ \ddot{\mathbf{q}}_c \end{bmatrix}} + \underbrace{\begin{bmatrix} \mathbf{C}_{uu}^{mech} + \mathbf{C}_{uu}^{mag}(\mathbf{q}) & \mathbf{C}_{uA}(\mathbf{q}) & \mathbf{0} \\ \mathbf{C}_{Au}(\mathbf{q}) & \mathbf{C}_{AA}(\mathbf{q}_u) & \mathbf{0} \\ \mathbf{0} & \mathbf{C}_{cA}(\mathbf{q}) & \mathbf{0} \end{bmatrix}}_C \underbrace{\begin{bmatrix} \dot{\mathbf{q}}_u \\ \dot{\mathbf{q}}_A \\ \dot{\mathbf{q}}_c \end{bmatrix}} + \underbrace{\begin{bmatrix} \mathbf{K}_{uu}^{mech} + \mathbf{K}_{uu}^{mag}(\mathbf{q}) & \mathbf{K}_{uA}(\mathbf{q}) & \mathbf{0} \\ \mathbf{K}_{Au}(\mathbf{q}) & \mathbf{K}_{AA}(\mathbf{q}_u) & \mathbf{K}_{Ac}(\mathbf{q}_u) \\ \mathbf{0} & \mathbf{0} & \mathbf{K}_{cc} \end{bmatrix}}_K \underbrace{\begin{bmatrix} \mathbf{q}_u \\ \mathbf{q}_A \\ \mathbf{q}_c \end{bmatrix}} = \underbrace{\begin{bmatrix} \mathbf{F}_{ext} \\ \mathbf{J}_{PM} \\ \mathbf{V}_{ext} \end{bmatrix}} \quad (2.170)$$

Linearized Coupled Eigenvalue Problem

2.6

To analyse the changes that the magneto-mechanical coupling has on the vibrational behaviour of a structure, it is necessary to conduct a modal analysis of the coupled system. To achieve that, a monolithic coupled eigenvalue problem needs to be formulated.

Such a monolithic formulation has been done in [131] for electrostatic mechanical couplings. It makes it possible to calculate the eigenvalues and mode shapes of the coupled system.

Assuming that the displacements \mathbf{u} are small, the effects of the displacement on the system matrices can also be assumed to be small. In that case, the values of the matrices can be approximated linearly around a linearisation point \mathbf{q}_0 . The system described by (2.170) can then be transformed into a monolithic linear eigenvalue problem that calculates the vibration behaviour of the system around the point, \mathbf{q}_0 . Usually the system for zero displacement $\mathbf{q}_{0,u} = \mathbf{0}$ and a static magnetic field $\mathbf{q}_{0,A}$ is chosen as linearisation point, \mathbf{q}_0 . That yields the coupled eigenvalue problem

$$(\mathbf{K} + \lambda \mathbf{i} \mathbf{C} - \lambda^2 \mathbf{M}) \Phi = \mathbf{0} \quad (2.171)$$

where Φ denotes the columns matrix of eigenvectors, λ the eigenvalues of the system and \mathbf{i} the imaginary number.

Inserting the various terms for the stiffness, mass and damping matrices into (2.171) yields

$$\begin{aligned} & \left(-\lambda^2 \begin{bmatrix} \mathbf{M}_{uu} & \mathbf{0} & \mathbf{0} \\ \mathbf{0} & \mathbf{0} & \mathbf{0} \\ \mathbf{0} & \mathbf{0} & \mathbf{0} \end{bmatrix} + \mathbf{i} \lambda \begin{bmatrix} \mathbf{C}_{uu}^{mech} + \mathbf{C}_{uu}^{mag}(\mathbf{q}_0) & \mathbf{C}_{uA}(\mathbf{q}_0) & \mathbf{0} \\ \mathbf{C}_{Au}(\mathbf{q}_0) & \mathbf{C}_{AA}(\mathbf{q}_{0,u}) & \mathbf{0} \\ \mathbf{0} & \mathbf{C}_{cA}(\mathbf{q}_0) & \mathbf{0} \end{bmatrix} + \right. \\ & \left. + \begin{bmatrix} \mathbf{K}_{uu}^{mech} + \mathbf{K}_{uu}^{mag}(\mathbf{q}_0) & \mathbf{K}_{uA}(\mathbf{q}_0) & \mathbf{0} \\ \mathbf{K}_{Au}(\mathbf{q}_0) & \mathbf{K}_{AA}(\mathbf{q}_{u,o}) & \mathbf{K}_{Ac}(\mathbf{q}_{u,o}) \\ \mathbf{0} & \mathbf{0} & \mathbf{K}_{cc} \end{bmatrix} \right) \Phi = \mathbf{0} \end{aligned} \quad (2.172)$$

2.7

Summary

In this chapter, the fundamental mathematical relations and numerical methods were introduced to model magneto-mechanical coupling in a monolithic way. Nonlinear as well as linear magnetic materials were taken into account and several ways to calculate the magnetic forces were presented. Finally, a way to calculate the effects of a magnetic field on structural dynamics behaviour was introduced which incorporated the linearisation of the nonlinear coupled equation.

The introduced methods will be used in Chapter 4, 5 and 6 to simulate the coupled dynamic behaviour of electric machines and in particular wind turbine generators.

Remember that all models are wrong; the practical question is how wrong do they have to be to not be useful.

George Edward Pelham Box and Norman Richard Draper [18, p. 74]

This Chapter is based on the papers:

Kirschneck, M., Rixen, D.J., Polinder, H., van Ostayen, R.A.J.
Effects of Magneto-Mechanical Coupling on Structural
Modal Parameters. Topics in Modal Analysis II, 2014,
Volume 8

Abstract:

Structures that are exposed to a magnetic field experience magnetic forces. As these forces are geometry dependent, they vary with the displacement of the structure that can result in an additional stiffness. Furthermore, eddy currents, which are induced by the movement of the structure, can lead to an increased dissipation resulting in a higher damping value for the mechanical part of the system. This chapter presents measurements intended to quantify these effects and verify the modelling techniques introduced in Chapter 2. For that purpose a simple lab test rig is used.

3.1

Introduction

By the above quote, the problem of every model becomes apparent. Models are based on simplification to cast the real behaviour of a system into mathematical formulas. This makes it possible to predict the behaviour of systems. However, the accuracy of the model and its validity for a certain set of states depends on the simplification made during its derivation. Therefore, it needs to be ensured that the simplifications made are applicable and do not lead to a model describing a different behaviour than the behaviour of the system of interest. Therefore, it is necessary to verify a model with either another more detailed model or by measurements to increase the confidence in the validity and correctness of the model.

This chapter will describe the procedures and techniques that were used to validate the simulation methods introduced in Chapter 2. Although the simulation methods for continuum mechanics and magnetic fields for themselves are well validated, it is necessary to ensure the correctness of the coupled system and of the linearisation for the coupled eigenvalue problem. The experiments to do this validation are presented in this chapter. It eventually concludes that the modelling methods introduced in Chapter 2 are sufficient to predict the magneto-mechanical coupled behaviour.

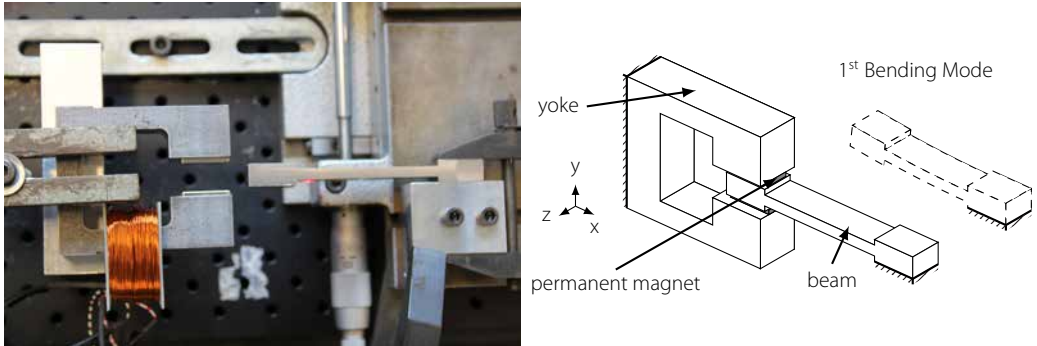
3.2

The Test Set Up

To verify the calculation methods introduced in Chapter 2, a simple system has to be found that includes all the effects that the calculation method can cover. The system has to satisfy some conditions to make it suitable for the verification process. First, it needs to exhibit a frequency change due to the interaction between the structural dynamics and the magnetic field. Although many systems can be identified that show this behaviour, it is difficult to find a system in which the interaction can be switched off or rendered inactive while the rest of the system stays unaltered. Secondly, the system's uncertainty needs to be as small as possible. All material properties, geometries and physical constants in the system should be known as accurately as possible. Any deviation between the simulation and the measurements can then be reduced to the errors in the simulation. Very little materials exist for which both magnetic and mechanical properties are well known. This is because either they were intended for mechanical applications and, thus, the electric properties were not of interest, or they were designed for electric application, which means that the exact mechanical properties are not important for their intended use.

Characteristics of the Test Set-Up

3.2.1



a) Photo of the measurement set-up. The set-up is depicted in the configuration without coupling the beam completely out of the air gap. The coil in the photo was not used for the experiments. b) Schematic of the test set up and first bending mode

Fig. 3.1 shows the test rig used for the purpose of verifying the modelling technique. It consists of an unlaminated yoke with a gap and a flexible beam. The gap of the yoke is wide enough so that the beam can be inserted into the air gap. The magnetic field is created by two permanent magnets on either side of the air gap. The yoke is fixed while the beam is mounted on a table that can be moved. This allows the beam to be moved into and out of the air gap. This set up was chosen for several reasons.

- It was readily available.
- The beam can be moved in and out of the air gap, making it possible to 'activate' or 'deactivate' the coupling between the beam and the magnetic field.
- It is as simple as possible while showing a change of resonance frequency and increased damping due to the coupling.

The test set-up also shows some significant drawbacks. The permeability and the conductivity of the yoke and beam are unknown. The magnetic field in the system is excited by permanent magnets that cannot be 'switched off' or be removed. Further, the system changes when the beam is removed because the new table position might lead to a different stiffness of the mounting.

The beam is constructed in such a way that the first bending frequency in y-direction is much lower than the frequency of the first bending mode in z-direction. This way the two bending modes do not couple. The bending mode in y-direction, which is shown in Fig. 3.1b, will decrease the air gap length on one side of the beam

Figure 3.1
The test rig used for measurements

while it is increased on the other side of the beam. This will change the magnetic field in the air gap.

3.2.2

Mechanisms Affecting the Modal Parameters

There are four different effects that can influence the modal parameters of the coupled system. Three of them influence the resonance frequency due to additional stiffness introduced into the system by the magnetic field and one increases the damping due to additional losses. All but one of the effects can be explained using the system in Fig. 3.1 as an example. The last effect is present in electric machines but cannot be explained with the test rig.

For the additional stiffness, the differentiation between positive and negative stiffness needs to be done. Stiffness is created when a force acting on a structure is changed by the displacement of that structure

$$k = -\frac{\partial f}{\partial u} \quad (3.1)$$

where f denotes the force, u the displacement from the equilibrium position at which the force is zero, and k the stiffness value.

A positive stiffness is created when the force change opposes the displacement, i.e. the force is directed in the opposite direction than the movement and increases with the movement. This is the usual stiffness found in a spring or in an oscillating pendulum.

A negative stiffness is created when the force is aligned with the displacement and acts in the same direction as the displacement. This kind of stiffness can be found in unstable systems such as a pendulum that is balancing above its attachment point. Only a slight deviation will cause the system to leave that point because the force increases with the displacement pulling the mass further away.

Magnetic Stiffness due to Reluctance Change

The first mechanism involves a change of the magnetic forces due to a change of reluctance of the system. This mechanism cannot be found in the beam test set-up. However, it will be of importance in a magnetic field and is listed here for completeness.

In Sec. 2.2.4 it was shown that the reluctance of a magnetic circuit depends on the length of the air gaps. In this case, (2.15) can be used to calculate the reluctance change of the magnetic circuit. An increase in air gap length will increase the reluctance and thus decrease the magnetic flux density and the specific magnetic energy. The attracting forces will decrease as they depend on the magnetic flux density. The force depends thus indirectly on the displacement.

For the attracting forces between two ferromagnetic materials in a magnetic field this creates a negative stiffness. The attracting forces increase with a decreasing distance between the two objects. Because the forces are attracting they point towards the other object. When the distance decreases they point in the same direction as the displacement and create a negative stiffness and an instability.

Everyone who has held a magnet in his hand before is familiar with this instability. It can be witnessed when a permanent magnet is moved towards a piece of iron. At some point the attracting forces become so big that the piece of iron moves towards the PM and sticks to it. The attracting forces become thus bigger when the distance between permanent magnet and piece of iron decreases.

For the test set-up this mechanism is not valid. The reluctance of the system does not change when the beam moves in y -direction, because one air gap always increases by the same amount as the other air gap decreases. The total reluctance stays the same and the magnetic flux density is constant.

Magnetic Stiffness due to Axial Displacement

This stiffness is important for a displacement in axial direction of an electric machine. The same mechanism creates stiffness when the beam is displaced in z - or in x -direction.

Consider a movement of the head of the beam in x -direction. This movement will decrease the overlap of the the PM on the beam with the stator yoke. The magnetic field creates a force that pulls the beam back into a position in which the beam head is perfectly aligned with the stator yoke. This force is created, because in this configuration the air gap length is shortest and thus the energy stored in the magnetic field is minimal.

The force is directed in the opposite direction of the displacement that causes it. It is thus a positive stiffness that gives the system additional stability.

Magnetic Stiffness due to Fringe Effects

The second mechanism which influences the air gap is caused by fringe effects. The 1D magnetic circuit model cannot explain this effect as it depends on the spatial distribution of the magnetic flux density in the air gap. In the first mechanism, we saw an increase or decrease of total magnetic flux due to a change of reluctance. For the second mechanism, the total flux does not change. Only the distribution in the air gap changes. In Sec. 2.4, it was shown that the normal magnetic force depends on the specific magnetic energy. An increase in magnetic flux density will thus cause an increase in magnetic force.

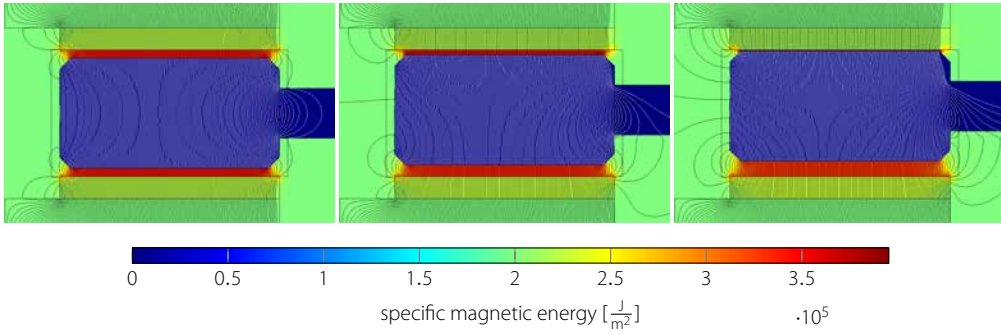


Figure 3.2

The magnetic field lines and the specific magnetic energy for the head of the beam

Fig. 3.2 depicts the magnetic flux lines and the specific magnetic energy of a cutting plane for varying amounts of bending deformation depicted in Fig. 3.4. The larger the air gap on the bottom side of the beam, the lower the specific magnetic energy in the air gap and the further apart are the magnetic flux lines. Consequently, the attracting force on that side of the beam will decrease as it is proportional to the specific magnetic energy.

At the upper part of the picture, the specific magnetic energy increases and the attracting force with it. The net force on the beam will thus point upward, the same direction as the displacement of the beam. Since the magnitude of this net force depends on the displacement of the beam, a negative stiffness is created.

Additional Damping due Eddy Currents

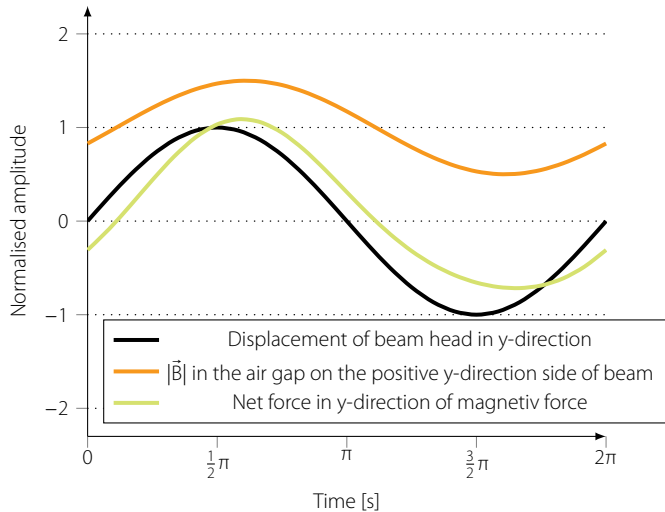


Figure 3.3

Development of magnetic field strength, displacement of the beam head and attracting force over time for a period of the first bending mode. The magnetic force and the displacement are normalised with the maximal value they reach during an oscillation. The magnetic flux density norm is normalised with its value for a displacement of $u = 0$

The last mechanism that influences the modal parameters is caused by eddy currents. An oscillating structure will result in a oscillating

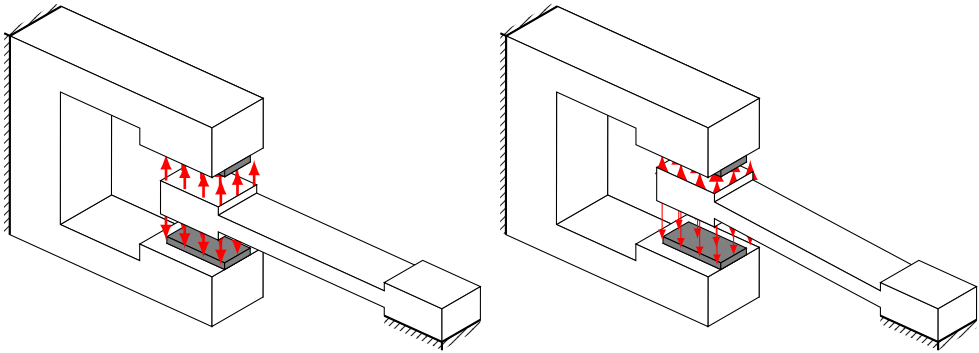


Figure 3.4

The first bending mode of the test set up. The red arrows represent the acting magnetic forces. The thickness of the arrows the strength of the force

magnetic force in the air gap, due to the dependency of the magnetic force on the displacement. This will create currents in the yoke and the beam which produce heat due to the ohmic resistance of the structure. From an energy point of view, an additional method to dissipate energy and create heat is introduced into the system.

In order to be able to measure an increased damping ratio mechanically, the eddy currents causing this dissipation must somehow affect the mechanical system. Due to the eddy currents, the magnetic field does not change instantaneously with the displacement of the beam, but will show a slight delay. This delay causes a delay of the magnetic force acting on the beam leading to increased damping.

Fig. 3.3 shows the various quantities needed to explain this effect for the first bending mode as depicted in Fig. 3.4. The eddy currents introduce a small delay in the magnetic response of the system, so that the maximal magnetic field strength on the top part of the beam (on the positive y -direction of the beam) is reached when the beam head is already moving back towards the centre position. Fig. 3.3 shows this delay of the amplitude of the magnetic field in the air gap. Because of this delay, the total magnetic force in y -direction, i.e. the magnetic force in y -direction created in both air gaps, is stronger when the beam moves back towards the centre position than when it was moving away from the centre position. Integrating (2.89) over a whole period of the oscillation will result in a value which is not zero, indicating a change of energy in the system.

In an electric machine, the lamination in the stator back iron minimises the amount of eddy currents and thus the additional damping introduced by this effect. The test trig used here is not laminated and, consequently, the damping effect is much stronger than

for electric machines. Therefore, it is expected that this effect is much smaller in electric machines than in the oscillating beam.

Emerging Effects

The above discussed effects that introduce additional damping and stiffness into a system affect the modal parameters of that system. For the first bending mode additional damping due to eddy currents and additional stiffness due to fringe effect play a role. Because of these two effects the frequency of the measured mode will be lower when the dynamics of the beam couple with the magnetic field. Additionally, the measured mechanical damping ratio will increase due to the coupling. These are the two effects that the measurements conducted in the next subsection will verify. These two effects can be identified by the FE model introduced in Sec. 3.4 and will be verified by the measurements in Sec. 3.3.

3.3

Verification Measurements

In order to quantify the influence of the magneto-mechanical coupling on the modal parameters, it is necessary to measure the dynamic response of the system with and without the magneto-mechanical coupling. This is the only way to rule out that the measured effects do not originate from other sources than the coupling of interest.

Because some parameters of the system are unknown, it is necessary to verify the two physics separately before the coupled system can be verified.

Considering all limitations of the test set-up, the following measurement approach was chosen:

1. Measure the dynamic behaviour of the beam without coupling.
2. Identify the set of mechanical parameters that simulate the dynamic behaviour closest to the one measured.
3. Identify the set of electric parameters that simulate the resistance and impedance closest to the impedance and resistance measurements.
4. Measure the dynamic behaviour with the beam fully inserted into the air gap.
5. Measure the dynamic behaviour with the beam half inserted into the air gap.

6. Compare the measured and the simulated dynamics.

This approach includes some assumptions that might not be satisfied. First of all, it is assumed that the dynamic behaviour of the beam does not depend on its position on the table. The table position might have an influence on the stiffness of the mounting of the beam and thus may also influence the first bending frequency. Secondly, it was assumed that the Young's modulus and the Poisson's ratio are known. Although the beam was manufactured from standard structural steel whose properties are known, it is unknown to what extent these properties are exact or if they might have changed during the shaping process.

Parameter Identification

3.3.1

In the previous section, two parameter identifications were listed as steps within the verification process. These two parameter identification steps are presented in more detail here.

Mechanical Properties

The mechanical model's parameters that could be used for tuning consisted of the Rayleigh damping coefficients, the geometry of the beam and the Young's modulus and the Poisson's ratio. The Rayleigh damping coefficients were set in such a way that the damping of the first bending modes coincides with the measured damping of the first damping modes. Of the remaining parameters the length of the beam was chosen to tune the frequency of the first bending mode to match the measured frequency. Small deviations from the measured length of the beam of about 0.1mm, which is within the measure tolerance needed to be applied to match the frequencies. Young's modulus and Poisson's ratio were considered known.

Property	Value
Young's Modulus [Pa]	200e9
Density [$\frac{\text{kg}}{\text{m}^3}$]	7850
Poisson's ratio [-]	0.29

Table 3.1

Mechanical properties of the beam and yoke

Magnetic Properties

To determine the magnetic properties of the steel used for the beam and the yoke, impedance measurements were conducted. The permeability of metals can change during metal working process, such as milling, turning or drilling. Therefore, it is difficult to predict the

Table 3.2
Documented specification of
permanent magnets

Property	Value
Height	2 mm
Length	20 mm
Width	10 mm
Remanence Flux Density	1.32 – 1.37 T
Coercity	860 – 995 $\frac{\text{kA}}{\text{m}}$
relative permeability	1.056 – 1.26
Conductivity	5882 - 9090.9 $\frac{\text{S}}{\text{m}}$

permeability beforehand. However, the permeability can be determined by measuring the impedance of a coil wound around the beam or the yoke. The coils are depicted in Fig. 3.5. The inductance of the coils depends mainly on the conductivity and permeability of the material. For structural steel, which is used in this case, the conductivity is roughly known. Therefore, the permeability can be approximated by matching the simulated to the measured impedance.

Simulating the yoke and the beam numerically, the permeability of the material can be estimated. Fig. 3.6 shows the comparison between the measured values for the inductance and resistance and the calculated values for different permeabilities and conductivities of the iron material. The instrument used could not measure below a frequency of 20 Hz. It is presumed that due to the skin effect in the iron, the inductance is much higher for frequencies below 20Hz and drops sharply for higher frequencies. Being able to measure this drop at very low frequencies would increase the impact of different permeability and conductivity values on the inductance leading to a more accurate determination of the material properties. At the frequencies measured it can be seen in Fig. 3.6 that the variation of the values has little effect on the inductance making a property identification difficult.

It should also be noted that the device used to measure the resistance and impedance of the coil has a higher accuracy at higher frequencies. At 20 Hz the error is around 1% of the measured value. Therefore, it is more important to properly fit the measured data to the simulated one at higher frequencies. Tab. 3.3 lists the material

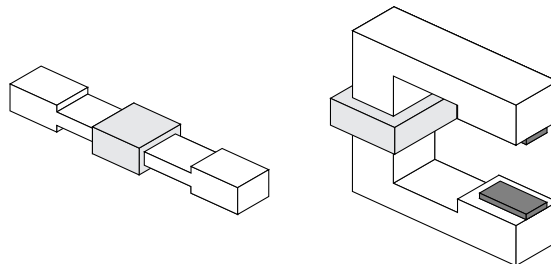


Figure 3.5
Position of the coils (depicted in
grey) used to determine the
permeability and resistivity of the
beam and yoke

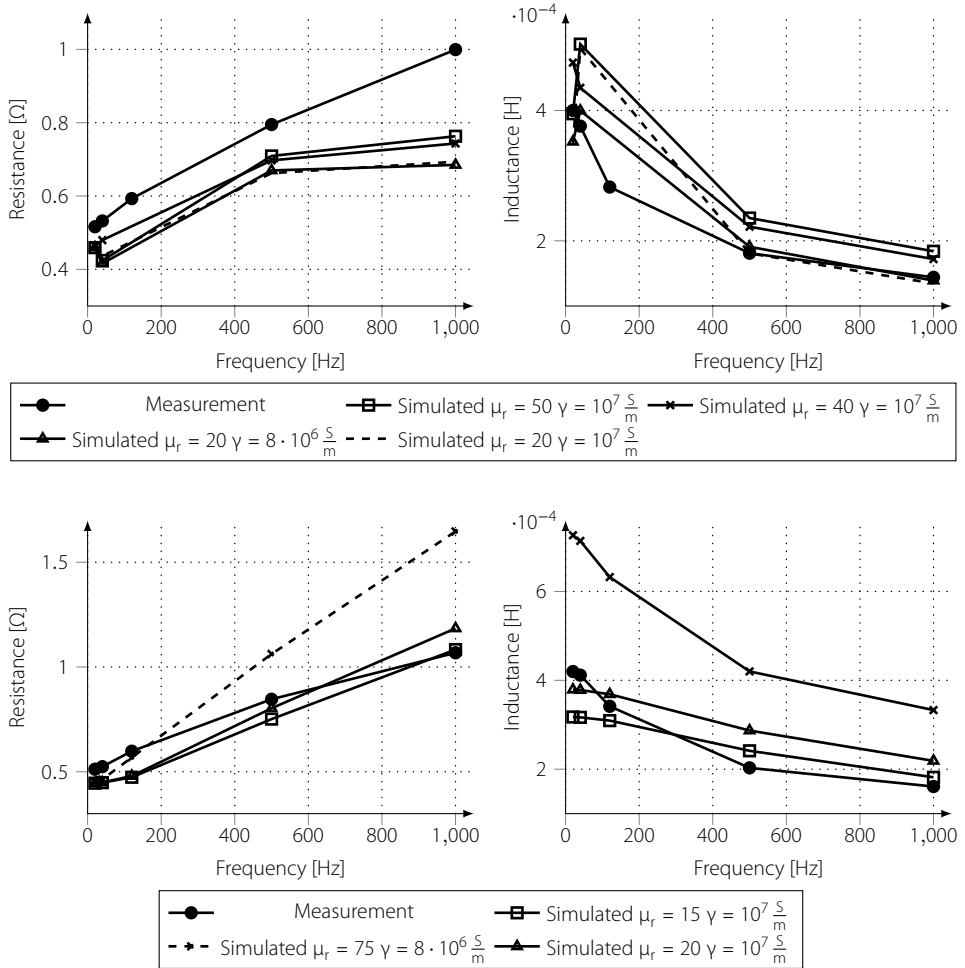


Figure 3.6 Resistance and impedance measurements of the solid stator yoke (top) and the beam (bottom)

parameters that were eventually chosen to simulate the system. The choice has been based on the plots in Fig. 3.6. No parameter identification technique was employed, due to the complexity of the FE system and the associated computational costs. The remaining deviation of the used parameter set to the optimised parameter set is considered to be small.

Vibration Measurements

3.3.2

Using a laser doppler vibrometer (LDV), impact tests were conducted to measure the frequency and damping behaviour of the first bending mode of the beam. These measurements were done for three different positions of the beam: completely out of the air gap (no coupling), completely inserted in the air gap (full coupling)

Properties of Magnets	
Remanence Flux Density	1.32 T
relative permeability	1.06
Conductivity	$0.6 \cdot 10^6 \frac{\text{S}}{\text{m}}$
Properties of stator-yoke	
Conductivity	$10^7 \frac{\text{S}}{\text{m}}$
relative Permeability	20
Properties of beam	
Conductivity	$10^7 \frac{\text{S}}{\text{m}}$
relative Permeability	20
mass matrix Rayleig damping coefficient	40
stiffness matrix Rayleig damping coefficient	$6 \cdot 10^{-6}$

Table 3.3

Chosen parameters for the models

and half way inserted in the air gap (to some extent coupled). The modal parameters were evaluated by fitting a decaying sinusoidal function

$$y(t) = y_o e^{-2\pi\omega_n(\zeta + \sqrt{\zeta^2 - 1})t}$$

to the data using a least square evaluation.

$$\underset{y_o, \omega_n, \zeta}{\text{minimize}} \left[\sum_t (x(t) - y(t - t_o))^2 \right] \quad \text{for } t \in [t_o, t_o + \Delta t] \quad (3.2)$$

where ζ , ω_n and y_o are the parameters to identify and $x(t)$ the measurement data.

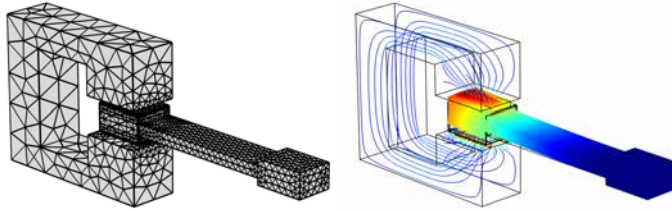
The measured data $x(t)$ and the decaying sinusoidal function $y(t)$ are aligned by setting $x(t_o) = \max(x(t))$ and choosing an arbitrary length Δt . The parameters that were eventually chosen for the model are shown in Tab. 3.3.

3.4

3D Finite Element Model

A 3D FE model is used to predict the change of the modal parameters. Although a three dimensional magnetic field formulation results in large numbers of DoFs, it is necessary to build such a model to include the fringe effects, described in Sec. 3.2, in the air gap appropriately. The model consists of approximately 315 000 DoFs. This high number of degrees of freedoms is necessary to ensure that the gradients of the magnetic field as well as the deformation are described accurately.

Fig. 3.7 shows the mesh of the model and the predicted deformation of the first bending mode. It was assumed that saturation plays



Mesh of the 3D FE model

Displacement of the beam and magnetic flux lines for the first bending mode. the colours indicate displacement, the lines the magnetic flux lines

Figure 3.7
Mesh of the 3D finite element model of the test rig

no role for this model. A linear material model for the yoke and the beam was used.

Results

The measurements show clearly a trend towards more damping and a lower resonance frequency in the system when the magneto-mechanical coupling is introduced. This trend was also simulated by the 3D finite element model. Tab. 3.4 lists the simulated and measured eigenfrequencies and damping ratios of the system. A relative error of 4.4% for the fully inserted beam and an error of 3.2% for the half inserted beam were recorded. The relative error of the damping values is higher. A relative error of 14.4% for the fully inserted beam and 39% for the half inserted beam were recorded. Considering that the system introduced is nonlinear, the

3.5

	3D-Model		Measurement	
	Frequency	Damping	Frequency	Damping
no EM coupling	417 Hz	$\zeta = 1.66\%$	417 Hz	$\zeta = 1.66\%$
with EM coupling	372 Hz	$\zeta = 3.32\%$	370 Hz	$\zeta = 3.6\%$
half EM coupling	386 Hz	$\zeta = 2.48\%$	384.6 Hz	$\zeta = 2.25\%$

Table 3.4
Simulation Results and Measurements, ζ denotes the damping coefficient

frequency and damping estimates of the linear 3D model is reasonable accurate. This shows that a prediction of the coupled modal parameters is possible using the linearised set of equations and a linear modal analysis.

Summary

This chapter showed that the modelling methodologies introduced in Chapter 2 can be used to predict the changes to the dynamic be-

3.6

haviour of a coupled system caused by the coupling. However, it was discussed that in order to yield accurate predictions, the material properties of the structure need to be known exactly. This is always a problem when materials that are produced with a mechanical application in mind also affect the magnetic field and vice-versa. In those cases, the material's magnetic properties are not well defined because for most uses of that particular material it is not necessary to know them.

This chapter further showed that the coupling can have an influence on dynamic systems under certain circumstances. This is the case, when the structural stiffness is low enough so that the magnetic forces and the magnetic stiffness is significant. The models from Sec. 2 are accurate enough to predict the dynamic behaviour of magneto-mechanical coupled systems and, thus, can also be used to take those dynamics into account when simulating generators of direct-drive wind turbines. This will be done in Chapter 5.

This Chapter is based on the papers:

Kirschneck, M., Rixen, D.J., Polinder, H.
Model Reduction Methods for Magnetic Fields Based on
Modal Analysis. IEEE Transactions on Magnetics, vol. 5,
no. 11, November 2014

Abstract:

For the magneto-mechanical coupled analysis of large direct-drive generators in 3D, an enormous amount of DoFs are necessary to model the magnetic field over the whole circumference of the generator. Model reduction techniques is one approach to reduce the computation cost of solving the model. These techniques sacrifice accuracy of the solution for a reduced number of DoFs.

This chapter introduces model reduction techniques based on various methods known from mechanical engineering. These techniques are applied to electrical machines reducing the number of degrees of freedom and hence computation time for transient and eigenvalue analyses. It further introduces magnetic super elements for the stator and the rotor of these machines and combines them with suitable coupling methods from literature. The various approaches are compared with respect to accuracy and computation time. Eventually, ideas for model order techniques for magneto-mechanical coupled systems are presented.

4.1

Introduction

To identify the dynamics of the coupled system, (2.170) needs to be solved. The formulation introduced in Chapter 2, in particular the one of the magnetic field, can lead to very large models with millions of degrees of freedom. The sheer size of these models makes them difficult to handle, even when large computing power is available.

Model reduction techniques can help to alleviate the problems encountered when trying to solve systems of that size. These techniques reduce the number of DoFs of the model at the expense of decreased accuracy. In general, three types of problems can be distinguished for which these techniques are useful: static-like problems, including formulations for stationary problems and problems in the frequency domain, transient problems and eigenvalue problems. This chapter will concentrate on the last two types of problems.

In mechanical engineering, and dynamic analysis of structures in particular, various methods have been developed for the reduction of models for structural dynamics in the past. These methods are based on the concept of a modal decomposition of the dynamic behaviour of the structure into a number of decoupled ordinary differential equations. This is achieved by solving an eigenvalue problem. The results of the eigenvalue problem are physical meaningful quantities, because the eigenvalues of the structure correspond to its resonance frequencies and the eigenvectors correspond to its mode shapes.

These techniques can be adapted so that they can be applied to FE models of quasi-static magnetic fields. As will be explained, the methods work in particular well for the magnetic fields of electric machines due to the design of electric machines.

This chapter will first introduce the modal analysis for quasi-static magnetic fields. Afterwards, it introduces several reduction methods that are based on modes for the simulation of dynamic magnetic fields. The reduction methods are based on reduction methods developed for the dynamic analyses of mechanical systems. In Sec. 4.5, the model reduction techniques are applied to a test case, a small 600 W wind turbine generator. The various techniques are compared with respect to accuracy and calculation time. It is shown that modal analysis based reduction techniques can also be adapted for and employed to magnetic fields and yield substantial computation cost reductions. Finally, ideas are presented to facilitate model reduction of magneto-mechanical systems, as those introduced in Chapter 2.

Test Cases

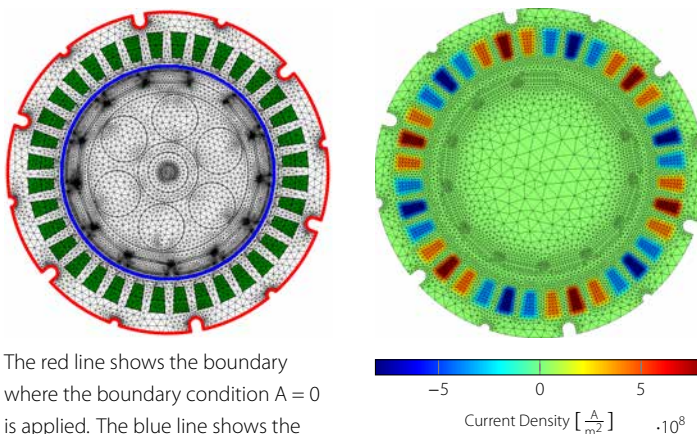
4.1.1

The techniques introduced in this chapter will be tested on a 2D model of a 600 W wind turbine. The 600 W wind turbine model is based on the Ampair 600, a small direct-drive wind turbine for private use. Fig. 4.1 shows the 2D model used. The model consists of a rotor and stator which will be separated at the air gap of the machine (the interface is indicated by the blue line on the left of Fig. 4.1). The system is excited by the currents in the coils in the stator (indicated by green elements). In the real turbine, the rotor field is created by PMs. However, for simplicity the excitation of the PMs is not modelled in the test case. At the outer line of the stator, the magnetic vector potential is set to zero (on the red line in Fig. 4.1).

In a 2D model of laminated iron, the conductivity is usually assumed to be zero, to account for lamination. However, a conductivity of zero in some regions of the FE model might lead to numerical instability for some solver types. Therefore, the conductivity of the laminated iron domains was set to $\gamma = 1$. This value is so low, that hardly any eddy currents are present, while it is large enough, that most solvers do not run into any problems during the solution process.

Three test cases are analysed: a step response, a rotating magnetic field and an eigenvalue problem.

- For the step response, a time integration is conducted. The load that is depicted on the right hand side of Fig. 4.1 is applied at $t = 0$. This load corresponds to the current density distribution of a three phase current at the moment when



The red line shows the boundary where the boundary condition $A = 0$ is applied. The blue line shows the interface between the two sub parts of the electric machine. Green are the coil domains

The source vector used for the step response

Figure 4.1
The 12 pole direct-drive wind turbine generator

phase a is at its peak current value and thus phase b and phase c at minus half their peak current values. The response for the machine is simulated for the next 10 s. Due to eddy currents, the magnetic field will not be created instantaneously, but will reach its full strength after some seconds.

- For the second test case, the three phase current that create the load that is shown on the right hand side of Fig. 4.1 is changed, so that the magnetic field created by the coils rotates just like during operation of the machine. The rotor is not rotated with the stator field for the test case. This rotating stator field is simulated for 100 seconds.
- An eigenvalue problem of the rotor and stator is conducted. For this, no excitation is used.

4.2

Modal Analysis for Quasi-Static Magnetic Fields

A system of partial differential equations that describes the dynamic behaviour can be rewritten as a series of uncoupled differential equations. This can be achieved by a basis transformation. Instead of describing the amplitude of the magnetic vector potential at every node, the amplitude of certain pre-defined distributions is described. The method that is used for finding the spatial distributions in structural dynamics is called *Modal Analysis*. The basis change decouples the spatial and temporal information of the system. The values of the nodes \mathbf{q} can be written as

$$\mathbf{q} = \sum_m \boldsymbol{\varphi}_m \eta_m(t) \quad (4.1)$$

where $\eta_m(t)$ denotes the amplitude of the spatial distribution of the m^{th} basis vector and $\boldsymbol{\varphi}_m$ the m^{th} basis vector. Inserting the basis transformation into the numerical version of the governing partial differential equation yields

$$\mathbf{C}_{AA} \boldsymbol{\Phi} \dot{\boldsymbol{\eta}}(t) + \mathbf{K}_{AA} \boldsymbol{\Phi} \boldsymbol{\eta}(t) = \mathbf{J}(t) \quad (4.2)$$

where \mathbf{C}_{AA} and \mathbf{K}_{AA} are the magnetic mass and stiffness matrices, respectively, as defined in Sec. 2.5. $\boldsymbol{\eta}$ is a vector containing all amplitudes of the basis vectors that are stored in the matrix $\boldsymbol{\Phi}$.

The modes $\boldsymbol{\varphi}_m$ and the eigenvalues λ_m can be computed by solving the eigenvalue problem

$$\mathbf{K}_{AA} \boldsymbol{\varphi}_m = -\lambda_m \mathbf{C}_{AA} \boldsymbol{\varphi}_m \quad (4.3)$$

where λ_m , the eigenvalue of the system, is defined by

$$\lambda_m = -\frac{\dot{\eta}_m}{\eta_m} \quad (4.4)$$

Solving the eigenvalue problem in (4.3) for λ_m and $\boldsymbol{\varphi}_m$ yields the modes and eigenvalues of the system.

It is now possible to write the homogeneous solution of (4.2) as

$$\mathbf{q}_{hom} = \sum_m \boldsymbol{\varphi}_m \eta_m e^{t\lambda_m} \quad (4.5)$$

Opposite to structural systems, the eigenvalues computed by solving (4.3) are real. There is, therefore, no oscillation possible in the solution. This can easily be explained as the governing equations in (4.2) are first order PDEs in time whereas structural equations are second order PDEs in time. The homogenous solution in (4.5) is, thus, a sum of exponentially decaying spatial distributions.

Physically, this corresponds to the following effect: when a load, i.e. a current, is suddenly switched off, the magnetic field will not change instantaneously. The decaying of the magnetic field will induce eddy currents in the structure and the conductor, where the current was applied. These eddy currents create a magnetic field that counter acts the diminishing magnetic field that was created by the current. Over time, when the magnetic field does not change that quickly anymore, the eddy currents will subside. Consequently, the magnetic field will disappear when the eddy currents disappear.

Mode Truncation for Magnetic Fields

4.2.1

Modes of first order systems show some significant different dynamic behaviour than modes of a second order systems. To explain this, consider a mode of a first and second order system excited by a harmonic load.

$$\begin{aligned} (i\omega_{ext}c_m + k_m)\eta_m e^{i\omega_{ext}t} &= \boldsymbol{\varphi}_m^T \mathbf{J} e^{i\omega_{ext}t} \\ (-\omega_{ext}^2 m_r + k_r)\eta_r e^{i\omega_{ext}t} &= \boldsymbol{\varphi}_r^T \mathbf{F} e^{i\omega_{ext}t} \end{aligned} \quad (4.6)$$

where c_m denotes the magnetic modal mass, m_r denotes the structural modal mass, k_m the magnetic modal stiffness and k_r the structural modal stiffness. η_m and η_r are constant complex participation factors and ω_{ext} denotes the excitation frequency. The modal stiffnesses and modal damping values can be calculate in the same way as for structural systems

$$\text{diag}(k_m) = \boldsymbol{\Phi}^T \mathbf{K}_{AA} \boldsymbol{\Phi} \quad (4.7a)$$

$$\text{diag}(c_m) = \boldsymbol{\Phi}^T \mathbf{C}_{AA} \boldsymbol{\Phi} \quad (4.7b)$$

$$\text{diag}(m_r) = \boldsymbol{\Phi}^T \mathbf{M}_{uu} \boldsymbol{\Phi} \quad (4.7c)$$

$$\text{diag}(k_r) = \boldsymbol{\Phi}^T \mathbf{K}_{uu} \boldsymbol{\Phi} \quad (4.7d)$$

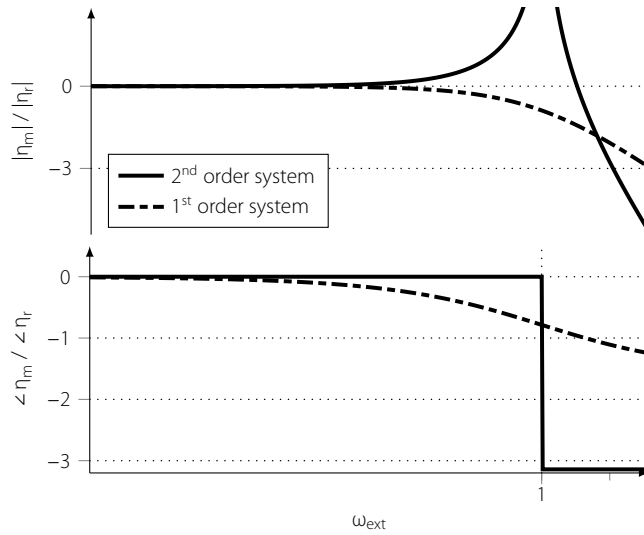


Figure 4.2

Bode Diagram comparing the dynamic behaviour of magnetic and structural modes

Fig. 4.2 shows the Bode plot of the response of a first and second order system. The first order system lacks the peak representing a resonance frequency, which the second order system shows. Instead, the amplitude of the response starts to decrease at a certain frequency. However, it does not decrease as quickly as the amplitude of a second order system.

When doing a modal analysis, only a certain set of modes are calculated. The rest of the modes are neglected because their influence is considered insignificant. This approximation can be explained with the transfer function of the second order system in Fig. 4.2. Usually, the dynamics up to a certain frequency are of interest in an application. From Fig. 4.2, it is clear that the response of a mode is the same as the static response, for frequencies far below the resonance frequency. Thus, all modes that have a significantly higher resonance frequency than the frequency range of interest can be neglected as their response is instantaneous to the dynamic load. Resonances that have a much lower frequency than the excitation frequency can be neglected too, because they do not contribute to the response of the system. This can be seen in Fig. 4.2 by a response amplitude that approaches zero for high frequencies. The technique to use only the lower modes of a system is called *Mode Truncation*.

For 1st order systems, such as magnetic fields, this technique brings additional challenges. In this case, the amplitude of the modes do not decrease as quickly as they do for second order systems above the resonance frequency (see Fig. 4.2). It is, therefore, more difficult to distinguish which modes are important and which can be neglected.

Physical Values Expressed by Modes

4.2.2

Eigenvectors have no amplitude. They merely express the relation between the various amplitude of DoFs. They can be normalised with respect to the mass or the stiffness matrix. For a stiffness normalisation (4.7a) is equal to one, for a mass normalisation (4.7c) is equal to one.

A stiffness normalisation means that the amplitude of each mode is set to a value so that the energy stored at that amplitude is one. In that case, the dissipated energy, which is expressed by the modal magnetic mass, differs between the modes. In that case, we can write

$$\boldsymbol{\varphi}_m^2 k_m = 1 \quad (4.8)$$

For the mass normalisation, the dissipated energy of each mode is one while the stored energy differs. The eigenvalue of a mode expresses the relation between the dissipated energy and the stored energy: The eigenvalue of a mode can be calculated by

$$\lambda_m = -\frac{k_m}{c_m} \quad (4.9)$$

It quantifies thus how quickly all energy of a mode is dissipated and thus indicates the time constant of the particular mode. In other words, how quickly this mode reacts to change. It is similar to the real part of the eigenvalue of damped second order systems.

The eddy currents resulting from a change of magnetic vector potential of a mode can be expressed by

$$\mathbf{J}_{eddy,m} = \mathbf{C}_{AA} \boldsymbol{\varphi}_m \dot{\eta}_m(t) \quad (4.10)$$

The dissipated energy per mode can be expressed by

$$\frac{dW_{eddy,m}}{dt} = \dot{\eta}_m(t) \boldsymbol{\varphi}_m^T \mathbf{C}_{AA} \boldsymbol{\varphi}_m \dot{\eta}_m(t) \quad (4.11)$$

Rigid Magnetic Modes

4.2.3

The eigenvalue problem in (4.3) can have trivial results. The reason for this is that solutions to the magnetic PDE (2.47) are not unique. The trivial solutions are characterised by a uniform value for the magnetic vector potential. They are the magnetic equivalent to rigid body modes in structural dynamics. Opposite to rigid body modes, there are only three rigid magnetic modes, as the rotation does not exist for magnetic fields.

For many reduction techniques, these rigid magnetic modes pose an additional challenge, as they need to be treated separately from

'normal' modes. For the stator, these trivial solutions of the eigenvalue problem do not exist, because at the outer side of the stator a constraint is applied. For the rotor however, there is a trivial solution, because the absolute value of the magnetic vector potential is only determined by the interface values. This leads to 'rigid body modes' when using free interface reduction methods such as the Dual-Craig-Bampton method, Rubin's or McNeal's method.

4.2.4

Magnetic Modes of Electric Machines

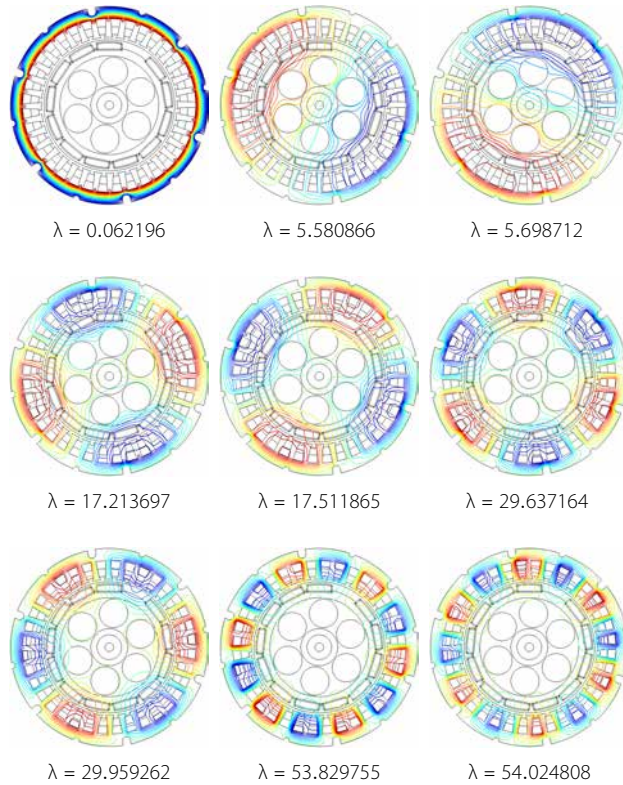


Figure 4.3
Modes of the electro-magnetic field in a 12 pole pm synchronous generator

For electric machines, magnetic modes are of particular interest. The reason for this can be found in the shape of the machine. Electric machines are constructed in a way that only two modes play a major role for the magnetic field in an electric machine. Fig. 4.3 depicts several modes of a 2D model of a 12 pole permanent magnet machine. Because the machine is a twelve pole machine only the modes at $\lambda = 53.83$ and $\lambda = 54.025$ play a role for the machine as these modes show the same cyclic symmetry as the machine and, thus, the same as the currents applied in the coils. This emphasis of only two modes can be used in many aspects for calculating mag-

netic fields of electric machines.

The similarity of the modes and space harmonic can mislead to the assumption that they are the same. The decomposition of a mode's magnetic field strength in the air gap into a Fourier series yields the space harmonics of that mode.

Coil Participation Factors

4.2.5

The magnetic modes introduced in Sec. 4.2.4 depend only on the geometry and the material properties of the system. Which mode is excited depends on the location where the currents in the system are applied. The currents in the coils can be seen as a forced harmonic excitation. The response of the system can be computed by solving

$$(\mathbf{i} \operatorname{diag}(c_m) \omega_{ext} e^{\mathbf{i} \omega_{ext} t} + \operatorname{diag}(k_m) e^{\mathbf{i} \omega_{ext} t}) \hat{\boldsymbol{\eta}} = \boldsymbol{\Phi}^T \hat{\mathbf{J}} e^{\mathbf{i} \omega_{ext} t} \quad (4.12)$$

where $\hat{\mathbf{J}}$ denotes the amplitude of the force excitations \mathbf{J} . For a forced excitation, the relative importance of an individual mode is expressed by its participation factor. The participation factor for this harmonic excitation can be calculated by

$$\eta_m = \frac{\boldsymbol{\Phi}_m^T \hat{\mathbf{J}}}{\mathbf{i} \omega_{ext} c_m + k_m} \quad (4.13)$$

The participation factor might be complex, because the denominator and/or the excitation can be complex. In that case, the absolute value of the participation factor indicates the relative magnitude of the mode while the angle of the participation factor represents the phase delay relative to the excitation force.

Introduction to Model Order Reduction and Dynamic Substructuring

4.3

Dynamic Substructuring (DS) and *Model Order Reduction* (MOR) are two techniques that have been developed in structural dynamics over the last decades. These techniques can be extended to magnetic fields and magneto-mechanical systems. Although the term *Dynamic Substructuring* is misleading in this context, since magnetic fields are no structures, it will be used throughout the thesis to show the tradition of these methods and where the inspiration comes from.

The introduction to DS and Component Mode Synthesis that is given here is based on [165]. For more details on the topic, please refer to that thesis, as it gives a very good overview of the topic.

4.3.1

Dynamic Substructuring for Electric Machines

DS is based on the idea to divide a complex structure into subparts and describe the dynamic behaviour per subpart. This approach has several advantages over an integral dynamic analysis. The following list was assembled in [165]. It lists the advantages and disadvantages of DS

1. It allows evaluating the dynamic behaviour of structures that are too large or complex to be analysed as a whole.
2. By analysing the subsystem, local dynamic behaviour can be recognised more easily.
3. When a single component is changed only that component needs to be reanalysed; the total system can be analysed at low additional cost.
4. It gives the possibility to combine modelled parts and experimentally identified components. This is especially useful for components that are very difficult to model correctly.
5. When a structure consists of several identical parts, dynamic substructuring allows these parts to be taken into account very efficiently in the total model.
6. It enables sharing and combining substructures from different project groups.
7. The level of detail of the component models can be matched with the intended usage of the model.

Opposite to all these benefits, the only drawback is the increased complexity of the algorithms that are introduced here.

DS for electric machines is mainly interesting because the rotor and the stator can be separated easily into two substructures and analysed separately. All the above advantages are valid for the DS of electric machines. Some entries of the list above play a larger role for modelling magnetic fields than others.

As will become apparent in Chapter 5, the major motivation to look into dynamic substructuring for electric machines was, in fact, the first point on the list, i.e. the reduced computational cost. 3D magnetic models can easily grow to a size that even super computers struggle with. DS promises some relieve in this area.

Since an electric machine is always a system that includes a mechanical component and a magnetic component, there are several ways to substructure the system. The first method is to split the system by its geometrical characteristics. This will lead to a substructure containing the rotor and one containing the stator. Dur-

ing rotation the interface between rotor and stator has to be reassembled in every time step, because of the movement of the rotor mesh. It is, therefore, a natural choice to compute one super element for the rotor and one for the stator, so that a reassembly of the air gap is still possible.

Additionally, a separation by physical domain is possible. In Sec. 2.5.10, it was explained that only the nodes of the ferromagnetic and conducting structures are part of both physical domains. The rest of the model belongs only to one domain. This can be used for dynamic substructuring by forming an interface between the mechanical and magnetic domain that contains all DoFs of the nodes in the ferro-magnetic structure. Depending on the geometry of the system, this can lead to large reductions of DoF in combination with MOR techniques. Magneto-mechanical substructuring will be covered in Sec. 4.6.

Component Mode Synthesis

4.3.2

Component Mode Synthesis (CMS) is a dynamic substructuring technique, which combines the concept of component wise analysis with MOR techniques. CMS decomposes the total system in several components. Each component's dynamic behaviour is approximated by a so called super element. The super elements are computed by applying a MOR technique to the component's model. This way, the number of DoFs is reduced while the dominant dynamic characteristics are retained in the super element. After each component is substituted by its super element, the dynamics of the total structures can be approximated by assembling all super elements.

As mentioned in Sec. 4.1, these techniques can be applied for transient analysis and eigenvalue problems. The decreased computational cost are realised by different effects for transient and eigenvalue problems

For the transient analysis, where the load arbitrarily changes over time, the system of partial differential equations needs to be solved for a set of time steps. The model reduction techniques introduced here help to reduce the required computation time at each time step. That is paid for by an additional computation at the beginning of the transient analysis. There are some computational cost linked to the reduction basis computation that is done before the transient analysis. This, however, has to be done only once. So the longer the transient analysis, the lower the computational cost. Fig. 4.4 compares the computational cost of reduced and non-reduced models for transient problems.

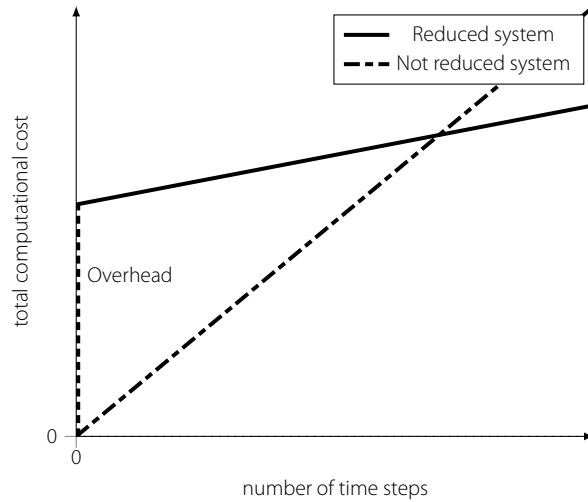


Figure 4.4
Computational cost for transient systems when model reduction is applied

For eigenvalue problems, computational cost reductions are realised by exploiting the scaling of eigenvalue problems. Eigenvalue problems scale with approximately n^3 , where n denotes the number of DoFs. It is, thus, computationally less expensive to compute k eigenvalue problems of the size $\frac{n}{k}$ than one large problem. Splitting the system in several substructures and solving the eigenvalue problem of the system of assembled super elements exploits this. The eigenvalue problems that have to be solved to assemble each substructure are computationally much cheaper than the eigenvalue problem of the total system.

Work on these techniques started in the 60's and 70's by Hurty [67, 68]. Subsequently, numerous methods were developed that employed this idea [8, 57, 93, 130, 132]. These methods are currently part of several finite element packages for structural analysis.

These 'classic' methods can be applied to magnetic fields. In combination with DS of the finite element model of electric machines, large computation cost reductions can be achieved.

4.3.3

General Formulation of Component Model Reduction

Starting point for any CMS method is the system of partial differential equation in their discrete form

$$M\ddot{\mathbf{q}} + C\dot{\mathbf{q}} + K\mathbf{q} = \mathbf{f} + \mathbf{g}_b \quad (4.14)$$

where \mathbf{f} denotes the external load applied to the substructure and \mathbf{g}_b the load on the interface applied to the substructure by another substructure. Tab. 4.1 gives an overview over various variables used to described reduction methods covered here.

Description	Symbol
internal DoF	\mathbf{q}_i
DoF on the interface with another substructure	\mathbf{q}_b
modal DoF for internal modes	$\boldsymbol{\eta}$
DoF after model reduction	\mathbf{q}_r
DoF before reduction method is applied	\mathbf{q}_{nr}
interface force	\mathbf{g}_b

Table 4.1

Various variables for MOR and DS techniques

The component model reduction methods use a basis transformation to describe the system of PDEs in a basis of lower order than the original one.

$$\begin{aligned}\mathbf{q}_{nr} &= \mathbf{R}\mathbf{q}_r \\ \mathbf{q}_{nr} &\in \mathbb{R}^n \quad \mathbf{q}_r \in \mathbb{R}^m \\ n &> m\end{aligned}\quad (4.15)$$

For the projection, the reduction matrix \mathbf{R} is used, which projects the system from the non-reduced DoFs, \mathbf{q}_{nr} , to the DoFs that are left after the reduction method was applied, \mathbf{q}_r . This matrix consists of the basis vectors in column form. Which basis is used depends on the reduction method. A selection of reduction methods will be introduced in Sec. 4.4.

The reduced matrices of the system can be calculated by pre- and postmultiplying the system matrices by the reduction matrix \mathbf{R} .

$$\begin{aligned}\tilde{\mathbf{M}} &= \mathbf{R}^T \mathbf{M} \mathbf{R} \\ \tilde{\mathbf{C}} &= \mathbf{R}^T \mathbf{C} \mathbf{R} \\ \tilde{\mathbf{K}} &= \mathbf{R}^T \mathbf{K} \mathbf{R}\end{aligned}\quad (4.16)$$

The forces in \mathbf{g} and \mathbf{f} are projected onto the new basis by

$$\begin{aligned}\tilde{\mathbf{g}} &= \mathbf{R}^T \mathbf{g} \\ \tilde{\mathbf{f}} &= \mathbf{R}^T \mathbf{f}\end{aligned}\quad (4.17)$$

This results in the following reduced system of partial differential equations

$$\tilde{\mathbf{M}}\ddot{\mathbf{q}}_r + \tilde{\mathbf{C}}\dot{\mathbf{q}}_r + \tilde{\mathbf{K}}\mathbf{q}_r = \tilde{\mathbf{f}} + \tilde{\mathbf{g}}\quad (4.18)$$

The DoFs that are retained during the component model reduction, \mathbf{q}_r contain the interface DoFs \mathbf{q}_b , that are needed to assemble various components to the total system. This is covered in Sec. 4.3.4.

Assembly Methods for Dynamic Substructuring

4.3.4

For the reduction methods introduced in this thesis, two assembly methods for the various substructuring methods are used. Which

method is used depends on the component model reduction technique. Only a selection of existing assembly methods are introduced here.

The methods and notation introduced here are based on the thesis by Voormeeren [165] and the paper by Voormeeren et al. [164].

Primal Stiffness Assembly

For an interface of two substructures, the interface DoF exist in both substructures. They are redundant, because the compatibility condition dictates that the displacements/vector potential on both sides of the interface are equal. When forming the assembly, it is therefore beneficial to eliminate one set of boundary DoFs. For that, the intermediate DoFs \mathbf{q}_y are introduced, which are unique. To associate these intermediate DoFs to the boundary DoFs on both sides of the interface the Boolean matrix \mathbf{L}_b is introduced. It is defined by

$$\mathbf{q}_b^{(s)} - \mathbf{L}_b^{(s)} \mathbf{q}_y = \mathbf{0} \quad (4.19)$$

where the superscript in $(\bullet)^{(s)}$ denotes the substructure.

Starting point for the assembly is the unassembled system in the form of

$$\begin{aligned} \begin{bmatrix} \check{M}_{ii} & \check{M}_{ib} & \mathbf{0} & \mathbf{0} \\ \check{M}_{bi} & \check{M}_{bb} & \mathbf{0} & \mathbf{0} \\ \mathbf{0} & \mathbf{0} & \mathbf{0} & \mathbf{0} \\ \mathbf{0} & \mathbf{0} & \mathbf{0} & \mathbf{0} \end{bmatrix} \begin{bmatrix} \check{\mathbf{q}}_i \\ \check{\mathbf{q}}_b \\ \check{\mathbf{g}}_b \\ \check{\mathbf{q}}_y \end{bmatrix} + \begin{bmatrix} \check{C}_{ii} & \check{C}_{ib} & \mathbf{0} & \mathbf{0} \\ \check{C}_{bi} & \check{C}_{bb} & \mathbf{0} & \mathbf{0} \\ \mathbf{0} & \mathbf{0} & \mathbf{0} & \mathbf{0} \\ \mathbf{0} & \mathbf{0} & \mathbf{0} & \mathbf{0} \end{bmatrix} \begin{bmatrix} \check{\dot{\mathbf{q}}}_i \\ \check{\dot{\mathbf{q}}}_b \\ \check{\dot{\mathbf{g}}}_b \\ \check{\dot{\mathbf{q}}}_y \end{bmatrix} + \\ + \begin{bmatrix} \check{K}_{ii} & \check{K}_{ib} & \mathbf{0} & \mathbf{0} \\ \check{K}_{bi} & \check{K}_{bb} & -\mathbf{I} & \mathbf{0} \\ \mathbf{0} & -\mathbf{I} & \mathbf{0} & \check{L}_b \\ \mathbf{0} & \mathbf{0} & \check{L}_b^T & \mathbf{0} \end{bmatrix} \begin{bmatrix} \mathbf{q}_i \\ \mathbf{q}_b \\ \mathbf{g}_b \\ \mathbf{q}_y \end{bmatrix} = \begin{bmatrix} \check{\mathbf{f}}_i \\ \check{\mathbf{f}}_b \\ \mathbf{0} \\ \mathbf{0} \end{bmatrix} \end{aligned} \quad (4.20)$$

The nature of the internal DoFs in (4.20) depend on the model reduction method used. These can either be normal DoFs or DoFs associated with a mode that describes the internal dynamics of the substructure.

In (4.20) the following block diagonal forms are used

$$\begin{aligned} \check{K}_{ii} &= \text{diag}(\mathbf{K}_{ii}^{(1)}, \dots, \mathbf{K}_{ii}^{(n)}) \\ \check{K}_{ib} &= \text{diag}(\mathbf{K}_{ib}^{(1)}, \dots, \mathbf{K}_{ib}^{(n)}) \\ \check{K}_{bi} &= \text{diag}(\mathbf{K}_{bi}^{(1)}, \dots, \mathbf{K}_{bi}^{(n)}) \\ \check{K}_{bb} &= \text{diag}(\mathbf{K}_{bb}^{(1)}, \dots, \mathbf{K}_{bb}^{(n)}) \end{aligned} \quad (4.21)$$

and analog for the mass and damping matrices. The Boolean matrix $\check{\mathbf{L}}_b$ is defined by

$$\check{\mathbf{L}}_b = \begin{bmatrix} \mathbf{L}_b^{(1)} \\ \vdots \\ \mathbf{L}_b^{(n)} \end{bmatrix} \quad (4.22)$$

and the force vectors $\check{\mathbf{f}}_i$ and $\check{\mathbf{f}}_b$

$$\check{\mathbf{f}}_b = \begin{bmatrix} \mathbf{f}_b^{(1)} \\ \vdots \\ \mathbf{f}_b^{(n)} \end{bmatrix} \quad \text{and} \quad \check{\mathbf{f}}_i = \begin{bmatrix} \mathbf{f}_i^{(1)} \\ \vdots \\ \mathbf{f}_i^{(n)} \end{bmatrix} \quad (4.23)$$

This definition yields the following transformation for a substructure.

$$\begin{bmatrix} \mathbf{q}_i \\ \mathbf{q}_b \\ \mathbf{g}_b \\ \mathbf{q}_y \end{bmatrix} = \begin{bmatrix} \mathbf{I} & \mathbf{o} & \mathbf{o} \\ \mathbf{o} & \mathbf{o} & \mathbf{L}_b \\ \mathbf{o} & \mathbf{I} & \mathbf{o} \\ \mathbf{o} & \mathbf{o} & \mathbf{I} \end{bmatrix} \begin{bmatrix} \mathbf{q}_i \\ \mathbf{g}_b \\ \mathbf{q}_y \end{bmatrix} \quad (4.24)$$

Pre- and postmultiplying (4.20) with (4.24) yields the assembled system

$$\begin{bmatrix} \check{\mathbf{M}}_{ii} & \check{\mathbf{M}}_{ib}\check{\mathbf{L}}_b \\ \check{\mathbf{L}}_b^T\check{\mathbf{M}}_{bi} & \check{\mathbf{L}}_b^T\check{\mathbf{M}}_{bb}\check{\mathbf{L}}_b \end{bmatrix} \begin{bmatrix} \check{\mathbf{q}}_i \\ \check{\mathbf{q}}_y \end{bmatrix} + \begin{bmatrix} \check{\mathbf{C}}_{ii} & \check{\mathbf{C}}_{ib}\check{\mathbf{L}}_b \\ \check{\mathbf{L}}_b^T\check{\mathbf{C}}_{bi} & \check{\mathbf{L}}_b^T\check{\mathbf{C}}_{bb}\check{\mathbf{L}}_b \end{bmatrix} \begin{bmatrix} \check{\mathbf{q}}_i \\ \check{\mathbf{q}}_y \end{bmatrix} + \begin{bmatrix} \check{\mathbf{K}}_{ii} & \check{\mathbf{K}}_{ib}\check{\mathbf{L}}_b \\ \check{\mathbf{L}}_b^T\check{\mathbf{K}}_{bi} & \check{\mathbf{L}}_b^T\check{\mathbf{K}}_{bb}\check{\mathbf{L}}_b \end{bmatrix} \begin{bmatrix} \mathbf{q}_i \\ \mathbf{q}_y \end{bmatrix} = \begin{bmatrix} \check{\mathbf{f}}_i \\ \check{\mathbf{L}}_b^T\check{\mathbf{f}}_b \end{bmatrix} \quad (4.25)$$

Note that this is the way structures are usually assembled in finite elements.

Dual Assembly

In the Dual assembly, the interface forces are reduced to one set of forces. This is possible because the interface forces have the same magnitude and opposite direction per node. Retaining the unique interface forces makes this assembly method suitable for the Dual-Craig-Bampton method, which will be introduced in Sec. 4.4. For that, the same approach is used that was used for the interface displacements in the primal assembly. A Boolean matrix is defined that associates the unique magnitudes of the interface forces \mathbf{g}_y with the interface forces on both sides of the boundary.

$$\mathbf{g}_b = -\mathbf{B}_b^T \mathbf{g}_y \quad (4.26)$$

Opposite to \mathbf{L}_b , \mathbf{B}_b is a signed Boolean to realise the opposite direction of the interface forces.

Pre- and postmultiplying (4.20) with

$$\begin{bmatrix} \mathbf{q}_i \\ \mathbf{q}_b \\ \mathbf{g}_b \\ \mathbf{q}_y \end{bmatrix} = \begin{bmatrix} \mathbf{I} & \mathbf{o} & \mathbf{o} & \mathbf{o} \\ \mathbf{o} & \mathbf{I} & \mathbf{o} & \mathbf{o} \\ \mathbf{o} & \mathbf{o} & -\mathbf{B}_b^T & \mathbf{o} \\ \mathbf{o} & \mathbf{o} & \mathbf{o} & \mathbf{I} \end{bmatrix} \begin{bmatrix} \mathbf{q}_i \\ \mathbf{g}_b \\ \mathbf{g}_y \\ \mathbf{q}_y \end{bmatrix} \quad (4.27)$$

eliminates the interface forces \mathbf{g}_b and replaces them with the unique force field \mathbf{g}_y . This yields the assembled system

$$\begin{bmatrix} \check{\mathbf{M}}_{ii} & \check{\mathbf{M}}_{ib} & \mathbf{o} \\ \check{\mathbf{M}}_{bi} & \check{\mathbf{M}}_{bb} & \mathbf{o} \\ \mathbf{o} & \mathbf{o} & \mathbf{o} \end{bmatrix} \begin{bmatrix} \check{\mathbf{q}}_i \\ \check{\mathbf{q}}_b \\ \check{\mathbf{g}}_y \end{bmatrix} + \begin{bmatrix} \check{\mathbf{C}}_{ii} & \check{\mathbf{C}}_{ib} & \mathbf{o} \\ \check{\mathbf{C}}_{bi} & \check{\mathbf{C}}_{bb} & \mathbf{o} \\ \mathbf{o} & \mathbf{o} & \mathbf{o} \end{bmatrix} \begin{bmatrix} \dot{\check{\mathbf{q}}}_i \\ \dot{\check{\mathbf{q}}}_b \\ \dot{\check{\mathbf{g}}}_y \end{bmatrix} + \begin{bmatrix} \check{\mathbf{K}}_{ii} & \check{\mathbf{K}}_{ib} & \mathbf{o} \\ \check{\mathbf{K}}_{bi} & \check{\mathbf{K}}_{bb} & \check{\mathbf{B}}_b^T \\ \mathbf{o} & \mathbf{B}_b & \mathbf{o} \end{bmatrix} \begin{bmatrix} \mathbf{q}_i \\ \mathbf{q}_b \\ \mathbf{g}_y \end{bmatrix} = \begin{bmatrix} \mathbf{f}_i \\ \mathbf{f}_b \\ \mathbf{o} \end{bmatrix} \quad (4.28)$$

where $(\check{\bullet})$ denotes again the block diagonal form of the matrices that was introduced for (4.20).

Node Collocation

In an electric machine, two substructures, which move relative to each other, are present. The interface nodes of two adjacent substructures will thus not always coincide. Instead, some or all of the nodes of one substructure are located between the nodes of the other substructure. In such a case, the assembly process becomes more complicated, as in this case, it is necessary to interpolate between two nodal values.

The assembly can be implemented, according to [47], by defining a unique set of degrees of freedom that define the nodal values on the interface. Since the location of the nodes on both sides of the interface are not necessarily the same, two matrices relating the values of the interface to the unique set of values are necessary

$$\mathbf{q}_b^{(s)} = \mathbf{D}_b^{(s)} \mathbf{q}_y \quad \text{for } s = 1, 2 \quad (4.29)$$

where $\mathbf{D}_b^{(s)}$ is the substructure *collocation* matrix. The values of \mathbf{D}_b are evaluated by evaluating the shape function on the associated substructure. Since this depends on the position of the interface field, the collocation matrixes needs to be reevaluated whenever one of the meshes is moved or changed.

4.4

Linear Reduction Methods Based on Modal Analysis

In Sec. 4.2, the modal analysis for quasi-static magnetic fields were introduced. In this section, a series of mode based reduction meth-

ods for estimating the dynamic behaviour of these systems will be introduced. The reduction techniques investigated here include *Guyan's method*, also called *Static-Condensation method* [57], the *Craig-Bampton method* [8], the *Augmented-Craig-Bampton method* [128] and the *Dual-Craig-Bampton method* [130]. All these methods were developed for the reduction of models describing the dynamics of structures.

Guyan's Method

4.4.1

Guyan's method or static-condensation method [57] projects the internal DoFs \mathbf{q}_i on the boundary DoFs \mathbf{q}_b using the static response related to boundary unit inputs. Boundary DoFs are considered to be all DoFs on the interface to another subsection of the model and all DoFs where an external current/force is applied. For electric machines, that means that all DoFs on the interface between the rotor and the stator as well as DoFs in the coil domains of the stator model are considered as boundary DoFs. The reduction matrix can be computed by

$$\mathbf{q}_{nr} = \begin{bmatrix} \mathbf{q}_i \\ \mathbf{q}_b \end{bmatrix} = \underbrace{\begin{bmatrix} \mathbf{\Psi}_s \\ \mathbf{I} \end{bmatrix}}_{\mathbf{R}} \mathbf{q}_r = \begin{bmatrix} \mathbf{K}_{ii}^{-1} \mathbf{K}_{ib} \\ \mathbf{I} \end{bmatrix} \mathbf{q}_b \quad (4.30)$$

where \mathbf{K}_{ii} and \mathbf{K}_{ib} are sub matrices of \mathbf{K} defined in (4.20). Although Guyan's method neglects the internal dynamics of the system during the reduction, it can still yield good results because the internal dynamics within electric machines are of minor importance due to the lamination of the machine. That is why Guyan's method yields relatively accurate results for electric machines.

The Craig-Bampton-Method

4.4.2

The Craig-Bampton (CB) method, [8], uses the condensation introduced by Guyan's method. On top of that, it takes the internal dynamics of the substructure into account by including fixed interface modes. To calculate the fixed interface modes, the boundary degrees of freedom are fixed in the eigenvalue problem that is solved to compute the modes. The Craig-Bampton method yields better results when there are no internal forces applied to the structure ($\mathbf{f}_i = \mathbf{0}$). This can be achieved by including the DoFs where an external force is applied into the boundary DoFs \mathbf{q}_b .

Fig. 4.5 shows fixed interface modes for the stator and rotor. The interface between the two substructures is located on the inside of the stator and outside of the rotor. Additionally, the DoFs in

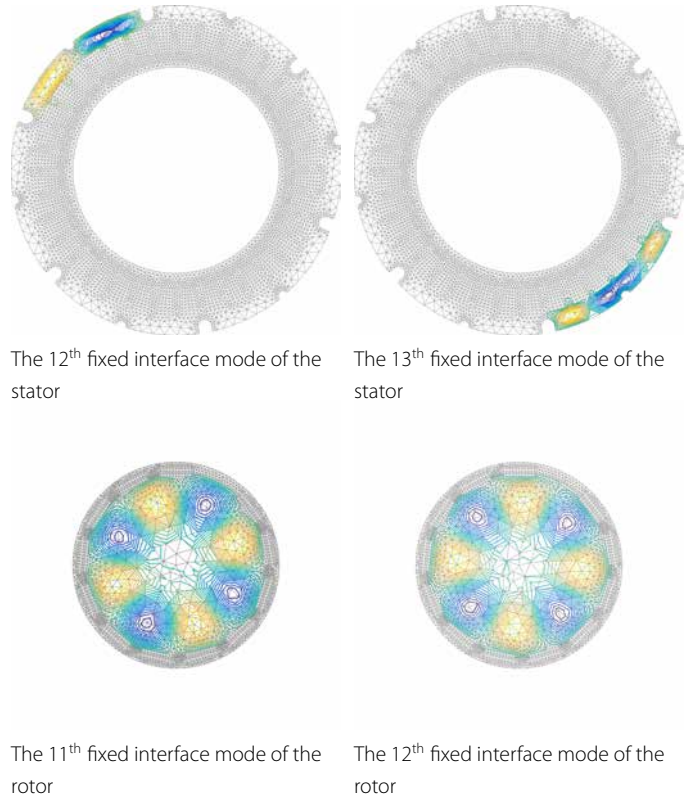


Figure 4.5

Contour plots of the magnetic vector potential. Depicted are two fixed interface modes and two free interface modes

the coil domains (depicted in green in Fig. 4.1) are retained during the reduction process, because external currents are applied to these DoFs. The stator plots in Fig. 4.5 illustrate the problem that arise from using the Craig-Bampton Method. The stator modes are restricted to rather local modes, because the coil domains, of which the DoFs are fixed during the mode computation, account for a large portion of the total domain of the stator. The calculated modes, therefore, will play a minor role in the internal dynamics of the system.

The reduction matrix for the CB method can be computed by

$$\mathbf{q}_{nr} = \begin{bmatrix} \mathbf{q}_i \\ \mathbf{q}_b \end{bmatrix} = \underbrace{\begin{bmatrix} \Phi_{CB} & \Psi_s \\ \mathbf{0} & I \end{bmatrix}}_{\mathbf{R}_{CB}} \begin{bmatrix} \eta \\ \mathbf{q}_b \end{bmatrix} \quad (4.31)$$

where Φ_{CB} denotes the fixed interface modes retained during the model reduction and Ψ_s the static condensation projection that was introduced in (4.30) for Guyan's method.

The Augmented-Craig-Bampton Method

4.4.3

The CB method showed some significant disadvantages when approximating the internal dynamics of the electric machine. The reason for the bad performance of the method was the requirement that there are no external forces applied to the internal DoFs of the system. The Augmented-Craig-Bampton method (ACB) [34, 129] offers the possibility to enrich the basis of the generic Craig-Bampton method to account for forces applied to the internal DoFs. The force distribution needs to be known a priori. In that case, the static and/or pseudo-dynamic system response to this force distribution, so called Modal Truncation Augmentation vectors (MTAs), can be used to enrich the basis. This way, the static response of the modes that were not included in the reduction basis can be included in the model.

For electric machines, this method facilitates the use of modes that are not constraint in the coil domains. Fig. 4.6 shows the modes calculated with free DoFs in the coil domains. For electric machines, the internal forces (in this case currents) have a fixed distribution, which is defined by the coil pattern of the machine. It is, thus, possible to represent the static response to the system by three vectors, one for every phase of the machine.

The additional basis vector can be calculated from the force distributions that are applied to the internal DoFs of the system. The static response of the system can be calculated by

$$\Phi_M = K_{ii}^{-1} F \quad (4.32)$$

where F denotes a matrix in which the columns represent the force/current distributions that are known a priori. Just like the retained modes from the generic Craig-Bampton method, the MTAs should be mass normalised

$$\Phi_M^T M_{ii} \Phi_M = I \quad (4.33)$$

Finally, it needs to be ensured that the reduction basis consists of orthogonal vectors. In the generic Craig-Bampton method, this is ensured as the results of the eigenvalue problem are by definition orthogonal to each other. The MTAs, however, are not necessarily orthogonal to all these vectors. By applying an orthonormal projection, P , this can be achieved

$$P = I - \Phi_{CB} \Phi_{CB}^T M_{ii} \quad (4.34)$$

The total reduction matrix consists of the ortho-normalised static response of the neglected modes and the fixed interface modes

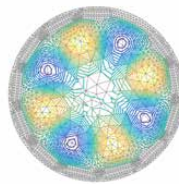
$$\begin{bmatrix} \mathbf{q}_i \\ \mathbf{q}_b \end{bmatrix} = \underbrace{\begin{bmatrix} \Phi_{CB} & \Phi_M & \Psi_s \\ \mathbf{0} & \mathbf{0} & I \end{bmatrix}}_{R_{ACB}} \begin{bmatrix} \eta_{CB} \\ \eta_M \\ \mathbf{q}_b \end{bmatrix} \quad (4.35)$$



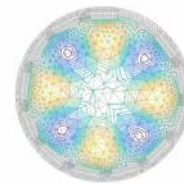
The 12th fixed interface mode of the stator for the ACB method



The 13th fixed interface mode of the stator for the ACB method



The 11th fixed interface mode of the rotor for the ACB method



The 12th free interface mode of the rotor for the ACB method



The 1st MTA of the stator for the ACB method



The 2nd MTA of the stator for the ACB method

Figure 4.6

Plots of the magnetic vector potential. Depicted are two fixed interface modes for the Augmented-Craig-Bampton method of the stator (top) and the rotor (middle). The bottom two plots show two MTAs.

4.4.4

The Dual-Craig-Bampton Method

The idea behind the Dual-Craig-Bampton (DCB) method is retaining the interface force rather than the interface displacements as the DoFs in the reduced component model. The forces are mathematical dual to the displacements, giving the methods its name. The difference to Rubin's method, which also retains the interface forces, is that even in the assembled total structure model, these forces are retained. Because of the forces retained in the reduced set of DoFs, a different assembly method needs to be used. This method is called dual assembly.

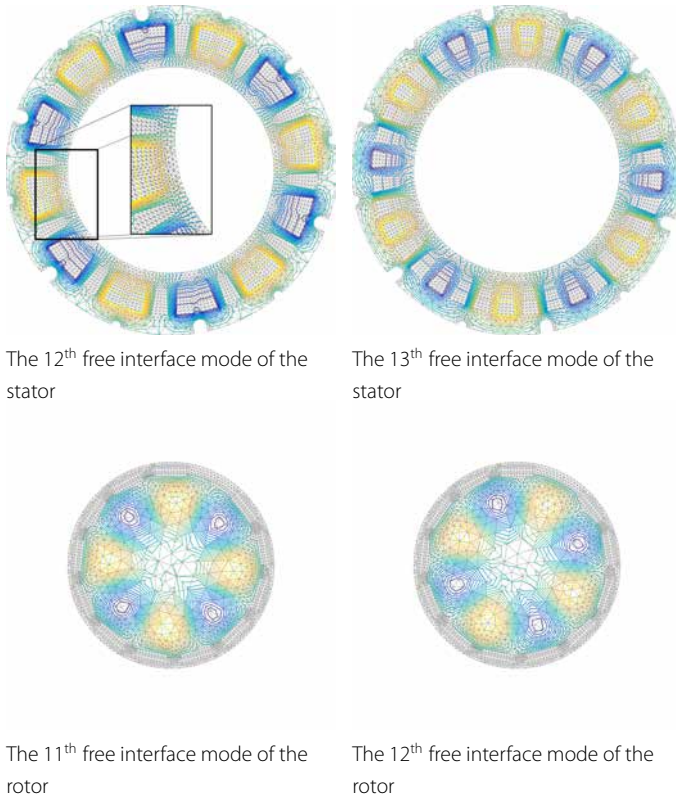


Figure 4.7
Free interface modes used in the Dual-Craig-Bampton method

The reduction matrix reads as follows

$$\begin{bmatrix} \mathbf{u} \\ \mathbf{g}_b \end{bmatrix} = \underbrace{\begin{bmatrix} \Phi_r & \Phi_f & \Psi_r \\ \mathbf{0} & \mathbf{0} & \mathbf{I} \end{bmatrix}}_{\mathbf{R}_{DCB}} \begin{bmatrix} \eta_r \\ \eta_f \\ \mathbf{g}_b \end{bmatrix} \tag{4.36}$$

where Φ_r denotes the rigid body modes, Φ_f the free vibration modes and Ψ_r the residual attachment modes. The version of the Dual-Craig-Bampton method that employs attachment modes instead of residual attachment modes can also be used. It was not explicitly derived here (see [164] for more details).

The Dual-Craig-Bampton method introduces the interface forces as additional DoFs. For structural systems the interface forces introduce infinite eigenfrequencies, whereas for first order systems they introduce infinite real eigenvalues. While for a time dependent study, these eigenvalues pose a problem as the system becomes unstable, they do not pose a problem for an eigenvalue analysis, as usually the algorithms are set up in such a way that the eigenvalues with the lowest magnitude are found.

Attachment Modes for Magnetic Fields

For magnetic fields, the computation of attachment modes known from the Rubin's method, varies slightly from the usual way how attachment modes are calculated. The reason for this is the different order of the system and the smaller number of 'rigid body modes'.

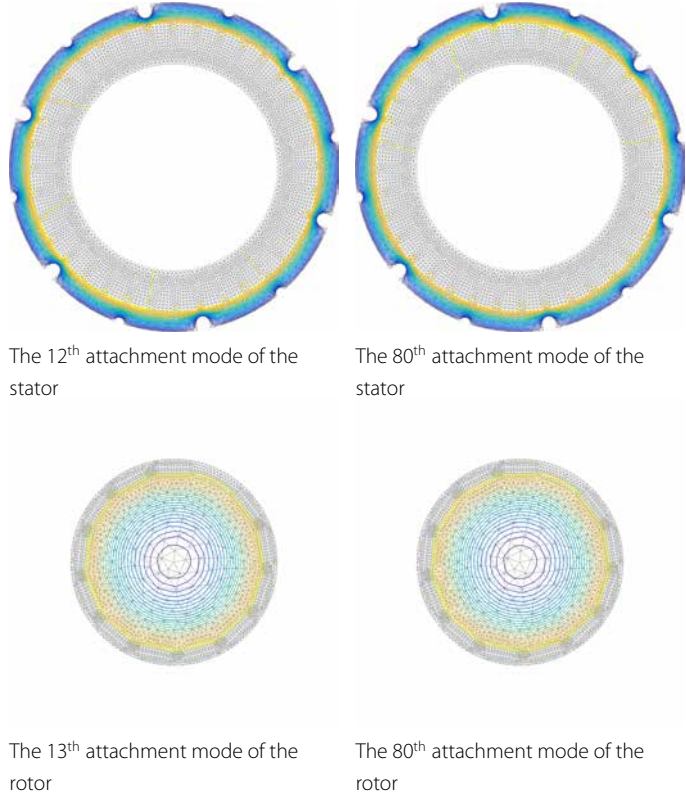


Figure 4.8

Some Attachment Modes of the stator and rotor used for the Dual-Craig-Bampton Method

Attachment modes are the static response of the system to the application of a loading at the DoFs. For dynamic substructuring, only the response of the system to forces on the interface are important.

$$\mathbf{q}_{stat} = \mathbf{K}^+ \mathbf{A}^T \mathbf{g}_b \quad (4.37)$$

where \mathbf{K}^+ denotes the generalised inverse of \mathbf{K} and \mathbf{A} a Boolean matrix that selects the interface DoFs. The attachment modes can then be calculated as

$$\boldsymbol{\Psi}_a = \mathbf{K}^+ \mathbf{A}^T \quad (4.38)$$

While for constrained systems without rigid body modes, $\mathbf{K}^+ = \mathbf{K}^{-1}$ and \mathbf{q}_{stat} is easily computable, the computation of \mathbf{q}_{stat} is more lengthy when 'rigid body modes' are present in the system. In that

case, the stiffness matrix, \mathbf{K} , is singular and an inverse is not easily computable. The system needs to be constrained in such a way that the stiffness matrix, \mathbf{K} , becomes non-singular. For structural dynamics, determining the best isostatic constraint is a lengthy procedure [158]. The procedure for magnetic fields is shorter as there are no rotational 'rigid body modes' and, thus, which DoF are constraint does not matter. After the constraints are applied the remaining stiffness matrix is positive definite and, thus, invertible.

$$\mathbf{K}^+ = \begin{bmatrix} 0 & 0 \\ 0 & \mathbf{K}^{-1} \end{bmatrix} = \mathbf{G}_c \quad (4.39)$$

Applying a nodal force to a system with rigid body modes would lead to an infinite static solution, as the rigid body modes would be excited. By self-equilibrating the nodal forces, i.e. making sure the applied forces are statically in equilibrium, the 'rigid body modes' are not excited and the solution becomes finite. To do that, the interface forces need to be projected to the null space of the rigid body modes.

$$\mathbf{A}_{eq}^T = \underbrace{(\mathbf{I} - \mathbf{C}\Phi_r\Phi_r^T)}_{\mathbf{P}} \mathbf{A}^T \quad (4.40)$$

where \mathbf{P} denotes the so called inertia-relief projector [29]. (4.40) shows the difference for attachment modes of magnetic systems to structural systems, as the damping matrix \mathbf{C} instead of the mass matrix is used.

As a final step, the attachment modes and rigid body modes need to be made orthogonal with respect to the magnetic mass matrix. To do so, the same projection matrix as for MTAs is used.

Application to the 600 W Ampair Wind Turbine

4.5

The test cases that are used to evaluate the reduction methods were introduced in Sec. 4.1.

Tab. 4.2 shows the current participation factors of the first 14 modes for the ACB and DCB methods. The Craig-Bampton method was excluded from Tab. 4.2, because there are no loads applied to internal DoFs. Consequently, all participation factors would be zeros. The internal modes of the CB method are thus not directly excited by the external load. They still contribute to the description of the dynamic response of the systems because within the super elements they can be excited. However, their contribution is very small. It can be concluded that the criterium to determine important modes in (4.13) is not suitable for the Craig-Bampton method.

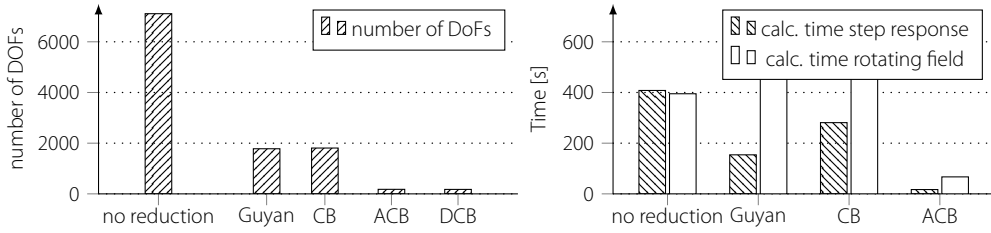


Figure 4.9

Reduction of calculation time and DoFs for the reduction methods introduced

According to Tab. 4.2, the 12th and 13th modes were chosen for the DCB and ACB method, as these modes show the highest participation factors. This is the case because the 12th and 13th mode have the same cyclic symmetry as the electro-magnetic active material. Therefore, they represent the magnetic field that is created by the coils very well. For the rotor, the first 14 modes were chosen, because no participation factors can be calculated here.

The choice for the CB method cannot be based on participation factors. Therefore, the 14 modes with the lowest eigenvalues were used for the stator as well as the rotor.

4.5.1

Time Integration

To compare the results of the time integration, the proper orthogonal decomposition method was used [74]. This method calculates the proper orthogonal modes (POM) and the proper orthogonal values (POV). The first POM represents the mode that captures the most energy of the time series it is calculated from. The corresponding POV represents the energy of that POM. Comparing the first three POM/POV couples of the reduced and reference

Table 4.2

The coil participation factors of the various stator modes used in various linear reduction methods: Augmented Craig-Bampton method (ACB) and Dual-Craig-Bampton method (DCB)

Mode number	ACB [$\cdot 10^8$]		DCB [$\cdot 10^8$]	
1	0.0018	-i 0.0110	0.0013	+i 0.0008
2	0.0150	+i 0.0005	-0.0001	-i 0.0000
3	0.0031	+i 0.0183	0.0001	+i 0.0000
4	0.0010	-i 0.0181	0.0001	+i 0.0002
5	0.0001	-i 0.0060	0.0002	-i 0.0001
6	-0.0246	+i 0.0061	0.0003	-i 0.0003
7	-0.0028	+i 0.0207	0.0003	+i 0.0000
8	0.0512	-i 0.0517	0.0014	+i 0.0005
9	-0.0086	+i 0.0920	-0.0007	-i 0.0006
10	-0.0389	+i 0.7298	-0.0405	-i 0.0516
11	0.6252	+i 0.1240	0.0539	-i 0.0405
12	-1.5762	-i 3.1884	-4.1184	-i 2.3070
13	-3.3662	+i 1.6365	-2.0429	+i 3.6471
14	-0.1100	-i 0.5524	-0.0165	+i 0.0714

	no reduction	Guyan	CB	ACB
number of DoFs	7109	1780	1808	179
Step Response				
Calc. timewithout basis assembly [s]	408	153	258	17
Calc. time with basis assembly [s]	408	154	281	28
time red. with basis assembly [%]	0	62	31.2	93.2
MAC values of first three Proper Orthogonal Modes (POM)	–	1	1	1
		1	1	1
		1	1	1
relative error of first three Proper Orthogonal Values (POV) [%]	–	0	0	0
		0.1	0	0.28
		0.1	0	–3.23
Rotating Magnetic Field				
Calc. time without basis assembly [s]	395.8	464	442	57.6
Calc. time with basis assembly [s]	395.8	465	465	67
time red. with basis assembly [%]	0	–17.6	–17.6	83.1
MAC values of first three Proper Orthogonal Modes (POM)	–	1	1	1
		1	1	1
		1	1	1
relative error of first three Proper Orthogonal Values (POV) [%]	–	0	0	0
		0	0	0
		0	0.12	0.5

Table 4.3

The results of the various linear reduction methods: Guyan's Method, Craig-Bampton method (CB) and Augmented Craig-Bampton method (ACB)

solutions gives an impression how accurately the reduced model reproduces the reference solution. The POMs are compared by a modal assurance criterion (MAC), whereas the POV are compared by calculating the relative error between them. A MAC value for the POM close to 1 indicates that the shape of those modes are very close together. A low relative error for the POV value indicates that the amplitude of the associated POM are similar.

Tab. 4.3 and Fig. 4.9 show the reduction of computation time for Guyan's Method, the Craig-Bampton Method and the Augmented-Craig-Bampton method. The Dual-Craig-Bampton method was not included, because the time integration was unstable using standard solver. A reduction of computation time could only be realised for the ACB method. Guyan's method and the CB method actually increase the computation time.

Eigenvalue Analysis

4.5.2

To compare the eigenvalue analysis, the eigenvalues of the reduced and the full system are compared. Tab. 4.4 lists the first 14 eigenvalues for each reduction method and the full model.

The CB method and Guyan's method yield very accurate results for the eigenvalues. The DCB method is also quite accurate with only two modes for stator and rotor each. The ACB method shows some deviation from the exact eigenvalues.

	Full Model	CB	Guyan	ACB	DCB
Calculation Time w/o reduction time	0.18	0.52	0.52	0.027	0.025
Eigenvalues					
Mode 1	-0.0630	-0.0630	-0.0630	-0.0631	-0.0630
Mode 2	-5.8292	-5.8964	-5.8292	-6.3481	-5.8969
Mode 3	-5.8964	-5.8292	-5.8964	-6.4279	-5.8297
Mode 4	-19.0030	-18.8359	-18.8359	-25.6092	-19.0168
Mode 5	-18.8359	-19.0030	-19.0030	-25.9182	-18.8484
Mode 6	-32.4917	-32.3049	-32.3049	-55.6167	-32.3513
Mode 7	-32.3049	-32.4917	-32.4917	-56.7684	-32.5400
Mode 8	-43.1158	-43.1158	-43.1158	-57.4105	-43.1887
Mode 9	-43.2891	-43.2891	-43.2891	-58.6921	-43.3640
Mode 10	-51.0733	-51.2148	-51.0733	-59.9809	-51.1492
Mode 11	-51.2148	-51.0733	-51.2148	-60.2857	-51.2927
Mode 12	-56.7912	-56.7912	-56.7912	-74.6095	-56.8538
Mode 13	-56.9744	-56.9744	-56.9744	-111.5550	-57.0390
Mode 14	-61.1375	-61.1375	-61.1375	-109.9829	-61.1853

Table 4.4

Value of computed eigenvalues

4.5.3

Discussion

The CB and Guyan's method retain the coil domain DoFs in the reduced system. These DoFs are the only DoFs that have a significant entry in the damping matrix as only the coil domains have a conductivity larger than one. Hence, the reduced part does not significantly contribute to the internal dynamics of the system. Therefore, these methods yield very accurate results. The numbers in Tab. 4.3 indicate this. The calculation times of these two reduction methods are actually higher than for the full system for the rotating field load case. This increase in computation time is caused by an extended computation time to find a feasible initial state.

The results of the time dependent analysis of the ACB method are less accurate for the step response than for the rotational magnetic field. The step response excites many modes whereas the rotating field excites mainly the two modes that are retained in the basis of the ACB. Neglecting a considerable amount of modes, the ACB method cannot capture the entire dynamics caused by a load step. The reference response, on the other side, are able to do so, be-

cause no reduction is applied and thus all dynamic information is still contained in the system. For the rotating field, the important internal dynamics are contained in the two modes that are retained in the ACB method. Therefore, the ACB method can describe the solution to the rotating excitation accurately.

The ACB method performs worse in approximating the eigenvalues of the total system, although it retains the same amount of modes than the DCB method. Most likely, the static condensation used in the ACB method cannot accurately describe the coupled dynamics of the system, while the attachment modes, used for the DCB method, can. Further research is necessary, to single out the cause of this error.

Reduction of Magneto-Mechanical Coupled Systems

4.6

The reduction methods introduced in Sec. 4.4 can also facilitate computations of large coupled eigenvalue problems. (2.172) needs to be solved monolithically. This requires an enormous amount of memory when the system has a lot of DoFs. To reduce the required memory, the system can be split up in several subsystems. As described in Sec. 4.3.2, this reduces the computational cost. It also reduces the needed amount of memory.

Magneto-mechanical coupled models of electric machines can be decomposed in two ways. The first way is the one already introduced for the purely magnetic substructuring. The rotor and the stator represent each a substructure and the super elements are coupled in the air gap. In this case, remeshing is necessary when the rotor is rotated relative to the stator.

It is possible to split each of the above substructures by physics, yielding four substructures. This way a magnetic and a mechanical substructure are created for rotor and stator. This idea is explored in this section. Sadly, there was no time to investigate this method in detail.

Coupling of Multi-Physical Substructures

4.6.1

As described before, one of the possibilities to split the total system into substructures is by separating it in different physical domains. In that case, an assembly has to be made that has one physical model on one side of the boundary, while the other substructure describes another physics.

To better understand the concept of multi-physical substructuring, consider the system in Fig. 4.10. The system consists of a deformable structure of which one part is part of a magnetic field. The round nodes in Fig. 4.10 are part of both domains. At these nodes the coupling between the two physics take place. The nodes that are indicated by a cross are only part of one physics. All degrees of freedom that are part of the coupled domain are considered boundary DoFs and are retained during the component model reduction of the magnetic domain and the mechanical domain. All DoFs at nodes represented by crosses are considered internal DoFs and will not be part of the reduced system. The coupling is indicated by the dashed lines.

Looking at the assembly equations, the multi-physical coupling can be seen as an assembly with interface physics (see [164] for an explanation of the purely mechanical case). In the multi-physical case for magneto-mechanical coupled systems, the interface physics consist of a damping term, represented by the C_{uA} and C_{Au} terms in (2.170), and a stiffness term represented by the K_{uA} and K_{Au} . The domain that is coupled, i.e. that combines the magnetic field and the elastic field in one domain, is considered the boundary now. Therefore, all boundary DoFs are part of that domain

$$\mathbf{q}_b \in \Omega_{cpl} \quad (4.41)$$

The matrices C_{Au} , C_{uA} , K_{Au} and K_{uA} only affect the DoFs in this coupled domain. The rows and columns of the other DoFs are empty. The subpart of the coupling matrices that are associated to the boundary DoFs are denoted by

$$C_{bAbu} \quad C_{bubA} \quad K_{bAbu} \quad K_{bubA}$$

To indicate which value belongs to which substructure/domain the same notation as before is used, but instead of numbers indicating the substructure, u and A are used to indicate the structural and the magnetic domain, respectively.

Because there are no redundant variables for the multi-physical coupling, no DoFs or force terms can be eliminated. This distin-

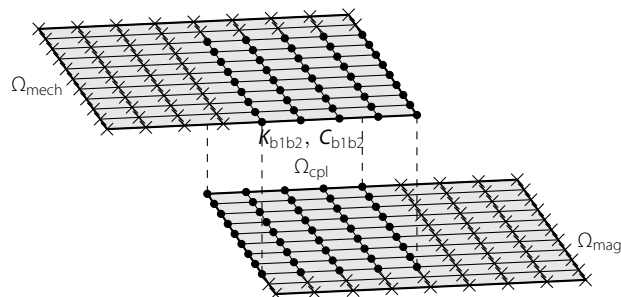


Figure 4.10
Link between nodes of
substructures with different
physics

guishes the multi-physical coupling from the primal and dual assembly introduced in Sec. 4.3.4. There is no compatibility condition:

$$\mathbf{q}_b^{(u)} \neq \mathbf{q}_b^{(A)} \quad (4.42)$$

Also the interface forces do not have the same magnitude with opposite pre-sign:

$$\mathbf{g}_b^{(u)} \neq -\mathbf{g}_b^{(A)} \quad (4.43)$$

The interface forces result from the coupling matrices in (2.172).

$$\begin{aligned} \mathbf{g}_b^{(u)} &= -\mathbf{K}_{bubA} \mathbf{q}_b^{(A)} - \mathbf{K}_{bubu} \mathbf{q}_b^{(u)} - \mathbf{C}_{bubA} \dot{\mathbf{q}}_b^{(A)} - \mathbf{C}_{bubu} \dot{\mathbf{q}}_b^{(u)} \\ \mathbf{g}_b^{(A)} &= -\mathbf{K}_{bAbu} \mathbf{q}_b^{(u)} - \mathbf{C}_{bAbu} \dot{\mathbf{q}}_b^{(u)} \end{aligned} \quad (4.44)$$

The matrices in (4.44) are derived from the coupling matrices in (2.170). As the matrices in (2.170), they depend on the DoFs of the system and, consequently, create a nonlinearity. Separating the physics in (4.44), yields the two coupling matrices

$$\check{\mathbf{g}}_b = \begin{bmatrix} \mathbf{g}_b^{(u)} \\ \mathbf{g}_b^{(A)} \end{bmatrix} = - \underbrace{\begin{bmatrix} \mathbf{K}_{bubu} & \mathbf{K}_{bubA} \\ \mathbf{K}_{bAbu} & \mathbf{0} \end{bmatrix}}_{\mathbf{K}_{cpl}} \begin{bmatrix} \mathbf{q}_b^{(u)} \\ \mathbf{q}_b^{(A)} \end{bmatrix} - \underbrace{\begin{bmatrix} \mathbf{C}_{bubu} & \mathbf{C}_{bubA} \\ \mathbf{C}_{bAbu} & \mathbf{0} \end{bmatrix}}_{\mathbf{C}_{cpl}} \begin{bmatrix} \dot{\mathbf{q}}_b^{(u)} \\ \dot{\mathbf{q}}_b^{(A)} \end{bmatrix} \quad (4.45)$$

For the case that the physics are the same on both sides, the matrices in (4.45) become symmetric. With (4.45), it is possible to assemble the global coupled equation:

$$\begin{aligned} \begin{bmatrix} \mathbf{M}_{ii}^{(u)} & \mathbf{M}_{ib}^{(u)} & \mathbf{0} & \mathbf{0} \\ \mathbf{M}_{bi}^{(u)} & \mathbf{M}_{bb}^{(u)} & \mathbf{0} & \mathbf{0} \\ \mathbf{0} & \mathbf{0} & \mathbf{0} & \mathbf{0} \\ \mathbf{0} & \mathbf{0} & \mathbf{0} & \mathbf{0} \end{bmatrix} \begin{bmatrix} \dot{\mathbf{q}}_i^{(u)} \\ \dot{\mathbf{q}}_b^{(u)} \\ \dot{\mathbf{q}}_i^{(A)} \\ \dot{\mathbf{q}}_b^{(A)} \end{bmatrix} + \begin{bmatrix} \mathbf{C}_{ii}^{(u)} & \mathbf{C}_{ib}^{(u)} & \mathbf{0} & \mathbf{0} \\ \mathbf{C}_{bi}^{(u)} & \mathbf{C}_{bb}^{(u)} + \mathbf{C}_{bubu} & \mathbf{0} & \mathbf{C}_{bubA} \\ \mathbf{0} & \mathbf{0} & \mathbf{C}_{ii}^{(A)} & \mathbf{C}_{ib}^{(A)} \\ \mathbf{0} & \mathbf{C}_{bAbu} & \mathbf{C}_{bi}^{(u)} & \mathbf{C}_{bb}^{(u)} \end{bmatrix} \begin{bmatrix} \mathbf{q}_i^{(u)} \\ \mathbf{q}_b^{(u)} \\ \mathbf{q}_i^{(A)} \\ \mathbf{q}_b^{(A)} \end{bmatrix} + \\ + \begin{bmatrix} \mathbf{K}_{ii}^{(u)} & \mathbf{K}_{ib}^{(u)} & \mathbf{0} & \mathbf{0} \\ \mathbf{K}_{bi}^{(u)} & \mathbf{K}_{bb}^{(u)} + \mathbf{K}_{bubu} & \mathbf{0} & \mathbf{K}_{bubA} \\ \mathbf{0} & \mathbf{0} & \mathbf{K}_{ii}^{(A)} & \mathbf{K}_{ib}^{(A)} \\ \mathbf{0} & \mathbf{K}_{bAbu} & \mathbf{K}_{bi}^{(u)} & \mathbf{K}_{bb}^{(u)} \end{bmatrix} \begin{bmatrix} \mathbf{q}_i^{(u)} \\ \mathbf{q}_b^{(u)} \\ \mathbf{q}_i^{(A)} \\ \mathbf{q}_b^{(A)} \end{bmatrix} = \begin{bmatrix} \mathbf{f}_i^{(u)} \\ \mathbf{f}_b^{(u)} \\ \mathbf{f}_i^{(A)} \\ \mathbf{f}_b^{(A)} \end{bmatrix} \end{aligned} \quad (4.46)$$

(4.46) shows that the inner dynamics of the individual single physical systems stay the same during coupling. The coupling physics, which is introduced to the system, is only applied to the interface DoFs.

Because no DoFs or forces are eliminated, any of the reduction methods introduced in Sec. 4.4 can be used to reduce the DoFs in the subsystems, assuming all interface DoFs are retained.

In magneto-mechanical coupled systems, the structural dynamics are dominated by the free interface modes. The magnetic forces

have a minor influence on the dynamics. Therefore, it seems beneficial to use the Dual-Craig-Bampton method for reducing the structural part. This way free interface modes are used to approximate the solution, which resemble the final solution more than fixed interface modes.

The magnetic field in electric machines, on the other side, is mainly dominated by its static response. The internal dynamic are not so important due to lamination. Furthermore, the stiffness change due to the geometry change, i.e. the part that is represented by $\mathbf{K}_{Au}\mathbf{q}_u$ in (2.170), has a strong influence on the magnetic field. In this case, it seems better to use the CB method, as the CB method super imposes the internal dynamics on the dominant static solution.

A mixed assembly method as introduced in [164] for the two physics seems thus best to yield a reduced model that is as accurate as possible for a certain amount of retained modes.

4.6.2

Multi Physical Guyan

For magneto-mechanical systems, there is a special way to apply Guyan's method. Assuming that one physic is linear, it is possible to condensate that physic onto the other physic. There are, therefore, two ways to apply this Guyan's method.

In Chapter 2 the structural PDE were assumed to be linear. It is thus possible to condensate the whole structure onto the nodes that represent the boundary between the structural and the magnetic domain. This boundary consists of all magnetic DoFs within the structure of which the dynamics are condensed. Starting from the coupled numerical equations (2.170) the reduction matrix can be written as

$$\mathbf{q}_{nr} = \begin{bmatrix} \mathbf{q}_u \\ \mathbf{q}_{Ai} \\ \mathbf{q}_{Ab} \end{bmatrix} = \underbrace{\begin{bmatrix} \circ & \mathbf{K}_{uu}^{-1}\mathbf{K}_{uAb} \\ \mathbf{I}_{AiAi} & \circ \\ \circ & \mathbf{I}_{AbAb} \end{bmatrix}}_{\mathbf{R}} \begin{bmatrix} \mathbf{q}_{Ai} \\ \mathbf{q}_{Ab} \end{bmatrix} \quad (4.47)$$

where \mathbf{q}_{Ab} denotes the magnetic field DoFs on the interface and \mathbf{q}_{Ai} the internal magnetic field DoFs. The reduction matrices can then be calculated according to (4.16). This way only the magnetic DoFs are retained in the system.

For linear magnetic systems the condensation of the magnetic domain onto the structural domain is possible. In this case, only the DoFs where a coil current is applied and the DoF within the permanent magnet domains are retained, because at those location ex-

ternal loads are applied. The reduction matrix can be written as

$$\mathbf{q}_{nr} = \begin{bmatrix} \mathbf{q}_{ui} \\ \mathbf{q}_{ub} \\ \mathbf{q}_A \end{bmatrix} = \underbrace{\begin{bmatrix} \mathbf{I}_{uiui} & \mathbf{0} \\ \mathbf{0} & \mathbf{I}_{ubub} \\ \mathbf{0} & \mathbf{K}_{AA}^{-1} \mathbf{K}_{Aub} \end{bmatrix}}_R \begin{bmatrix} \mathbf{q}_{ui} \\ \mathbf{q}_{ub} \end{bmatrix} \quad (4.48)$$

Which physics condensation yields more accurate results depends highly on the system. As Guyan's method neglects internal dynamics of the system, it yields good results when the dynamics play a minor role in the system. That is the case for the magnetic field of electric machines, as these machines are designed in such a way that the eddy currents are minimal. However, usually a nonlinear model is necessary to yield accurate results for the magnetic fields as saturation and hysteresis needs to be taken into account. In such a case, Guyan's method cannot be applied as explained in (4.48)

On the other side, the structural system is mainly linear. However, the internal dynamics are quite important or even dominant. Therefore, a reduction method should be used that includes these internal dynamics.

Estimating the Frequency Change

For the case that the influence of the magnetic field on a structural mode is of interest, the statement made above about the nonlinearities of the magnetic field no longer holds. In this case the magnetic field can be linearised around a linearisation point, much like it was done in Chapter 2.

Using the multi-physical Guyan method, it is possible to roughly estimate the influence of the magnetic field on a structural mode. For a certain structural mode it is possible to estimate the coupling energy (2.78) without computing a coupled modal analysis. Assuming that a modal analysis for the structural part of the system has been done and the matrices for the magnetic part of the system are known, the system can be described by:

$$\begin{aligned} \begin{bmatrix} \text{diag}(m_r) & \mathbf{0} \\ \mathbf{0} & \mathbf{0} \end{bmatrix} \begin{bmatrix} \ddot{\eta}_r \\ \dot{\mathbf{q}}_A \end{bmatrix} + \begin{bmatrix} \text{diag}(c_r) & \Phi^T C_{uA} \\ \mathbf{C}_{Au} \Phi & C_{AA} \end{bmatrix} \begin{bmatrix} \dot{\eta}_r \\ \dot{\mathbf{q}}_A \end{bmatrix} \\ + \begin{bmatrix} \text{diag}(k_r) & \Phi^T K_{uA} \\ \mathbf{K}_{Au} \Phi & K_{AA} \end{bmatrix} \begin{bmatrix} \eta_r \\ \mathbf{q}_A \end{bmatrix} = \mathbf{0} \end{aligned} \quad (4.49)$$

It is now possible to calculate how the magnetic field behaves when it is influenced by the displacement of the r^{th} mode. The magnetic field can be described by the first order system in which the displacement of the r^{th} mode is seen as excitation.

$$\mathbf{C}_{AA} \dot{\mathbf{q}}_{A,r} + \mathbf{K}_{AA} \mathbf{q}_{A,r} = \mathbf{J}_{ext} - \mathbf{K}_{Au} \boldsymbol{\varphi}_r - \mathbf{C}_{Au} \dot{\boldsymbol{\varphi}}_r \quad (4.50)$$

$\mathbf{q}_{A,r}$ denotes the changes of the nodal values of the magnetic field generated by the movement of the r^{th} mode. Only the steady state solution is of interest. The steady state solution for the r^{th} mode is described by

$$\mathbf{q}_{A,r} = \underbrace{[\dot{\mathbf{i}}\omega_r \mathbf{C}_{AA} + \mathbf{K}_{AA}]^{-1} [-\mathbf{K}_{Au} - \dot{\mathbf{i}}\omega_r \mathbf{C}_{Au}]}_{\mathbf{K}_{A\Phi}} \boldsymbol{\varphi}_r \quad (4.51)$$

where ω_r denotes the eigenfrequency of the r^{th} mode. Due to the first order ODE $\mathbf{K}_{A\Phi}$ has an imaginary term as well as a real term. Therefore the change of the magnetic field created by the movement of the mode is not necessarily in phase with the structural mode.

(4.49) can be written in terms of the modal coordinates η projecting the magnetic degrees of freedoms onto the modes.

$$\text{diag}(m_r)\ddot{\eta}_r + \text{diag}(c_r)\dot{\eta}_r + (\text{diag}(k_r) - \boldsymbol{\varphi}_r^T [\mathbf{K}_{uA} + \dot{\mathbf{i}}\omega_r \mathbf{C}_{uA}] \mathbf{K}_{A\Phi} \boldsymbol{\varphi}_r) \eta_r = 0 \quad (4.52)$$

The coupling energy for the r^{th} mode, $W_{ex,m,r}$, can be calculated by

$$W_{ex,m,r} = \boldsymbol{\varphi}_r^T \mathbf{K}_{uA} \mathbf{K}_{A\Phi} \boldsymbol{\varphi}_r \quad (4.53)$$

$W_{ex,m,r}$ has a real and an imaginary part. The real part gives an indication on how the frequency of the mode changes due to coupling while the imaginary part of $W_{ex,m,r}$ gives an indication about the increase in damping.

Comparing the exchanged energy (4.53) with the energy associated with a mode

$$W_r = \boldsymbol{\varphi}_r^T \mathbf{K}_{uu} \boldsymbol{\varphi}_r = \omega_r^2 m_r \quad (4.54)$$

gives an indication to what extend the mode is affected by the coupling. The new eigenfrequency $\omega_{r,cpl}$ can be estimated by taking the square root of the new energy stored in the mode

$$\omega_{r,cpl} = \sqrt{\omega_r^2 - \text{Real}\left\{\frac{1}{m_r} W_{ex,m,r}\right\}} \quad (4.55)$$

4.7

Discussion

The results in Sec. 4.5 clearly show that using the four introduced methods for rotating electric machines yield a significant reduction of DoFs and thus calculation time for magnetic fields of electric machines. However, there are some issues associated with the methods proposed here that still need some further research.

Electric machines are designed to operate in saturation. The linear FE models introduced in this paper cannot take saturation of the

iron into account. Saturation will lead to a B-H curve that is nonlinear and therefore will lead to a nonlinear finite element formulation, resulting in a stiffness matrix that depends on the magnetic flux density (see Sec. 2.5.6). Normally, that problem is overcome by reassembling the stiffness matrix for every time step. However, this method is not applicable here as the assembly of the reduction matrices is computationally expensive. In mechanical engineering, there are some reduction methods that are based on modal analysis that can deal with this problem, for instance [152]. Furthermore, hyper reduction methods such as ECSW [44] can be applied. These reduction methods have to be adapted for magnetic fields.

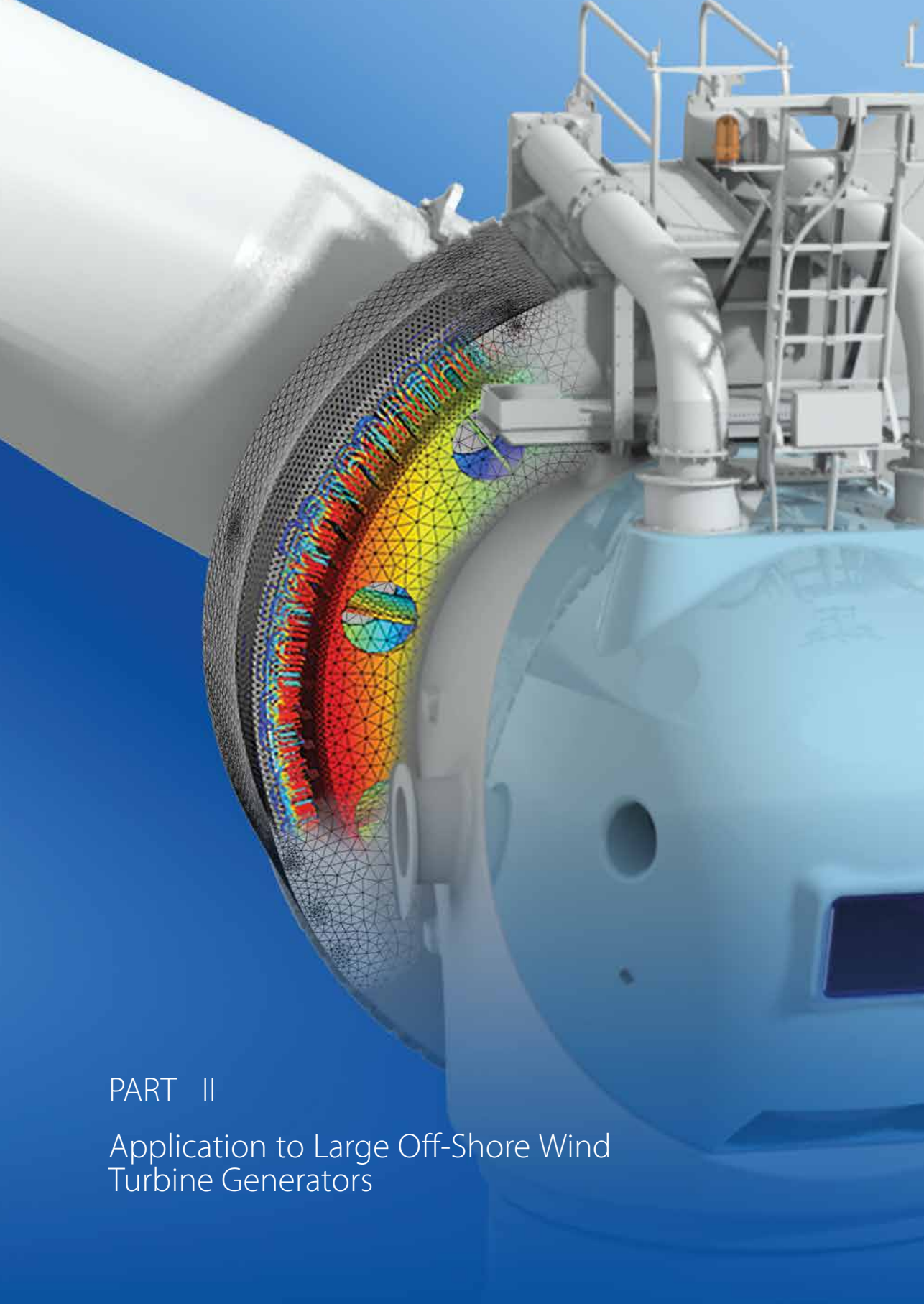
The methods introduced here take a whole machine into account. For time dependent analysis of magnetic fields in electric machines, only a section of the machine is computed exploiting the machine's cyclic symmetry. This can also be done for modal analysis of cyclic structures. In the past, methods based on Floquet theory have been developed to calculate modes for cyclic-symmetric structures, modelling only a section of the cyclic-symmetric structure [82, 127]. This method can be adapted for the introduced methods for magnetic fields in electric machines.

Summary

4.8

In this chapter, the modal analysis for quasi-static magnetic fields was introduced. It was shown that magnetic modes can be used to reduce computationally expensive finite element problems, using methods developed for structural dynamics. The methods need to be adapted slightly, because the magnetic PDEs represent a first order system, while the structural PDEs represent a second order system. It was shown that because of the specific design of electric machines, this modal approach to model reduction yields accurate results in particular for electric machines. By applying the methods to a 2D model of an electric machine, their potential was demonstrated. Significant time reduction could be achieved by the tested methods. However, the reduction methods lack the capability to include nonlinear effects such as hysteresis and saturation.

Furthermore, ideas were presented for model order reduction of dynamic magneto-mechanical coupled systems. These methods can reduce the computational cost and the memory requirements for the coupled eigenvalue problem introduced in Chapter 2 significantly. As the eigenvalue problem is linear, applying linear reduction techniques for magnetic fields, will not introduce significant errors due to linearisation.



PART II

Application to Large Off-Shore Wind
Turbine Generators

This Chapter is based on the papers:

Kirschneck, M., Rixen, D.J., Polinder, H., van Ostayen, R.A.J.;
Electro-Magneto-Mechanical Coupled Vibration Analysis
of a Direct-Drive Off-Shore Wind Turbine Generator.
Journal of Computational and Nonlinear Dynamics, 2014

Kirschneck, M., Rixen, D.J., Polinder, H., van Ostayen, R.A.J.;
Modal analysis of a large direct-drive off-shore wind
turbine generator rotor; ISMA2014

Kirschneck, M., Rixen, D.J., Polinder, H., van Ostayen, R.A.J.;
In-Situ Experimental Modal Analysis of a Direct-Drive
Wind Turbine Generator; IMAC 2015

Abstract:

The dynamic behaviour of wind turbine generators is influenced by the coupling between the structural dynamics and the magnetic field in the generator. This coupling necessitates specialised approaches to accurately capture the dynamics of the coupled system. These approaches were introduced in Chapter 2.

This chapter applies the methodology introduced in Chapter 2 to a multi-megawatt wind turbine. First, a two-way coupled model is introduced to determine the internal dynamics of the coupled system. Afterwards, a 2D magnetic model is used to predict the excitation frequency created by the magnetic field. Finally, the introduced models are validated by in-situ vibration measurements in the generator. For that impact and operational measurements were conducted.

5.1

Introduction

Part I of this thesis covered the fundamental modelling techniques for magneto-mechanical coupled systems. Those modelling techniques make it possible to predict the dynamic properties of the generator. Furthermore, it makes it possible to see the influence of the coupling on the dynamic properties. This chapter will apply the introduced techniques to the generator of the XD-115, a multi-megawatt wind turbine, to get a thorough understanding of the dynamics of the turbine's rotor. The presented models will afterwards be validated using measurements from the turbine.

From a dynamic point of view, the generator of a direct-drive wind turbine is a unique system. The direct connection of the generator to the hub of the turbine, i.e. the absence of a gear box, leads to low rotation speeds in the generator. This drive train topology results in huge torque values, as the nominal power of the turbine needs to be transmitted at low rotation speeds. When possible, this relation between torque and rotation speed is avoided in electric machines, as it leads to unfavourable effects, such as large displacements, large rotating masses, low resonance frequencies, a large amount of electro-magnetic active parts and, thus, expensive generator designs. Additionally, due to the large pole number, usually encountered in this kind of machines, the excitation frequencies of the magnetic force are especially high compared to the rotation speed. They are, thus, the main excitation source for the structure of the generator.

As a first step of the dynamic analysis, a 3D two-way coupled model of the generator is presented in Sec. 5.3.2. This model identifies the values of the modal parameters and their changes compared to the uncoupled system. The results show that the influence of the magneto-mechanical coupling on the modal parameters is of minor importance for the XD-115. Consequently, a one-way coupled model, which consists of a 2D magnetic model and a 3D structural modal, is used for the rest of the chapter. This model is presented in Sec. 5.3.3 and considers the 2D magnetic forces as excitation forces for the structural model. The excitation generated by the space harmonics and cogging torque will be identified as the main source of vibrations within the generator rotor. An in depth analysis of the mechanisms, creating these harmonic forces is done in Sec. 5.3.4 and the effects they have on the rotor structure is presented. Sec. 5.4, the last part of the chapter, presents an experimental validation of the models. This is done by in-situ vibration measurements in the turbine. Finally, the measurement results and the simulations are compared with each other and the discussed.

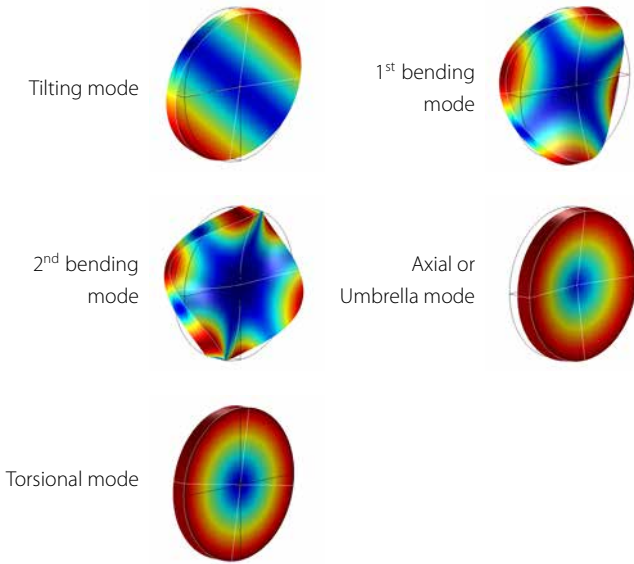


Table 5.1
Various mode shapes of importance for the XD-115 generator rotor structure

Mode Shape Description

In this chapter, various types of mode shapes will be discussed. The name of a certain shape can be misleading. A clear definition of the mode shapes is, therefore, necessary.

The rotor structure of the XD-115 can be roughly described as a disc. As such, its lowest modes are generally the same shape as those of a disc. Tab. 5.1 lists the most important mode shapes of a disc and the generator of the XD-115 and the names used in this thesis to describe them.

5.1.1

The XD-115 Wind Turbine

5.2

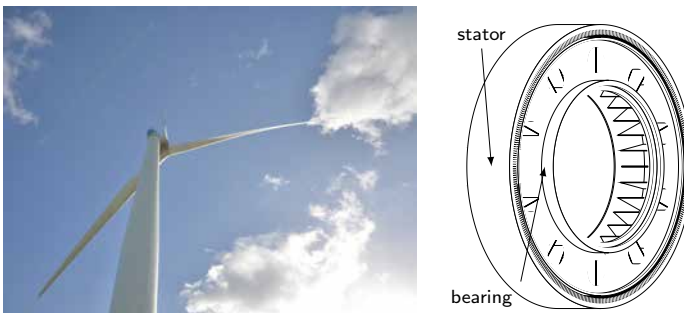


Figure 5.1
The XD-115 wind turbine. Exterior photo of the turbine prototype in North Holland (left) and a schematic of the generator structure (right)

The XD-115 is a 5 MW wind turbine built by XEMC-Darwind, designed for off-shore locations. This wind turbine exhibits all char-

Turbine Type	XD115
Rated Power	5MW
Operational Data	
Cut-in wind speed [m/s]	4
Cut-out wind speed [m/s]	25
Rated wind speed [m/s]	14
Designed for wind class (According to IEC 61400-1)	IC
Noise at hub height [dBA]	112
Rotor	
Diameter [m]	115
Speed [rpm]	Variable (nominal 18 rpm)
Power regulation	Full span pitch
Tilt angle	6°
Blade material	Glass fiber reinforced epoxy
Generator	
Type	Synchronous Permanent magnet direct-drive
Cooling	Dehumidified forced air
Main bearing	Single main bearing multiple row, cylindrical roller bearing
Converter	
Type	Voltage source inverter
Voltage [V]	3000
Grid coupling	AC-DC-AC
Tower	
Material	Steel tubular
Hub height [m]	80 to 140 (project dependent)
Masses [ton]	
Rotor (hub + blades)	97
Generator	137
Nacelle	47
Total top mass	281

Table 5.2
Specification of the XD-115. Data
taken from [174]

acteristics of a direct-drive wind turbine, such as a large generator rotor diameter (ca. 5 m), a high generator mass and large torque values necessary to generate the nominal power of 5 MW. Fig. 5.1 shows the exterior of the turbine and the generator rotor structure. Tab. 5.2 lists important properties of the turbine.

The rotation speed of the turbine during operation is between 9 and 18rpm.

The XD-115 rotor stiffener construction is a welded steel construction with stiffener plates. The difference of the outer rotor diameter and the bearing diameter is around 2 m. The large difference between the outer rotor diameter and bearing diameter makes a stiff rotor construction necessary. The air gap length is approximately 0.1 % of the outer rotor diameter.

The Coupled Dynamics of the XD-115 Generator

5.3

The system introduced in Chapter 3 is an academic example of a coupled system, in which the system's dynamics differ from the purely structural dynamics. In a similar fashion, the structure of the XD-115 generator is influenced by the magnetic field in the air gap. Naturally, the modes of the XD-115 and the magnetic field are more complex. Still, it is expected that under certain circumstances the modes are affected and their modal parameters change.

In this thesis, only the rotor of the generator is analysed. It was assumed that the stator is stiffer than the rotor and thus the rotor dynamics are more likely to be influenced by the magneto-mechanical coupling. This assumption was made because the stator back iron, which represents a considerable amount of steel, is again supported by another steel structure. Another reason that led to the decision of neglecting the deformation of the stator was the large amount of DoFs that is necessary to model the stator structure, the rotor structure and the magnetic field simultaneously. This amount of DoFs could not be handled by any available hardware. Sadly, there was no time to apply the reduction techniques developed in Chapter 4. Furthermore, the stator structure is more difficult to model, because of the lamination of the stator back iron. Coupling that can occur between modes of the rotor and the stator could not be considered by omitting the stator deformation.

It is assumed that the response to an external loading can be predicted in two steps, which are independent of each other. In a first step, the resonance frequencies, mode shapes and damping values, i.e. the modal parameters, are estimated. This is done while the turbine is standing still. It is, thus, assumed that neither, the gyroscopic forces originating from the rotation of the turbine, nor the armature field will influence the modal parameters. This assumption is valid, because the rotation speed of the turbine is low and the strength of the armature field is lower than the strength of the field created by the permanent magnets. In a second step, the excitation mechanism is analysed and it is identified to what extent these excitation forces excite the dynamics of the rotor. The armature field and the interaction of the permanent magnets with the stator will be identified as the main source of excitation.

Structural modeling

5.3.1

The structural model predicts the static and dynamic deformation of the rotor structure under the magnetic load in the air gap. A 3D model of the structure is necessary to capture all displacements in three dimensions. A 2D model, as often used in modelling electric

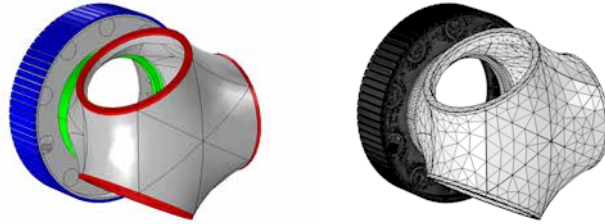


Figure 5.2
Domains of the model of the XD115 (left) and the mesh of the model (right)

machines, cannot account for axial displacement and axial magnetic forces. The geometry of the model was extracted from the Computer Aided Design (CAD) model of the turbine. No measurements or validation of the CAD model were conducted to verify conformity with the actual rotor in the turbine.

Fig. 5.2 depicts the model of the rotor used for the finite element analysis. To account for the blades additional mass and moment of inertia were added to the domains that represent the blades (in Fig. 5.2 coloured in red). These domains were modelled as rigid bodies to suppress modes that involve a deformation of the blade root. For that, the DoFs in those domains, were substituted by a rigid domain with 7 DoFs (3 for the translation, 3 for the rotation direction and 1 for the magnitude of the rotation). A survey of the influence of gyroscopic forces showed that they are negligible during the modal analysis. Due to the low rotation speed of up to 18 rpm, the gyroscopic forces are so low that they have hardly any influence on the resonance frequencies and damping values of the system.

The magnet assembly, i.e. the permanent magnets and the structure to mount them on the rotor, was modelled as a solid block instead of a complex assembly of bolts, holders and magnets. This was necessary to reduce the number of DoFs to a value that could be handled by the hardware available. To account for the lower stiffness of the actual assembly in the real turbine, the Young's modulus of the connecting part between the magnet and the structure was lowered by 99.75% of the original stiffness. Additional mass was added to the block representing the magnet assembly, to match the mass of the magnet assembly in the turbine.

The discretisation is done using tetrahedral volume elements. Geometric nonlinearities were not taken into account. Since the analysis was done in the rotating reference frame that is fixed to the rotor, it was assumed that the displacements were small.

The geometry of the rotor structure includes thin stiffener plates. The discretisation of these plates by volume elements can lead to an over estimation of the stiffness when not enough elements are used. The stiffness of the stiffener plates is crucial to compute accurately the overall stiffness of the generator rotor. To ensure that the stiff-

ness is not overestimated, a convergence study was conducted. Fig. 5.3 shows the normalised frequency of the first bending mode of the rotor over the number of degrees of freedom used in the model. As normalisation frequency, the measured resonance frequency of the first bending mode was used. To avoid large models, the mesh consisting of approximately 1.1 million DoFs was used in the structural model, which is sufficient to estimate the stiffness of the stiffener plates and calculate the frequency accurately up to 2 %.

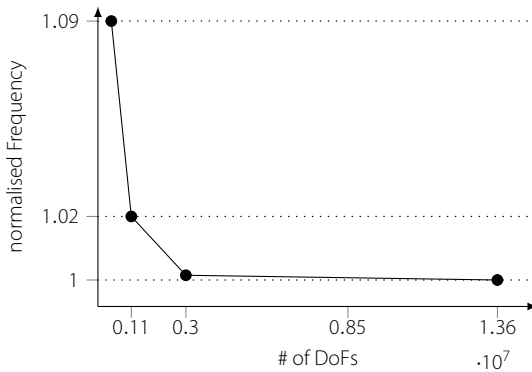


Figure 5.3

Frequency of the first bending mode over the number of degrees of freedoms of the model. For the normalisation the first bending mode of the measured frequencies was used.

The Bearing Model

The bearing, which is located between the hub and the generator, supports the entire rotor structure, including hub, blades and generator rotor. The XD-115 incorporates a single bearing design. It consists of three raceways, two in axial direction and one in radial direction. The rolling bearing elements are cylindrical in both bearings.

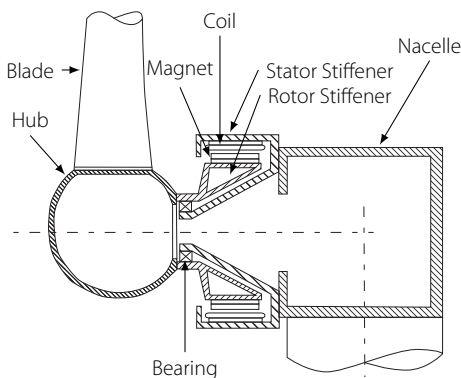


Figure 5.4

Schematic representation of a direct-drive generator. This figure is the same as Fig. 1.4. It is reprinted here for more convenience during reading

Fig. 5.4 shows a single bearing design that is often encountered in direct-drive wind turbines, and which resembles the design of

the XD-115. The outer part of the bearing is, thus, rotating, the inner part is fixed and rests on a cone shaped support structure. The bearing is stiffened by a bearing stiffener to prevent ovalisation of the bearing rings. This bearing stiffener is not included in the FE model as it has little effect on the modes under consideration.

The stiffness of a bearing element was computed analytically using the contact theory by Hertz (see for instance [10] for details). According to this theory, the force of a line contact between two cylinders with parallel rotation axis can be described by

$$F_{elem} = \frac{1}{2} \frac{\pi}{4} l_{elem} E^* \delta \quad (5.1)$$

where F_{elem} is the contact force of one element, l_{elem} the length of the bearing element, δ the indentation and E^* denotes the equivalent Young's modulus which can be calculated by

$$\frac{1}{E^*} = \frac{1 - \nu^2}{E_1} + \frac{1 - \nu^2}{E_2} \quad (5.2)$$

where E_1 and E_2 denote the Young's modulus of the two materials in contact. The half in (5.1) originates from the fact that there are two contacts with the same properties for each element. Taking the derivative of (5.1) with respect to the indentation δ yields a constant contact stiffness of.

$$k_{elem} = \frac{\pi}{8} l_{elem} E^* \quad (5.3)$$

where k_{elem} denotes the stiffness of one bearing element. This formula computes the values of the bearing element's stiffness. The values shown in Tab. 5.3 give an approximate value, because they are rounded to the closes order of magnitude. From these values the total bearing stiffness can be calculated. Assuming that all elements are in contact in the axial bearing, the total axial bearing stiffness can be calculated by multiplying the stiffness per element with the number of elements.

Table 5.3

Approximate stiffness values of bearings and bearing elements (rounded to the closest order of magnitude)

Description	Value
element stiffness axial bearing $\frac{N}{m}$	$1 \cdot 10^{10}$
total bearing stiffness, axial $\frac{N}{m}$	$1 \cdot 10^{12}$
element stiffness radial bearing $\frac{N}{m}$	$1 \cdot 10^{10}$
total bearing stiffness, radial horizontal $\frac{N}{m}$	$1 \cdot 10^{10}$
total bearing stiffness, radial vertical $\frac{N}{m}$	$1 \cdot 10^{11}$

The calculation of the radial stiffness is more complex, because in this case not all bearing elements are in contact. See Fig. 5.5 for the geometry and explanation of the various variables necessary for this derivation. According to [171], the radial displacement at

any position within a bearing can be calculated by

$$\delta(\theta) = \delta_m \cos \theta - \frac{1}{2}c_p \tag{5.4}$$

where c_p denotes the clearance of the bearing, δ_m the maximal dis-

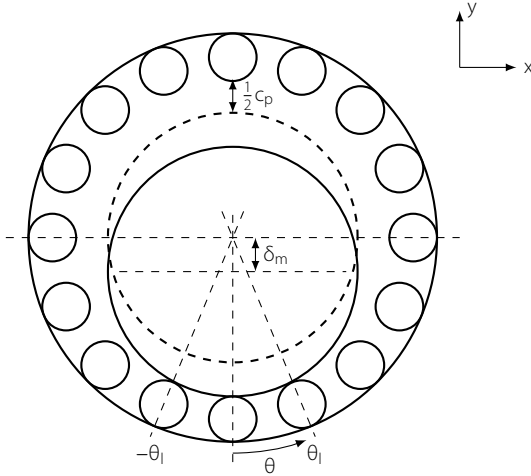


Figure 5.5
Schematic of a radial bearing with rolling elements

placement at $\theta = 0$ and θ the angle around the rotation axis. The total force of the bearing can be calculated by

$$F_{bearing}(\delta_m) = \sum_{\theta_k=-\theta_l}^{\theta_l} F_{element,k}(\delta(\theta_k)) \cos(\theta_k) \tag{5.5}$$

where $-\theta_l$ and θ_l denote the position of the first and last bearing element in contact, respectively. θ_k denotes the angles at which there are bearing elements in contact with both raceways. (5.5) can be used to calculate the bearing force resulting from a deflection of the shaft. Preloading plays a major role for the bearing stiffness in radial direction as the angle θ_l and consequently the number of bearing elements in contact depend on the load. (5.5) can be solved iteratively for δ_m , when a load $F_{bearing} = P$ is given.

After the initial displacement δ_m is calculated, the stiffness of the total bearing can be calculated by deriving the bearing force with respect to the displacement at the computed displacement.

$$k_{bearing} = - \left. \frac{\partial F_{bearing}}{\partial \delta_m} \right|_{F_{bearing}=P} \tag{5.6}$$

To compute the bearing stiffness, some assumptions need to be made about the parameter values, as the exact details of the bearing are unknown. For the radial stiffness that is listed in Tab. 5.3, the gravitational force was used as preloading in vertical direction and

the play in the bearing c_p was assumed to be 10^{-3} m. In horizontal direction, no preloading was assumed. Therefore, the total bearing stiffness in this direction is the same as the element stiffness, as under no load only one element is in contact. A sensitivity analysis of the bearing stiffness revealed, that the influence of the preloading and the radial clearance on the eigenfrequencies is small. The computed eigenvalues for the modes change by a couple of tenths of Hertz.

To include the bearing stiffness in the modal analysis, it needs to be modelled as constant stiffness. To comply with this requirement, the bearing is modelled as a uniform constant stiffness per area that is applied to the raceway of the bearing in the FE model. The value of the stiffness per area is calculated by dividing the total stiffness of the bearing, calculated according to (5.4) - (5.6), by the area of the race ways. For simplicity a uniform radial bearing stiffness about of $1 \cdot 10^{11} \frac{\text{N}}{\text{m}}$ has been used in the finite element model.

In a finite element model the bearing stiffness has to be applied to the nodes. For that, the total bearing stiffness needs to be re-computed to a nodal level. The bearing force of the radial bearing should only be applied in radial direction. Otherwise a stiffness in tangential direction is applied, that will affect the torsional mode of the rotor. The bearing force in radial direction depends on the displacement in radial direction.

$$\vec{f}_{b,rad} = -\frac{k_{tot}}{A_b} \vec{n}_b \cdot \vec{u}(\vec{x}) \quad (5.7)$$

where $\vec{f}_{b,rad}$ denotes the bearing force density in radial direction, \vec{n}_b the normal vector on the raceways of the bearing. k_{tot} the total bearing stiffness and A_b the surface of the raceway.

The discretisation is done by deriving the energy associated with the bearing force and differentiating twice with respect to the structural degrees of freedom.

$$\mathbf{k}_{bearing} = \frac{\partial^2}{\partial \mathbf{q}_u^2} \int_{\Omega} \vec{u} \cdot \vec{f}_{b,rad} \, d\Omega \approx \int_{\Omega} \mathbf{N}_{u,s}^T \mathbf{n}_b \frac{k_{tot}}{A_b} \mathbf{n}_b^T \mathbf{N}_{u,s} \, d\Omega \quad (5.8)$$

where $\mathbf{k}_{bearing}$ denotes the element matrix containing the nodal values of the bearing stiffness per area and \mathbf{n}_b the discrete version of the normal vector on the race way. $\mathbf{N}_{u,s}$ denotes the surface shape functions of the part of the mesh describing the raceway surface of the bearing.

The contact mechanics within the bearing result in a nonlinear stiffness of the bearing. Depending on the loading, the number of bearing elements in contact and, thus, the number of elements that can transmit forces between the two raceways of the bearing changes.

Quite contrary to that, the modes that are calculated by the modal analysis are based on linear force displacement relations for the bearing. The modes can thus not accurately take the contact mechanics of the bearing into account. Accordingly, an error will be made during the modal analysis for modes that are affected by the bearing stiffness.

Two-Way Coupled Dynamics

5.3.2

The academic example in Chapter 3 showed that magnetic forces acting on a structure can lead to additional stiffness for the mechanical system. It was already mentioned that there are four effects that can influence the modal parameters (see Sec. 3.2.2). For an electric machine, these four effects also exist and can influence the dynamic behaviour of the electric machine.

In a two-way coupled system, the magnetic forces depend on the movement of the structure. In general, a positive stiffness is created by the changing magnetic force, if the magnetic force increases with a movement in the opposite direction of the magnetic force. If the magnetic force decreases for the same movement, then a negative stiffness is created.

To capture the influence of the magnetic field on all modes accurately, a 3D structural as well as a 3D magnetic model is needed. A 2D model has the advantage that it consists of much fewer degrees of freedom, but it has the decisive disadvantage that it cannot simulate the reaction of the magnetic field to displacements in axial direction. Since bending modes are expected to be of interest, this simplification cannot be made for the model predicting the coupled dynamics.

3D Magnetic Modelling

The large size of DoFs that is necessary to capture the 3D magnetic field accurately could not be reached. The memory requirements for such a model with $12 \cdot 10^6$ DoFs was too large for any hardware available. It is therefore assumed, that the magnetic field at the singularities around the magnet assemblies are not accurately computed, leading to inaccurate values for the magnetic forces. The force comparison in Sec. 2.5.9 indicates that Maxwell's stress tensor, which is used for the calculations, underestimates the forces.

The geometry of the magnets and the magnet holders is strongly simplified, in the two-way coupled model. As the geometry deviates from reality, so do the flux lines and thus the magnetic field.

Property Name	Value
Permanent Magnet properties	
Young's Modulus [GPA]	200
Density [$\frac{\text{kg}}{\text{m}^3}$]	7500
Poisson's ration [-]	0.29
Conductivity [$\frac{\text{S}}{\text{m}}$]	$0.6 \cdot 10^6$
Relative Permeability [-]	1.05
Remanence Flux Density [T]	1.25
Coercivity [$\frac{\text{A}}{\text{m}}$]	985000
Lamination properties	
Young's Modulus [GPA]	200
Density [$\frac{\text{kg}}{\text{m}^3}$]	7870
Poisson's ration [-]	0.29
Conductivity in radial/circumferential direction [$\frac{\text{S}}{\text{m}}$]	$8 \cdot 10^6$
Conductivity in axial direction [$\frac{\text{S}}{\text{m}}$]	0
H-B Curve	$ \vec{H} = 150 \vec{B} + 10 \vec{B} ^2$
Copper properties	
Conductivity [$\frac{\text{S}}{\text{m}}$]	$6 \cdot 10^7$
Relative Permeability [-]	1
Air properties	
Conductivity [$\frac{\text{S}}{\text{m}}$]	1
Relative Permeability	1
Structural Steel properties	
Young's Modulus [GPA]	200
Density [$\frac{\text{kg}}{\text{m}^3}$]	7850
Poisson's ration [-]	0.3
Conductivity [$\frac{\text{S}}{\text{m}}$]	$8 \cdot 10^6$
Relative Permeability	100
Magnet holder properties	
Young's Modulus [GPA]	0.5
Density [$\frac{\text{kg}}{\text{m}^3}$]	7850
Poisson's ration [-]	0.29
Conductivity in radial/circumferential direction [$\frac{\text{S}}{\text{m}}$]	$8 \cdot 10^6$
Conductivity in axial direction [$\frac{\text{S}}{\text{m}}$]	1
H-B Curve	$ \vec{H} = 150 \vec{B} + 10 \vec{B} ^2$

Table 5.4

Magnetic and structural material properties used for modelling the XD-115. For IP reasons, the values have been slightly changed from the actual values in the turbine

The geometry used for the model reduces the leakage flux compared to the actual design in the turbine. The magnetic flux density in the air gap, and thus also the effect of the magnetic field on the structural dynamics, are overestimated.

The analysis is done without any current in the coils. It is, thus, a closed system according to the derivation in Sec. 2.5. The force calculation in the model has been done according to (2.102). Although this technique is less accurate than the method using nodal values, it has the advantage that it is integrated in the software package used. The material constants and properties used for the model are listed in Tab. 5.4.

Internal Dynamics

Tab. 5.5 lists the modes of the rotor structure with and without magneto-mechanical coupling. Tab. 5.5 clearly indicates that the change of the resonance frequencies due to coupling is minimal. Hence, it can be neglected for predicting the dynamic response of the generator of the XD-115. Also the damping increase caused by the coupling is negligible, because the structural damping of steel is an order of magnitude higher. The shape of the modes are not significantly changed by the magneto-mechanical coupling.

One-Way Coupled Model of The XD-115 Generator

5.3.3

The two-way coupled analysis in Sec. 5.3.2 showed that the change of the modal parameters due to the magneto-mechanical coupling is negligible for the rotor of the XD-115. It is, therefore, sufficient to conduct a one-way coupled analysis, in which the effects of the magnetic field on the modal parameters are neglected. The model still contains a coupling, as the mechanical system is excited by magnetic forces. However, the length of the air gap, as well as any other displacements or displacement velocities, do not influence the magnetic field. The interaction between the elastic field and the magnetic field occurs only in the direction from the magnetic domain to the mechanical domain.

For this analysis, a 2D magnetic model is sufficient as it is only used to compute the excitation forces that are generated by the interaction of the armature field with the rotor field. These forces are assumed to have a radial and a tangential component only and can, thus, be computed by a 2D model. An axial component, which would be created by an axial misalignment of the rotor and stator, is assumed to be zero.

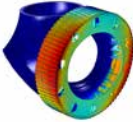
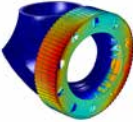
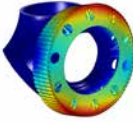
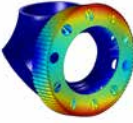
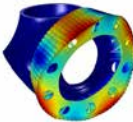
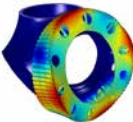
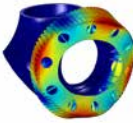
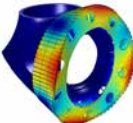
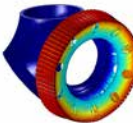
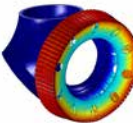
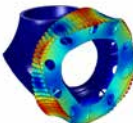
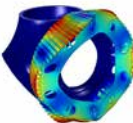
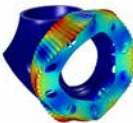
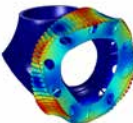
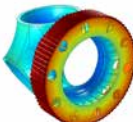
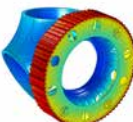
Mode description	Results without coupling		Results with coupling	
	normalised Frequency	Mode shape	normalised Frequency	Mode shape
tilting mode	0.81		$0.00045i + 0.81$	
	0.82		$0.0005i + 0.82$	
1 st bending modes	1.02		$0.003i + 1.02$	
	1.02		$0.003i + 1.02$	
axial mode mode	1.45		$0.00005i + 1.45$	
2 nd bending mode	2.6		$0.0013i + 2.6$	
	2.6		$0.0013i + 2.6$	
torsional mode	2.66		$0.005i + 2.67$	

Table 5.5 Mode shapes of the two-way coupled problem with and without magneto-mechanical coupling. The colour represents the magnitude of the displacement

2D Magnetic Model

This model consists of an eighth of the total circumference of the rotor. An eight is sufficient to depict the whole magnetic field as the magnetic-active parts of the generator are cyclic-symmetric. The stator iron material and the casing of the magnets were modelled taking saturation into account.

The 2D model consist of approximately 260000 DoFs, which is only a fraction of the 3D magnetic model used to determine the modal parameters. The material properties are the same as the ones used for the 3D model, listed in Tab. 5.4. To determine the excitation, a parameter sweep of a stationary solver over various rotor positions has been conducted. This approach neglects dynamic effects of the magnetic field as well as the dynamics of the coil circuits. These are considered small in the generator due to segmentation and lamination. Global forces have been calculated using the method of global virtual work as introduced in Sec. 2.5.8. When local forces were needed Maxwell's stress tensor was used.

Analysing the Excitations

5.3.4

Within an electric machine, there are several possible excitation mechanisms that are important to analyse, when looking at the electric machine as a dynamic system. Depending on the type of machine and its operation conditions, some of the excitation mechanisms are less important or can even be ignored completely.

Rotational Excitation: The turbine is excited during operation by the rotation of the rotor. Eccentricity of the rotor, which is unavoidable during production, results in a rotating force acting on the stator. The excitation frequency of this unbalance force is either the rotation frequency itself or a multiple of the cyclic symmetry of the rotor multiplied with the rotation frequency. The later can occur when the mass distribution of the rotor is not uniform due to the cyclic symmetry. In wind turbines, there are also the $3p$ and $9p$ frequencies which results from the aerodynamics of the blades. These frequencies are always multitudes of 3, because there are 3 blades attached to the hub. However, these frequencies play a minor role for the dynamics of direct-drive wind turbine generators.

Electro-Magnetic Excitation: This excitation source is the main cause for vibrations for the generator rotor. It is created by the interaction between the electro-magnetic active parts of the rotor with the electro-magnetic active parts on the stator. The most pronounced effect is the interaction between the

magnetic field created by the permanent magnets on the rotor and the slots of the stator, called cogging torque. Furthermore, space harmonics of the armature field are an important source of excitation.

The rotation frequency and the 3p and 9p frequencies are too low to excite the structural modes of the generator and the rotor's mass distribution is too homogeneous to cause a significant unbalance force. According to their importance the excitation resulting directly from the rotation of the shaft will be neglected and not further analysed.

Cogging Torque

To understand the underlying mechanism of cogging torque, the contribution of one magnets to the total torque of the machine is analysed. [155–157] conduct an extensive analysis of the influences of various parameters on torque cogging in slow rotating permanent magnet machines. [156] is dedicated to the combination of pole and slot numbers.

The torque contribution of one magnet in no-load condition is determined by the interaction of the magnet's field with the stator slotting. The energy of the field created by one magnet is minimal, when the volume of the air gap above that magnet is minimal. This is the preferred configuration for that magnet and the torque it creates will pull it into this configuration.

For one magnet, this preferred configuration occurs as often per revolution as there are stator teeth. In other words, a configuration minimising the volume of the air gap above a magnet, can be reached for each stator tooth. During rotation, one magnet creates thus a harmonic torque content at n_{slots} the rotation frequency, where n_{slots} denotes the number of slots¹.

The harmonic content of the total torque of the generator can be determined by analysing how often, during one revolution, the same relative position of stator slots and magnets is reached. To clarify this, consider the two configurations in Fig. 5.6. The top of Fig. 5.6 shows a configuration in which magnet 0 is aligned with stator tooth 0. At the bottom of Fig. 5.6, the same slot pole combination is shown rotated, so that magnet 1 is aligned with stator tooth 5.

Because neither the distances between stator teeth nor the distance between magnets have changed, the two subfigures of Fig. 5.6 show

¹Assuming that the spatial force distribution over the magnet varies harmonically

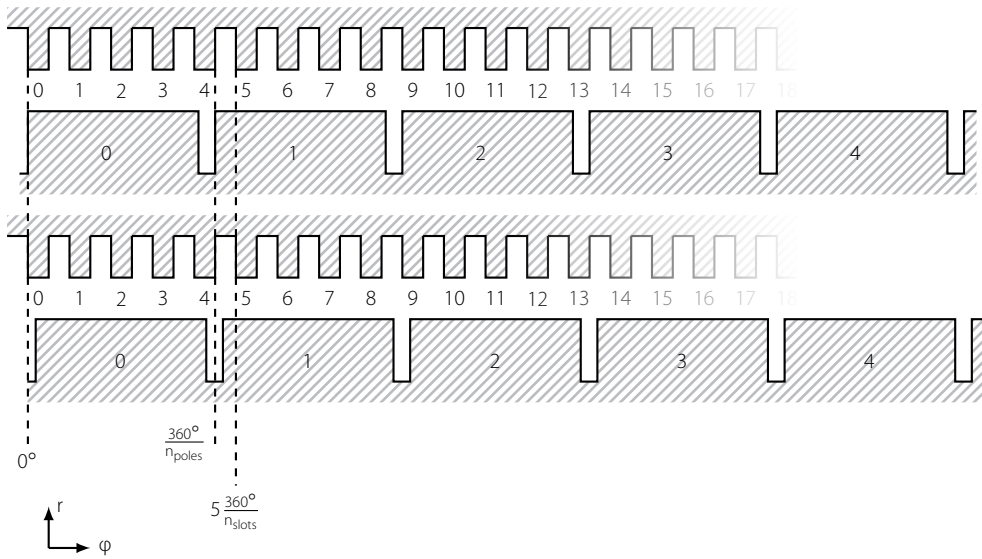


Figure 5.6
Magnets passing the slots of the stator. The same configuration is reached when a magnet and stator tooth are aligned again.

the same configuration rotated by

$$5 \frac{360^\circ}{n_{slots}} - \frac{360^\circ}{n_{poles}} \tag{5.9}$$

where n_{slots} denotes the number of slots and n_{poles} the number of poles. In general, the next configuration that is identical with the original configuration is reached after a rotation that is equal to

$$\frac{360^\circ}{n_{lcm}} \tag{5.10}$$

where n_{lcm} denotes the least common multiple of the number of slots and the number of poles. This configuration will thus reoccur n_{lcm} times during one revolution. This reoccurring configuration between rotor magnets and stator teeth creates a periodicity when the rotor is rotating that depends linearly on the rotation frequency. Because the torque depends on the magnetic flux density in the air gap, the above mechanism creates a periodic component of the total torque.

It can be shown that the same configuration reoccurs after a rotation of $\frac{360^\circ}{n_{lcm}}$ by considering a cyclic symmetric section of the generator. That sections contains an integer number of poles and slots so that:

$$k \frac{360^\circ}{n_{poles}} = m \frac{360^\circ}{n_{slots}} = \frac{360^\circ}{n_{sym}} \tag{5.11}$$

where n_{sym} denotes the number of cyclic-symmetric parts of the electro-magnetic active parts of the generator. k denotes the num-

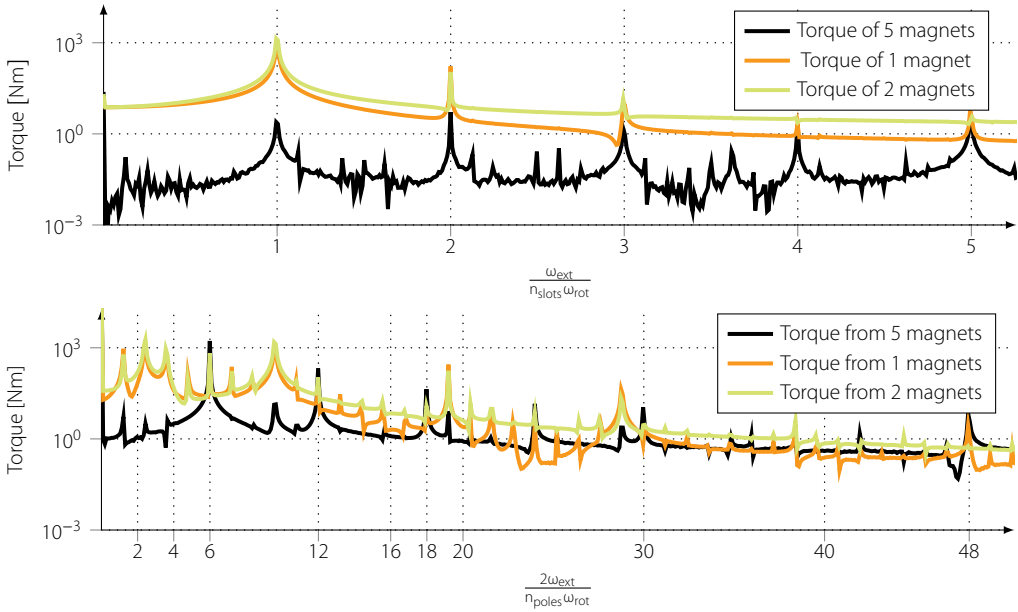


Figure 5.7

Spatial spectral analysis of the torque contribution of 1, 2 and 5 neighbouring magnets for the no-load case (top) and the load case (bottom)

ber of poles per symmetric section and m the number of slots. From (5.11) it can be derived that

$$mn_{poles} = kn_{slots} = n_{lcm} \quad (5.12)$$

Bringing all fractions in (5.11) on the smallest denominator yields thus

$$km \frac{360^\circ}{mn_{poles}} = mk \frac{360^\circ}{kn_{slots}} \quad (5.13)$$

$\frac{360^\circ}{n_{lcm}}$ denotes thus the largest angle which contains $\frac{360^\circ}{kn_{slots}}$ as well as $\frac{360^\circ}{mn_{poles}}$ in its multiples. Taking the difference between two arbitrary multiples of $\frac{360^\circ}{n_{slots}}$ and $\frac{360^\circ}{n_{poles}}$, yields again a multiple of $\frac{360^\circ}{n_{lcm}}$.

$$l \frac{360^\circ}{n_{poles}} - n \frac{360^\circ}{n_{slots}} = s \frac{360^\circ}{n_{lcm}} \quad (5.14)$$

with $l, n \in \mathbb{N}$ and $s \in \mathbb{Z}$
and $n < m, l < k$

The smallest possible rotation angle between two configurations that are equal is reached for $s = 1$.

The top of Fig. 5.7 shows the spatial spectral analysis of the torque of one, two and five neighbouring magnets in no-load condition. These were computed using Maxwell's stress tensor on the outer surface of the magnets. For one and two magnets n_{slots} times the

rotation speeds, and multiples of it, is the dominant excitation frequency. For five magnets, the torque cogging at n_{slots} times the rotation speed decrease, while it increases for the multiples of this frequency. This is caused by a small phase shift of the torque harmonics for neighbouring magnets. This phase shift diminishes the amplitude of the torque cogging, while it increases the number of frequencies as can be seen in Fig. 5.7

The excitation frequencies created by torque cogging are exactly in the frequency range in which some resonance frequencies of the rotor structure are located. It is, thus, possible that the resonance frequencies are excited by them.

Influence of Space- and Time Harmonics

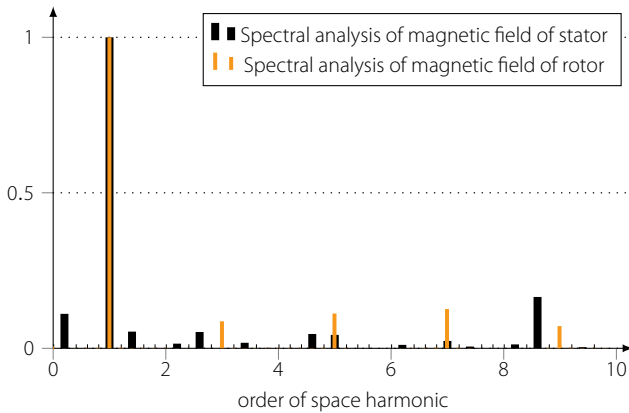


Figure 5.8

Spatial spectral analysis of the MMF for the stator at $i_a = 1$, $i_b = -0.5$ and $i_c = -0.5$ and the rotor

Time harmonics are the result of the switching in the frequency converter of the generator. Ideally, the current waveform is sinusoidal in time. The switching causes the current to deviate from this ideal sinusoidal waveform. The resulting frequencies depend on the switching frequency of the frequency converter. For direct-drive generators the switching frequency is so high compared to the resonance of the structure that time harmonics play no role. The resulting frequencies are too high to excite any of the global modes. For smaller machines these frequencies can be very important (see [112] for an example).

Space harmonics are the harmonics in the magnetic flux density in the air gap of an electric machine that result from the spatial distribution of the windings. The windings are never distributed ideally sinusoidal, because they are located in slots. These slots allow only discrete distributions of the coils. Fig. 5.8 shows the spectral analysis of the MMF of the stator and the rotor in the XD-115. Besides the fundamental, there are several higher and lower harmonics.

Comparing the torque spectrum for 5 magnets in Fig. 5.7 shows that under load different orders are dominant. The dominant orders for the load are the ones created by the space harmonics. In order to create a torque, the same harmonic must be present in the rotor and the stator. The rotor MMF follows a square wave profile and, thus, only the odd higher harmonics are present in this spectral analysis. Due to the winding of the stator, the spectral analysis of the stator MMF shows harmonic content higher and lower than the fundamental. But only the harmonic at 5, 7, 11, 13, ... create a torque, because only those are also present in the rotor.

When the 5th and 7th space harmonic of the stator field interact with the rotating field of the rotor, they both create an oscillating torque at $\omega_{ext} = 6\omega_{rot} \frac{n_{poles}}{2}$. The same happens with the 11th and 13th harmonic, which create a dynamic excitation force at $\omega_{ext} = 12\omega_{rot} \frac{n_{poles}}{2}$. This torque harmonic can be seen in Fig. 5.7. It is the dominant torque ripple harmonic in operation of the turbine. See Sec. C for a derivation of this behaviour using an analytical model of an electric machine.

The additional peaks in the plots for one and two magnets in Fig. 5.7 are probably created by the sub harmonics that are present due to the winding scheme of the XD-115 generator. These subharmonics create a torque contribution when they interact with the rotor field, when only one or two magnets are analysed. For five magnets they cancel out.

Spatial Distribution of the Magnetic Forces

The top part of Fig. 5.9 shows the torque distribution over the surface of the rotor. The bottom part of Fig. 5.9 shows the radial force acting on the rotor. The torque is strongest at the edges of the magnets enclosure, while the radial forces are strongest under the stator teeth.

When the turbine rotates, the stator teeth pass the magnets and the maximum of the normal forces with them. This can be seen in Fig. 5.9 by the moving force intensity on the surface of the magnets. The magnets experience a changing torque density over time due to the slotting. For both plots the armature field rotates with the rotor as it would do in normal operation. In the first couple of seconds, the speed up of the rotor can be seen

Analysing Fig. 5.9, two assumptions can be made. Firstly, the force on the outer rotor surface next to the magnets can be neglected. All magnetic forces concentrate on the magnets' surfaces. Secondly, it is convenient to use a uniform force distribution per magnet. The magnitude of this uniform force distribution depends on the pos-

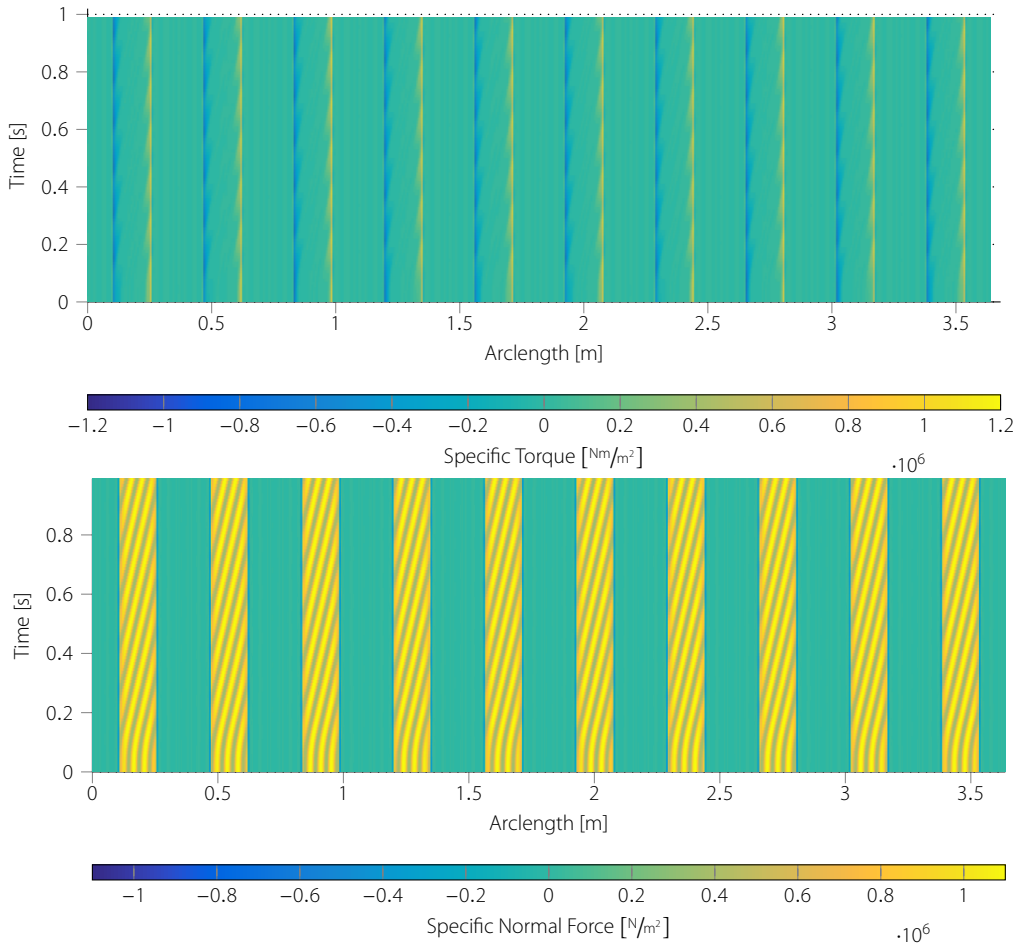


Figure 5.9
The computed torque distribution (top) and specific radial force (bottom) on the outer surface of the rotor.

ition of the rotor to the stator. Due to symmetry, every fifth magnet shows the same configuration and, thus, the same normal force and torque. Fig. 5.10 shows the development of the radial force and torque for two neighbouring magnets. The delay between the normal forces and torque of the two magnets is visible by the horizontal shift of the plots.

Approximating Magnetic forces

5.3.5

Making the simplifying assumptions about the magnetic force distribution above, the magnetic force can be described by a simple analytical expression. This is necessary, as the structural model has much less DoFs than the 2D magnetic model on the magnets' surfaces. The details of the force distribution cannot be described ac-

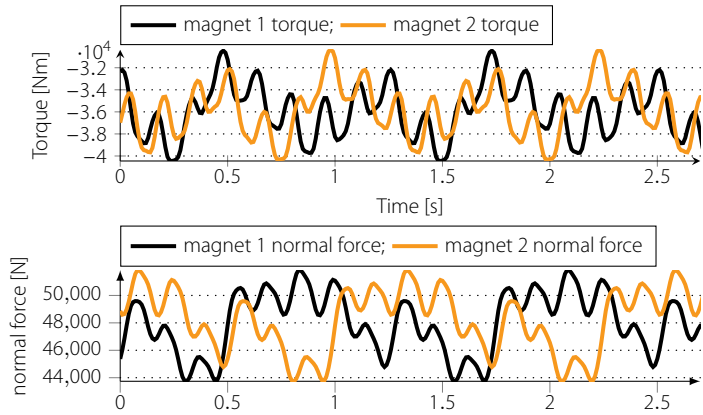


Figure 5.10
Total normal force and torque per
magnet under load

curately by the coarse mesh. Furthermore, the shape of the magnets is much simpler in the structural model. This was done to reduce the number of DoFs of the structural model and keep them within a limit that can still be handled.

For the analytic description, it is convenient to separate the force term in a static part and a dynamic part.

Static Forces

The static part describes the average force in time in radial and tangential direction. It results from the applied torque of the generator and the attracting forces between stator and rotor. They can be described by multiplying three quantities.

$f_{pos}(\theta)$ is a scalar quantity that identifies where the magnets are located over the circumference of the rotor. Its output values are between 0 and 1. By multiplying this quantity with a force vector, the force vector will only be applied at the locations where f_{pos} is not zero.

\vec{f}_{rel} contains the information about the relation between radial and tangential component. In electric machines, the attracting forces between stator and rotor are higher than the tangential forces that create the torque. This is expressed by this vector, which multiplies the radial component with the factor 3.58. This factor was extracted from Fig. 5.9 by dividing the average torque per magnet by the radius of the rotor and comparing it with the average radial force per magnet.

\hat{f}_{mag} , the last component, determines the magnitude of the forces. To ensure that the total torque created by the static forces is equi-

valent to the nominal torque value T_{nom}

$$\iint_{\Omega_{mag}} r_{r,out} \vec{e}_\theta \cdot \vec{f}_{mag,stat} d\Omega_{mag} = T_{nom} \quad (5.15)$$

needs to be solved for the force vector amplitude \hat{f}_{mag} . In (5.15), $r_{r,out}$ denotes the outer radius of the rotor, Ω_{mag} denotes the surface of the cylinder barrel, where the magnetic force is applied, and \vec{e}_θ a vector pointing in tangential direction.

All these considerations lead to the following expression for the static magnetic force density.

$$\vec{f}_{mag,stat}(\vec{x}_{mag}) = \underbrace{\hat{f}_{mag}}_{\vec{f}_{rel}} \left[\begin{array}{c} 3.58 \\ 1 \\ 0 \end{array} \right] \underbrace{\frac{1}{2}(1 - \sin(n_{poles}\theta))}_{f_{pos}} \quad (5.16)$$

where θ denotes the circumferential coordinate in cylindrical coordinates. The radial component of the static force distribution is depicted on the right of Fig. 5.11.

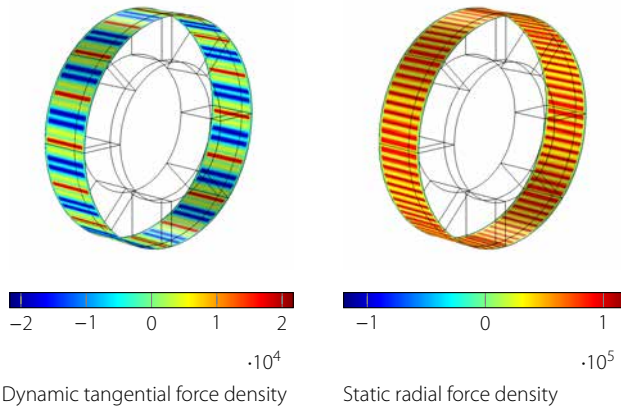


Figure 5.11 Force distribution of magnetic forces

Dynamic Forces

The dynamic part of the force describe the deviation of the tangential and radial forces from the average values in Fig. 5.9. As shown in that figure, the dynamic content of the total magnetic forces that the generator creates is much smaller than the static content. The dynamic force acts at the same locations as the static force, the surface of the magnets. Therefore, the quantity indicating the position of the magnets f_{pos} can be reused.

The vector $\vec{f}_{mag,dyn}$ is described in the frequency domain as complex quantities. The magnitude of the complex vector denotes the magnitude of the force, where as the phase angle gives the time shift between certain components of the excitation force vector. The frequency of the excitation forces is not specified but can vary. This is beneficial as the excitation frequencies in the generator vary a lot.

Fig. 5.9 shows that the amplitude of the dynamic part of the torque is about a fifth of the static value. The vector $\vec{f}_{rel,dyn}$ contains the relation between the tangential static force and the dynamic force amplitudes.

The last term in (5.17) describes the phase lag of some parts of the dynamic force. As discussed in `secretway:excitation`, there is a small phase lag of about $\frac{360^\circ}{2n_{sym}}$ between neighbouring magnets. All these consideration can be condensed to the following equation for the dynamic forces

$$\vec{f}_{mag,dyn}(\vec{x}_{mag}) = \hat{f}_{mag} \underbrace{\begin{bmatrix} 0.5 \\ 0.2 \\ 0 \end{bmatrix}}_{\vec{f}_{rel,dyn}} f_{pos} \underbrace{\begin{bmatrix} e^{i\theta_{shift}} \\ e^{i(\theta_{shift} + \frac{\pi}{2})} \\ 0 \end{bmatrix}}_{\vec{f}_{shift}} \quad (5.17)$$

$$\text{with } \theta_{shift} = 2n_{sym}\theta$$

In (5.17), θ_{shift} denotes the phase shift of the magnetic force that depends on the location around the rotor. The $\frac{\pi}{2}$ in \vec{f}_{shift} originates from the delay between the normal force and the torque that can be seen in Fig. 5.10, which is about a fourth of the period. \vec{x}_{mag} is the subset of \vec{x} that includes all points, where the magnetic force \vec{f}_{mag} is applied. The radial dynamic force distribution is depicted on the left of Fig. 5.11.

5.3.6

Simulation Results

After the structural system was determined in Sec. 5.3.1, the response of the system to the loads defined in Sec. 5.3.5 can be computed. A run up of the turbine in time domain cannot be simulated due to the high number of DoFs in the system. Therefore, the response is estimated by a frequency sweep and by computing the modal participation factors to the system.

The response to the static magnetic forces, defined in (5.16), can be computed. For that the displacement at the blade roots was set to zero, to simulate the wind induced torque that is applied there. This way the displacements of the generator rotor can be computed. The maximal displacement in tangential direction is $1.4 \cdot 10^{-7} \text{ m}$,

in radial direction $6.8 \cdot 10^{-5} \text{ m}$ and $2.8 \cdot 10^{-6} \text{ m}$ in axial direction, at the outer surface of the generator rotor. The maximal displacement of any node is $7.9 \cdot 10^{-5} \text{ m}$.

Frequency Sweep

To identify the magnitude of the amplitude and the system's behaviour, the magnetic forces identified in (5.17) were applied to the structural model. A frequency sweep was simulated for which the harmonic magnetic forces were applied to the structure at frequency steps of 0.015 between 0.59 and 2.94. This way any resonance frequencies are identified by increased amplitudes.

For stability reasons, an isotropic loss factor of 1 % was added, so that resonances do not lead to amplitudes that are too high. This damping factor moves the resonance frequencies slightly compared to the ones listed in Fig. 5.5

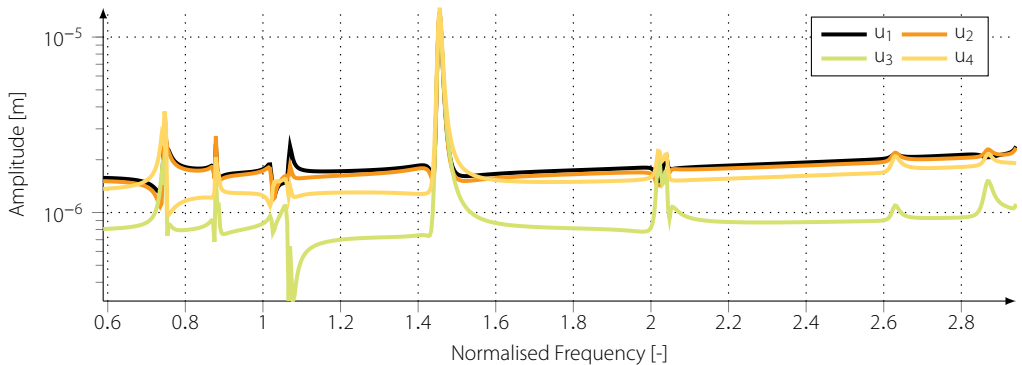


Figure 5.12

The amplitudes of four locations on the outer surface of the rotor during the frequency sweep

Fig. 5.12 shows the amplitudes of four locations on the outer surface of the rotor. Looking at the simulated deflection shapes, identifies the peak at $\omega/\omega_{ref} = 0.89$ and $\omega/\omega_{ref} = 0.74$ as a tilting motion. The shape of the peak at $\omega/\omega_{ref} = 1.43$ corresponds to the axial mode at $\omega/\omega_{ref} = 1.45$. The shape of the peaks at $\omega/\omega_{ref} = 2.71$, $\omega/\omega_{ref} = 2.01$ and at $\omega/\omega_{ref} = 2.9$ could not be identified and, thus, could not be matched with any of the modes in Tab. 5.5.

Integrating the amplitudes of all simulated frequencies gives an indication of the magnitude of the total amplitude of the system.

$$u_{tot} = \int_{0.59}^{2.94} \hat{u}(\omega) d\omega \quad (5.18)$$

For the four plots in Fig. 5.12, this yields the total amplitude of

$u_{tot,1} = 0.29$ mm, $u_{tot,2} = 0.3$ mm, $u_{tot,3} = 0.16$ mm and $u_{tot,4} = 0.26$ mm

Participation Factors

Analysing the participation factors of the modes is another way to examine the response of the system to external periodic excitations. Participation factors for magnetic systems were already introduced in (4.13). For structural modes, they can be computed by

$$\eta_r = \frac{1}{\omega_{ext}^2 - \omega_r^2 + 2\zeta_r\omega_{ext}\omega_r} \int_{\Omega} \bar{\varphi}_r \cdot \bar{\mathbf{f}}_{mag} \, d\Omega \quad (5.19)$$

where $\bar{\varphi}_r$ denotes the mass normalised shape of r^{th} mode, Ω its excitation frequency, ω_r is the resonance frequency, η_r the participation factor, ζ_r the damping coefficient and $\bar{\mathbf{f}}_{mag}$ the dynamic excitation force (5.17). The discrete form of (5.19) reads as

$$\eta_r = \frac{\boldsymbol{\varphi}_r \cdot \mathbf{f}_{mag}}{\omega_{ext}^2 - \omega_r^2 + 2\zeta_r\omega_{ext}\omega_r} \quad (5.20)$$

where the magnetic force and the the structural mode are substituted by their discrete counterpart, $\boldsymbol{\varphi}_r$ and \mathbf{f}_{mag} , respectively

The participation factors, as described in (5.20), are computed for a certain excitation frequency. In the XD-115, however, the excitation frequencies cover such a large frequency range that it is difficult to determine which excitation frequency to use for the computation of (5.20). Fortunately, the force distribution stays the same for all excitation frequencies. Using only the nominator of (5.20), it is possible to make an analysis to what extend a certain mode can be excited by the dynamic force distributions defined in (5.17), when the excitation and resonance frequencies coincide. In this analysis, the distance between the resonance and excitation frequency is not accounted for.

Tab. 5.6 lists the participation factors for the mode shapes identified by the finite element method with respect to the magnetic force distribution. The fifth column, headed by $(\max(\boldsymbol{\varphi}_r)(\boldsymbol{\varphi}_r \cdot \mathbf{f}_{mag}))$, lists the maximal amplitude of each mode under the computed excitation.

The participation factors reflect the frequency sweep computation in Sec. 5.12. The largest participation sees the axial mode. The other modes are less pronounced. Especially, the 1st mode is hardly excited.

Experimental Validation

5.4

In Sec. 5.3, the dynamic behaviour of the XD-115 generator was predicted. Although the techniques used were already validated in Chapter 3, it is necessary to verify that the parameters chosen to simulate the XD-115 generator are correct. This is done by in-situ vibration measurements of the rotor structure.

In this section only the measurements used to validate the models in Sec. 5.3 are presented. Further measurements were conducted that are not used for this purpose. They are presented in Appendix B.

The main problem during the measurements is a sufficient excitation of the structure. The rotor structure of the XD-115 weights about 110 tons. That includes the hub, the blades and the generator rotor. The generator rotor alone, the structure of interest for this research, weighs about 20 tons. It is necessary to excite this structure to an extent that the accelerometers can pick up the vibration. To accomplish that, the vibration amplitudes need to reach a certain level. Ideally, only the structure of interest, i.e. the rotor stiffer, is excited while the rest of the turbine does not vibrate. However, it is not possible to excite the rotor of the turbine without exciting the rest of the structure too, making the identification of the resonance frequencies and modal damping parameters of only the rotor structure difficult.

For 'normal' vibration measurements either a shaker or an impact hammer is used to excite the structure. Although, these two tools come in all variations and sizes, they are difficult to employ in the turbine due to the limited space available within the nacelle and the accessibility of the rotor structure.

Besides a manual excitation, the structure can be excited by the forces and movements that arise during the operation of the turbine. This technique is called operational modal analysis (OMA). The structure of the rotating generator is excited by unbalanced forces and the higher harmonics created by the magnetic field in the air gap. By comparing the identified resonance frequencies in

Normalised freq.	description	$\varphi_r \cdot f_{mag}$	$\max(\varphi_r)(\varphi_r \cdot f_{mag})$
1.02	1 st bending	0.0644 - i 0.0636	$6.3 \cdot 10^{-7} - i 6.3 \cdot 10^{-7}$ m
1.02	1 st bending	0.0036 + i 0.0132	$5.1 \cdot 10^{-8} + i 1.9 \cdot 10^{-7}$ m
1.45	axial	0.5987 + i 1.9053	$1.7 \cdot 10^{-6} + i 5.4 \cdot 10^{-6}$ m
2.6	2 nd bending	0.1068 - i 0.1402	$3.3 \cdot 10^{-6} - i 4.3 \cdot 10^{-6}$ m
2.6	2 nd bending	-0.1152 + i 0.0734	$-6.5 \cdot 10^{-6} + i 4.1 \cdot 10^{-6}$ m
2.66	torsional	-0.3649 + i 0.2304	$-0.0013 + i 0.0008$ m

Table 5.6
The participation factors for various modes identified by the finite element method.

Sec. 5.3.2 and the excitation frequencies in Sec. 5.3.4, it becomes apparent that the resonance frequencies of the structure are in the same frequency range as the frequencies created by space harmonics and cogging torque in the generator. Other excitation frequencies, coming for instance from the rotation directly or from supply harmonics, are either too high or too low to be of importance for the XD-115.

In this section, the measurement set-up is presented first. Afterwards, the results of the various excitation methods are presented. Finally in Sec. 5.4.5, the measurements results are compared with each other and to the simulation results.

5.4.1 The Experimental Set-Up

The left side of Fig. 5.13 shows the set-up of the measurement during rotation.

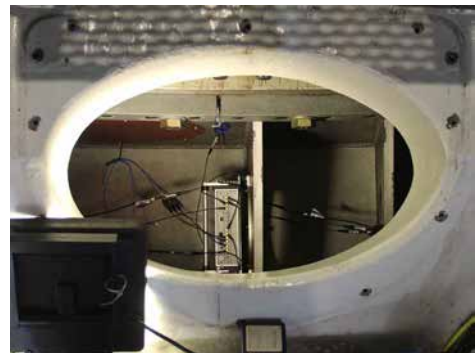
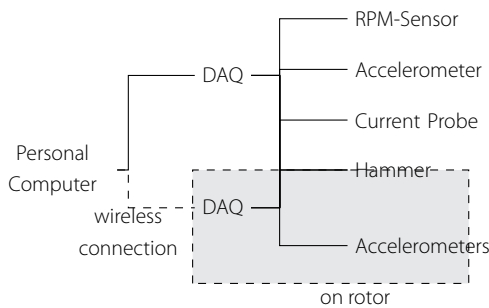


Figure 5.13

Measurement Set Up for the XD-115. The grey box indicates equipment that is located on the rotor

Measuring during Rotation

Measuring on the rotor and stator simultaneously during rotation requires two data acquisition systems (DAQs) that are synchronised. One is installed in the rotor, depicted on the right side of Fig. 5.13, the other one is connected to the sensors in the rest of the nacelle. A hammer is used for synchronising the two systems. Its signal is split and fed to both systems. Before the start of the turbine, it is disconnected from the rotor DAQ. After the measurements are completed, a cross correlation analyse between the two hammer channels at either DAQ will yield the time difference between the two signals. This method has one significant disadvantage. Any delay introduced in either of the DAQs during the measurement cannot be identified. Thus, at the beginning of the measurements

the stator and rotor measurements are synchronised, but the longer a measurement is the more likely the two DAQs desynchronise.

The measurement set-up in Fig. 5.13 shows various sensors on the stator. After investigating the rotor and stator acceleration data, no correlation between the stator and rotor side for the structural vibrations could be identified. The measurement data of the stator data was thus neglected for the modal analysis and only the RPM-sensor is used on the stator side. However, this sensor is crucial because all order tracking methods require accurate values of the instantaneous rotation speed at all times of the measurements. Further measurements using the other sensors were conducted but did not lead to any research results. These measurements concerned the monitoring of the bearing using the current of the generator. The measurements are presented in the Appendix B.

Measuring at Stand Still

For measurements at stand still, the rpm sensor is not necessary. Therefore, the stator side can be neglected completely and only the DAQ and the sensors on the rotor are used. The sensor placement is the same as for the measurement during rotation. For the impact measurements, the excitation points are indicated in blue on the right hand side in Fig. 5.14.

Sensor Positions

In total, 11 channels were used for acceleration measurements on the rotor. Fig. 5.14 shows the positions of the accelerometers in the rotor of the XD-115. The position of the sensors were chosen in such a way that bending modes can be distinguished from tilting modes. There are not enough sensors to distinguish the second from the first bending mode and only one channel measures accelerations in tangential direction. Channels 1 and 3 as well as channels 4 and 6 are purposely located at different distances from the rotation centre of the rotor. This allows to distinguish bending modes from rigid motion of the rotor. On position C, this is not necessary as there is an additional measurement channel in z-direction. In this case, one of the channels 11 and 10 is, indeed, redundant.

Measurement Techniques

5.4.2

To perform the modal analysis, four different methods of excitation were used: hammer impact, operational forces, wind forces during idling and yawing forces. Various analyse algorithms were

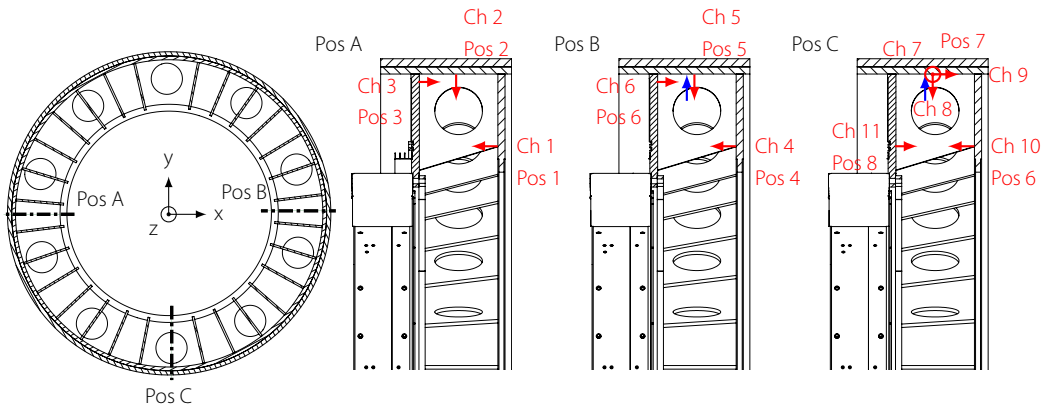


Figure 5.14

Accelerometer positions in rotor stiffener. Sensors directions indicated in red. Impact directions indicated in blue.

used for the operational measurements which are listed here as separate methods. This subsection lists the various measurement techniques and analysis methods employed. Tab. 5.7 lists all the various excitation methods and its characteristics.

The measurement methods can be classified in methods for which the excitation force is measured and methods for which only accelerations are measured. In this thesis, the impact measurement is the only method for which the excitation is measured. All other methods are output-only measurement techniques.

For output-only measurements techniques, the vibrations of the turbine, induced by wind or by the operation of the turbine, are used to conduct a modal analysis. Because the excitation forces are not measured, some assumptions about the forces occurring in the system are made. This makes these techniques convenient to use for large structures, as for these excitation proves difficult. However, the assumptions made over the excitation forces are often not accurate and can, thus, lead to questionable results of the modal parameter identification, if the violation of the assumptions is too extensive.

Impact Measurements

The excitation during hammer testing is accomplished by applying an impulse force to the structure with a hammer, measuring the hammer force simultaneously. Ideally, a Dirac impulse is created that way, of which the Fourier transform is a constant line, exciting thus all frequencies. Practically, the quality of the Dirac impulse depends on the elasticity of the hammer tip, the elasticity of the structure that is tested and the skill of the test engineer. These influences limit the excitation to the lower frequencies.

Excitation technique	Advantages	Disadvantages
Hammer Testing	<ul style="list-style-type: none"> No excitation harmonics 	<ul style="list-style-type: none"> Hardly enough energy input to excite whole structure Pole necessary because impact point not accessible
Yawing testing (Free decay)	<ul style="list-style-type: none"> Huge amount of energy brought into the system 	<ul style="list-style-type: none"> Only lower frequencies excited Short system response, making damping estimate difficult
Operational Modal Analysis (OMA)	<ul style="list-style-type: none"> No excitation necessary 	<ul style="list-style-type: none"> Assumption not satisfied Long measurements necessary Excitation harmonics deteriorate system identification quality
Vold-kalman filtered Operational Modal Analysis	<ul style="list-style-type: none"> Assumption not satisfied Better identification of modes than normal OMA No manual excitation necessary 	<ul style="list-style-type: none"> Data preparation necessary Might filter system response from data Long measurements necessary
Order based modal analysis (OBMA)	<ul style="list-style-type: none"> Uses harmonics for system identification No excitation necessary 	<ul style="list-style-type: none"> Questionable if assumption are satisfied

Table 5.7

Advantages and drawbacks of all excitation techniques used

For the impact hammer tests, the rotor does not rotate. This has the advantage, that any harmonics produced by the rotation will not be present in the measured data, and therefore will also not disturb the modal parameter estimation. On the other side, the drawback of this methods is that any effects the rotation has on the system dynamics, such as varying bearing stiffness or gyroscopic forces, are not measured.

Because there is only limited space around the rotor structure, a hammer excitation was difficult. Using a pole of approximately 2 meters length made it possible to excite the structure in radial direction. This way, the hammering action could be relocated to an easily accessible location, because the hammer did not have to hit the rotor structure directly. The excitation location and direction was chosen to be next to the measurement point of channel 5 and 8 in radial direction (see Fig. 5.14).

The time it takes the impulse to travel through the pole was estimated to be about $3.7697 \cdot 10^{-4}$ seconds. That is about 7.5 % of a period at 200 Hz. The phase delay for a resonance frequency is usually 90° . Due to the delay introduced by the pole a resonance frequency will be found at a different phase lag. 7 % of 360° is about 25° . This will introduce inaccuracies for the modal parameter identification.

Although using the pole made hammer measurements possible, the method shows significant disadvantages. Using the pole led to unavoidable double impacts. Furthermore, the impact force is measured at the upper end of the pole, including the pole into the system that is measured. These two effects lead to a deterioration of the measurement quality, but could not be avoided when using a hammer as excitation.

The parameter identification was performed using the *SDTools* software package [6]. The algorithms employed are based on [4, 5].

Operational Modal Analysis during Idling

This technique conducts an operational modal analysis on the turbine while it is idling. The excitation for the structure is provided by the wind that passes the turbine. The turbulence of the wind creates a dynamic force that is characterised by a good approximation to white noise. For the parameter identification the Canonical Variant Analysis (CVA) method was used. This is an operational modal analysis method based on a state space representation of the system (See [109] for further explanation). Additionally, the Enhanced Frequency Domain Decomposition (EFFD) method was applied.

The EFDD technique is based on the Frequency Domain Decomposition (FDD) technique. The FDD technique applies a singular value decomposition to the power spectral density matrix for each measured frequency. This decomposes the spectral matrix into a set of spectral density functions of which each corresponds to a single degree of freedom (SDOF) system. The singular values represent the auto power spectral density of that particular SDOF system at a certain frequency. The number of singular values that are significantly higher than the rest of the SV corresponds to the number of SDOF systems that are contributing to the global system response at that particular frequency.

The modal parameters are identified by calculating the power spectral density function for the SDOF system around peaks of the first singular value in the singular value plot. Whether the calculated power spectral density still belongs to the same SDOF system that was identified at the peak is determined by comparing the singular vector at the peak with the singular vector of the current frequency. As long as they are the same, it is assumed that the same SDOF system is still dominant at this frequency. From the auto power spectral density function calculated around a peak, the damping and natural frequency can be estimated.

The EFDD method determines the modal parameters differently. I

uses the power spectral density function identified around a peak to calculate the time response of the SDOF system. The modal parameters are identified in the time domain by counting the zero crossings per time unit and the logarithmic decrement of the response. In the proprietary software used in this thesis, the kurtosis is calculated to distinguish harmonic excitation from natural frequencies. (For further reading about the EFDD and FDD methods, refer to [20, 71].)

The SSI-CVA algorithm transforms the system to the state-space representation. Afterwards, a singular value decomposition is applied to the weighted output values of the system (See [109] for further explanation).

As mentioned, a single singular value that is significantly larger than the rest indicates that only one SDOF system dominates the global response. Two singular values that show a significant larger value than the rest indicate that the oscillation at that particular frequency can be represented by two single degree of freedom systems. This means that two modes are contributing to the global response of the system at that frequency. The case that all singular values at a certain frequency are significantly larger than zeros, indicates a forced vibration at that frequency.

According to [122], operational modal analysis makes the following assumptions about the system and the excitation forces that is measured:

- The system is time invariant.
- The structure is excited by uncorrelated white noise.
- The structure is reciprocal, i.e. the transfer function (TF) measure from point A to point B is the same as from point B to point A.

The quality of the modal parameter identification depends to what extent the assumptions above are satisfied. At idling of a turbine these assumptions are almost all satisfied. Only the excitation force deviates from the assumptions as wind induced forces are not perfect white noise.

Operational Modal Analysis during Rotation

As discussed in Sec. 5.3.4, the interaction between the permanent magnets and the stator slots create harmonic magnetic forces during the rotation of the turbine. These forces are also created when no torque is generated, because the field originating from the permanent magnets cannot be switched off. Although the magnetic

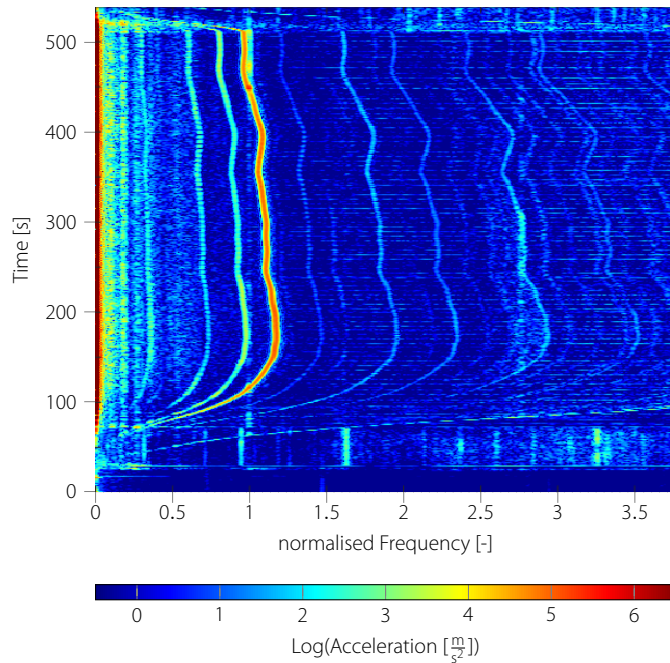


Figure 5.15
Spectrogram of a vibration measurement during rotation without power production.

forces cannot be measured, it is possible to apply output only analysis techniques on the vibrations induced by the magnetic forces.

Fig. 5.15 shows the spectrogram of a vibration measurement during rotation of the turbine without power production. In the first 150 seconds, the turbine starts up. After that, the turbine operates for several seconds at almost constant speed, before it shuts down at the end of the measurement. The lines that vary with the rotation speed are the increased vibration amplitudes caused by the harmonic excitation forces.

A colouring of the noise content of the excitation forces poses some challenges for the output only modal analysis. Extensive research has been done to overcome this issue. [103] gives a good overview about available techniques and under what circumstances they improve the results of an OMA.

In this thesis, three different approaches are followed to deal with the harmonic content of the excitation forces. The first technique ignores the problem all together and employs standard frequency domain and stochastic subspace techniques to identify the modal parameters. The second technique attempts to diminish the effects that the harmonic excitation forces have on the structure by filtering them from the signal. The third approach of techniques uses these harmonic excitation forces to identify the system.

Generic Operational Modal Analysis

The generic operational modal analysis conducts an operational modal analysis without employing any methods to alleviate the effects that the force harmonics have on the parameter identification. The same techniques are employed as for the operational modal analysis during idling.

This technique makes the same assumptions as the idling OMA, but because of the rotation of the turbine, the first two assumptions are violated. The gyroscopic forces, which are introduced by the rotation, depend on the rotation speed and the distance to the rotation axis. During the duration of a measurement, the rotation speed is never perfectly constant. Therefore, the gyroscopic forces introduce a stiffness that varies with time as the rotation speed varies with time. Additionally, the bearing stiffness depends on the position of the bearing elements and thus on the rotor position. The second assumption is violated by the magnetic forces in the system that introduce a harmonic content into the excitation forces in the generator.

It is assumed, that the first of the violated assumptions has a minor influence on the measurements because of the low rotation speed of the rotor. The assumption that the system is time invariant is thus reasonably satisfied. The second violation poses a larger challenge than the first one, as the encountered harmonic excitation is quite strong and coincide with resonance frequencies that are subject to the parameter identification.

Vold-Kalman Filtered Operational Modal Analysis

In a second approach, a Vold-Kalman filter was used to filter the harmonics from the measurement signal [91]. The Vold-Kalman filter is a particular formulation of the Kalman filter that can be used to extract a certain frequency, which can change over time, from a signal. The extraction of the harmonics is possible because the frequencies of the harmonic forces are known from the analysis done in Sec. 5.3.4.

Removing the harmonic frequencies from the measurement signal helps to distinguish the excitation frequencies from the resonance frequencies. In the case that a resonance frequency is close to an excitation frequency, the resonance frequency is also filtered from the signal. This is an issue, when the whole measurement is done at a fixed rotating frequency, because in that case a resonance frequency that is too close to an excitation frequency is filtered completely from the measurement. When measuring at changing rotation speeds, the resonance frequency is only filtered from the signal when the excitation frequency and the resonance frequency coincide. After filtering, the same parameter identification techniques

that were used for the first method are applied to conduct the modal parameter identification.

Order Based Modal Analysis

The *Order-Based Modal Analysis* (OBMA) method (details can be found in [33]) assumes a constant sinusoidal excitation at a changing frequency that depends on the rotation speed. It deviates from the assumption of the perfect white noise excitation that the previously introduced OMA methods use. During a start-up or run-down of the turbine, the excitation sweeps over a certain frequency range of which the maximal frequency depends on the maximal rotation speed and the relation between excitation frequency and rotation speed.

The assumption of a constant excitation amplitude is not necessarily satisfied in variable speed wind turbines. The excitation forces are created by the same effect as the total torque in the generator. They both depend on the magnetic flux density in the air gap. The torque is set by the controller of the turbine which determines the rotation speed of the rotor. In normal operation, the rotor speed is supposed to be constant. To accomplish that, the controller sets the torque in the generator according to the wind speed to keep the wind torque and generator torque balanced. During a run up, no power is produced in the turbine. In that case, the generator torque does not match the wind torque, as the intention is to speed up the turbine.

To extract the modal parameters, a particular order is chosen that excites the resonance frequencies in the frequency range of interest. This order is extracted from the signal using a Vold-Kalman order tracking algorithm [91]. The modal parameters can be identified using the same method as for shaker measurements that apply a sinusoidal sweep [4, 5]. The frequency response functions of the accelerometers can be taken as the transfer functions from the shaker to the sensor, assuming that the force amplitude is equal to one over all excited frequencies.

For the extraction of the phase information the RPM signal was used as reference (for other possibilities see [33]). Assuming that the excitation force is a sinusoidal force with a magnitude of one, the transfer function is the same as the measured frequency response function (FRF). These TFs can be used in any single input multiple output modal parameter estimation algorithm. Because the magnitude of the force is not known, the scaling of the modes is not possible. Assuming that the excitation force amplitude is the same for every frequency, the parameters of interest, i.e. the mode shapes, frequencies and damping, can be extracted.

Yawing Test

This method is based on the force that acts on the rotor structure, when the yawing motion is stopped suddenly. During yawing, the nacelle is moved around the centre axis of the tower. Because the generator's centre of gravity is not aligned with this axis, it experiences a translational movement. When this movement stops, inertia forces are generated acting on the rotor. The time distribution of this force resembles an impulse force used for the impact hammer tests. Measuring the response to this force makes it possible to identify the modal parameters of the system.

The excitation by yawing forces shows some properties that cannot be found for the other excitation methods. This technique is especially suited to excite lower structural modes, because the excitation is weak in the higher frequency range. This method can introduce a lot of energy into the system which is necessary to excite large, heavy structures. The applied inertia forces excite the structure everywhere instead of locally as it is done for the impact measurements.

The forces used to excite the structure in this method cannot be measured, necessitating an output-only parameter identification technique. For the identification of the modal parameters, the Least Square Complex Exponential method (LSCE) (see for instance [94] for an description) was applied to the part of the measurement that was recorded directly after the yawing stopped. In this time frame the vibration show a free decay.

Measurement Results

5.4.3

In this subsection, the results of the various measurement techniques will be discussed in detail.

Impact Measurement

In the measurement data of the impact measurement, five peaks could be identified in the frequency range of interest. The results can be seen in Fig. 5.16. Most peaks were fitted double, because theoretically every mode should have a symmetric counter part at the same frequency. This was not done for the peak at $\omega/\omega_{ref} = 1.62$, because this peak is in the range where the axial mode was expected. The figure shows that the modal fit for the collocated measurement points is rather good over the whole frequency range of interest. This is not the case for the non-collocated points as

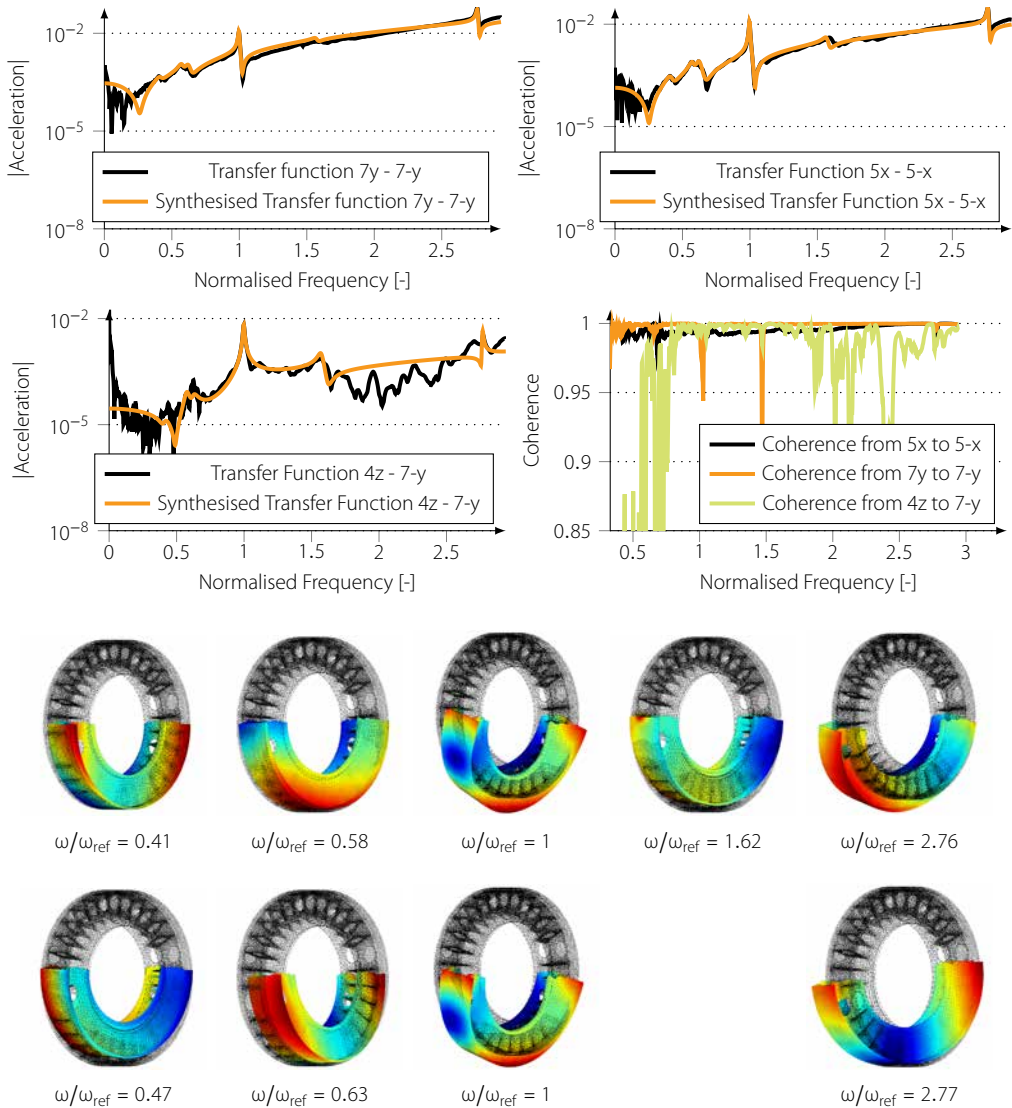


Figure 5.16

Transfer functions (TF) of the collocated hammering positions (top), Transfer function from 4z to 7-y (middle left) and the coherence for the three different transfer functions (middle right).

The bottom part of the figure shows the mode shapes identified by the impact measurements. The colour indicates the magnitude of the displacement

shown in the middle left plot in Fig. 5.16. This is especially true for the frequency range that shows a low coherence.

The modes shown in Fig. 5.16 were expanded using linear interpolation. No data was available at the top of the modes, as there were no sensors located at that position. It was consequently left blank, though the behaviour of the modes there can be estimated from the rest of the mode.

The two peaks at $\omega/\omega_{ref} = 1$ and $\omega/\omega_{ref} = 2.76$ are especially pronounced in the impact measurements. These two resonance frequencies can be fit in any of the transfer functions. Fig. 5.16 indic-

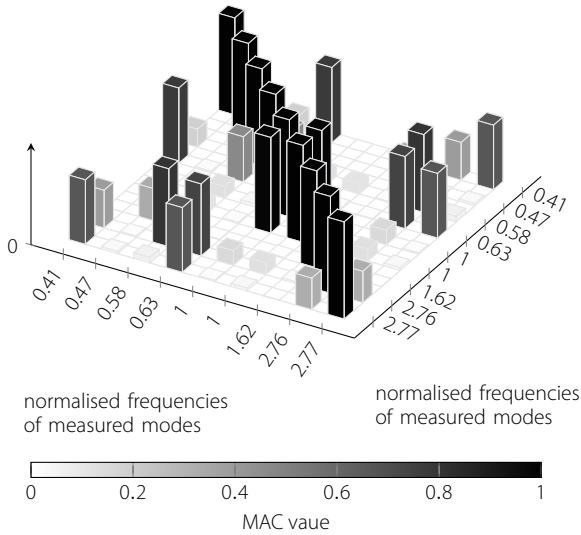


Figure 5.17

The auto mac plot of the impact measurements.

ates that the mode at $\omega/\omega_{ref} = 1$ is the first bending mode. The modes at the frequencies $\omega/\omega_{ref} = 0.41$ and $\omega/\omega_{ref} = 0.6$ seem to be rigid tilting modes around the bearing. They are clearly not as strongly excited as the bending modes. The mode type for the modes at $\omega/\omega_{ref} = 1.62$ and $\omega/\omega_{ref} = 2.76$ is not as easily identifiable. The FE model indicates that the second bending mode should be at $\omega/\omega_{ref} = 2.6$. So the mode at $\omega/\omega_{ref} = 2.76$ might in fact be the second bending mode.

The bottom part of Fig. 5.16 shows two modes for each peak in the TF. For all frequencies but $\omega/\omega_{ref} = 1$ and $\omega/\omega_{ref} = 1.62$, two symmetric modes could be identified. For the modes $\omega/\omega_{ref} = 1$, this is not possible, because both excitation points were located at fixed points of the associated symmetric mode. This way the same mode was fitted twice which leads to the same mode shape for the two identified modes of $\omega/\omega_{ref} = 1$, as can be seen in Fig. 5.16 .

Fig. 5.17 shows the Auto-MAC plot of the impact measurements. High off-diagonal values indicate that too few sensors were used to distinguish a mode from the modes on the diagonal. Fig. 5.17 indicates that the tilting modes at $\omega/\omega_{ref} = 0.41$, $\omega/\omega_{ref} = 0.47$, $\omega/\omega_{ref} = 0.58$ and $\omega/\omega_{ref} = 0.63$ are not distinguishable from the second bending modes at $\omega/\omega_{ref} = 2.76$ and $\omega/\omega_{ref} = 2.77$. All of these modes show mainly a displacement in axial direction (see Fig. 5.1). They differ by the number of locations where the maximum displacement is reached. When too few accelerometers are used this number cannot be determined accurately and the modes seem to be the same.

Operational Modal Analysis during Idling

Fig. 5.18 shows the spectrogram and the singular values (SV) for an OMA conducted during idling of the turbine.

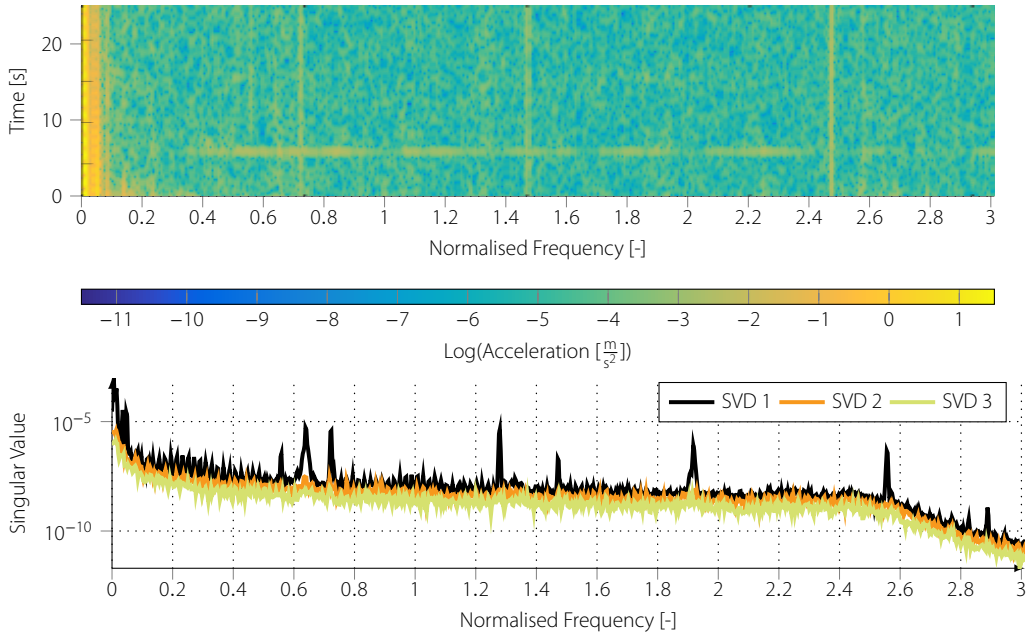


Figure 5.18

The spectrogram and the singular value plot of the no-rotation operational modal analysis

Comparing the measurements in Fig. 5.18 and Fig. 5.19 reveals that the noise level in the non-rotating measurement is, as expected, much lower than the noise level in the rotating turbine. The few peaks visible in Fig. 5.18 have a much lower maximum value than the peaks in the measurement during operation in Fig. 5.19 and Fig. 5.20. The SV plot indicates that there might be modes at $\omega/\omega_{ref} = 0.55$, $\omega/\omega_{ref} = 0.64$, $\omega/\omega_{ref} = 0.72$, at $\omega/\omega_{ref} = 1.27$, $\omega/\omega_{ref} = 1.91$ and at $\omega/\omega_{ref} = 2.56$.

The mode shape of all these frequency cannot be identified as bending or torsional modes. In fact, all of them do not look 'physical'. Consequently, it is assumed that the peaks in the SV plot in Fig. 5.18 are not modes of the rotor structure under consideration.

Operational Modal Analysis during Rotation

The plot in Fig. 5.19 shows the spectrogram of the generic operational modal analysis. The OMA was applied to the part of the measurement that shows an almost constant speed (starting after

90 seconds of the measurement). The singular value plot in Fig. 5.19 indicates that there might be modes at $\omega/\omega_{ref} = 0.1$, $\omega/\omega_{ref} = 0.17$, $\omega/\omega_{ref} = 0.27$, $\omega/\omega_{ref} = 1$ and $\omega/\omega_{ref} = 1.34$. The other peaks at $\omega/\omega_{ref} = 0.52$, $\omega/\omega_{ref} = 0.7$, $\omega/\omega_{ref} = 0.84$, $\omega/\omega_{ref} = 1.05$, $\omega/\omega_{ref} = 1.18$, $\omega/\omega_{ref} = 1.41$, $\omega/\omega_{ref} = 1.69$ and $\omega/\omega_{ref} = 2.53$ are generated by harmonics, as can be deduce from the excitation analysis in Sec. 5.3.4.

As explained in Sec. 5.4.2, a peak in the SV plot corresponds to a SDOF system that is dominant at that peak. When for a certain frequency two SVs are significantly higher than the rest of the SVs, it indicates that two SDOF systems are contributing to the vibrational behaviour of the system at that frequency. When all SVs show a peak at a certain frequency, then the same amount of number of SDOF contribute at that frequency. It is, however, unlikely that three or more modes have the same frequency, so that the increased SVs in this case do not indicate the contribution of a mode but instead a harmonic excitation. The peak at $\omega/\omega_{ref} = 2.78$ is peculiar, as at that peak, three singular values increase, although there is no harmonic present at that frequency.

At the bottom of Fig. 5.19, the stability plot of the SSI-CVA method is shown. This plot is produced by using the settings as shown in Tab. 5.8 for the CVA-SSI algorithm. These indicators have to be fulfilled to declare a mode stable, when comparing the mode with the same mode of the model one model order lower. Most harmonics (indicated by a blue vertical line) are identified as stable modes. Besides the wrongly as modes identified harmonic excitations, there are two stable modes at $\omega/\omega_{ref} = 1$ and $\omega/\omega_{ref} = 2.78$.

Parameter Name	Parameter Values CVA
Maximum Deviation of parameters	
Frequency [Hz]	0.05
Damping [%]	2
Mode Shape MAC	0.01
Expected Range of Damping	
Min [%]	0.05
Max [%]	2

Table 5.8
Modal indicators for the SSI-CVA algorithm

Vold-Kalman Filtered Operational Modal Analysis

The top of Fig. 5.20 shows the spectrogram and the bottom the singular value decomposition plot of the Vold-Kalman filtered operational modal analysis. The harmonic frequency, clearly visible in Fig. 5.19, have now disappeared from the spectrogram in Fig. 5.20. Plotting the singular values over the frequencies shows a gap

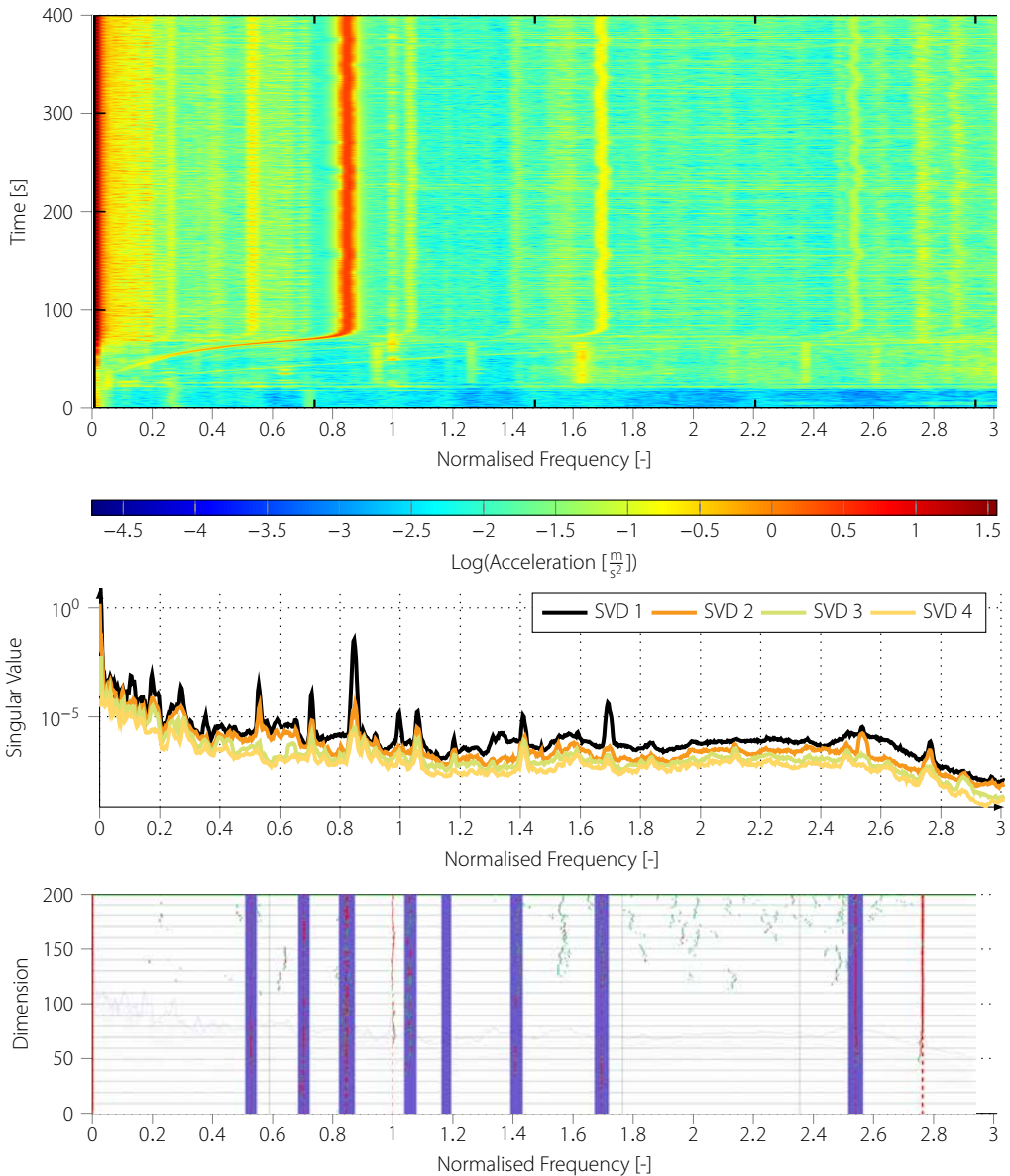


Figure 5.19 Spectrogram (top), SVD plot (middle) and stability plot of the SSI-CVA algorithm (bottom) of the operational measurement. The blue regions in the bottom plot indicate harmonic excitation frequencies, identified in Sec. 5.3.3

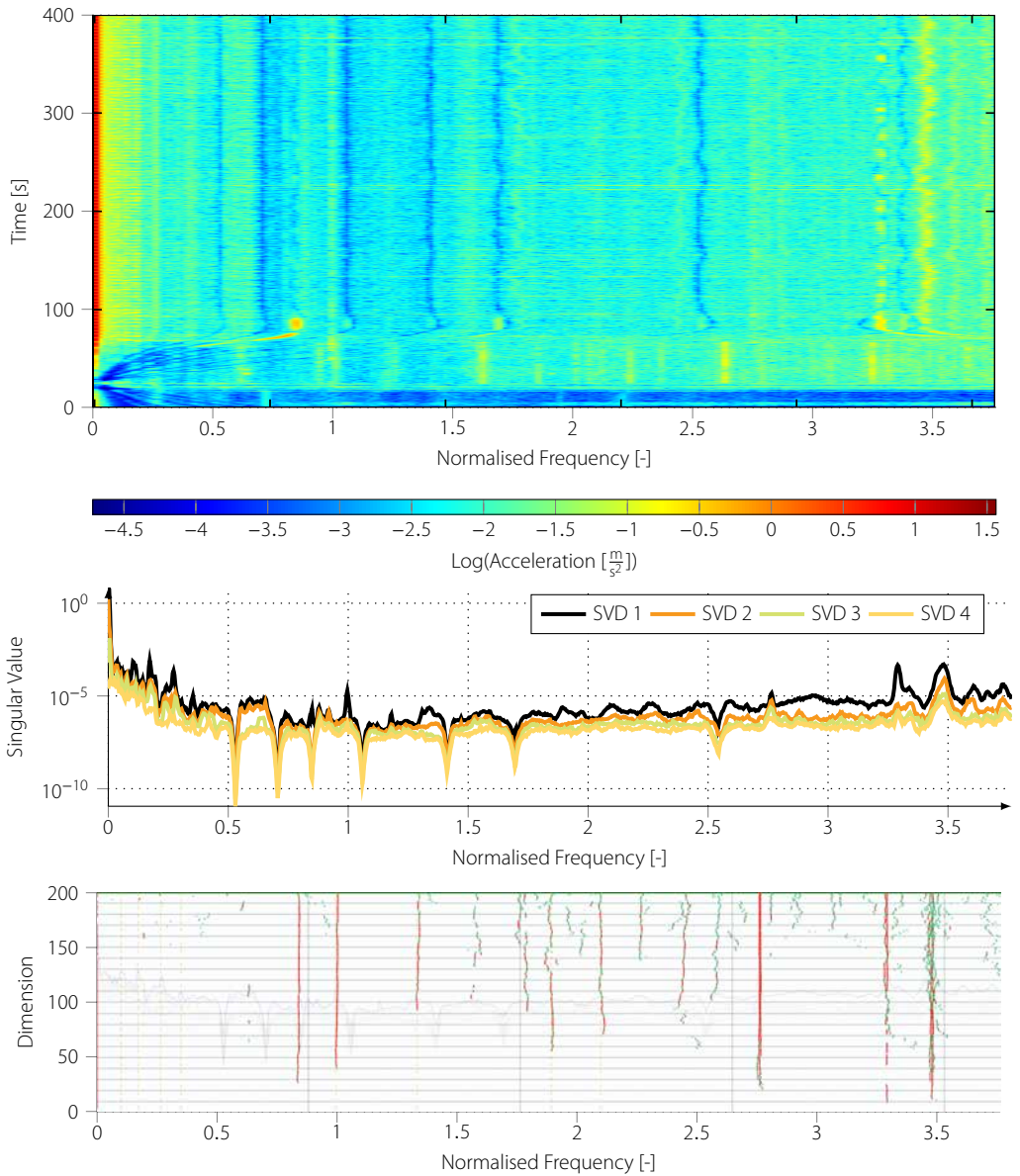


Figure 5.20 Spectrogram (top), SVD plot (middle) and stability plot of the SSI-CVA algorithm (bottom) of the Vold-Kalman filtered measurement

at each location where a harmonic excitation was present in the SV plot in Fig. 5.19.

Applying the Vold-Kalman filter, enables the SSI-CVA algorithm to identify more stable resonance frequencies. This is shown in Fig. 5.20 at the bottom. Additional frequencies that could be identified this way include $\omega/\omega_{ref} = 1.34$, $\omega/\omega_{ref} = 1.89$, $\omega/\omega_{ref} = 2.10$, $\omega/\omega_{ref} = 2.26$ and $\omega/\omega_{ref} = 2.6$. The identified modes and damping values for this method are listed in Tab. 5.9.

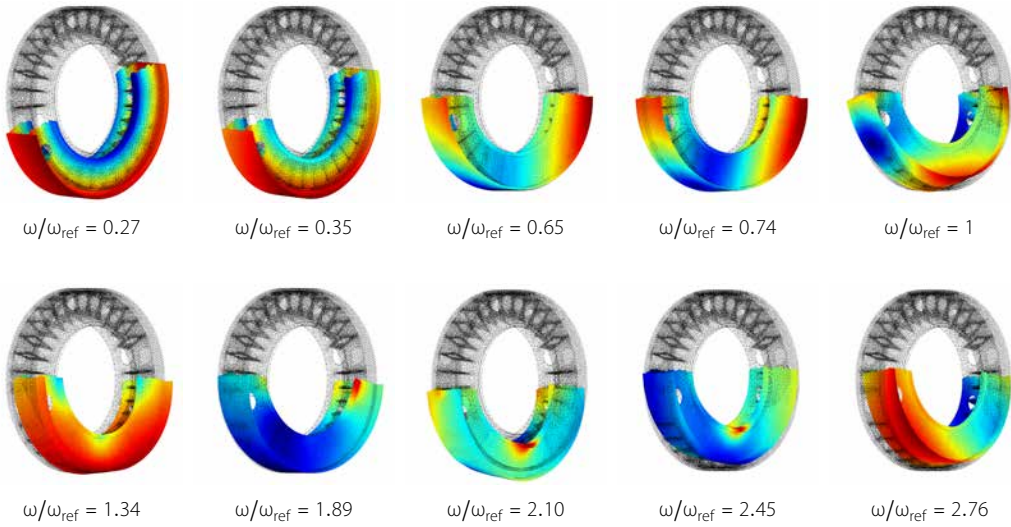


Figure 5.21

A selection of modes identified by the operational modal analysis

Fig. 5.21 shows the modes that were identified by applying the OMA to the Vold-Kalman filtered measurements. The mode at $\omega/\omega_{ref} =$

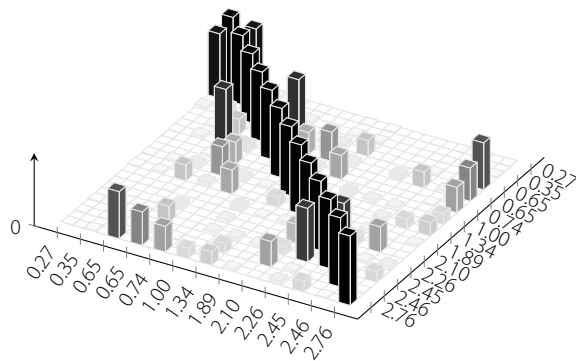
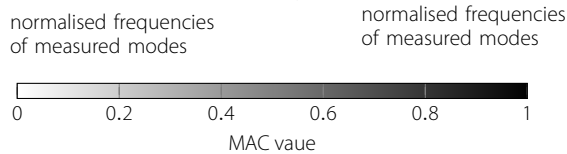


Figure 5.22

The Auto-MAC plot of the Vold-Kalman filtered measured modes



1 can be identified as the first bending mode, whereas the mode at $\omega/\omega_{ref} = 1.33$ seems to be the axial mode identified by the FE model. Although, hardly visible in the SV plot in Fig. 5.20, the two small peaks at $\omega/\omega_{ref} = 0.65$ match the mode shapes identified by the impact measurement method at $\omega/\omega_{ref} = 0.65$. The mode shapes of both measurements show a tilting mode at that frequency. The peaks are so small, that the SSI-CVA method does not identify them as modes.

Fig. 5.22 shows the Auto-MAC of the modes identified by applying the OMA to the Vold-Kalman filtered measurements. Significant off-diagonal entries exist only for the modes at $\omega/\omega_{ref} = 0.27$ and $\omega/\omega_{ref} = 0.35$ and for $\omega/\omega_{ref} = 0.65$ and $\omega/\omega_{ref} = 2.76$. The lower off-diagonal entries indicate that the modes measured by the Vold-Kalman OMA are better distinguishable than the modes measured by the impact measurements. The sensor position is still the same as for the impact measurements, thus the identified mode shapes must have changed.

Order-Based Modal Analysis

The top of Fig. 5.23 shows the vibration measurement of channel 8, as indicated in Fig. 5.14, during the run up of the XD-115. The diagonal lines represent an excitation which depends linearly on the rotation speed. During a start up of the turbine such an excitation harmonic excites various frequencies. When the excitation frequency coincides with a resonance frequency the measured amplitude of the vibration increases.

The bottom part of Fig. 5.23 shows the extracted $2n_{slots}^{th}$ and $5n_{slots}^{th}$ orders. The modal parameters of the peak at $\omega/\omega_{ref} = 1$ were identified by a local fit around that peak. This way the damping value of that resonance frequency could be identified. It is listed in Tab. 5.9.

Yawing Test

5.4.4

Fig. 5.24 shows the stability plot of the LSCE method on the left and the spectrogram of the measurement on the right. In the spectrogram, the noise generated by the yawing motion and engines is clearly visible. After the movement stops at around 21 seconds, some frequencies seem to be damp out slower than others. Assuming that the lower damping at those frequencies originates from the fact that there is a resonance at those frequencies, a modal parameter identification can be conducted on the time frame directly after the movement stops.

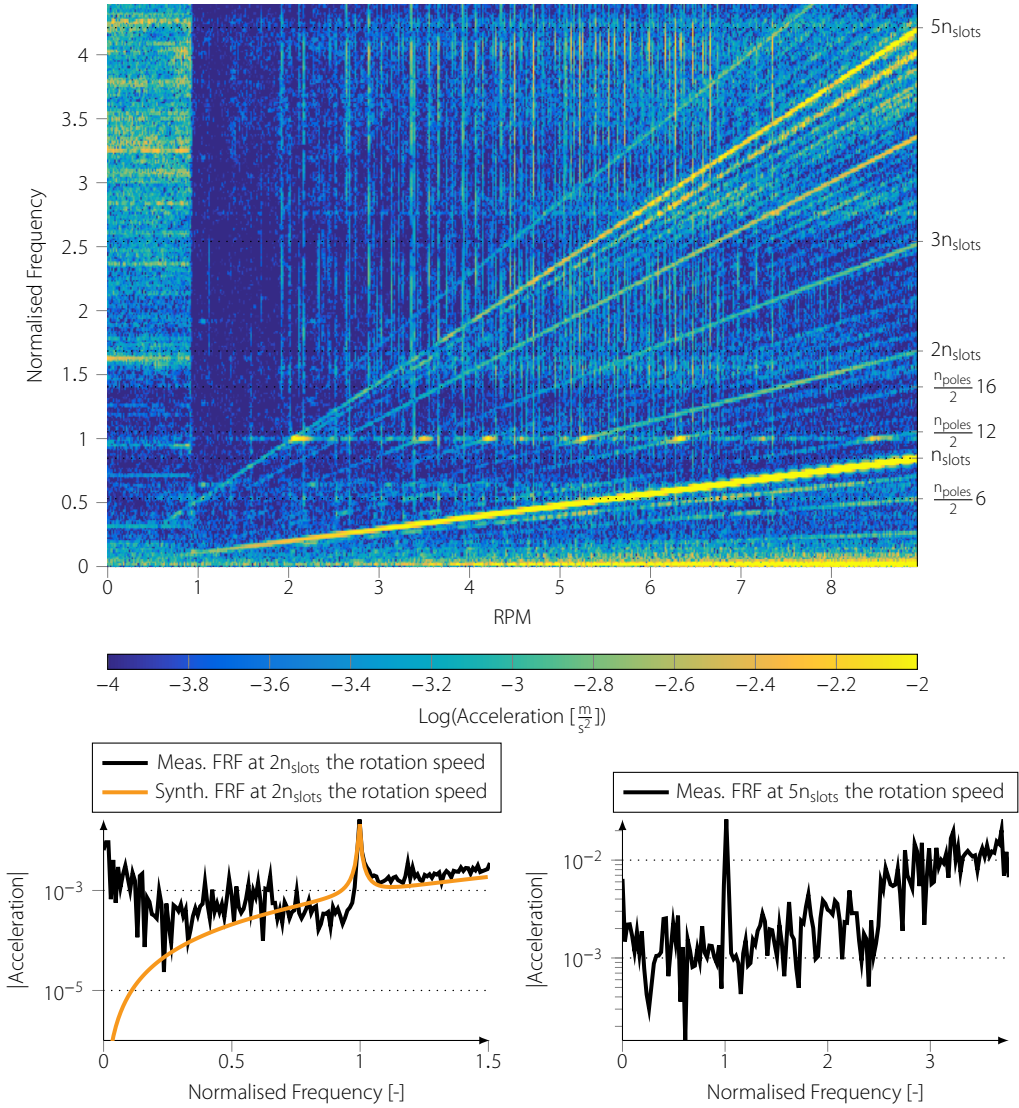


Figure 5.23 Spectrogram of the run up, normalised with the rotation speed (top). Orderplot of the harmonic at $2n_{slots}$ times the rotation speed and its modal fit (bottom left). The harmonic at $5n_{slots}$ the rotation speed (bottom right). Both plots are done for the 8th channel, indicated in Fig. 5.14

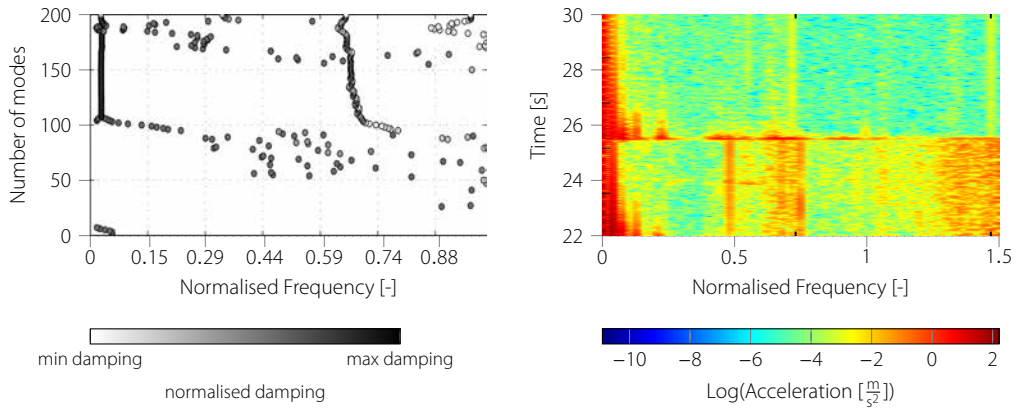


Figure 5.24

Stability plot of the LSCE method (left) and spectrogram of the measurement (right)

The LSCE method was applied to a time interval from 22 to 25 seconds of the measurement shown in Fig. 5.24. The stability plot on the left side of Fig. 5.24 shows that the lower frequencies, which were mainly excited by this method are relatively unstable. Even the modal parameters of the mode at $\omega/\omega_{ref} = 1$, which is easily identifiable in the other methods, could not be extracted. Only some modes around $\omega/\omega_{ref} = 0.05$ are stable. Those are probably modes of other turbine parts, such as tower or blades modes, which also get excited during the sudden stop of the rotating motion of the nacelle. The frequencies of those modes are too low to interact with the resonances of the generator structure. Consequently, they are not of interest in the scope of this thesis.

Discussion

The difficulties encountered when exciting the structure, resulted in measurements of which the results are less certain than hoped for. This section discusses the quality of the measurements.

By comparing the results of the various identification methods, it becomes apparent that the strong harmonic excitation in the frequency range of interest poses a large problem for the operational modal analysis methods. Filtering them out before applying the parameter identification method yields better results. Other methods, such as a cepstrum analysis (see [103]) or [19], probably improve the parameter identification. Only the excitation methods that are directly present in the generator seem to excite the modes of the generator structure. Other excitation techniques such as yawing excitation failed to excite the modes of interest.

The yawing method was omitted from the following two subsections as no modes of interest could be identified with this method.

5.4.5

Normalised Frequencies ω/ω_{ref}	0.27	1	1.34	1.88	2.09	2.25	2.44	2.78
Method	Damping values [%]							
OBMA	-	0.0734	-	-	-	-	-	-
Constant Speed Measurement EFFD	1.173	0.346	1.827	-	-	-	-	0
Constant Speed Measurement SSI-CVA	-	1.23	-	-	-	-	-	0.073
Vold-Kalman Filtered OMA EFFD	1.35	0.387	1.762	0.49	0.796	0.772	0.3	0.081
Vold-Kalman Filtered OMA SSI-CVA	-	1.11	0.941	0.891	1.334	1.274	0.118	0.246
Impact Hammer	-	0.35	-	-	-	-	-	0.12

Table 5.9

Overview over identified damping values by the Operational Modal Analysis (OMA), the impact measurements and the Order-Based Modal Analysis (OBMA) for various resonance frequencies

Comparison Among Measured Methods

Tab. 5.9 presents the identified damping values of several resonance frequencies and for various methods employed. For resonance frequencies that were not identified by a certain method a dash was used.

Only the damping value of the resonance frequency at $\omega/\omega_{ref} = 1$ is consistent over 3 modal parameter identification methods. All other damping values do not show any consistency or trend. The modal damping is difficult to extract for operational modal analysis methods, so that it is not surprising that the identified values are not consistent [110].

The low damping values for the second bending mode at $\omega/\omega_{ref} = 2.78$ are curious. A low damping value in operational modal analysis is usually associated with harmonic excitations that are mistaken as resonance frequencies. Taking into account the odd fact that more than two singular values show a peak around $\omega/\omega_{ref} = 2.78$, it cannot be ruled out that the peak at $\omega/\omega_{ref} = 2.78$ is actually a forced response to a harmonic force. On the other hand, this mode was identified in the impact measurements too, which rules out a harmonic excitation from rotation. This could indicate that the measured excitation is caused by a device in the turbine that excites the structure even when the turbine stands still. However, the spectrogram at stand still in Fig. 5.18 does not show a vibration at $\omega/\omega_{ref} = 2.78$. Therefore, further research is necessary, to undoubtedly identify the effect that causes the peak at $\omega/\omega_{ref} = 2.78$.

In Tab. 5.9, it is possible to identify the trend, that the damping of the two modes at $\omega/\omega_{ref} = 1$ and $\omega/\omega_{ref} = 2.78$, that were identified by almost all methods, are lower than the other measured mode.

Comparison with Simulation

Comparing the measured with the simulated modes reveals that not all modes predicted by the finite element method in Sec. 5.3

could be identified by the measurement. In fact, most techniques could only identify the two modes at $\omega/\omega_{ref} = 1$ and $\omega/\omega_{ref} = 2.78$. The absence of the modes missing in the measurements can be explained by taking a closer look at the measurement results and excitation techniques.

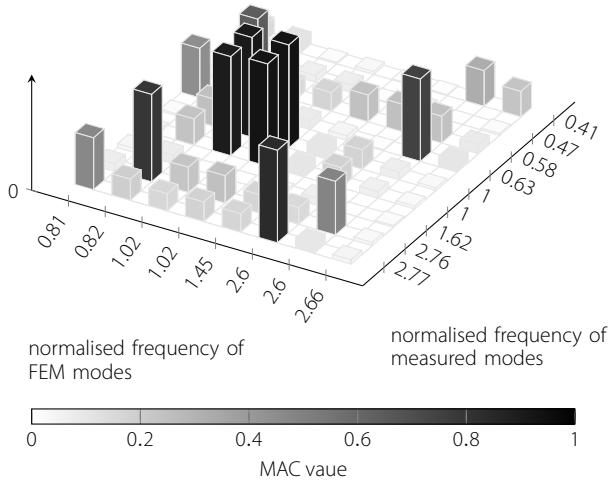


Figure 5.25

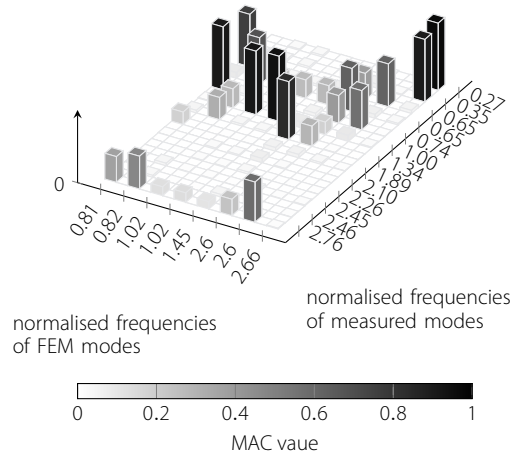
MAC plot, comparing modes recorded by the impact measurement with calculated modes.

Fig. 5.25 depicts the MAC plot that compares the mode shapes which were computed by the finite element model to the shapes measured by the impact hammer test. The only mode for which the agreement between the measured and the simulated modes is relatively good are the first bending modes (modes around $\omega/\omega_{ref} = 1$). This mode is also the most excited mode during the measurement.

Most likely, the reason for the unsatisfying identification of some modes by the impact measurements is their weak excitation. In the case of the impact measurements, this is easily explained. Only the bending modes show a significant displacement in the excitation direction. i.e. in radial direction. Because, the excitation force was applied in radial direction, these modes were excited while the axial mode and torsional modes are hardly affected.

The high off-diagonal values in Fig. 5.25 can be explained by the low number of accelerometers used for the measurement. The Auto-MAC in Fig. 5.17 suggests that the 2nd bending mode and the tilting modes are not distinguishable. The location of the sensors was chosen in such a way that it was possible to distinguish the first bending mode from the second bending modes and from the tilting modes. It is, however, not possible to distinguish the second bending mode from tilting modes, leading to a linear dependency of the measured modes of these two mode types. That can be seen by the increased values for certain MAC entries.

Figure 5.26
Mac plot to compare the operational mode shapes, measured by the vold-kalman filtered measurement and the simulated mode shapes



In Fig. 5.26, the MAC plot is depicted that compares the mode shapes measured by the operational testing to the shapes computed by the finite element model. There is only agreement for the modes at lower frequencies. The OMA identified only one mode for the frequencies $\omega/\omega_{ref} = 1$ and $\omega/\omega_{ref} = 0.77$, although it was expected that for each of these frequencies two modes can be identified due to the symmetry of the rotor. For the higher modes, no agreement between measured and computed modes can be identified. This bad match between measurements and computation is probably caused by the difficult measurement conditions. As the Auto-MAC in Fig. 5.22 suggested, the 2nd bending mode and the tilting modes are hard to distinguish.

The excitation forces used for the operational modal analysis are mainly in torsional and radial direction. It is expected, that modes showing a displacement in these two directions are excited during operation, while the axial mode at $\omega/\omega_{ref} = 1.33$ is not excited. It is, thus, astonishing that the first bending mode is more excited than the axial mode and that no torsional mode is visible in the measurements.

There are three possible reason, why a mode is not excited and thus cannot be measured during operation. All of them can be derived from the formula to calculate modal participation factors, which was introduced in (5.20).

- The damping ζ_r of the mode is so high that it is not excited.
- The force distribution \mathbf{f}_{mag} does not match the mode shape Φ_r , so that their scalar product $\mathbf{f}_{mag} \cdot \Phi_r$ is low.
- The excitation frequency Ω is too far from the resonance frequency ω_r .

Looking at the identified damping values in Tab. 5.9, the first reason

can be ruled out, as the damping values are too small to significantly influence the participation of a mode. The third reason can be ruled out too, because the measurement was done at a frequency sweep, during which various frequencies were excited, including the resonance frequencies. That leaves the second point as possible reason why the structure is not excited.

The mode shapes of the 1st bending mode and axial mode are validated by the vibration measurements in the turbine. Therefore, the cause for an excitation of the 1st bending mode that is higher than expected is most likely the incorrect approximation of the magnetic forces. The local magnetic forces cannot be measured directly and thus no experimental validation was conducted.

In what way the magnetic forces do not resemble the actual force distribution in the turbine, remains a task for future research. Possible reasons include imperfections or manufacturing tolerances in the generator such as ovalisation of rotor and stator, eccentricity of stator and rotor, and axial misalignment of stator and rotor.

Conclusion

Although difficult measurement conditions were encountered in the turbine, a successful experimental dynamic analysis of the generator rotor could be concluded. Some of the measured modes were matched to the modes computed by the FE model. The mode shapes of various modes seem to match very well the computed modes, although the computed frequencies deviate.

The reasons for the less accurate match at higher frequencies and the deviation of the frequencies has two probable causes. The difficult measurement conditions and the placement and low number of sensors deteriorates the quality of the measurements. Furthermore, the simplifications applied to the FE model do not take the surrounding nacelle and turbine dynamics into account. These dynamics could have an impact on the dynamics of the rotor structure, which leads to the encountered deviation between measured and simulated dynamics.

The FE model suffered from the maximum limit of DoFs imposed on the model by the available hardware. This limitation decreases the accuracy of the computed modes as well as the accuracy of the magnetic forces. For this problem, the model reduction techniques developed in Chapter 4 could help to improve the accuracy.

It was identified that for the XD-115 generator structure, the two way coupled dynamics are less important. This indicates that the design of the turbine's generator is robust and can withstand the

5.5

dynamic forces with ease. It also indicates that the generator structure is over engineered and significant weight reduction is possible without compromising the functionality of the generator.

This result does not indicate that the two-way coupling can be neglected for direct-drive wind turbine generators all together. For designs that are more compliant, i.e. the lowest eigenfrequencies are lower, the two-way coupling can be of major importance and influences the dynamics significantly.

Furthermore, the measurements showed that in-situ operational modal analysis of the generator structure of direct-drive wind turbines is possible, making structural health monitoring during operation possible. Further measurements, conducted on the static part of the bearing, indicate that structural health monitoring of the rotor resonance frequencies is even possible by measuring stator vibrations. These measurements are shown in Appendix B.

Improvements for future Dynamic Analyses of Generators

The analysis of the XD-115 was rather thorough and could explain the dynamic behaviour that was measured. However, there was some uncertainty left about the results. Several points could be improved for the identification process of the dynamic behaviour of wind turbine generators in the future.

More sensors: The measurements were carried out with too few sensors. Ambiguity remained about the exact shape of some of the modes.

Include the stator: Some of the vibrations might have originated in the stator. This could not be determined ultimately, because the stator was not equipped with sensors. Including the stator in the measurements could also yield valuable information explaining noise generation in the turbine as noise is usually generated on the stator side.

Lab measurements of generator: Several of the vibrations measured in the generator might be caused by other parts of the turbine. To distinguish the generator vibrations from the vibrations originating in other parts of the turbine, the generator's dynamics should be measured before it is installed in the turbine. This way, the change of the dynamic behaviour caused by coupling with the nacelle or other structures can be identified.

Increase frequency range: The frequency range was limited to up to 200Hz. However, the frequency range should be reach up

to the resonance frequency of the bending mode or ovalisation mode that has the same order as the cyclic symmetry as the electro-magnetic part. Those modes are especially likely to be excited and should thus be carefully analysed.

Use other OMA and filtering techniques: [103] lists a number of techniques to improve parameter identification of output-only measurement techniques in the presence of harmonic excitations. Some of these techniques are expected to improve the results of the measurements present here.

Summary

5.6

In this chapter, a dynamic analysis of the XD-115 was conducted, including a 3D structural analysis, a 3D magnetic model interacting in two directions with the structural model and a 2D magnetic model estimating the influence of the armature field on the structure. The two-way coupled analysis, conducted first, identified that a two-way coupled analysis is not necessary for the generator of the XD-115. The one-way coupled analysis, conducted afterwards, could simulate the dynamics of the generator of the XD-115 reasonably well. Measurements showed that in the frequency range of interest, several eigenmodes could be predicted by the simulations. This was seen as strong indications, that the models indeed are a representation of the vibrational behaviour of the turbine. In the higher frequency range, the agreement between simulation and measurements was weaker, so that some doubts about the model could not be dispelled.

The source of and the mechanisms causing the excitation frequencies could be identified, so that for other generators, the excitation frequencies were predicted. Furthermore, a methodology was developed to identify modes that can possibly be excited by the magnetic harmonics.

Abstract:

Reducing the weight of off-shore wind turbine nacelles is currently a key driver of innovation within the wind turbine industry. Weight reduction will not only lead to smaller mass and thus smaller towers of the turbine, but also reduce logistic costs during the turbine's installation. A reduced nacelle weight will, subsequently, lead to reduced cost of wind energy.

For direct-drive turbines, the generator is one of the heaviest parts of the wind turbine nacelle. Due to the low rotational speed of the generator, the loads are especially high in this type of turbine, which increases the necessary structural mass of the rotor. Recently, designed flexibility has been identified as one approach to achieve weight reduction. However, reducing the weight of the support structure has proven difficult, due to the complex pattern of dynamic excitation forces. Until now, density based topology optimisation has hardly been employed for the design of wind turbine parts. This chapter investigates the possible weight reduction, which results from applying this method to the support structure of the generator rotor.

6.1

Introduction

In Chapter 5, the dynamic behaviour of the XD-115 generator was analysed. The insights in the load cases for the stationary operation of the turbine can be used to improve the dynamic behaviour of the generator.

Vibrations in wind turbine generators are of interest, because of the following reasons. Firstly, vibrations during operation can cause a noise annoyance for the surrounding area. Furthermore, vibration amplitudes that exceed a secure limit, can compromise the functionality of the turbine. The second aspect is the focus of this thesis. When analysing the vibrations for either of the two reasons above, insights and recommendations for the other cause are also gained. It is, therefore, helpful keeping both aspects in mind during the following analysis.

Topology Optimisation, the method mainly used in this chapter, is still subject to extended research. As such, there are still issues that need to be addressed before this method can show its full potential. This chapter focuses on identifying the potential that this method develops, when using it to improve designs of generator structures. For that, this thesis adapts the method for wind turbine generators, including identification of suitable constraints and ways to measure the performance of a design. The chapter does not focus on improving the methods itself. It uses a self developed version of the algorithm that does not include the latest, cutting edge methods that improve the optimisation result. Accordingly, the results presented in this chapter suffer from practical difficulties during the implementation of the optimisation algorithm and can be improved significantly, when the latest research results from the field of topology optimisation is incorporated. Approaches that potentially improve the results are pointed out.

6.1.1

Effects of Torque Ripple in Electric Machines

Torque Ripple is caused by the interaction of the magnetic field of the rotor with the armature field and the stator teeth. It causes a variation of the torque during the rotation of the turbine. This effect is undesirable as it can excite the structure of the generator and, consequently, causes noise and high vibration amplitudes. Furthermore, it can complicate the start-up of the generator, as it might create a magnetic torque that opposes the torque induced by the wind, even when there are no currents present in the coils.

To avoid vibrations in wind turbines generators in particular and electric machines in general, efforts have concentrated on minim-

ising the cause for the vibrations, i.e. torque ripple, in the past. The various approaches for minimising these torque fluctuations were listed in Sec. 1.3.3. Instead of minimising the cause of torque ripple, analysing the impact it has on the machine can identify new approaches to minimise its effects. The vibrations caused by torque ripple can be minimised, by designing the structure in such a way that it does not excite the structure of the electric machine. This will reduce noise and vibration amplitudes. It does not improve the start-up characteristics of the generator.

To find a mechanical design that minimises the effects of torque ripple, topology optimisation was chosen. This method is most suited for this task, as it is not limited by what shapes it can describe.

Optimisation for Weight Reduction

6.1.2

The insights in the load cases, gained in Sec. 5.3.4 and Sec. 5.3.5, for the steady-state operation of the turbine can be used to optimise the design of the generator structure, so that the deflection resulting from those forces is minimal. In the past, many different topologies to optimally support the electro-magnetic active parts of the generator were suggested [145]. The proposed designs can be categorised in constructions using arms, spokes, discs and tension rods. The various designs that were proposed are thus quite diverse.

The challenge of the optimisation is finding the optimal topology and identifying the optimal design, while ensuring that the result is still manufacturable. Shape optimisation is based on a parametrisation of the geometry. Parametrisation is difficult when there are many topologies to consider. Topology optimisation is not parameter based and can thus represent any design listed in [145]. However, the designs yielded by topology optimisation are often difficult to manufacture with conservative production techniques, i.e. without a 3D printer. A combination of topology optimisation and shape optimisation was chosen for this optimisation. This way, all possible geometries listed in [145] are included, yet the resulting geometries consist of shapes that are manufacturable.

Content of the Chapter

6.1.3

This chapter will introduce a dynamic optimisation problem, which quantifies and optimises the dynamic performance of the generator rotor structure of the XD-115. The method can be used in the same way for any electric machine but yields the largest improvements in electric machines that are very flexible, like direct-drive generators.

It can be used to address either of the two effects mentioned above: reduce generator vibrations and reduce the weight of the structure. The method is used for single bearing direct-drive topologies as well as multi bearing designs. The results of the optimisation of single bearing designs are compared to the current design, which is used as benchmark.

6.2

The Dynamic Optimisation Problem

This section will introduce the various methods used during the optimisation. Due to the large variety of generator topologies that need to be considered, topology optimisation was chosen as optimisation method. Topology optimisation is a technique that mathematically determines the optimal distribution of material for a given cost function within a certain control volume. Compared to shape optimisation, topology optimisation is not limited by parametrisation. However, it leads to a large number of design variables that lead to models that consist of many DoFs and are computationally expensive.

6.2.1

The Dynamic Optimisation Problem

How can the optimal design be measured for a certain set of functions that a structure needs to fulfil? The functions that the generator rotor structure needs to perform were mentioned in Sec. 1.2.3. The first objective requires a stiff connection between all electromagnetic active materials on the rotor. To ensure this, a hollow cylinder is needed, on which the magnets are mounted.

The other two objectives can be quantified by taking the displacement caused by the magnetic forces during steady-state operation of the turbine. In this thesis, the focus rests on the dynamic behaviour of the generator. That means that not only the static forces of the generator, described in (5.16), are taken into consideration but also the dynamic forces, that were identified in (5.17).

Another indicator for the performance of the rotor structure is its weight and its cost. The objectives have to be reached with the least weight possible at the cheapest price. The first of these indicators is easily measurable as the weight can be computed directly from the volume. The second indicator is difficult to determine, because it heavily depends on the geometry of the rotor. Therefore, it is neglected here during the optimisation. It is however accounted for by using a shape optimisation after the topology optimisation that yields shapes that are easier to manufacture.

The optimisation problem can be phrased into the qualitative statement:

Determine the structural generator design that uses the least amount of material, while not exceeding a certain maximal displacement under dynamic forces found at steady state operation

Shaping this expression into a mathematical formula, as necessary for optimisation algorithms, will be complex, due to the limitation of current algorithms.

A solid steel ring is necessary for a feasible electro-magnetic design, because the magnetic flux lines need to be able to close. This steel ring gives enough support to the magnets, so that the first function defined in Sec. 1.2.3 is automatically performed.

Quantifying the Performance of the Design

6.2.2

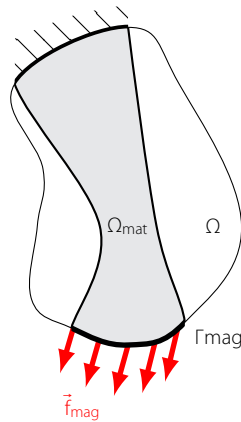


Figure 6.1

Domain of a structural optimisation. Ω_{mat} denotes the volume of the material. For the topology optimisation, Ω denotes the whole optimisation domain and Γ_{mag} denotes the surface where magnetic forces are applied

The qualitative statement in the previous section needs to be transformed into a mathematical formulation. For that, the constraints as well as the optimisation criteria need to be quantified. For the mass constraint, this is rather easy as the maximal mass of the total structure may not exceed a certain value

$$m_{max} > \int_{\Omega_{mat}} \rho(\vec{x}) \, d\Omega_{mat} \quad (6.1)$$

where ρ denotes the density of the structure, Ω_{mat} the material domain and m_{max} the maximal allowed mass of the structure. See Fig. 6.1 for a schematic of the system that is optimised. The second constraint ensures that there is a solid steel ring at the locations where

the magnetic force is applied

$$m_{max,mag} = \int_{\Gamma_{mag}} \rho(\vec{x}) d\Gamma_{mag} \quad (6.2)$$

where Γ_{mag} denotes the surface where the magnetic force is applied, and $m_{max,mag}$ a minimal value for the average density of the surface. Note that $m_{max,mag}$ is not a mass. Its unit is $\frac{kg}{m}$.

For formulating the mathematical optimisation performance criteria, two different kinds of displacement need to be distinguished. The static displacement created by static forces in the generator. In addition, there are the dynamic displacements that are the result of periodic forces in the generator. These two kinds of displacement have to be computed separately.

Static Performance

For the static case, the displacements can be determined by solving the equilibrium equation (see Chapter 2 for details)

$$\vec{f}_{mag,static} = -\nabla \cdot \underline{\underline{\sigma}}(\vec{u}) \quad (6.3)$$

where $\vec{f}_{mag,static}$ denotes the magnetic forces as defined in (5.16).

The performance of the structure is determined by the displacement in the air gap, i.e. at Γ_{mag} . When the absolute value of the displacement in Γ_{mag} is minimal, the second and third functions of the support structure are fulfilled as best as possible. Minimising the absolute value of every DoF in Γ_{mag} will lead to as many objective functions as there are DoFs in Γ_{mag} . Most algorithms are designed for one scalar objective function, because this makes the optimisation computational cheaper. One objective function means that only one gradient needs to be determined. So instead of minimising every DoF in the domain, the integral over all displacements is formed.

$$\min \int_{\Gamma_{mag}} |\vec{u}| d\Gamma_{mag} \quad (6.4)$$

This is minimal, when the square of the displacement is minimal

$$\min \int_{\Gamma_{mag}} \vec{u}^2 d\Gamma_{mag} \quad (6.5)$$

Minimising (6.5) will lead to an optimal design in terms of static performance. For numerical reasons, (6.5) is not ideal as it increases computation time drastically. Computing the sensitivities of (6.5) is expensive. Why that is the case will be explained in Sec.

6.2.4. Instead of the square of the displacement, the strain energy is minimised.

$$\begin{aligned} \min g_{obj} &= \min \int_{\Gamma_{mag}} \bar{\mathbf{u}}^T \bar{\mathbf{f}}_{mag} \, d\Gamma_{mag} \\ &= \min \int_{\Omega_{mat}} \underline{\underline{\boldsymbol{\varepsilon}}}(\bar{\mathbf{u}})^T \underline{\underline{\boldsymbol{\sigma}}}(\bar{\mathbf{u}}) \, d\Omega_{mat} \end{aligned} \quad (6.6)$$

Dynamic Performance

The dynamic performance of a structure can be measured by the overall displacement of the structure under a dynamic loading. In a steady state operation point of the generator, only periodic excitation forces are generated by the system. The partial differential equation describing the response of the system is

$$\nabla \cdot \underline{\underline{\boldsymbol{\sigma}}}(t, \bar{\mathbf{x}}) + \bar{\mathbf{f}}_{mag}(t, \bar{\mathbf{x}}) = \rho \frac{\partial^2 \bar{\mathbf{u}}(t, \bar{\mathbf{x}})}{\partial t^2} \quad (6.7)$$

This equation can be optimised in two ways. The used approach depends on the system properties and has a significant influence on the formulation of the optimisation problem.

The Harmonic Approach

The first approach is the *harmonic approach*. In this case, the displacement field $\bar{\mathbf{u}}$ is calculated for a certain harmonic excitation frequency ω_{ext} . The solution is a forced vibration at the same frequency as the excitation.

$$\nabla \cdot \underline{\underline{\hat{\boldsymbol{\sigma}}}}(\bar{\mathbf{x}}) e^{i\omega_{ext}t} + \hat{\mathbf{f}}_{mag}(\bar{\mathbf{x}}) e^{i\omega_{ext}t} = -\rho \omega_{ext}^2 \hat{\mathbf{u}}(\bar{\mathbf{x}}) e^{i\omega_{ext}t} \quad (6.8)$$

where $\hat{\mathbf{u}}$ and $\hat{\mathbf{f}}_{mag}$ denote the amplitude of the response over Ω and the spatial distribution of the displacement and magnetic force, respectively and the exponential terms $e^{i\omega_{ext}t}$ the time information. The same separation has been done for the stress tensor $\underline{\underline{\boldsymbol{\sigma}}}$.

The solution is only valid for that particular frequency. To get an impression of how the system performs at various excitation frequencies, (6.8) has to be solved repeatedly for those frequencies. Once the PDE is solved, the displacement for that frequency can be used to calculate the performance. As performance indicator, the dynamic energy is used

$$W_{dyn}(\omega_{ext}) = \int_{\Omega_{mat}} \underline{\underline{\boldsymbol{\varepsilon}}}^T(\bar{\mathbf{u}}, \omega_{ext}) \underline{\underline{\boldsymbol{\sigma}}}(\bar{\mathbf{u}}, \omega_{ext}) \, d\Omega_{mat} \quad (6.9)$$

When a certain frequency range is of interest, (6.8) needs to be solved for all frequencies in that frequency range. There are infinite frequencies in any frequency range. Thus, a frequency sweep with a certain step size needs to be done. The size of the step should not exceed a certain value, as then resonance frequencies that are located between the evaluated frequencies might not be picked up. On the other side, it should not fall below a certain length as this increases the computational costs.

This approach has the disadvantage that the larger the frequency range of interest, the more often (6.8) needs to be solved. The advantage is that the sensitivity analysis for the various performances is rather simple and can thus be calculated easily as shown in Sec. 6.2.4.

The Modal Approach

The *modal approach* transforms (6.7) into a system of independent ordinary differential equations, using modal analysis according to the description in [52]. It is then possible to identify the amplitude of each of these modes with the help of the participation factor

$$\eta_r = \frac{\int_{\Omega_{mat}} \vec{\varphi}_r \cdot \vec{f}_{mag} d\Omega_{mat}}{\omega_r^2 - \omega_{ext}^2} \quad (6.10)$$

Often, only a certain frequency range is of interest for the optimisation. In that case, the participation factor of modes within that frequency range are considered for the optimisation function. Considering only a certain frequency range has one disadvantage. The frequencies of the modes change when the density distribution, and with it the design, changes. It is, thus, possible that due to a change of the design parameters a mode is no longer considered, when its resonance frequency is no longer in the frequency range for which the amplitudes are evaluated. Furthermore, it is possible that a certain mode starts being considered when its resonance frequency is changed in such a way that it enters the frequency range of interest. This problem could be addressed by employing mode tracking methods [40, 75] or using a Hanning window so that modes just outside the frequency range of interest are still taken into account but at a lower weighting factor.

This method has the advantage that the resonance frequencies are identified and, thus, the evaluation of the response is independent of the difference in frequency between resonance frequency and evaluation frequency. This way, it can be ensured that all resonance frequencies in the optimisation function are weighted equally, if desired. However, the computational cost to analyse each mode is more expensive than for each frequency in the harmonic method.

This is balanced by the fact that there are usually less modes than frequencies in a certain frequency range and thus the number of evaluations per optimisation step is lower.

Multi-Objective Optimisation

Optimisation functions that consist of a sum of several terms do not necessarily minimise all these terms. An optimisation algorithm that minimises such an expression will concentrate on minimising the largest term. A step that increases one of the smaller terms while leading to a huge decrease for the largest term, will still yield an overall decrease of the optimisation function. Only when the various terms are of the same magnitude, the algorithm will take the other terms into account.

To overcome this problem, only one of the terms is used in the optimisation function, while the other terms are used to define a set of constraint which ensures that these terms do not exceed a certain value. By computing the optimal value for several constraint value sets, the so called Pareto front can be determined. This front indicates the optimal solution for the optimisation problem, over a parameter space.

For the static optimisation problem, a Pareto front is computed by minimising the static performance indicator defined in (6.6) for several maximal mass values. This is done for the static optimisation in Sec. 6.3.1 and shown in Fig. 6.6

The performance indicators for the harmonic and modal approach are both sums of several terms. Because there are so many terms, computing a Pareto front is expensive. That is why instead the optimisation function consisting of the sum of various terms is optimised.

For the modal approach, this means, that mainly the largest participation factor will be minimised. All other participation factors might increase during the optimisation process. The same is valid for the various frequencies in the harmonic approach. In this case, mainly the largest dynamic energy computed at one of the evaluated frequencies is minimised. That could lead to the situation that a resonance frequency that is located between two evaluated frequencies is not minimised for two possible reasons. Because the resonance frequency does not coincide with an evaluation frequency, its contribution to the dynamic energy at the nearest evaluated frequency is small. Furthermore, the summand of that frequency might be small and thus neglected by the optimisation algorithm.

6.2.3

Topology Optimisation

This short introduction to topology optimisation is based on the introduction in [160].

Topology optimisation is an optimisation technique that has the aim to find the optimal distribution of material within a certain design space Ω under a certain loading and set of constraints. To formulate the topology optimisation problem and indicator function χ is introduced that can take values of 1, i.e. material and 0, i.e. no material

$$\chi(\bar{x}) \in \{0, 1\} \quad (6.11)$$

The topology optimisation finds the field of $\chi(\bar{x})$ that minimises a certain objective function g_{obj} . The optimisation problem can then be written as:

$$\begin{aligned} \min_{\chi, \bar{u}} \quad & g_{obj}(\chi, \bar{u}) \\ \text{subject to} \quad & 0 = \delta (W_{strain}(\bar{u}, \chi) + \mathcal{T}(\bar{u}, \chi) - W_{ext,m}(\chi)) \\ & g_{constr} \leq 0 \\ & \chi(\bar{x}) \in \{0, 1\} \end{aligned} \quad (6.12)$$

where g_{constr} denotes a constraint, g_{obj} the objective function. The second line represents the variational form of the partial differential equation as derived in Chapter 2 with W_{strain} the potential energy and $W_{ext,m}$ the external energy as described in (2.59).

To solve (6.12) various approaches have been derived in the past. The two most common ones are level-set methods [159, 167] or density based topology optimisation [14]. This thesis will only employ the latter method.

Density Based Topology Optimisation

Density based topology optimisation is currently the most widely used method to solve optimisation problems such as (6.12). The approach of density based topology optimisation is to relax the problem in (6.12) to a problem that is solvable by gradient based optimisation algorithms. To do that, the discrete indicator function is substituted by a continuous density function $\rho_f(\bar{x}) \in [0, 1]$. Regions within the design without material are modelled as very compliant material that hardly has an influence on the deformation behaviour of the structure. Usually, (6.12) is given in its nested form, i.e. ρ_f is the only design variable and \bar{u} is an implicit function of ρ_f through the second line of (6.12). The second line of (6.12) is omitted from the optimisation problem.

To compute the displacements, the domain is discretised using the finite element method, where the elements of the stiffness and mass

matrix depend on the design parameters ρ_f .

$$\begin{aligned} \min_{\rho_f} \quad & g_{obj}(\bar{\mathbf{u}}(\rho_f)) \\ \text{subject to} \quad & g_{constr}(\bar{\mathbf{u}}(\rho_f)) \leq 0 \\ & \rho_f(\bar{\mathbf{x}}) \in [0, 1] \end{aligned} \quad (6.13)$$

Because, the equilibrium equation, which was still part of (6.12), is now implicitly solved when computing $\bar{\mathbf{u}}$, all possible solutions for (6.13) satisfy the equilibrium equation. The stiffness and mass matrix, needed to compute $\bar{\mathbf{u}}$, depend on the design parameters ρ_f

$$\mathbf{M} = \mathbf{M}(\boldsymbol{\rho}(\rho_f)); \quad \mathbf{K} = \mathbf{K}(\mathbf{E}(\rho_f)) \quad (6.14)$$

where $\boldsymbol{\rho}$ and \mathbf{E} are vectors containing the scaled values of the density and Young's modulus respectively at the nodes within the design domain. The total stiffness matrix and mass matrix are assembled from the element matrices, which depend on the nodal values of the density and Young's modulus.

$$\mathbf{K} = \sum_e \mathbf{K}^e(\mathbf{E}_e) \quad (6.15)$$

where \mathbf{K}^e denotes the stiffness matrix of the e^{th} element and \mathbf{E}_e the nodal values of the Young's modulus at the nodes associated to the e^{th} element.

Scaling the Young's modulus nonlinearly, while scaling the density linearly makes intermediate densities ($10^{-3} < \rho_f < 1$) less feasible. This is the case, because the intermediate densities show a relative low stiffness compared to their density. This way the achieved stiffness is paid for by a lot of weight. The optimal solution will thus not include material that has intermediate densities but tends to a black and white, i.e. material/no-material, design. Fig. 6.2 shows the relation between the normalised density and elasticity and the design variable ρ_f . This method is called modified Solid Isotropic Material with Penalisation (SIMP) method [139, 150]. The Young's modulus is defined by

$$E_n = E_{max} \rho_f^3 \quad (6.16)$$

In dynamic topology optimisation, local modes with low resonance frequencies can occur due to the penalisation function applied to the Young's modulus. This problem is tackled by lowering the density for low values of the design parameter.

$$\rho_n = \begin{cases} \rho_{max} \rho_f & \text{for } \rho_f \geq 0.1 \\ \rho_{max} \rho_f^5 & \text{for } \rho_f < 0.1 \end{cases} \quad (6.17)$$

Solving the topology optimisation problem was done by using the Method of Moving Asymptotes (MMA) [149]. The code was adapted from the code supplied by the author of [149] in Matlab.

6.2.4

Computing Sensitivities

Topology optimisation requires optimisation algorithms that evaluate the gradients analytically. The large number of design variables make algorithms based on finite differences infeasible. For topology optimisation, remeshing between iteration steps is not necessary. This makes gradient based topology optimisation possible.

The sensitivity of a value is its change with respect to another. For the optimisation the change of the objective function $g_{obj}(\bar{u})$ with respect to the design variables are the sensitivities that need to be determined. In the case of density based topology optimisation, the design variables are the densities at each node of the mesh $\rho_f(\bar{x})$. The value of interest is, thus, the gradient of the objective functions with respect to the densities. Various methods exist to calculate the sensitivities. Which method to use depends on the objective functions and how it depends on the design parameters. For this thesis, the objective function is a scalar function depending only on the design parameters where a load is applied. In such a case, the adjoint method for calculating sensitivities is the computational least expensive method.

The Adjoint Method

The adjoint method adds a design parameter independent part to the optimisation function. It does depend on the current solution of the system $\bar{u}(\bar{x})$. This part includes adjoint variables, which need to be solved only once for each optimisation iteration regardless of the number of design parameters. This way, the computation of the sensitivity of the objective function or constraint with respect to each design parameter can be avoided. Instead, only one set of

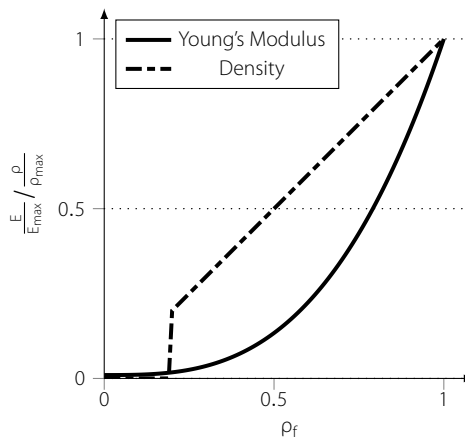


Figure 6.2

The normalised density and elasticity plotted over the design variable ρ_f

equations for every constrain or optimisation function needs to be solved to compute the sensitivities, reducing computational cost significantly. The adjoint problem is tailored to a certain load case and needs to be adapted for each load case.

Stationary Optimisation

For stationary optimisation problems, the calculation of the sensitivities is easier than in the harmonic or modal case. For the discrete case, the system equation is

$$\mathbf{K}\mathbf{q}_u = \mathbf{f} \quad (6.18)$$

The adjoint methods introduces the performance measure g_{obj}^*

$$g_{obj}^* = g_{obj} - \lambda^T (\mathbf{K}\mathbf{q}_u - \mathbf{f}) \quad (6.19)$$

where λ denotes the adjoint variables.

Instead of computing the sensitivities for g_{obj} , the sensitivities for g_{obj}^* are computed.

$$\frac{dg_{obj}^*}{d\mathbf{p}_f} = \left(\frac{\partial g_{obj}}{\partial \mathbf{q}_u} \right)^T \frac{d\mathbf{q}_u}{d\mathbf{p}_f} - \lambda^T \left(\frac{d\mathbf{K}}{d\mathbf{p}_f} \mathbf{q}_u + \mathbf{K} \frac{d\mathbf{q}_u}{d\mathbf{p}_f} \right) \quad (6.20)$$

By a wise choice for λ the first term can be eliminated

$$\lambda^T \mathbf{K} = \left(\frac{\partial g_{obj}}{\partial \mathbf{q}_u} \right)^T \quad (6.21)$$

leaving for the sensitivity of g_{obj}^*

$$\frac{\partial g_{obj}^*}{\partial \mathbf{p}_f} = -\lambda^T \frac{d\mathbf{K}}{d\mathbf{p}_f} \mathbf{q}_u \quad (6.22)$$

Because, (6.22) contains the solution to the static problem, \mathbf{q}_u , the linear systems (6.18) and (6.21) need to be solved. The derivation of the adjoint variables for calculating the sensitivities of constraints is analog.

If the objective function g_{obj} only consists of the strain energy W_{pot} , the system is self-adjoint. This means that the adjoint variables λ are the same as the displacement solution \mathbf{q}_u . This can be shown by considering that the potential energy for the discrete case can be calculated by

$$W_{pot} = \frac{1}{2} \mathbf{q}_u^T \mathbf{K} \mathbf{q}_u \quad (6.23)$$

in this case (6.21) becomes

$$\lambda^T \mathbf{K} = \mathbf{q}_u^T \mathbf{K} \quad (6.24)$$

Self-adjoint systems are cheaper to optimise as (6.21) does not need to be solved explicitly.

Modal Optimisation

The adjoint method for modal sensitivities was used by Lee [89, 90].

$$\mathbf{g}_{obj}^* = g_{obj} - \boldsymbol{\xi}^T (\mathbf{K} - \lambda_k \mathbf{M}) \boldsymbol{\varphi}_k + \zeta \left(\frac{1}{2} - \frac{1}{2} \boldsymbol{\varphi}_k^T \mathbf{M} \boldsymbol{\varphi}_k \right) \quad (6.25)$$

where $\boldsymbol{\xi}$ and ζ denote the adjoint variables and λ_k denotes the square of the eigenfrequency ω_k . The derivative of the objective function with respect to the design parameters becomes then

$$\begin{aligned} \frac{d\mathbf{g}_{obj}^*}{d\boldsymbol{\rho}_f} &= \frac{\partial g_{obj}}{\partial \lambda_k} \frac{\partial \lambda_k}{\partial \boldsymbol{\rho}_f} + \left(\frac{\partial f}{\partial \boldsymbol{\varphi}_k} \right)^T \frac{\partial \boldsymbol{\varphi}_k}{\partial \boldsymbol{\rho}_f} + \\ &+ \boldsymbol{\xi}^T \left(\frac{\partial \mathbf{K}}{\partial \boldsymbol{\rho}_f} - \frac{\partial \lambda_k}{\partial \boldsymbol{\rho}_f} \mathbf{M} - \lambda_k \frac{\partial \mathbf{M}}{\partial \boldsymbol{\rho}_f} \right) \boldsymbol{\varphi}_k \\ &+ \boldsymbol{\xi}^T (\mathbf{K} - \lambda_k \mathbf{M}) \frac{\partial \boldsymbol{\varphi}_k}{\partial \boldsymbol{\rho}_f} + \\ &+ \zeta \left(-\boldsymbol{\varphi}_k \mathbf{M} \frac{\partial \boldsymbol{\varphi}_k}{\partial \boldsymbol{\rho}_f} - \frac{1}{2} \boldsymbol{\varphi}_k^T \frac{\partial \mathbf{M}}{\partial \boldsymbol{\rho}_f} \boldsymbol{\varphi}_k \right) \end{aligned} \quad (6.26)$$

Solving the following system of equations to calculate the adjoint variables ζ and $\boldsymbol{\xi}$, will eliminate the terms depending in the original optimisation function

$$\begin{bmatrix} (\mathbf{K} - \lambda_k \mathbf{M}) & -\mathbf{M} \boldsymbol{\varphi}_k \\ -(\mathbf{M} \boldsymbol{\varphi}_k)^T & 0 \end{bmatrix} \begin{bmatrix} \boldsymbol{\xi} \\ \zeta \end{bmatrix} = \begin{bmatrix} -\frac{\partial g_{obj}}{\partial \boldsymbol{\varphi}_k} \\ -\frac{\partial g_{obj}}{\partial \lambda_k} \end{bmatrix} \quad (6.27)$$

Calculating the adjoint variables this way leads to

$$\frac{d\mathbf{g}_{obj}^*}{d\boldsymbol{\rho}_f} = \boldsymbol{\xi}^T \left(\frac{\partial \mathbf{K}}{\partial \boldsymbol{\rho}_f} - \lambda_k \frac{\partial \mathbf{M}}{\partial \boldsymbol{\rho}_f} \right) \boldsymbol{\varphi}_k - \zeta \frac{1}{2} \boldsymbol{\varphi}_k^T \frac{\partial \mathbf{M}}{\partial \boldsymbol{\rho}_f} \boldsymbol{\varphi}_k \quad (6.28)$$

for the sensitivities. (6.27) has to be solved for each eigenvalue and vector individually. So in order to calculate the sensitivities for all modes within a certain frequency range, first the eigenvalue problem itself has to be solved and then (6.27) for each mode within that range.

Finding a solution to (6.27) is the most computationally expensive part of the modal method for large systems. The zeros on the main diagonal in (6.27) can pose a problem for some preconditioners for iterative solvers. This leads to a slow convergence rate of the iterative solver, which are preferred for large systems, due to reduced memory requirements compared to direct solver methods. Finding a way to solve (6.27) iteratively and efficiently is still a topic of research.

Harmonic Optimisation

The sensitivity analysis for the harmonic case is different from the two cases covered above. To increase the possibility that a resonance frequency is excited by the excitation force that does not perfectly coincide with the resonance frequency, damping is added to the system. This increases the width of the peak of a resonance frequency in the FRF of the system and thus increases the chance of an increase response to an excitation frequency. However, the damping complicates the sensitivity analysis as the displacement of the system becomes complex.

The adjoint sensitivity analysis for time harmonic systems including damping is derived in [170]. The objective function g_{obj} is extended by two adjoint variables ξ and ζ , one for the complex and the other one for the complex conjugate residual.

$$g_{obj}^* = g_{obj} + \xi^T (\mathbf{S}\mathbf{q}_u - \mathbf{f}) + \zeta^T (\overline{\mathbf{S}\mathbf{q}_u} - \bar{\mathbf{f}}) \quad (6.29)$$

where $\bar{\cdot}$ denotes the conjugate complex of a value and \mathbf{S} denotes the sum of the system matrices

$$\mathbf{S} = \mathbf{K}(\boldsymbol{\rho}) + \mathbf{i}\omega\mathbf{C}(\boldsymbol{\rho}) - \omega^2\mathbf{M}(\boldsymbol{\rho}) \quad (6.30)$$

as shown in [170], one of the sets of adjoint variables can be eliminated by

$$\zeta = \bar{\xi} \quad (6.31)$$

The remaining adjoint variables can be computed by solving the system

$$\mathbf{S}(\boldsymbol{\rho})^T \xi = -\frac{1}{2} \left(\frac{\partial g_{obj}}{\partial \Re(\mathbf{q}_u)} - \mathbf{i} \frac{\partial g_{obj}}{\partial \Im(\mathbf{q}_u)} \right)^T \quad (6.32)$$

After the adjoint variables have been computed, the sensitivities can be calculated by

$$\frac{\partial g_{obj}^*}{\partial \boldsymbol{\rho}_f} = 2 \Re \left(\xi^T \frac{\partial \mathbf{S}}{\partial \boldsymbol{\rho}_f} \mathbf{q}_u \right) \quad (6.33)$$

For the case that

$$\mathbf{f} = \mathbf{q}_u \mathbf{S} \mathbf{q}_u \quad (6.34)$$

as defined for the harmonic approach, the system is self-adjoint and the solution of (6.32) is obtained by computing the dynamic displacements.

6.2.5

Shape Optimisation

The topology optimisation explained in Sec. 6.2.3 can identify the optimal topology for a certain load case and domain. However, due to the coarse mesh the computed stiffness is probably overestimated. It is, therefore, necessary to validate the results with a shape optimisation where this overestimation is avoided. For that the results of the topology optimisation are used to identify a parametrisation for the shape optimisation.

Furthermore, the shape optimisation yields results that do not require a 3D printer to be manufactured. Because of the parametrisation, the shape optimisation yields geometries that consist of easy shapes.

For every iteration step of the shape optimisation, the structure is remeshed. This makes the usage of methods determining the gradient analytically difficult (using a moving mesh, would theoretically make a gradient based method possible). It is, thus, necessary to use an optimisation method that is based on finite differences or does not try to identify the gradient at all. There are several algorithms that fit this description, including particle swarm optimisation [39], algorithms based on evolution or the BOBYQA algorithm [119]. In this thesis, the Nelder-Mead algorithm is used [106].

6.3

Optimisation of Single Bearing Topologies

The focus of this thesis is on single bearing direct-drive topologies. The XD-115, analysed in Chapter 5, also belongs to this type of wind turbine.

For the optimisation of the single bearing design, the forces described in (5.16) and (5.17) were used. In a first step, a topology optimisation was used to determine the rough design of the turbine. In a second step, a design parametrisation was conducted, which was inspired by the result of the topology optimisation. This parametrisation makes a shape optimisation of the system possible.

The current design of the XD-115 was used as benchmark for the optimised designs. It is depicted in Fig. 6.3. The compliance, the total mass and the participation factors for selected modes are listed in Tab. 6.2.

The optimisation relates only to the part of the rotor that is located between bearing and air gap. For the optimisation, the magnet assembly was left out and thus excluded from the optimisation process. Only the steel stiffener structure, including the ring the mag-

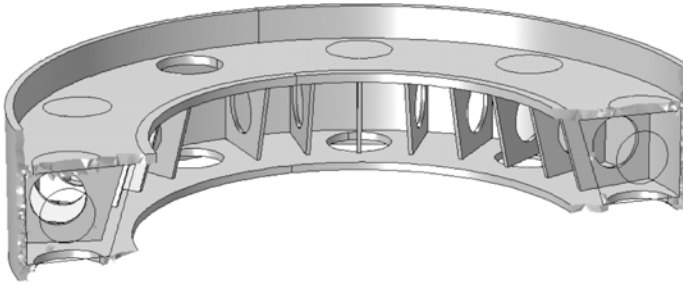


Figure 6.3

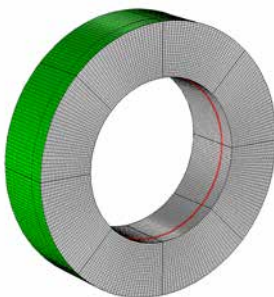
The benchmark design, i.e. the current design of the XD-115

nets are mounted on, was included. For simplicity, the bearing was modelled as fixed displacements. The hub was omitted, although it was discovered that the hub structure has a small influence on the dynamic response of the rotor stiffener structure. All these simplification were also applied to the benchmark design, to ensure comparability between the benchmark and the optimised designs.

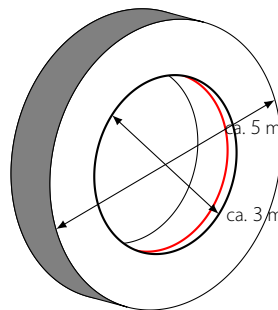
Topology Optimisation

Fig. 6.4 shows the mesh and the optimisation domain used for the topology optimisation. The topology optimisation was coded in Matlab and run on a computer cluster node with 48 cores. The static optimisation took about a day while the modal optimisation took about one to two weeks. The harmonic optimisation was carried out in Comsol and took about six days.

While using the topology optimisation, it crystallised that the resolution of the material distribution is the bottleneck of the method. The volume of the structure of direct-drive wind turbines is large. Furthermore, structures that consist of thin plates, beams or spokes are usually the stiffest. Therefore, a high resolution is necessary to represent the thins structures, while at the same time the large volume needs to be covered. This gives rise to models with huge amount of DoFs.



The mesh used for the topology optimisation



The Design Domain used for the Topology Optimisation

Figure 6.4

Force distribution and schematic of the topology optimisation

6.3.1

The topology optimisation was conducted with and without density filter. The filter was based on [84] and prevents the optimisation algorithm from including checkerboard-like structures. These occur in solutions of topology optimisation, because the stiffness computed by the FEM for structures including material distributions in checkerboard patterns is greatly overestimated. They perform better when a large stiffness is desired with limited amount of mass available. A comparison of homogenous designs with designs including checkerboard-like structures is thus not fair.

The solutions of the unfiltered topology optimisation can still be used as a starting point for a shape optimisation. The unfiltered topology optimisation can create thinner structures. Consequently, the resulting designs can look very different from the filtered solutions. The above mentioned problem of comparing various results is overcome by comparing the solution of the shape optimisation, which does not include checkerboard-like structures, with the benchmark solution.

Static Optimisation

In a first step, the system was optimised for a static load case using the load identified in (5.16) and depicted in Fig. 5.11. This was done in order to ensure that the solution computed with the used mesh is able to excel the current benchmark design in terms of statical performance.

Discretising the general optimisation problem, (6.13), yields the following discrete optimisation problem

$$\begin{aligned}
 & \min_{\rho_f} \quad \mathbf{q}_u \cdot \mathbf{f}_{mag,stat} \\
 & \text{subject to} \quad \sum_n \rho_n v_n - m_{max} \leq 0 \\
 & \quad \quad \quad - \sum_{n \in \Gamma_{mag}} \rho_n v_n + 0.999 \sum_{n \in \Gamma_{mag}} v_n \leq 0 \\
 & \quad \quad \quad \rho_f \in [10^{-3}, 1]
 \end{aligned} \tag{6.35}$$

where \mathbf{q}_u denotes the values of the structural DoFs as defined in (2.104), ρ_n is the density at node n , v_n the volume associated with node n and ρ_f denotes the vector of all design parameters. The objective function denotes the strain energy of the system that is minimised. The first constraint ensures that the mass m_{max} is not exceeded, while the second constraint ensures that the design is feasible from a magnetic point of view by imposing a solid steel ring at the outer surface of the design domain.

To identify the minimal mass at a given compliance a Pareto front was computed for filtered and unfiltered topology optimisation.

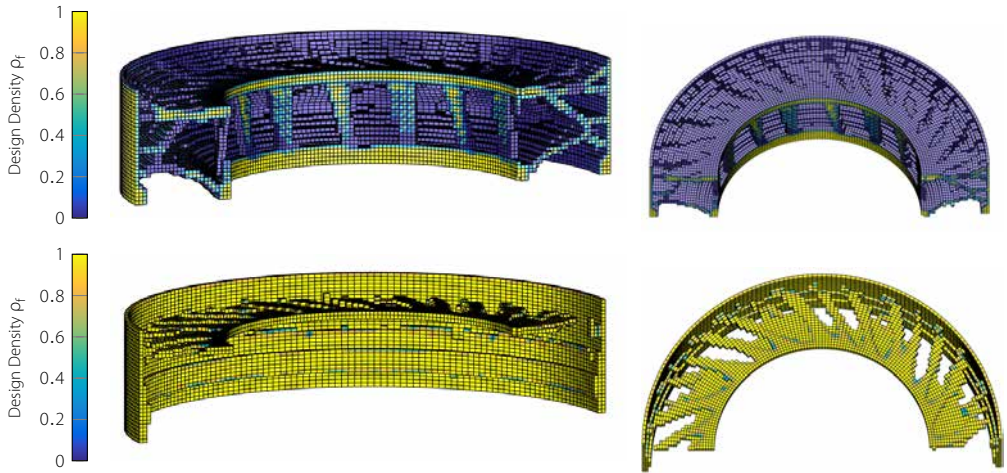


Figure 6.5

The result of the static topology optimisation without density filter for $m = 13039\text{kg}$ (top) and the result of the static filtered topology optimisation for $m = 20525\text{kg}$ (bottom)

This front, shown in Fig. 6.6, identifies minimal values of the static compliance for various values of the constraint limiting the maximum mass. Fig. 6.6 shows the influence of the density filter. The unfiltered topology optimisation yields lower compliances than the benchmark design for the same mass, whereas the filtered topology optimisation, on the other side, yields a compliance that is slightly higher than the compliance of the benchmark design. For very low mass constraints, the filtered topology optimisation yields very high compliances. This is caused by the density filter, because the mass cannot be distributed in a way, that a connection between the outer cylinder and the bearing is established.

The top part of Fig. 6.5 shows the resulting design of the static unfiltered topology optimisation at the point of the Pareto front that shows roughly the same compliance as the benchmark design. The total strain energy, which is an indication for the compliance of the system, is 157J and the mass is 13039kg. That is 96% of the total strain energy of the benchmark solution and 81% of the mass of the benchmark solution.

The bottom part of Fig. 6.5 shows the design that is produced by the filtered topology optimisation. This design performs slightly worse than the benchmark design. The mass at 99% slightly below the benchmark design, whereas the strain energy of 186J is slightly above the benchmark design of 164J. Tab. 6.2 shows the comparison of the various optimisation results.

Modal Optimisation

The static solution was used as an initial guess for the dynamic optimisation. This speeds up the optimisation process, because the

boundary conditions of the optimisation problem are a priori satisfied.

The load for which the structure is optimised is given by Sec. 5.3.5. For a rotation speed of 18rpm, which is the maximal rotation speed of the turbine the maximal excitation frequency is

$$\frac{\omega_{max}}{\omega_{ref}} = n_{lcm} \frac{2\pi n_{max}}{60\omega_{ref}} \quad (6.36)$$

where n_{max} denotes the maximal number of revolutions per minute of the turbine, ω_{max} the maximal frequency in the frequency range of interested. ω_{ref} the normalisation rotation speed introduced in Chapter 5 and n_{lcm} denotes the least common multiple of the number of slots and the number of poles defined in (5.12). For the used parameters the frequency range of interest is between $\omega/\omega_{ref} = 0$ and $\omega/\omega_{ref} = 3$. The modal topology optimisation intends to minimise the excitation of any modes in this frequency range. For that 10 modes were computed in each iteration step. If the number of modes in the frequency range of interest exceeds 10 modes, the lowest 10 modes were used for evaluating the optimisation function.

The excitation frequency of $\mathbf{f}_{mag,dyn}$ varies with the rotation speed of the turbine. That is the reason why only the nominator in (5.20) is used in the objective function. The nominator represents the correlation of the spatial distributions of excitation forces and modes. It is independent of the excitation frequency. The optimisation decreases the participation of the modes by either changing their shape, so that they are no longer excited, or it changes their resonance frequency so that they are no longer considered for the optimisation, because they are outside the frequency range of interest.

In contrast to the strain energy in the objective function in (6.35), the scalar product $\boldsymbol{\varphi}_k \cdot \mathbf{f}_{mag,dyn}$ can be positive as well as negative. Therefore, the square of that product needs to be minimised.

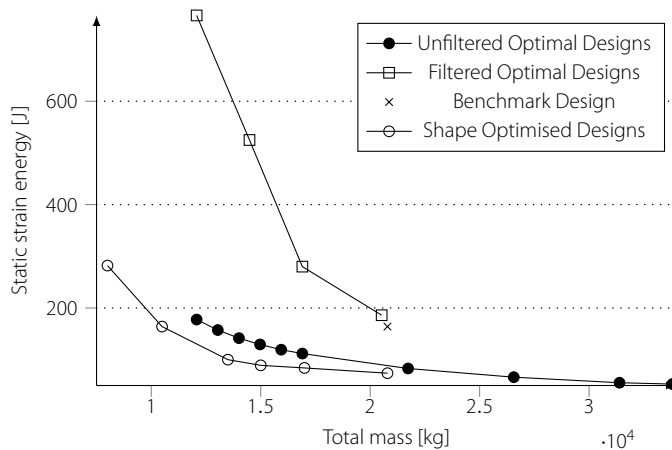


Figure 6.6

Pareto fronts of the various static optimisations

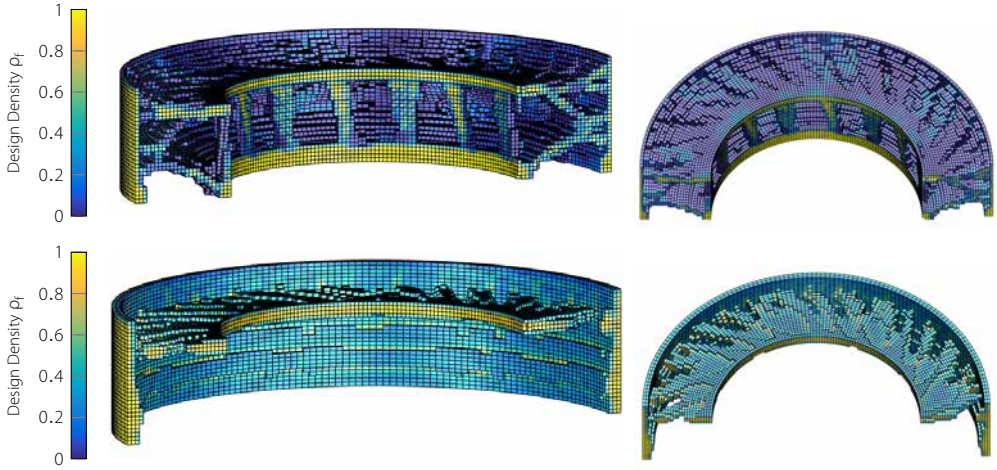


Figure 6.7

The result of the modal topology optimisation without density filter

Using the discrete version of the dynamic excitation forces, $\mathbf{f}_{mag,dyn}$, defined in (5.17), the modal optimisation problem can be written as

$$\begin{aligned}
 & \min_{\rho_f} \quad \sum_k |\boldsymbol{\varphi}_k \cdot \mathbf{f}_{mag,dyn}|^2 \\
 & \text{subject to} \quad \sum_n \rho_n \nu_n - m_{max} \leq 0 \\
 & \quad \quad \quad - \sum_{n \in \Omega_f} \rho_n \nu_n + 0.99 \sum_{n \in \Omega_f} \nu_n \leq 0 \quad (6.37) \\
 & \quad \quad \quad \mathbf{q}_{u,o}^T \mathbf{K} \mathbf{q}_{u,o} - W_{max} \leq 0 \\
 & \quad \quad \quad \rho_f \in [10^{-3}, 1]
 \end{aligned}$$

where W_{max} denotes a maximal strain energy for the static load case, $\boldsymbol{\varphi}_k$ the k^{th} eigenmode that is within the frequency range specified above. $\mathbf{q}_{u,o}$ denotes the static displacement caused by the static forces in (5.16).

The dynamic forces, $\mathbf{f}_{mag,dyn}$, are complex quantities. (6.27) shows that $\partial g_{obj} / \partial \boldsymbol{\varphi}_k$, the derivative of the objective function with respect to the mode shapes, is required to calculate the adjoint variables. Special attention is necessary, when deriving this quantity, because $\mathbf{f}_{mag,dyn}$ is complex. The required derivatives can be computed by

$$\begin{aligned}
 \frac{\partial g_{obj}}{\partial \boldsymbol{\varphi}_k} &= \frac{\partial}{\partial \boldsymbol{\varphi}_k} |\boldsymbol{\varphi}_k \cdot \mathbf{f}_{mag,dyn}|^2 = \frac{\partial}{\partial \boldsymbol{\varphi}_k} (\boldsymbol{\varphi}_k \cdot \mathbf{f}_{mag,dyn}) (\overline{\boldsymbol{\varphi}_k \cdot \mathbf{f}_{mag,dyn}}) \\
 &= \mathbf{f}_{mag,dyn} \cdot (\overline{\boldsymbol{\varphi}_k \cdot \mathbf{f}_{mag,dyn}}) + \bar{\mathbf{f}}_{mag,dyn} \cdot (\boldsymbol{\varphi}_k \cdot \mathbf{f}_{mag,dyn})
 \end{aligned} \quad (6.38)$$

Fig. 6.7 shows the result of the modal topology optimisation while Tab. 6.2 lists the values for compliance, mass and participation factors. All participation factors except the one for the axial mode, are lower than those of the benchmark design.

Comparing the results of the modal topology optimisations in Fig. 6.7 to the results of the static topology optimisations in Fig. 6.5 reveals that the changes are minimal. Apparently, small changes to the structure can have already a large effect on the participation of the modes. It is conspicuous that the modal topology optimisation introduces more intermediate density values, i.e. density values between 0.001 and 1, compared to the static topology optimisation.

Harmonic Optimisation

The harmonic optimisation minimises the dynamic energy associated with a certain excitation. The dynamic energy can only be calculated for a certain excitation frequency and force distribution. The distribution does not change in the case of an electric machine, but the frequency varies with the rotation speed. To cover a certain frequency range, the sum of the dynamic energies over several frequencies within the frequency range has to be minimised. The same frequency range as for the modal optimisation was used. The step size was set to approximately $0.15\omega/\omega_{ref}$. As an initial guess a homogeneous distribution of mass was used.

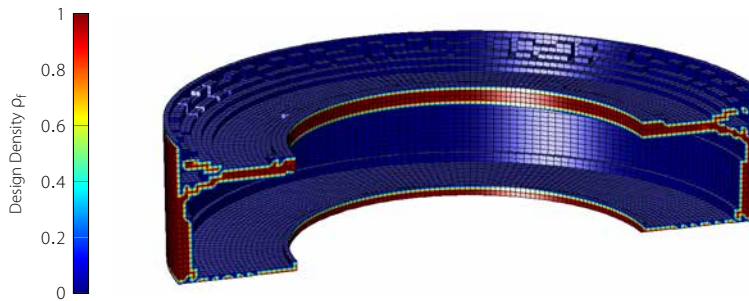


Figure 6.8

The result of the harmonic topology optimisation.

The optimisation problem for the harmonic case can be written as

$$\begin{aligned}
 & \min_{\rho_f} \quad \sum_k \mathbf{q}_u(\omega_k) \cdot \mathbf{f}_{mag,dyn} \\
 & \text{subject to} \quad \sum_n \rho_n v_n - m_{max} \leq 0 \\
 & \quad \quad \quad - \sum_{n \in \Omega_f} \rho_n v_n + 0.999 \sum_{n \in \Omega_f} v_n \leq 0 \quad (6.39) \\
 & \quad \quad \quad \mathbf{q}_{u,0}^T \mathbf{K} \mathbf{q}_{u,0} - W_{max} \leq 0 \\
 & \quad \quad \quad \rho_f \in [10^{-3}, 1]
 \end{aligned}$$

where $\mathbf{q}_u(\omega_k)$ denotes the displacement for an external forced har-

monic excitation that is computed by solving

$$(\mathbf{K}(\rho) + i\omega_k\mathbf{C} - \omega_k^2\mathbf{M}(\rho)) \mathbf{q}_u(\omega_k)e^{i\omega_k t} = \mathbf{f}_{mag,dyn}e^{i\omega_k t} \quad (6.40)$$

\mathbf{C} was created by using a Rayleigh damping with the mass damping parameter $\alpha = 7$ and the stiffness damping parameter $\beta = 2 \cdot 10^{-5}$.

Fig. 6.8 shows the result of the harmonic topology optimisation while Tab. 6.2 lists the values for compliance, mass and participation factors. Some of the optimised participation factors are higher than the participation factors of the benchmark design. Note that the torsional mode was excluded from the optimisation as its resonance frequency is too high.

Shape Optimisation

6.3.2

The shape optimisation uses the solution of the unfiltered topology optimisation and sets up a parametrisation that can represent this solution. Fig. 6.9 shows the parametrisation for the static shape optimisation. Tab. 6.1 lists the design parameters used. To avoid absolute values and use relative design parameters instead the following formulas were used for the parameters in Fig. 6.9 that are not listed in Tab. 6.1.

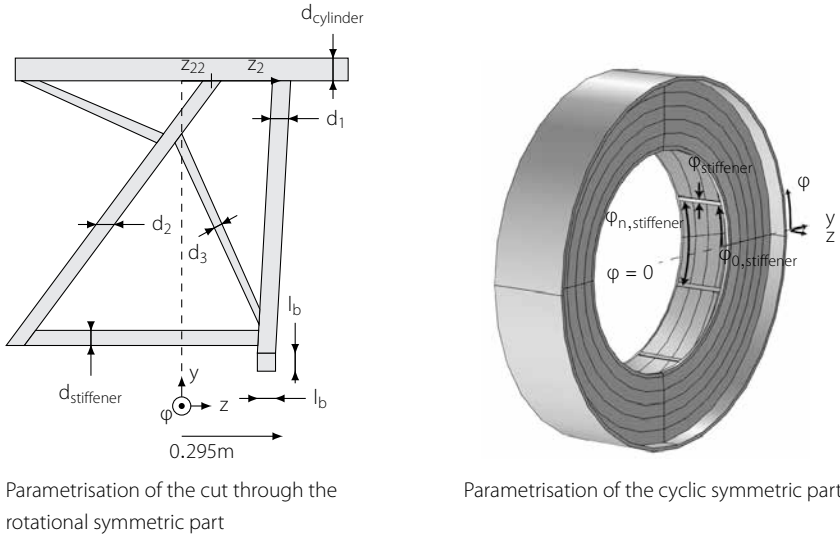
$$z_{22} = (z_2 - (0.55 - d_2/2))f_{22} - (0.55 - d_2/2)$$

$$n_{stiffener} = \text{round}(f_{stiffener}) \quad (6.41)$$

$$\varphi_{stiffener} = \frac{2\pi}{n_{stiffener}} f_{\varphi, stiffener}$$

Parameter Name	Initial Value	min	max	Description
z_2 [m]	0.3	0	0.55	Axial coordinate of outer end of disc 1
f_{22}	0.1	0	1	Dimensionless parameter for the outer end of disc 2
$d_{cylinder}$ [m]	0.02	0.01	0.1	Thickness of outer cylindrical
d_1 [m]	0.03	0.025	0.3	Thickness of disc 1
d_2 [m]	0.03	0.025	0.3	Thickness of disc 2
d_3 [m]	0.03	0.025	0.3	Thickness of disc 3
l_b [m]	0.05	0.025	0.15	Thickness of bearing ring
$f_{stiffener}$	14	4	14	Continuous parameter of number of stiffeners
$f_{\varphi, stiffener}$	0	0.01	1	Parameter for thickness of axial stiffeners in circumferential direction
$\varphi_{0, stiffener}$ [rad]	0	0	22.5	Angle between $\varphi = 0$ and first stiffener
$d_{stiffener}$ [m]	0.01	0.01	0.14	Thickness of stiffeners in radial direction

Table 6.1
Design parameters of the shape optimisation



Parametrisation of the cut through the rotational symmetric part

Parametrisation of the cyclic symmetric part

Figure 6.9

Parametrisation of the geometry for the shape optimisation

This way the absolute geometry values for the axial length z_{22} and the angle $\varphi_{stiffener}$ can be replaced by the values $f_{stiffener}$ and $f_{\varphi, stiffener}$, which relate the values of the former two variables to other design parameters. $n_{stiffener}$ is a discrete parameter that denotes the number of axial stiffener bars in the solution. Because the Nelder-Mead algorithm cannot cope with discrete parameters, $n_{stiffener}$ is computed from the continuous parameter $f_{stiffener}$ by rounding to the next integer.

The parametrisation used in the shape optimisation is very limited with respect to the number of designs that can be represented. But the only purpose of this optimisation is to fine tune the values of the parameters. The rough values were estimated by looking at the optimal design in Fig. 6.5.

The second reason for this shape optimisation is to verify the values for compliance computed by the topology optimisation. Additionally, the shape optimisation checks if the design identified by the topology optimisation as optimal is still stiffer than the benchmark design, when assembled from easy geometries.

The shape optimisation was carried out in Comsol using again the 48 core node already used for the topology optimisation. It took several hours to converge.

The shape optimisation reaches a static compliance of 73.8J at a total mass of 20790kg, the same mass as the benchmark design. With these values it shows a lower compliance than the topology optimised results at 20790kg. Also the shape optimised designs of lower mass constraints show a better static performance than the

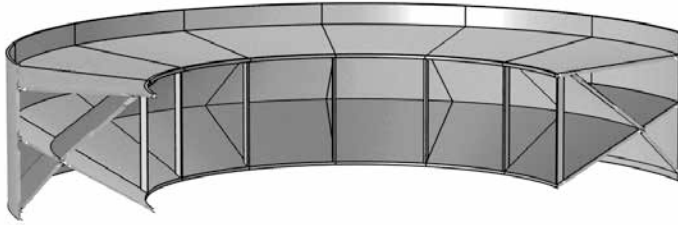


Figure 6.10
Result of the shape optimisation

	Benchmark	Static, unfiltered	Harmonic	Modal, unfiltered	Shape Opt.
Static Strain Energy [J]	164	157	159.1	158	164
Relative Strain Energy [%]	100	96	97	96	100
Total Mass [kg]	20790	13039	20785	15877	10492
Relative Mass [%]	100	62.7	99.9	76	50.4

Mode participation and Frequency						
1 st bending mode	part. fact.	-0.08 - 0.11i	-1.18 + 2.99i	0.11 + 4.14i	0.01 - 0.01i	-2.87 - 4.85i
	norm. Freq.	1.2	1.07	0.79	1.04	1.21
axial mode	part. fact.	0.003 - 0.007i	-26.57 - 12.27i	-0.096 - 0.07i	0.007 + 0.015i	12.05 - 4.65i
	Freq. [Hz]	1.29	1.34	1.02	1.27	1.307
torsional mode	part. fact.	0.1 + 0.27i	36.08 + 45.24i	1.1 + 1.42i	0.02 + 0.04i	
	Freq. [Hz]	3.24	2.925	3.46	2.73	
2 nd bending mode	part. fact.	53.94 + 12.2i	-6.86 + 9i	-2.74 + 9i	-0.14 + 0.19i	5.70 + 8.84i
	Freq. [Hz]	3.2	2.37	2	2.32	2.07

Table 6.2
Results of the optimisation of the single bearing design.

topology optimised designs.

Changing Boundary Conditions

6.3.3

In Sec. 6.3.1 the design of the XD-115 was optimised using topology optimisation. The results of that optimisation are only optimal for the configuration within the XD-115. The solution changes significantly, when the location of the bearing or the load is changed.

The top of Fig. 6.11 shows the solution for the static case when the static load in radial direction is increased by a factor of 14. The bottom of Fig. 6.11 shows the result of the modal analysis when the bearing is moved to the edge of the design domain.

The two parts of Fig. 6.11 show how volatile the results of the topology optimisation are. Even the slightest change of the boundary conditions has an effect on the design. That is why it is impossible to determine one optimal design, but the design should always be

determined in close coordination with the rest of the rotor design.

6.3.4

Discussion

The application of topology optimisation to the generator structure of the XD-115 showed that this method is suitable to improve the design of the XD-115, in particular, and of direct-drive wind turbine generator structures in general. The limited time that was available to implement the algorithms made a more thorough optimisation analysis impossible. The results of the topology optimisation reflect this as they are not as good as they could be if a cutting edge topology algorithm was used. But even this rudimentary code lead to an improved design. This proves the great potential of this method.

All results of the topology optimisation suffer from a coarse mesh that lowers the resolution and thus the minimal thickness of thin walled parts of the structure. An increase of DoFs was not possible due to the memory requirements of the algorithm and the available hardware. Using an algorithm that uses the available memory more efficiently will increase the limit of DoFs and improves the quality of the solution.

The result of the harmonic topology optimisation shows an ambiguous quality. Some of the participation factors increase due to the optimisation, where as others decrease. It is assumed that the problem of multiple summands in the optimisation function, dis-

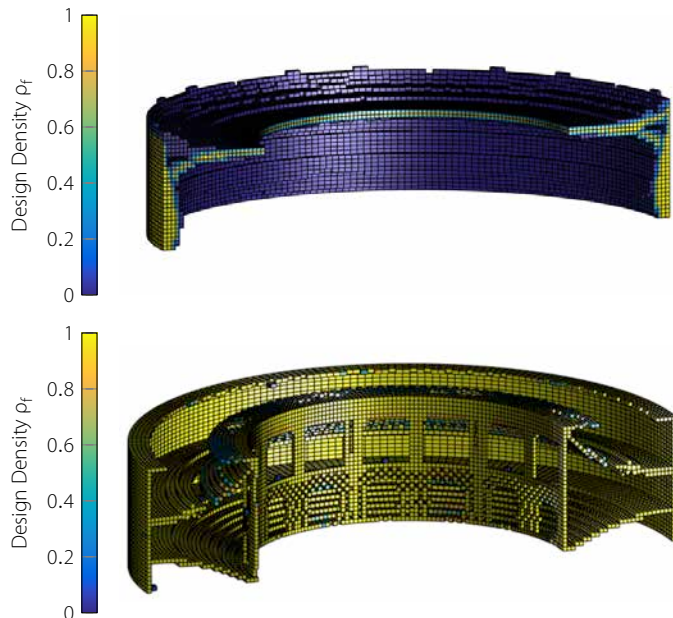


Figure 6.11
The results of the topology
optimisation with changed
boundary conditions

cussed in Sec. 6.2.2 leads to this result. The large step size between the frequencies for which the dynamic compliance is computed is probably the reason for this. The solution might improve by decreasing the step size between the frequencies at which the dynamic energy is evaluated or by increasing the damping in the structure and thereby increasing the participation of modes do not exactly coincide with the discrete frequency steps.

Although, the modal topology optimisation decreases the participation factors of the design, the density distribution is not as black and white as desired. The modal topology optimisation, compared to the static topology optimisation, introduced more intermediate density values, i.e. density values that are neither 1 nor 0.001 as desired. One possible explanation is that the modal topology optimisation does no longer optimise for the compliance, but instead for the participation factors. This way, the penalisation, introduced in (6.17) and (6.16), does not lead to a distinct separation of material and no-material. If this is the reason for the intermediate values, a topology optimisation that minimises the static compliance while setting constraints on the participation factors might resolve the problem. Further research is necessary to confirm this assumption.

The modal topology optimisation is not completely converged. The numbers in Tab. 6.2 indicate this as the mass is not close to the maximal allowed mass. The maximal density change per optimisation step needs to be much lower for the modal optimisation than for the other topology optimisation approaches described here. This, together with the high computational cost of the sensitivities, is the reason, why it took too long to let the solution converge completely. Consequently, a better result than the one presented here is possible.

The modal topology optimisation shows a lot of checkerboard-like structure, just like the unfiltered static solution. Using the solution of the static optimisation problem, the dynamic optimisation problem always converges to the local minimum that is closest to the static solution. This way, the solution of the modal optimisation problem is strongly influenced by the static solution. This is the reason why the solution of the static and modal topology optimisation hardly differ.

Cyclic symmetry plays a major role for dynamic excitation. Depending on the usage, it can either create a high response to a dynamic load or can minimise it. For electric machines, the magnetic forces have a certain cyclic symmetry that depends on the cyclic symmetry of the electro-magnetic active parts of the generator. A mode that does not have the same cyclic symmetry as the magnetic forces, does, theoretically, not get excited by these forces, because

the integral over the circumference of the rotor is zero. This can be explained by the fact that the integral over two sinus functions that have not the same periodicity is also zero

$$\int_0^{2\pi} \sin(k\varphi) \sin(n\varphi) d\varphi = 0 \quad n \neq k \quad (6.42)$$

However, no modes follows a perfect sinus function and so there will always be a small excitation possible.

Nonetheless it is expected, that the cyclic symmetry of the optimised structure will not be the same as the cyclic symmetry of the excitation forces as this reduces the excitation. It is expected that the solution either shows no cyclic symmetry at all or the combination of the cyclic symmetry of the forces and structure is as odd as possible. However, there are other major influences on the cyclic symmetry of the structure. Starting with a cyclic-symmetric design, as done for the dynamic optimisation, will decrease the number of possible solutions, because only a local minimum close to this design will be found. The local minimum will most likely have the same cyclic symmetry as the initial guess. Furthermore, the mesh, can have an influence on the cyclic symmetry, when it is too coarse to support a non-cyclic structure, like a thin disc.

6.4

Double Bearing Configurations

The goal of Sec. 6.3 was to find the optimal topology for the rotor support structure of single bearing generator designs. Now, the focus shifts towards designs incorporating two bearings.

Double bearing designs have the advantage that the bearing can have a smaller diameter, because the load of wind induced torques on the rotor blades can be distributed on two bearings. This has the advantage that the loads on each individual bearing are lower, when the distance between the bearings is large enough.

This section aims to give an impression what the possibilities of topology optimisation are when it is applied to other direct-drive generator designs. The description of the optimised systems will be shorter as for single-bearing designs.

6.4.1

Magnetic Load

Fig. 6.12 shows the domain for the double bearing generator. For this model, the location of the bearings is not a priori determined. They can be chosen freely by the algorithm. The whole area that

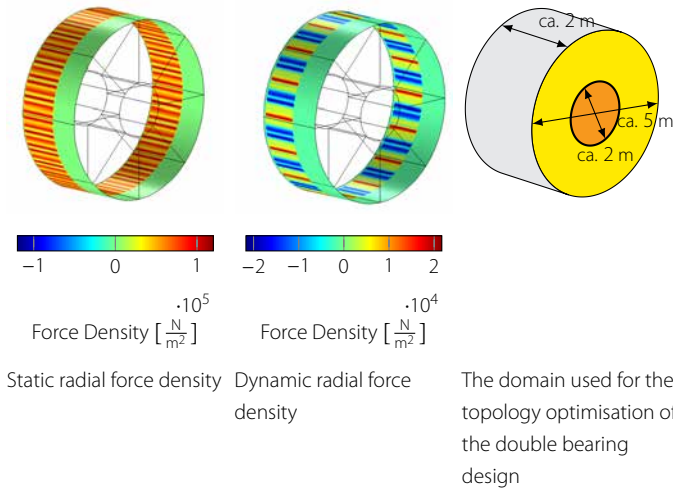


Figure 6.12 Force distribution and schematic of the topology optimisation for the double bearing design

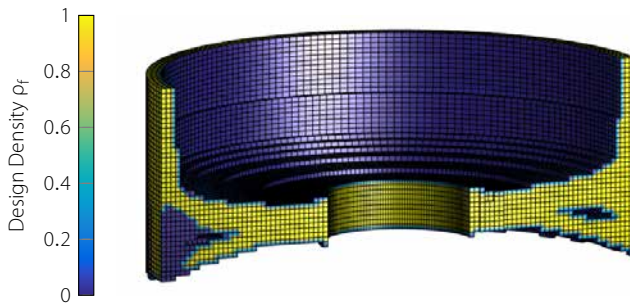


Figure 6.13 The design identified by the topology optimisation for the double bearing configuration

is coloured orange is clamped in radial and axial direction. The topology optimisation algorithm will chose distinct rings on this area for the bearing location. The same is done for the connection to the hub. The whole yellow area is clamped in tangential direction. This way the connection to the hub can be determined by the optimisation algorithm.

Because of a lack of time, only the static optimisation has been applied. The optimisation problem is the same as for the single bearing optimisation and is defined in (6.35). The applied load in the static and dynamic case stays the same as for the single bearing. Because it is not necessary to compare this design to an existing design, a coarser mesh was used, as only the optimal topology is of interest and to what extend it differs from the optimal topology found for single bearing designs.

Fig. 6.13 shows the result of the static topology optimisation for the double bearing design. Although the algorithm could choose the placement of the bearings freely along the inner cylinder (showed in orange in Fig. 6.12), there is only one bearing present. This shows that when only the magnetic forces are taken into account,

the single bearing design is superior to the double bearing design. The connection to the hub is done by a hollow cylinder, of which the diameter is as big as possible.

6.4.2

Including Wind Induced Forces

When looking at the topology of the turbine hub, the electro-magnetic force are not the only forces influencing the design. The wind induced forces play a much larger role when it comes to bearing placement. The bearing placement fundamentally influences the optimal design of the part of the rotor holding the magnets in place. It is, thus, not possible to look at the optimal design without taking into account all forces acting on the rotor.

For this analysis, additional loads were added to the system. A constant torque opposing the magnetic torque of the generator was added at the places where the blade roots are located. Furthermore, gravitational forces of the blade were added. Gravitational forces of the structure self depend on the density and, thus, complicate the optimisation problem significantly. Additionally, a bending moment around the horizontal axis orthogonal to the rotation axis was added that simulates the torque that is produced whenever a blade passes the tower.

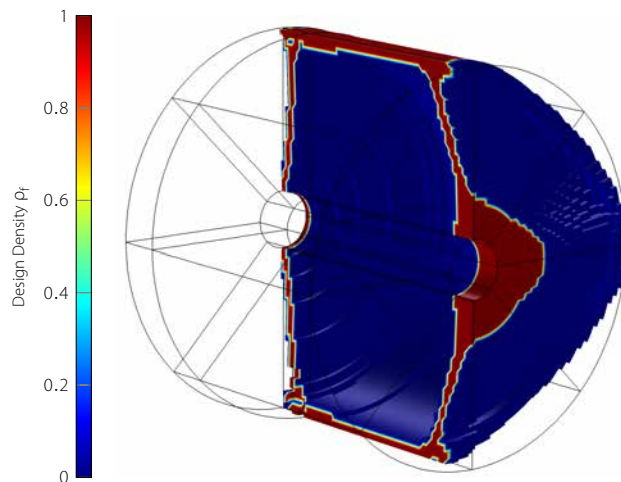


Figure 6.14
The result of the topology
optimisation when wind induced
forces are taken into account

The optimised system includes some constraints and parts of the objective function that are evaluated at rotation and some that are evaluated at stand still. This is necessary, because some forces, such as the gravitational force and some of the wind induced forces change with the rotation of the turbine. A harmonic topology optimisation was conducted with an excitation frequency of $\omega_{ext} =$

$2\pi\text{rad/s}$ for the dynamic forces. The frequency was so low, because its only purpose was to simulate the changing torque and the varying direction of the gravity force. Internal dynamics were not supposed to play a role for this optimisation. The static magnetic forces are the same as in the optimisations before, defined by (5.16).

Fig. 6.14 shows the results of this optimisation, which indicates that the two bearing should be as far apart as possible to support the torque around the horizontal axis. To carry the weight of the blades, the front bearing is directly underneath the blades. This way, the gravitational forces of the blades do not contribute to the torque that is created by the wind around the horizontal axis orthogonal to the rotation axis. The torque is transmitted from the blades to the magnetic active parts of the generators by a hollow cylinder with a diameter that is as big as possible.

Conclusions & Summary

6.5

This chapter covered the improvement of the current design of the XD-115 wind turbine generator rotor and the investigation to what extend the developed methods can be applied to other topologies to improve their designs.

Conclusions

6.5.1

Despite an rudimentary implementation of the topology optimisation algorithm, a substantial weight reduction for the generator rotor structure of the XD-115 could be achieved. This shows that topology optimisation can be used to improve the design of the generator structure of direct-drive wind turbines. However, the results should be used with caution as the optimisation is solely based on minimising the strain energy. The design of a wind turbine generator is, however, strongly influenced by manufacturing considerations. These are not taken into account in this optimisation. The results shown in this chapter can, thus, identify regions in space where material will decrease the compliance of the structure. Whether it is feasible or the resulting design is economically the best, cannot be answered.

During the application of the topology optimisation to wind turbine generators, the large number of DoFs necessary posed a substantial challenge. The structure spans a rather large volume, while individual elements of the design are comparatively fine. This way, a fine mesh on a large volume is needed, increasing the overall number of DoFs. This high number of DoFs makes expensive computer hardware necessary. Approaches, such as adaptive remesh-

ing, promise an improved DoFs to volume ratio, while retaining a high resolutions [21, 98, 144].

Some design aspects were not accounted for in this chapter. A more thorough analysis of the dynamic behaviour can be achieved when transient responses to wind induced forces and short-circuit failure modes are included in the optimisation. This way, the integrity of the generator could be ensured for extreme load cases. Another aspect, which was disregarded here, is fatigue. In wind turbines, fatigue is one of the main driver behind design improvements. The introduced analysis will have a direct influence on the fatigue of the generator rotor support structure. However, the influence of diminishing the vibration's amplitude on the fatigue was not quantified.

The analysis and optimisation introduced here can also be applied to the generator stator, which usually has the same light weight requirements as the rotor. The structural modelling of the stator is, however, more complicated, due to the lamination of the stator back iron. It is expected that the stator weight reduction can be substantial and even exceed the one for the rotor.

Ideally, the optimisation processes that were introduced here also include the electro-magnetic side of the generator. Research on topology optimisation for electric machines was conducted in [26, 108]. Chapter 2 showed that the structural dynamics and the magnetic field influence each other. Therefore, the design of the generator structure and of the magneto-active parts should be conducted simultaneously. A multi-physical topology optimisation, including the electro-magnetic design and the structure of stator and rotor, is the approach that promises the most light weight, most efficient and most cost effective results. Ideally, the rotation of the rotor is taken into account during the design and optimisation process.

6.5.2

Summary

This chapter showed how topology optimisation can be used to find the optimal structural design for a certain load case and bearing configuration in direct-drive wind turbine generators. These optimal designs do not consider manufacturability of the designs. In a second step, a shape optimisation was performed to verify the results found by the topology optimisation. This way the manufacturability was increased by basing the design on simple geometries.

Employing topology and shape optimisation, the mass of the rotor structure could be decreased by 37 % without any substantial increase in compliance. Instead of decreasing the weight, the re-

duce weight that is not needed to reach the same compliance as the benchmark solution can be used to improve the dynamic behaviour of the rotor structure compared to the benchmark solution. This was done in a second analysis, improving the dynamic performance of the generator structure.

In the final part of the chapter, bearing topology including more than one bearing were investigated, and the optimal topology for the structure identified. However, only few cases were computed due to limited time.



PART III

Discussion and Conclusions

Design Considerations

Abstract:

In Chapter 5 and 6, the dynamic analysis and optimisation of the generator structure was carried out. This research lead to some insights in the dynamics and interdependencies of the various parts of a generator.

This chapter will summarise the gained insights from the chapters before and assemble some guidelines what to look out for and ideas for improvements for the design of generator structures.

7.1

Introduction

In Chapter 5, the dynamic behaviour, including excitation frequencies, of the XD-115 was analysed. The gained insights into the dynamics of a large direct-drive wind turbine generator can be used to identify possible design flaws and short comings of the current generator design of the XD-115. In Chapter 6, several approaches were undertaken to improve the dynamic behaviour of the structure in generators of direct-drive wind turbines. The knowledge gained in these two chapter makes it possible to derive design guidelines for future generator designs.

The functions of the generator structure was already listed in Sec. 1.2.3. A 'good' or efficient design is achieved by fulfilling these functions. The effects discussed here will influence either one or several of those functions and diminish the efficiency or jeopardising the functionality of the generator by either increasing the deformation or the weight of the generator.

The design choices of direct-drive wind turbine generators are also determined by manufacturability and assembly concerns. These have a large impact on the cost of a wind turbine. The focus of the research in the previous sections was on minimising vibration amplitudes and weight reduction. Consequently, the manufacturing and assembly cost associated with the design changes proposed here are unknown.

7.1.1

Dynamic Load Cases

For the dynamic analysis of the turbine, two load cases have to be considered: harmonic and transient load cases. The transient cases include extreme wind conditions, such as the 50 year gust, and failure modes like the a short circuit failure in the generator. Theses load cases create extreme loads for a short amount of time that lead to a large displacement of the rotor. In this case, the maximal allowed stresses within the bearing may not be exceeded. Furthermore, the maximal displacement has to stay within the limits that ensure the integrity of the turbine. For that, the stiffness of the structure and the bearing needs to be sufficiently large.

For the performance under harmonic loading, fatigue plays a major role. Usually, the displacements are small compared to the displacements under transient loading, unless a resonance frequency is excited. The fatigue on the other side, is one of the main design considerations. The wear is usually reduced by reducing the load of the bearing, which can be greatly influenced by the placement and size of the bearing as well as the structural design.

Content of Chapter

7.1.2

This chapter will summarise the important influences on the dynamic behaviour of wind turbine generators and their origins. For that, various aspects of the generators are examined. Important points, to which attention needs to be paid during the design process, will be indicated. Further, ideas for design improvements are given.

This chapter will start by discussing the influence of the bearings on the structural dynamics. Although the focus of this thesis was on magneto-mechanical coupling, the bearing influence was not completely neglected as it has an effect on the structural dynamics and interacts with the magneto-mechanical coupling. Afterwards, the influence of the magneto-mechanical coupling on the modal parameters, as explained in Chapter 3, and the influence of the excitation mechanism in Chapter 5 are discussed. Finally, the influence of cyclic symmetry, which was identified in Chapter 6 is discussed.

For all these effects, important consideration affecting the design and possible solution approaches are identified.

The Influence of Bearings

7.2

Bearings have a major impact on the structural dynamics of the generator rotor structure. Therefore, they have to be taken into account when analysing the structural dynamics of the rotor or when analysing magneto-mechanical coupled dynamics.

There exist a number of various bearing topologies including one, two and even three bearings. The review paper by Stander et al. [145] gives a good overview of the various topologies of bearings and support structures of direct-drive wind turbine generators.

Functions of Bearings

7.2.1

The bearing within the generator of a wind turbine has three functions:

- Allow rotational movements of the rotor relative to the stator of the generator with as little friction as possible.
- Transmit any forces and bending moments induced by the wind or by gravity in axial and radial direction to the static part of the nacelle.
- Transmit any radial or axial forces of the magnetic field in the generator to the static part of the electric machine.

The requirements of the bearing include that it is as stiff as possible in radial and axial direction, in order to minimise the displacement caused by a certain force, and to produce as little friction as possible during rotation, to maximise the efficiency of the wind turbine. Furthermore, its life time should be as long as possible, i.e. the wear as small as possible. Some of these requirements contradict each other.

7.2.2

Magnetic Load

As shown in Sec. 6.4, the influence of the magnetic forces on the bearing design is small as these ideally even each other out over the circumference of the generator. Only due to imperfections, magnetic forces can act on the bearing. An eccentricity, for instance, usually leads to a radial rotating magnetic force on the bearing.

This is different, for transient loads. Short circuit failures will apply a radial forces as well as a huge torque to the rotor and stator of the turbine. While the torque in such a case is of minor importance for the bearing design, the reduced radial force at the location of the short circuit will create a net translational force acting on the bearing. To what extent this force is important for the bearing load and the total displacement of the rotor needs to be clarified in future research.

7.2.3

Wind Induced Forces

Wind induced forces and moments play a much larger role than magnetic loads for the bearing placement and design, as these apply large translational and rotational forces (bending moments) to the rotor that need to be counteracted by the supporting forces in the bearing.

As shown in Sec. 6.4, the various bearing topologies cope with wind induced bending moments around the horizontal axis of the turbine by increasing the distance between bearings or bearing elements. For designs including several bearing, the distance between the bearings is increased, while for single bearing designs, the diameter of the bearing is enlarged. This increases the leverage of the bearing forces and decreases the bearing loads, when the total wind induced torque is constant. Consequently, the stress on the bearing elements and, thus, the wear of the bearing is decreased. Designs including several bearings have an advantage in this case, as the maximum diameter of a rolling element bearing is limited. Designs including several bearings can, thus, reach a much larger leverage than a single bearing design.

Large single bearing designs with cylindrical bearing elements lead to additional wear in the bearing, because slipping is difficult to avoid, leading to increased friction and consequently to additional heat loss and wear on the bearing elements as well as on the race ways. A long distance between bearings has the disadvantage that the nacelle gets very long or the design becomes unfeasible.

The Influence of the Static Magnetic Field

7.3

The interaction between the magnetic field and the structure of the generator, which was thoroughly explained in Chapter 2 and 3, can lead to various effects. Using the test set up in Chapter 3, most of the resulting effects were explained. Chapter 5 showed that the structural dynamics are dominant in generators of wind turbines. However, the influence of the magnetic fields can cause the dynamics of the complete system deviate from the structural dynamics in several ways.

Changing Modal Parameters

7.3.1

For generators of wind turbines, the resulting effects of the coupling are the same as for the test set-up in Chapter 3. The modal parameters of the coupled system differ from the modal parameters of the uncoupled systems, when the structural dynamics interact with the magnetic field and vice versa. This can either mean that the resonance frequencies change or that the damping increases compared to the uncoupled systems. The modal parameters change when the energy transferred between structural system and magnetic field is sufficiently large, as explained in Sec. 4.4.1. This happens when the stiffness of the structure, and consequently the energy stored in the vibration of the structure, is so low that the exchanged energy represents a significant part of the total vibration energy.

The exchanged energy depends on the magnetic forces as well as the magnetic flux density in the air gap. The latter quantity hardly deviates from an average value over all generators, because generators are all designed to operate in saturation. The saturation limits the magnetic flux density to a certain value.

When designing a new generator, it is thus important to check the relation between internal forces of the structure, i.e. internal energy, and magnetic forces, i.e. energy that is exchanged between the two physical domains.

The changing modal parameters do not necessarily pose a problem. The change becomes important, when excitation frequencies are

present. In that case, it is imperative to know the modal parameters exactly to avoid excitation.

7.3.2

Rotor-Stator Coupling

Coupling of the beam and yoke or rotor and stator was left out in Chapter 3 and 5, respectively. The magnetic field between stator and rotor acts as a weak spring on the structure. Modes of the rotor and stator can be coupled by this spring, when they fulfil two conditions:

- The stator and rotor mode's resonance frequencies are close together.
- The shape of the stator and rotor modes are similar.

An ovalisation or bending mode of the rotor structure can thus couple with an ovalisation or bending mode of the stator structure, if the resonance frequencies are close together and both modes have the same shape. When designing the generator, the resonance frequencies of stator and rotor should not coincide.

7.3.3

Nonlinear Dynamics

The magnetic field can introduce nonlinear dynamics. The coupled system is nonlinear, as shown in Chapter 2. The linearisation introduced in that chapter is only valid around the linearisation point. The magnetic forces, however, do not change linearly with a displacement. When the amplitude of a mode is large enough, the nonlinear effects of the magnetic field can appear and lead to nonlinear dynamic behaviour of the structure. This can lead, for instance, to a dependency of the resonance frequency on the amplitude of the excitation.

7.3.4

Other Aspects

There are some other aspects, that are of minor importance but should be mentioned nonetheless.

A research area, which has not been looked into, are the interaction between modes influenced by rotor dynamics and the two-way magneto-mechanical coupling. This would answer questions about the influences of whirl on the magneto-mechanical coupling and the effect that the increased imbalance force caused by the magnetic field has on modes with whirl. The influence of the magnetic

field on a whirling eigenmode and other phenomena of rotor dynamics cannot be simulated by the models introduced in Chapter 2 as it does not include rotation.

Another aspect of the interaction between the magnetic field and the structure is the effect that the structural modes have on the currents in the coils. The movement of the modes change the inductance of the coils, inducing higher harmonics in the produced currents. For direct-drive generators, this aspect is however minor, as the full frequency converter in the turbine filters these higher harmonics. The current measurements, shown in Appendix B show that there are no resonance frequencies present in the generator current. Therefore, the resonance frequencies have no influence on the current quality of the turbine. According to [38], the current of smaller induction machines are influenced by bearing frequencies. It can be assumed that also DFIG generators are influenced by this. It needs to be investigated if structural frequencies can also be picked up in this case.

Excitation by Magnetic Forces

7.4

The excitation of structural modes by magnetic forces was covered extensively in Sec. 5.3.3. It was shown that the excitation forces have a significant impact on the vibrations of the generator structure. For the XD-115, they are the single source of excitation.

However, the case that the resonance forces and the excitation frequencies produced by the space harmonics coincide cannot be generalised. It is caused by a combination of pole numbers, slot numbers and a certain amount of stiffness of the structure. Changing any of these parameters may lead to a very different response of the system to the excitation originating from magnetic forces.

Space Harmonics

7.4.1

The interaction of space harmonics caused by the distributions of the coils with space harmonics of the rotor field create harmonic forces at frequencies which are a multiple of the rotation speed. Which harmonics are created depends on the number of slots and poles. Besides the explanations given in Sec. 5.3, [156] investigates this extensively. Other influences on the magnetic forces such as loading and shape of the pole shoes are investigated in [155, 157] for low speed direct-drive permanent magnet generators. In direct-drive wind turbine generators, these force harmonics can coincide with resonance frequencies, because the rotation frequencies are so low.

For the case that the force harmonics and resonance frequencies coincide, like in the XD-115, the frequencies can be separated by increasing the rotation frequencies. This will lead to higher excitation frequencies. At higher frequencies, local modes dominate the dynamic behaviour. These modes are usually not excited by global forces distributions such as the magnetic forces. It is, thus, expected that the dynamic behaviour of the generator structure improves. In this case, it needs to be ensured that the resonance frequencies of the global modes are higher than the highest excitation frequencies created by imbalances or ovalisation and lower than the lowest frequencies caused by space harmonics. These excitation frequencies are much lower than the magnetic force frequencies in machines with high pole numbers. A similar effect can be achieved by reducing the stiffness of the rotor, decreasing the resonance frequencies.

The pole/slot combination is usually chosen in a way that very large least common multiples and very small greatest common dividers are achieved. This guarantees that the torque cogging is small because this way the phase shift between neighbouring magnets is as low as possible and, consequently, more magnets generate a torque with a slight phase shift (see Sec. 5.3 for details). The decreased amplitude of the torque cogging is paid for by an increase in frequencies at which torque cogging happens. In the case for the XD-115, five neighbouring magnets create the same torque cogging with a slight phase shift. This means that there are four additional frequencies at which torque cogging is visible in Fig. 5.6.

From a structural dynamic point of view, there is no reason why torque ripple should be avoided. The mass and inertia of the rotor is so large that the torque ripple is negligible. Furthermore, dealing with only one frequencies makes it easier to separate the excitation frequency from the resonance frequencies. However, for the start up of the turbine a low torque cogging can be beneficial.

7.4.2

Time Harmonics

Another effect that can cause higher harmonics in the forces are time harmonics. Time harmonics are created by the switching of the frequency converter used in direct-drive wind turbines. The switching introduces higher harmonic in the current of the turbine and consequently also in the spatial distribution of the magnetic field. Therefore, the effect of space harmonics and time harmonics on the force harmonics is quite similar.

For smaller machines this effect, and its effect on vibrations in electric machines, has been studied in the past [86, 112]. In direct-drive wind turbine generators, these effects have not been studied. The measurements in Chapter 5 and in Appendix B indicate that for

direct-drive wind turbines, the time harmonics are too high frequent compared to the global resonance frequencies. They do not excite any of them.

Force Distribution

7.4.3

The method of separating the excitation and resonance frequencies from each other to avoid excitation was already mentioned in above. In Chapter 6, another method, based on the spatial distribution, was introduced. This method uses topology optimisation to find a design of the rotor support structure that is not excited by the magnetic forces because of the spatial distribution of the mass of the structure and the magnetic forces.

The method using the separation of frequencies has the drawback that either the ideal pole/slot combination cannot be used or the structure of the rotor and stator need to be modified that they do not coincide with the excitation frequencies. In the second approach, the resonance frequencies are pushed either towards very high or very low frequencies. This makes the structure of rotor and stator either very stiff or very compliant. Both have disadvantages, as either the structure becomes very heavy or the displacements created by static loads become very large.

The new method to optimise the generator design, introduced in Chapter 6, can decrease the excitation of the structure without any of the drawbacks mentioned above.

Cyclic Symmetry

7.5

When it comes to excitation, cyclic symmetry is important. The cyclic symmetry of the magnetic forces is determined by the cyclic symmetry of the electro-magnetic active parts of the generator. Choosing another cyclic symmetry for the structure than for the electro-magnetic construction, results in mode shapes that have a different cyclic symmetry than the electro-magnetic forces. This will most likely lead to mode shapes that are hardly excited by the magnetic forces.

Another phenomenon which is associated with cyclic symmetry are travelling waves in the structure. This happens when the rotor experiences a static force at a fixed position on the rotor. The rotation of the rotor transforms this force into a harmonic load in the rotating reference frame. For the case that the rotor is perfectly point symmetric or cyclic symmetric, i.e. there are two modes at the same resonance frequency that are rotated by 90° , this force can

create a travelling wave in the rotor, of which the amplitude is fixed in the stator frame.

7.6

Summary

This chapter collects various effects and design consideration that have an influence on the dynamics of a direct-drive wind turbine generator. Design challenges that are linked to the dynamics of the generator were identified and possible solutions discussed.

The chapter focuses on the influence of the bearing, the magneto-mechanical coupling and symmetry within the generator. All these aspects influence the dynamic performance significantly. Bearing placement and type have a huge effect on the dynamic behaviour of the turbine rotor, although they are of less importance for the magnetic loading within the generator. Depending on the stiffness of the structure, magneto-mechanical coupling can have a major influence on the structural dynamics of the generator, as it can affect the modal parameters as well as excite the structure. It is, therefore, essential to be aware of the excitation frequencies as well as the exact value of the modal parameters. Cyclic symmetry is a tool that can be used either to minimise or increase excitation. Proper use of it is essential for an efficient wind turbine design.

Using the XD-115 as a benchmark for current generator design, it can be concluded that there is potential for improving the design of wind turbine generators by taking into account the above aspects during the design phase of the turbine.



Conclusions & Outlook

8.1

Conclusions

In Chapter 1, it was discussed that one of the challenges for the success of direct-drive wind turbines in the future is the weight reduction of the nacelle. Many approaches have been proposed how to deal with this challenge (see Chapter 1.2.2). This thesis followed the approach of designed flexibility. It looked at the internal dynamics of the wind turbine generator and identified to what extend a detailed analysis of it could contribute to the goal of reducing the weight of the nacelle. Along the way, it developed methods to predict the coupled dynamics and investigated to what extend existing methods can be applied to wind turbine generators to achieve weight reduction.

In particular, the thesis looked at the appropriate modelling techniques to accurately simulate magneto-mechanical coupling. Afterwards it built a two-way coupled model of the generator structure and the magnetic field. The model was used to conduct an optimisation, to see to what extend the weight of the structure could be reduced and to determine the influence of the excitation forces created by the magnetic field on the general design trade-offs of the wind turbine.

This section will summarise the conclusions that were drawn in the various chapters of the thesis.

8.1.1

Modelling Dynamics of Direct-Drive Wind Turbine Generators

Part I of this thesis covered modelling techniques and reduction techniques of magneto-mechanical coupled systems in electric machines.

Magneto-Mechanical Coupling

In chapter 2, a method was introduced that made it possible to identify the dynamics of the coupled mechanical and magnetic systems. A literature survey showed that, although the methods to couple the magnetic and mechanical systems statically is well understood, the dynamic coupling of the two physics still needs to be investigated. Furthermore, the practical implications of this coupling, a change of modal parameters, need further research. It was argued for wind turbine generators that this coupling can be especially important. The conditions that need to be satisfied for this coupling to play a major role, a low stiffness of the structure and

large magnetic forces, can be satisfied in compliant direct-drive generators.

The measurements conducted in Chapter 3 identified that the accuracy of the magneto-mechanical coupled model depends largely on accurate values of the material parameters. This is a challenge, as usually either the mechanical or the magnetic properties of a material are known.

The scientific contributions of the Chapters 2 include the collection of all relevant modelling techniques and formulas to form a consistent set of equations for modelling magneto-mechanical coupled vibrations in electric machines. Furthermore, it derives the damping cross coupling terms for the coupled damping matrix of the system. These are required to form a monolithic eigenvalue problem, which makes it possible to predict the influence of the magnetic field onto the modal parameters, including the modal damping. The formulation of the monolithic eigenvalue problem is validated in Chapter 3 by lab measurements.

Model Reduction Techniques

In Chapter 4, model order reduction techniques were introduced that can address the challenge of solving large coupled problems, as those that arise when analysing wind turbine generators in 3D.

The techniques introduced in Chapter 4 can reduce computation time significantly and accelerate the analysis process of magneto-mechanical coupled systems. The reduction techniques can also be used for reducing the computational cost of purely magnetic systems. It was shown that they are especially effective for electric machines. However, for this application they lack the capability of taking nonlinear effects such as saturation and hysteresis into account.

The scientific contributions of Chapter 4 includes the introduction of modal analysis for quasi-static magnetic fields and the physical interpretation of its modal parameters. Furthermore, the investigation to what extent models of quasi-static magnetic fields can be reduced using reduction methods based on modal analysis. Finally, this chapter developed ideas how the reduction methods can be extended to magneto-mechanical coupled systems.

Application to Wind Turbine Generators

8.1.2

Part II of the thesis focused on the application of the methods introduced in Part I and on improving the design of the structure of

direct-drive wind turbine generators. Some major design improvements could be identified.

Dynamics of the XD-115

Applying the methods introduced in Chapter 2 to the XD-115 identified that the rotor structure is so heavy and stiff that the two-way coupling plays no role. Consequently, a one-way coupled analysis was conducted, for which the magnetic forces were seen as excitation forces.

The thorough dynamic analysis of the XD-115 generator showed that the generator is well designed, dynamically seen. Although the magnetic forces show a significant fluctuation locally, the resonances of the structure are not significantly excited. The dynamic forces created by space harmonics and torque cogging were identified as crucial, as they are in the same frequency range as global resonance frequencies. Measurements confirmed that these resonance frequencies do get excited, but the maximum amplitude is low and, consequently, the vibration pose no problem for the functionality of the turbine's generator. However, it was impossible to find the reason why certain modes are excited while other modes are not. It was assumed that this is caused by imperfections or manufacturing tolerance, but further research is necessary.

The model of the generator was validated using vibration measurements. These measurements were conducted in-situ, which posed some challenges, such as the large mass that needed to be excited. The use of a mix of experimental and operational modal analyses techniques eventually yielded results that could validate the generator model.

The scientific contributions of Chapter 5 include a two-way coupled modal analysis of an electric machine and, consequently, the identification to what extent the modal parameters change due to the magneto-mechanical coupling. Furthermore, this chapter conducted a thorough one-way coupled dynamic analysis of a generator of a direct-drive wind turbine, identifying excitation frequencies and their effect on the structure of the generator. The simulation results were validated by in-situ vibration measurements. During the vibration measurements, various excitation techniques were investigated for the generator of direct-drive wind turbine generators.

Topology Optimisation of Wind Turbine Generators

The goal of the optimisation in Chapter 6 was the improvement of the current design of the XD-115 as well as looking at other to-

pologies and identifying possible design improvements for them. For this analysis, the magnetic force distribution from Chapter 5 was used as load case for a topology and shape optimisation of the generator's rotor structure. It was shown that topology optimisation in combination with shape optimisation is a suitable method to identify ideal designs for the generator structures of direct-drive wind turbine generators.

The topology and shape optimisation showed that the generator of the XD-115 is rather heavy and could be lighten without any compromises for the performance. The topology optimisation indicated that a weight reduction of 37 % is possible. Furthermore, the dynamic behaviour, i.e. the amplitude of the response of the system to magnetic loads encountered during the operations of the turbine, could be significantly improved without increasing the weight of the generator.

The optimisation of the single-bearing design, as well as other generator topologies, singled out the optimal shape of the rotor and identified some ideas for design improvements. However, it was shown that the optimal design is very sensitive to the boundary conditions, such as bearing placement and exact loading. Further, it was identified that the magnetic forces only have an influence on the design of the the rotor between bearing and magnetic-active material. The design of the hub and in particular bearing placement and dimensions depend entirely on the wind induced forces.

The scientific contributions of this Chapter 6 includes the investigation to what extend topology optimisation can be sued to improve the design of wind turbine generator structures. Topology optimisation make it possible to realise the idea of minimising not the torque ripple, but the vibrations that torque ripple causes in the structure. Finally, it investigates to what extend an dynamic analysis can lead to an improved dynamic performance of direct-drive generator structures without compromising on the functionality and identifies a methodology how to identify the optimal static and dynamic design for direct-drive wind turbine generator structures.

Research Outlook

This thesis covered various topics that are important for the design improvement of the generator structure. Because of time limitations, it did not go deeper into the respective fields it covers. Further research, to improve the various methods introduced in this thesis, is of course desirable.

8.2

8.2.1

Calculation Methods

The modelling of magneto-mechanical coupling, which was introduced in Chapter 2 and the model reduction techniques introduced in Chapter 4 cover the basics of dynamic analysis and model reduction of systems including magneto-mechanical coupling. Further research to improve the accuracy and include more details can be conducted. In particular the following points present themselves for further research on magneto-mechanical coupled dynamics:

- Include the rotation of the rotor into the modal analysis by using so called pseudo modes [85, 87]. This method would allow the analysis of the generator dynamics under rotation. Taking the armature field into account would be possible and potential influences of the structural vibrations onto the generated currents would be visible.
- Include magnetic saturation into the coupled modal analysis to account for the nonlinear magnetic material behaviour. This is rather difficult as modal analysis is based on linear superposition which is not possible anymore for nonlinear systems.
- The armature field does have an effect on the modal parameters of the system, although it was neglected in this thesis. Including the strengthening of the field due to the coils in the stator, is implemented easily. The exact effects the rotating magnetic field has on the dynamics is more complex and requires extensive research.
- Explore the influence of stator-rotor coupling. In this thesis, the stator was assumed to be rigid. In a real turbine, however, the stator is just as flexible as the rotor and contributes further. On top of that, modes in the stator and rotor could couple through the magnetic field, and create new resonance frequencies. This analysis can be conducted with the modelling techniques introduced in Chapter 2. However, the necessary models would be too large to be solved without reduction techniques.
- Investigate nonlinearity of modes caused by the magnetic forces. Changing magnetic forces act as a nonlinear spring for the mechanical system, even when the materials in the magnetic field behave linearly. Consequently, the coupled modes should be nonlinear too. To what extent this effect is important and what kind of nonlinearity is created, remains unknown.
- Incorporate a better bearing model that includes nonlinear contact mechanics. In this thesis, the bearing model is rather

simple. It is approximated by a constant stiffness. The bearing is however a much more complex system, that includes nonlinear contact dynamics.

- The lamination in the stator is not an isotropic materials. Neither is it an orthotropic material. Further research is necessary to identify modelling methods that are able to accurately simulate this highly complex system. First approaches to this topic were introduced in Sec. 1.3.3.

Model Reduction

8.2.2

- The largest drawback of the methods described in Chapter 4 is their inability to handle saturation and hysteresis losses. This results from the modal analysis which is at the heart of all these reduction methods. Further methods to cope with the nonlinear effects need to be developed. For magneto-mechanical systems, an approach using modes and modal derivatives is beneficial as it integrates nicely with the reduction methods used for the structure.
- As mentioned in Sec. 4.6.1, it is expected that a mixed formulation of model order reduction techniques will yield good results. The dynamic of the structure is dominant, while the dynamic of the magnetic field has a rather limited influence. Therefore, it seems advantageous to use the CB method for the structural part of the system and the DCB method for the magnetic part. How well this reduction method simulates the coupled system needs to be researched.

Optimisation

8.2.3

The main challenge during the optimisation was the number of DoFs necessary to simulate the structure. Consequently, the proposed future research is aiming at overcoming this.

- Include cyclic symmetry in modal topology optimisation. Cyclic symmetry is a key property of electric machines and can be used to reduce the number of DoFs in the system. The Floquet theory is a method that allows to do this [85, 87]. This method can also be used in modal topology optimisation to reduce the DoFs
- As mentioned in Chapter 7, looking at the mechanical and the magnetic domain simultaneously in the design phase of the generator can alleviate many vibration problems. The

ideal solution for this, would be a coupled topology optimisation taking both domains into account. There are research approaches for topology optimisation for the electro-magnetic part of electric machines [24, 88].

- Include transient optimisation in the optimisation process. The optimisation methodology introduced in Chapter 6 only includes harmonic excitation frequencies. The performance of the structure under transient loads cannot be simulated using this method. Transient topology optimisation is necessary to reproduce the displacements seen during a 50 year gust or a short circuit in the generator.



Appendix

Q

Magnetic Energy in Structures

At the heart of the magneto-mechanical coupling lies the principle of virtual work as it is used to derive the mechanical force from the change of the magnetic energy. In this section, the equations used to describe the change of the magnetic energy will be derived. The derivation is based on the papers [2] and [131] where the same derivations was done for electro static fields. Fundamental for this derivation is the work in [62] as it derives the change of the magnetic flux density and magnetic field under deformation.

We will consider an infinitesimal small domain Ω with the volume V within a deformable structure. This domain can be either a surface in 2D or a volume in 3D. The derivation can be done in both spaces. For simplicity we will use a 2D element. Using the principal of virtual work the force can be calculated that acts on the underlying structure

$$\delta W_{mag} = \delta \bar{\mathbf{u}} \cdot \vec{\mathbf{F}}_{mag} \quad (\text{A.1})$$

where $\delta \bar{\mathbf{u}}$, denotes the virtual deformation that causes the change of the energy, is defined by

$$\bar{\mathbf{x}} = \delta \bar{\mathbf{u}}(\vec{\xi}) + \vec{\xi} \quad (\text{A.2})$$

The Jacobian of the coordinate transform from $\vec{\xi}$ to $\bar{\mathbf{x}}$ reads as

$$\mathbf{J} = \nabla_{\xi, \eta} \bar{\mathbf{x}} = \begin{pmatrix} \frac{\partial x}{\partial \xi} & \frac{\partial x}{\partial \eta} \\ \frac{\partial y}{\partial \xi} & \frac{\partial y}{\partial \eta} \end{pmatrix} = \begin{pmatrix} 1 + \frac{\partial \delta u_x}{\partial \xi} & \frac{\partial \delta u_x}{\partial \eta} \\ \frac{\partial \delta u_y}{\partial \xi} & 1 + \frac{\partial \delta u_y}{\partial \eta} \end{pmatrix} = \mathbf{I} + \nabla_{\xi} \delta \bar{\mathbf{u}}$$

where ∇_{ξ} denotes a spatial derivative with respect to the $\vec{\xi}$ coordinate frame. The inverse can be written as

$$\mathbf{J}^{-1} = \nabla_{x, y} \vec{\xi} = \begin{pmatrix} \frac{\partial \xi}{\partial x} & \frac{\partial \xi}{\partial y} \\ \frac{\partial \eta}{\partial x} & \frac{\partial \eta}{\partial y} \end{pmatrix} = \begin{pmatrix} 1 - \frac{\partial \delta u_x}{\partial x} & -\frac{\partial \delta u_x}{\partial y} \\ -\frac{\partial \delta u_y}{\partial x} & 1 - \frac{\partial \delta u_y}{\partial y} \end{pmatrix}$$

Assuming small deformations, we can assume

$$\frac{\partial \xi}{\partial y} = \frac{\partial y}{\partial \xi}$$

With this assumption

$$\mathbf{J}^{-1} \approx (\mathbf{I} - \nabla_{\xi} \delta \bar{\mathbf{u}})$$

Derivation of Maxwell's Stress Tensor

As shown in [62], the magnetic field and magnetic flux density behave differently under deformation. For the magnetic field strength the change of of the vector for a deformation $\delta \bar{\mathbf{u}}$ is

$$\delta \vec{\mathbf{B}}|_{\delta \Phi=0} = \nabla \delta \bar{\mathbf{u}} \vec{\mathbf{B}} - \vec{\mathbf{B}} \text{tr}(\nabla \delta \bar{\mathbf{u}}) \quad (\text{A.3})$$

For the magnetic field on the other side the variation comes down to

$$\delta \vec{H} \Big|_{\delta I=0} = -\nabla \delta \vec{u} \cdot \vec{H} \quad (\text{A.4})$$

This difference for the variation of the magnetic field and the magnetic flux density will result in the different formulation for Maxwell's Stress Tensor in the case of magnetised material.

It is now possible to calculate the variation of the energy and co-energy based on (A.3) and (A.4). Depending on the material in question the energy and co-energy equations vary. For the magnetic energy, the total flux should be held constant as this is an independent variable. Therefore, (A.3) is used to compute the energy change as (A.3) was computed with the total flux held constant. For a linear magnetic material this yields for the energy

$$\begin{aligned} \delta W_{mag} \Big|_{\delta \Phi=0} &= \delta \left(\frac{\vec{B}^T \vec{B}}{2\mu} V \right) = \delta \left(\frac{\vec{B}^T \vec{B}}{2\mu} \right) V + \delta V \left(\frac{\vec{B}^T \vec{B}}{2\mu} \right) \\ &= \frac{\vec{B}^T \delta \vec{B}}{\mu} V + \delta V \left(\frac{\vec{B}^T \vec{B}}{2\mu} \right) \end{aligned} \quad (\text{A.5})$$

δV denotes the change of the domain's volume. Neglecting second order terms it can be written as

$$\delta V = \text{tr}(\nabla \delta \vec{u}) V \quad (\text{A.6})$$

Inserting (A.6) into (A.5) yields

$$\begin{aligned} \delta W_{mag} &= V \frac{\vec{B}^T}{\mu} \left[\nabla \delta \vec{u} \vec{B} - \vec{B} \text{tr}(\nabla \delta \vec{u}) \right] + \text{tr}(\nabla \delta \vec{u}) \frac{\vec{B}^T \vec{B}}{2\mu} V \\ &= V \frac{\vec{B}^T \nabla \delta \vec{u} \vec{B}}{\mu} - \text{tr}(\nabla \delta \vec{u}) \frac{\vec{B}^T \vec{B}}{2\mu} V \end{aligned} \quad (\text{A.7})$$

Using the vector identity

$$\mathbf{C}(\mathbf{AB})\mathbf{D} = \mathbf{CD} : \mathbf{AB} \quad (\text{A.8})$$

(A.7) can be written as

$$\delta W_{mag} = V \nabla \vec{u} : \underbrace{\left(\frac{\vec{B} \vec{B}^T}{\mu} - \mathbf{I} \frac{\vec{B}^T \vec{B}}{2\mu} \right)}_{\underline{\underline{\mathbf{T}}}} \quad (\text{A.9})$$

where the part in the parenthesis denotes Maxwell's stress tensor.

Starting from the co-energy and using the variation for \vec{H} in (A.4) will yield the same result for Maxwell's stress tensor in linear ma-

terials.

$$\begin{aligned}
 \delta W'_{mag}|_{\delta I=0} &= \delta \left(\frac{\mu}{2} \vec{H}^T \vec{H} V \right) \\
 &= \mu V \vec{H}^T \delta \vec{H} + \frac{\mu V}{2} \vec{H}^T \vec{H} \delta \\
 &= -\mu V \vec{H}^T (\nabla \delta \vec{u}) \vec{H} + \text{tr}(\nabla \delta \vec{u}) \frac{\mu V}{2} \vec{H}^T \vec{H} \\
 &= \mu V (-\vec{H}^T (\nabla \delta \vec{u}) \vec{H} + \frac{1}{2} \text{tr}(\nabla \delta \vec{u}) \vec{H}^T \vec{H})
 \end{aligned} \tag{A.10}$$

This yields for Maxwell's stress tensor

$$\delta W'_{mag}|_{\delta I=0} = -V \nabla \vec{u} : \underbrace{\left(\mu \vec{H} \vec{H}^T - \mathbf{I} \mu \frac{\vec{H}^T \vec{H}}{2} \right)}_{\underline{\underline{\mathbf{T}}}} \tag{A.11}$$

which yields the same expression for Maxwell's stress tensor as in (A.9), when inserting $\vec{B} = \mu \vec{H}$.

Discretisation of Magnetic Forces

The discrete form of the magnetic force can be computed in two ways using Maxwell's stress tensor. The first way is by multiplying the tensor with a vector normal to a surface, which yield the force on that surface. This was introduced in (2.151).

The other way is to employ the principle of virtual work locally. (A.9) can be written in a way that the displacements gradients are at the front of the equations. For a 2D system this yields:

$$\begin{aligned}
 \delta W_{mag} &= -\vec{f}_{mag} \cdot \delta \vec{u} = \int_{\Omega} \nabla \delta \vec{u} : \underline{\underline{\mathbf{T}}} \, d\Omega \\
 &= \frac{1}{\mu} \int_{\Omega} \left(\frac{B_x B_x}{2} - \frac{B_y B_y}{2} \right) \frac{\partial u}{\partial \xi} + B_x B_y \frac{\partial u}{\partial \eta} + B_y B_x \frac{\partial v}{\partial \xi} + \left(\frac{B_y B_y}{2} - \frac{B_x B_x}{2} \right) \frac{\partial v}{\partial \eta} \, d\Omega
 \end{aligned} \tag{A.12}$$

where B_x and B_y denote the x and y components of the magnetic flux density.

This matrix can be written as a vector multiplication:

$$\delta W_{mag} = \int_{\Omega} \frac{1}{2\mu} \begin{bmatrix} \frac{\partial u}{\partial \xi} \\ \frac{\partial u}{\partial \eta} \\ \frac{\partial v}{\partial \xi} \\ \frac{\partial v}{\partial \eta} \end{bmatrix}^T \begin{bmatrix} B_x^2 - B_y^2 \\ 2B_x B_y \\ 2B_x B_y \\ B_y^2 - B_x^2 \end{bmatrix} \, d\Omega \tag{A.13}$$

Approximating the displacement gradient by using the finite element method yields for the gradient vector.

$$\begin{bmatrix} \frac{\partial u}{\partial \xi} \\ \frac{\partial v}{\partial \xi} \\ \frac{\partial u}{\partial \eta} \\ \frac{\partial v}{\partial \eta} \end{bmatrix} \approx \underbrace{\begin{bmatrix} \frac{\partial N_a}{\partial \xi} & 0 & \frac{\partial N_b}{\partial \xi} & 0 & \frac{\partial N_c}{\partial \xi} & 0 \\ 0 & \frac{\partial N_a}{\partial \xi} & 0 & \frac{\partial N_b}{\partial \xi} & 0 & \frac{\partial N_c}{\partial \xi} \\ \frac{\partial N_a}{\partial \eta} & 0 & \frac{\partial N_b}{\partial \eta} & 0 & \frac{\partial N_c}{\partial \eta} & 0 \\ 0 & \frac{\partial N_a}{\partial \eta} & 0 & \frac{\partial N_b}{\partial \eta} & 0 & \frac{\partial N_c}{\partial \eta} \end{bmatrix}}_{\mathbf{B}_{2u}} \underbrace{\begin{bmatrix} q_{ua} \\ q_{va} \\ q_{ub} \\ q_{vb} \\ q_{uc} \\ q_{vc} \end{bmatrix}}_{\mathbf{q}_u} \quad (\text{A.14})$$

for triangular 2D elements. In (A.14), N_a , N_b and N_c are the components of the shape functions defined in (2.104) and q_{ua} , q_{ub} , q_{uc} , q_{va} , q_{vb} , q_{vc} the nodal values for the displacement in ξ and η -direction at the three nodes of the triangular element. (A.14) defines the matrix \mathbf{B}_{2u} which contains the derivatives of the shape functions, which will be widely used in the following derivations for the various coupling matrices.

Then (A.13) can be written as

$$\delta W_{mag} \approx \frac{1}{2\mu} \int_{\Omega} \mathbf{q}_u \mathbf{B}_{2u}^T \mathbf{F}(\mathbf{q}_A) d\Omega \quad (\text{A.15})$$

where \mathbf{F} denotes a vector containing various products of the magnetic flux density components

$$\mathbf{F} = [B_x^2 - B_y^2 \quad 2B_x B_y \quad 2B_x B_y \quad -B_x^2 + B_y^2]^T \quad (\text{A.16})$$

The magnetic force can then be written as

$$\mathbf{F}_{mag} = -\frac{\partial W_{mag}}{\partial \mathbf{q}_u} = -\frac{1}{2\mu} \int_{\Omega} \mathbf{B}_{2u}^T \mathbf{F}(\mathbf{q}_A) d\Omega \quad (\text{A.17})$$

Maxwell's Stress Tensor in Permanent Magnets

The derivation for permanent magnets is analog. Because the formulation for the energy stored in permanent magnets follows (2.10) the resulting stress tensor will deviate from (A.9). Starting from the energy for permanent magnets as defined in (2.10)

$$W_{pm} = \left(\frac{\vec{\mathbf{B}}^T \vec{\mathbf{B}}}{2\mu} + \frac{\vec{\mathbf{B}}_r^T \vec{\mathbf{B}}_r}{2\mu} - \frac{\vec{\mathbf{B}}^T \vec{\mathbf{B}}_r}{\mu} \right) V \quad (\text{A.18})$$

Taking the variation for a virtual displacement $\delta\bar{\mathbf{u}}$ yields

$$\begin{aligned}\delta W_{pm} &= \frac{\bar{\mathbf{B}}^T \delta \bar{\mathbf{B}}}{\mu} V + \delta V \frac{\bar{\mathbf{B}}^T \bar{\mathbf{B}}}{2\mu} \\ &+ \frac{\bar{\mathbf{B}}_r^T \delta \bar{\mathbf{B}}_r}{\mu} V + \delta V \frac{\bar{\mathbf{B}}_r^T \bar{\mathbf{B}}_r}{2\mu} \\ &- \delta V \frac{\bar{\mathbf{B}}^T \bar{\mathbf{B}}_r}{\mu} - \frac{\bar{\mathbf{B}}_r^T \delta \bar{\mathbf{B}}}{\mu} V - \frac{\bar{\mathbf{B}}^T \delta \bar{\mathbf{B}}_r}{\mu} V\end{aligned}\quad (\text{A.19})$$

The change of the energy of the permanent magnets under deformation depends on the behaviour of the magnetic flux density, the magnetic field and the remanence flux density under deformation. The behaviour of the first two variables was established in (2.4.5) and in [62]. The behaviour of the remanence flux density is not finally settled. It could either behave like the magnetic flux density or it could behave like the magnetic field. Therefore, the two possible case are defined as

$$\delta \bar{\mathbf{B}}_r = \begin{cases} \nabla \delta \bar{\mathbf{u}} \bar{\mathbf{B}}_r - \bar{\mathbf{B}}_r \text{tr}(\nabla \delta \bar{\mathbf{u}}) & \text{case 1} \\ -\nabla \delta \bar{\mathbf{u}} \bar{\mathbf{B}}_r & \text{case 2} \end{cases}\quad (\text{A.20})$$

In this section the operator δ will be used for both cases. Which of the two cases is used will become apparent from the text.

Applying the first case to (A.19) yields

$$\begin{aligned}\delta W_{pm} &= V \frac{\bar{\mathbf{B}}^T (\delta \nabla \bar{\mathbf{u}}) \bar{\mathbf{B}}}{\mu} - V \text{tr}(\nabla \delta \bar{\mathbf{u}}) \frac{\bar{\mathbf{B}}^2}{\mu} + V \text{tr}(\delta \nabla \bar{\mathbf{u}}) \frac{\bar{\mathbf{B}}^2}{2\mu} \\ &+ V \frac{\bar{\mathbf{B}}_r^T (\delta \nabla \bar{\mathbf{u}}) \bar{\mathbf{B}}_r}{\mu} - V \text{tr}(\nabla \delta \bar{\mathbf{u}}) \frac{\bar{\mathbf{B}}_r^2}{2\mu} + V \text{tr}(\delta \nabla \bar{\mathbf{u}}) \frac{\bar{\mathbf{B}}_r^2}{\mu} \\ &- \text{tr}(\delta \nabla \bar{\mathbf{u}}) \frac{\bar{\mathbf{B}}^T \bar{\mathbf{B}}_r}{\mu} - V \frac{\bar{\mathbf{B}}_r^T (\delta \nabla \bar{\mathbf{u}}) \bar{\mathbf{B}}}{\mu} - V \frac{\bar{\mathbf{B}}^T (\delta \nabla \bar{\mathbf{u}}) \bar{\mathbf{B}}_r}{\mu} + 2 \text{tr}(\delta \nabla \bar{\mathbf{u}}) \frac{\bar{\mathbf{B}}^T \bar{\mathbf{B}}_r}{\mu}\end{aligned}\quad (\text{A.21})$$

which yields for Maxwell's Stress Tensor:

$$\begin{aligned}\underline{\underline{\mathbf{T}}} &= \frac{\bar{\mathbf{B}} \bar{\mathbf{B}}^T}{\mu} + \frac{\bar{\mathbf{B}}_r \bar{\mathbf{B}}_r^T}{\mu} - \frac{\bar{\mathbf{B}} \bar{\mathbf{B}}_r^T}{\mu} - \frac{\bar{\mathbf{B}}_r \bar{\mathbf{B}}^T}{\mu} - \mathbf{I} \left(\frac{\bar{\mathbf{B}}^T \bar{\mathbf{B}}}{2\mu} + \frac{\bar{\mathbf{B}}_r^T \bar{\mathbf{B}}_r}{2\mu} - \frac{\bar{\mathbf{B}}^T \bar{\mathbf{B}}_r}{\mu} \right) \\ &= \frac{\bar{\mathbf{B}} \bar{\mathbf{B}}^T}{\mu} + \frac{\bar{\mathbf{B}}_r \bar{\mathbf{B}}_r^T}{\mu} - \frac{\bar{\mathbf{B}} \bar{\mathbf{B}}_r^T}{\mu} - \frac{\bar{\mathbf{B}}_r \bar{\mathbf{B}}^T}{\mu} - \mathbf{I} \frac{(\bar{\mathbf{B}} - \bar{\mathbf{B}}_r)^2}{2\mu}\end{aligned}\quad (\text{A.22})$$

For the second case the magnetic flux density, $\bar{\mathbf{B}}$, and the remanence flux density, $\bar{\mathbf{B}}_r$ behave differently under deformation.

$$\begin{aligned}
\delta W_{pm} &= V \frac{\vec{\mathbf{B}}^T(\delta\nabla\vec{\mathbf{u}})\vec{\mathbf{B}}}{\mu} - V\text{tr}(\nabla\delta\vec{\mathbf{u}})\frac{\vec{\mathbf{B}}^2}{\mu} + V\text{tr}(\delta\nabla\vec{\mathbf{u}})\frac{\vec{\mathbf{B}}^2}{2\mu} \\
&\quad - V \frac{\vec{\mathbf{B}}_r^T(\delta\nabla\vec{\mathbf{u}})\vec{\mathbf{B}}_r}{\mu} + V\text{tr}(\delta\nabla\vec{\mathbf{u}})\frac{\vec{\mathbf{B}}_r^2}{2\mu} \\
&\quad - \text{tr}(\delta\nabla\vec{\mathbf{u}})\frac{\vec{\mathbf{B}}^T\vec{\mathbf{B}}_r}{\mu} - V \frac{\vec{\mathbf{B}}_r^T(\delta\nabla\vec{\mathbf{u}})\vec{\mathbf{B}}}{\mu} + V \frac{\vec{\mathbf{B}}^T(\delta\nabla\vec{\mathbf{u}})\vec{\mathbf{B}}_r}{\mu} + \text{tr}(\delta\nabla\vec{\mathbf{u}})\frac{\vec{\mathbf{B}}^T\vec{\mathbf{B}}_r}{\mu} \\
&= V \frac{\vec{\mathbf{B}}^T(\delta\nabla\vec{\mathbf{u}})\vec{\mathbf{B}}}{\mu} - V\text{tr}(\delta\nabla\vec{\mathbf{u}})\frac{\vec{\mathbf{B}}^2}{2\mu} \\
&\quad - V \frac{\vec{\mathbf{B}}_r^T(\delta\nabla\vec{\mathbf{u}})\vec{\mathbf{B}}_r}{\mu} + V\text{tr}(\delta\nabla\vec{\mathbf{u}})\frac{\vec{\mathbf{B}}_r^2}{2\mu}
\end{aligned} \tag{A.23}$$

which results in the following expression for Maxwell's stress tensor

$$\vec{\underline{\underline{\mathbf{T}}}} = \frac{\vec{\mathbf{B}}\vec{\mathbf{B}}^T}{\mu} - \frac{\vec{\mathbf{B}}_r\vec{\mathbf{B}}_r^T}{\mu} - \mathbf{I} \left(\frac{\vec{\mathbf{B}}^T\vec{\mathbf{B}}}{2\mu} - \frac{\vec{\mathbf{B}}_r^T\vec{\mathbf{B}}_r}{2\mu} \right) \tag{A.24}$$

Discretisation of Magnetic Forces in Permanent Magnets

Like for linear magnetic materials, the forces for permanent magnets can be discretised in two ways. The first one is the multiplication of Maxwell's stress tensor with a normal. This method was introduced in (2.151).

The other one, which is followed here, uses the local principle of virtual work. In the above section, the continuous formulation for Maxwell's stress tensor was derived. For the case the the remanence magnetisation behaves like the magnetic flux density (case one in (A.20)), (A.21) is yielded.

Reorganising (A.21) yields

$$\begin{aligned}
\delta W_{pm} = -f_{mag}\delta\vec{\mathbf{u}} &= \frac{\vec{\mathbf{B}}^T(\delta\nabla\vec{\mathbf{u}})\vec{\mathbf{B}}}{\mu} V - \text{tr}(\delta\nabla\vec{\mathbf{u}})\frac{\vec{\mathbf{B}}^T\vec{\mathbf{B}}}{2\mu} V \\
&\quad + \frac{\vec{\mathbf{B}}_r^T(\delta\nabla\vec{\mathbf{u}})\vec{\mathbf{B}}_r}{\mu} V - \text{tr}(\delta\nabla\vec{\mathbf{u}})\frac{\vec{\mathbf{B}}_r^T\vec{\mathbf{B}}_r}{2\mu} V \\
&\quad - \frac{\vec{\mathbf{B}}^T(\delta\nabla\vec{\mathbf{u}})\vec{\mathbf{B}}_r}{\mu} V - \frac{\vec{\mathbf{B}}_r^T(\delta\nabla\vec{\mathbf{u}})\vec{\mathbf{B}}}{\mu} V + \text{tr}(\delta\nabla\vec{\mathbf{u}})\frac{\vec{\mathbf{B}}^T\vec{\mathbf{B}}_r}{\mu} V
\end{aligned} \tag{A.25}$$

The first two and terms in (A.25) yield again (A.17). The third and fourth terms in (A.25) is the same as the first and second term with $\vec{\mathbf{B}}_r$ instead of $\vec{\mathbf{B}}$. So these two terms can be discretised as

$$\frac{\vec{\mathbf{B}}_r^T(\delta\nabla\vec{\mathbf{u}})\vec{\mathbf{B}}_r}{\mu} - \text{tr}(\delta\nabla\vec{\mathbf{u}})\frac{\vec{\mathbf{B}}_r^T\vec{\mathbf{B}}_r}{2\mu} \approx \frac{1}{2\mu} \int_{\Omega} \mathbf{q}_u^T \mathbf{B}_{2u}^T \mathbf{F}_{PM}(\mathbf{q}_A) d\Omega \quad (\text{A.26})$$

with

$$\mathbf{F}_{PM}(\mathbf{q}_A) = \begin{bmatrix} B_{rx}^2 - B_{ry}^2 & 2B_{rx}B_{ry} & 2B_{rx}B_{ry} & B_{ry}^2 - B_{rx}^2 \end{bmatrix}^T \quad (\text{A.27})$$

The last two terms can be discretised by

$$-\frac{\vec{\mathbf{B}}^T(\delta\nabla\vec{\mathbf{u}})\vec{\mathbf{B}}_r}{\mu} - \frac{\vec{\mathbf{B}}_r^T(\delta\nabla\vec{\mathbf{u}})\vec{\mathbf{B}}}{\mu} + \text{tr}(\delta\nabla\vec{\mathbf{u}})\frac{\vec{\mathbf{B}}^T\vec{\mathbf{B}}_r}{\mu} \approx -\frac{1}{\mu} \int_{\Omega} \mathbf{q}_u^T \mathbf{B}_{2u}^T \mathbf{F}_{PM2}(\mathbf{q}_A) d\Omega \quad (\text{A.28})$$

with

$$\mathbf{F}_{PM2}(\mathbf{q}_A) = \begin{bmatrix} B_{rx}B_x - B_{ry}B_y & B_{rx}B_y + B_{ry}B_x & B_xB_{ry} + B_{rx}B_y & B_{ry}B_y - B_{rx}B_x \end{bmatrix}^T \quad (\text{A.29})$$

Bringing the three terms together yields

$$\begin{aligned} \delta\mathbf{F}_{mag} &= -\frac{1}{2\mu} \int_{\Omega} \mathbf{B}_{2u}^T \mathbf{F}(\mathbf{q}_A) d\Omega \\ &\quad - \frac{1}{2\mu} \int_{\Omega} \mathbf{B}_{2u}^T \mathbf{F}_{PM}(\mathbf{q}_A) d\Omega \\ &\quad + \frac{1}{\mu} \int_{\Omega} \mathbf{B}_{2u}^T \mathbf{F}_{PM2}(\mathbf{q}_A) d\Omega \end{aligned} \quad (\text{A.30})$$

for the magnetic forces on permanent magnets.

For the second case, the remanence flux density behaves like the magnetic field, and the 'imaginary' currents in the permanent magnet are held constant. Starting from (A.23), the discretisation is analog to the first case, yielding

$$\begin{aligned} \delta W_{mag} &= \frac{1}{2\mu} \int_{\Omega} \mathbf{q}_u \mathbf{B}_{2u} \mathbf{F}(\mathbf{q}_A) d\Omega \\ &\quad + \frac{1}{2\mu} \int_{\Omega} \mathbf{q}_u \mathbf{B}_{2u} \mathbf{F}_{PM}(\mathbf{q}_A) d\Omega \end{aligned} \quad (\text{A.31})$$

The coupling matrices for permanent magnet materials can be derived analog to the derivation for the linear magnetic material in, starting from (A.21) and (A.23).

Derivation of Coupling Matrices

In the last section, Maxwells stress tensor was derived from the principle of virtual work. For the monolithic formulation in (2.170), the stiffness coupling matrices, \mathbf{K}_{uA} , \mathbf{K}_{Au} and \mathbf{K}_{uu}^{mag} , need to be derived from the energy. This can be done in two ways. The first way,

the one most FE packages use, takes the force computed according to (2.100) and differentiate it once with respect to \mathbf{q}_A . Here, the approach of the local virtual work is taken, which was introduced in Sec. 2.5.8. As stated in (2.125) \mathbf{K}_{uA} can be computed by deriving the magnetic energy once with respect to \mathbf{q}_A and once with respect to \mathbf{q}_u .

$$\mathbf{K}_{uA} = \frac{\partial \mathbf{F}_{mag}}{\partial \mathbf{q}_A} = \frac{1}{2\mu} \int_{\Omega} \mathbf{B}_{2u}^T \frac{\partial \mathbf{F}}{\partial \mathbf{q}_A} d\Omega \quad (\text{A.32})$$

defining \mathbf{F}_2 as

$$\mathbf{F}_2 = \frac{\partial \mathbf{F}}{\partial \vec{\mathbf{B}}} = \begin{bmatrix} B_x & B_y & B_y & -B_x \\ -B_y & B_x & B_x & B_y \end{bmatrix} \quad (\text{A.33})$$

(A.32) can be written as

$$\mathbf{K}_{uA} = -\frac{1}{2\mu} \int_{\Omega} \mathbf{B}_{2u}^T \mathbf{F}_2 \frac{\partial \vec{\mathbf{B}}}{\partial \mathbf{q}_A} d\Omega \quad (\text{A.34})$$

introducing the approximation (2.135) yields

$$\mathbf{K}_{uA} = \frac{1}{2\mu} \int_{\Omega} \mathbf{B}_{2u}^T \mathbf{F}_2 \mathbf{B}_A d\Omega \quad (\text{A.35})$$

which is the same equation as (2.158).

Analog, \mathbf{K}_{Au} can be derived by first differentiating W_{mag} with respect to \mathbf{q}_A yielding the internal current densities, and then taking the derivative with respect to \mathbf{q}_u .

The other stiffness coupling matrix, \mathbf{K}_{uu}^{mag} is derived by taking the derivative of the magnetic energy with respect to virtual displacements twice. For that, a second virtual displacement

$$\vec{\xi} = \delta^2 \vec{\mathbf{u}}(\vec{\mathbf{X}}) + \vec{\mathbf{X}} \quad (\text{A.36})$$

is introduced, so that

$$\vec{\mathbf{x}} = \delta^1 \vec{\mathbf{u}} + \vec{\xi} = \delta^1 \vec{\mathbf{u}}(\vec{\xi}) + \delta^2 \vec{\mathbf{u}}(\vec{\mathbf{X}}) + \vec{\mathbf{X}} \quad (\text{A.37})$$

To avoid confusion, the first virtual displacement is denoted by $\delta^1 \vec{\mathbf{u}}$. It is then possible to write

$$\delta^1 \vec{\mathbf{u}} \mathbf{K}_{uu}^{mag} \delta^2 \vec{\mathbf{u}} = \delta^2 (\delta^1 W_{mag}) \quad (\text{A.38})$$

The matrix \mathbf{K}_{uu}^{mag} can thus be derived by deriving how the energy change of the first displacement changes with the second displacement. For that the change of the first displacement with respect to the second displacement is needed. Using the Jacobian of the

second displacement, defined by $\mathbf{J}_2 = \mathbf{I} + \nabla \delta \bar{\mathbf{u}}$, this can be expressed by

$$\begin{aligned} \delta^2(\nabla \delta^1 \bar{\mathbf{u}}) &= (\nabla_X \delta^1 \bar{\mathbf{u}}) - (\nabla_\xi \delta^1 \bar{\mathbf{u}}) \\ &= \mathbf{J}_2(\nabla_\xi \delta^1 \bar{\mathbf{u}}) - (\nabla_\xi \delta^1 \bar{\mathbf{u}}) \\ &= (\nabla_X \delta^2 \bar{\mathbf{u}})(\nabla_\xi \delta^1 \bar{\mathbf{u}}) \\ &= \mathbf{J}_2(\nabla_\xi \delta^2 \bar{\mathbf{u}})(\nabla_\xi \delta^1 \bar{\mathbf{u}}) \end{aligned} \quad (\text{A.39})$$

neglecting higher order terms and retaining only squared derivatives yields

$$\begin{aligned} \delta^2(\nabla \delta^1 \bar{\mathbf{u}}) &= (\nabla_\xi \delta^2 \bar{\mathbf{u}})(\nabla_\xi \delta^1 \bar{\mathbf{u}}) \\ &= \left[\begin{array}{ccc} \frac{\partial \delta^1 u_x}{\partial \xi} \frac{\partial \delta^2 u_x}{\partial \xi} + \frac{\partial \delta^1 u_y}{\partial \xi} \frac{\partial \delta^2 u_x}{\partial \eta} & \frac{\partial \delta^1 u_x}{\partial \eta} \frac{\partial \delta^2 u_x}{\partial \xi} + \frac{\partial \delta^1 u_y}{\partial \eta} \frac{\partial \delta^2 u_x}{\partial \eta} \\ \frac{\partial \delta^1 u_x}{\partial \xi} \frac{\partial \delta^2 u_y}{\partial \xi} + \frac{\partial \delta^1 u_y}{\partial \xi} \frac{\partial \delta^2 u_y}{\partial \eta} & \frac{\partial \delta^1 u_x}{\partial \eta} \frac{\partial \delta^2 u_y}{\partial \xi} + \frac{\partial \delta^1 u_y}{\partial \eta} \frac{\partial \delta^2 u_y}{\partial \eta} \end{array} \right] \end{aligned} \quad (\text{A.40})$$

For the change of the trace of the first displacement, the derivation is analog.

$$\begin{aligned} \delta^2 \text{tr}(\nabla_\xi \delta^1 \bar{\mathbf{u}}) &= \text{tr}(\delta(\nabla_\xi \delta^1 \bar{\mathbf{u}})) \\ &= \text{tr}((\nabla_X \delta^2 \bar{\mathbf{u}})(\nabla_\xi \delta^1 \bar{\mathbf{u}})) \\ &= \frac{\partial \delta^2 u_x}{\partial \xi} \frac{\partial \delta^1 u_x}{\partial \xi} + \frac{\partial \delta^2 u_x}{\partial \eta} \frac{\partial \delta^1 u_y}{\partial \xi} + \frac{\partial \delta^1 u_x}{\partial \eta} \frac{\partial \delta^2 u_y}{\partial \xi} + \frac{\partial \delta^2 u_y}{\partial \eta} \frac{\partial \delta^1 u_y}{\partial \eta} \end{aligned} \quad (\text{A.41})$$

with the second displacement. Furthermore, the change of the domain's volume with respect to the displacement $\delta^2 u$ is

$$\begin{aligned} \delta^2 V &= V \text{tr}(\nabla_X \delta^2 \bar{\mathbf{u}}) \\ &= V \text{tr}(\mathbf{J}_2 \nabla_\xi \delta^2 \bar{\mathbf{u}}) \end{aligned} \quad (\text{A.42})$$

Starting at the expression for the perturbed energy for a displacement (A.7) and introducing the other perturbation yields

$$\delta^2(\delta^1 W_{mag}) = \delta^2 \left(V \frac{\bar{\mathbf{B}}^T(\nabla \delta^1 \bar{\mathbf{u}}) \bar{\mathbf{B}}}{\mu} - \text{tr}(\nabla \delta^1 \bar{\mathbf{u}}) \frac{\bar{\mathbf{B}} \cdot \bar{\mathbf{B}}}{2\mu} V \right) \quad (\text{A.43})$$

developing (A.43) by terms, keeps the formulas manageable. The first term in (A.43) yields:

$$1^{\text{st}} \text{ term (A.43)} = \frac{\delta^2 V}{2\mu} \bar{\mathbf{B}}^T(\nabla \delta^1 \bar{\mathbf{u}}) \bar{\mathbf{B}} + V(\delta^2 \bar{\mathbf{B}})^T(\nabla \delta^1 \bar{\mathbf{u}}) \bar{\mathbf{B}} + V \bar{\mathbf{B}}^T \delta^2(\nabla \delta^1 \bar{\mathbf{u}}) \bar{\mathbf{B}} + V \bar{\mathbf{B}}^T(\nabla \delta^1 \bar{\mathbf{u}})^T \delta^2 \bar{\mathbf{B}} \quad (\text{A.44})$$

Inserting (A.40), (A.42) and (A.7) into (A.44) yields:

$$\begin{aligned} 1^{\text{st}} \text{ term (A.43)} &= \frac{V}{2\mu} [\text{tr}(\nabla_X \delta^2 \bar{\mathbf{u}}) \bar{\mathbf{B}}^T(\nabla_\xi \delta^1 \bar{\mathbf{u}}) \bar{\mathbf{B}} \\ &\quad + ((\nabla_X \delta^2 \bar{\mathbf{u}}) \bar{\mathbf{B}} - \bar{\mathbf{B}} \text{tr}(\nabla_X \delta^2 \bar{\mathbf{u}}))^T(\nabla_\xi \delta^1 \bar{\mathbf{u}}) \bar{\mathbf{B}} \\ &\quad + \bar{\mathbf{B}}^T(\nabla \delta_\xi^2 \bar{\mathbf{u}})(\nabla_\xi \delta^1 \bar{\mathbf{u}}) \bar{\mathbf{B}} \\ &\quad + \bar{\mathbf{B}}^T(\nabla_\xi \delta^1 \bar{\mathbf{u}})^T((\nabla_X \delta^2 \bar{\mathbf{u}}) \bar{\mathbf{B}} - \bar{\mathbf{B}} \text{tr}(\nabla_X \delta^2 \bar{\mathbf{u}}))] \end{aligned} \quad (\text{A.45})$$

Inserting $\nabla_X \delta^2 \bar{\mathbf{u}} = \mathbf{J}_2 \nabla_\xi \delta^2 \bar{\mathbf{u}}$ and neglecting second order terms, (A.45) can be rewritten as a matrix vector multiplication, where $(\nabla \delta^2 \bar{\mathbf{u}})$ and $(\nabla \delta^1 \bar{\mathbf{u}})$ are expressed as vectors according to (A.14).

$$1^{\text{st}} \text{ term (A.43)} = \frac{V}{2\mu} (\nabla \delta^1 \bar{\mathbf{u}}) \begin{bmatrix} 4B_\xi^2 & 2B_\xi B_\eta & 4B_\xi B_\eta & -2B_\xi^2 \\ 0 & 2B_\xi^2 & 2(B_\xi^2 + B_\eta^2) & 2B_\xi B_\eta \\ 2B_\xi B_\eta & 2(B_\xi^2 + B_\eta^2) & 2B_\eta^2 & 0 \\ -2B_\eta^2 & 4B_\xi B_\eta & 2B_\xi B_\eta & 4B_\eta^2 \end{bmatrix} (\nabla \delta^2 \bar{\mathbf{u}}) \quad (\text{A.46})$$

The second term of (A.43) reads

$$\begin{aligned} 2^{\text{nd}} \text{ term (A.43)} &= \delta^2 (-V \text{tr}(\nabla \delta^1 \bar{\mathbf{u}}) \frac{\bar{\mathbf{B}} \cdot \bar{\mathbf{B}}}{2\mu}) \\ &= -\frac{V}{2\mu} \text{tr}(\nabla \delta^1 \bar{\mathbf{u}}) \text{tr}(\nabla \delta^2 \bar{\mathbf{u}}) \bar{\mathbf{B}} \cdot \bar{\mathbf{B}} \\ &\quad - \frac{V}{\mu} \text{tr}(\nabla \delta^1 \bar{\mathbf{u}}) \bar{\mathbf{B}}^T \delta^2 \bar{\mathbf{B}} \\ &\quad - \frac{V}{2\mu} \bar{\mathbf{B}}^T \bar{\mathbf{B}} \delta^2 \text{tr}(\nabla \delta^1 \bar{\mathbf{u}}) \end{aligned} \quad (\text{A.47})$$

Inserting (A.7) and (A.41) into (A.47) yields

$$\begin{aligned} 2^{\text{nd}} \text{ term (A.43)} &= -\frac{V}{2\mu} \text{tr}(\nabla \delta^1 \bar{\mathbf{u}}) \text{tr}(\nabla \delta^2 \bar{\mathbf{u}}) \bar{\mathbf{B}} \cdot \bar{\mathbf{B}} \\ &\quad - \frac{V}{\mu} \text{tr}(\nabla \delta^1 \bar{\mathbf{u}}) \bar{\mathbf{B}}^T ((\nabla \delta^2 \bar{\mathbf{B}} - \bar{\mathbf{B}} \text{tr}(\nabla \delta^2 \bar{\mathbf{u}})) \\ &\quad - \frac{V}{2\mu} \bar{\mathbf{B}}^T \bar{\mathbf{B}} \text{tr}((\nabla \delta^2 \bar{\mathbf{u}})(\nabla \delta^1 \bar{\mathbf{u}})) \\ &= \frac{V}{2\mu} \text{tr}(\nabla \delta^1 \bar{\mathbf{u}}) \text{tr}(\nabla \delta^2 \bar{\mathbf{u}}) \bar{\mathbf{B}} \cdot \bar{\mathbf{B}} \\ &\quad - \frac{V}{\mu} \text{tr}(\nabla \delta^1 \bar{\mathbf{u}}) \bar{\mathbf{B}}^T (\nabla \delta^2 \bar{\mathbf{u}}) \bar{\mathbf{B}} \\ &\quad - \frac{V}{2\mu} \bar{\mathbf{B}}^T \bar{\mathbf{B}} \text{tr}((\nabla \delta^2 \bar{\mathbf{u}})(\nabla \delta^1 \bar{\mathbf{u}})) \end{aligned} \quad (\text{A.48})$$

This can be rewritten as a multiplication of $(\nabla \delta^2 \bar{\mathbf{u}})$ and $(\nabla \delta^1 \bar{\mathbf{u}})$ in vector form with a matrix \mathbf{F}_3 , which contains the components of the magnetic flux density

$$2^{\text{nd}} \text{ term (A.43)} = \frac{V}{2\mu} (\nabla \delta^1 \bar{\mathbf{u}}) \begin{bmatrix} -2B_\xi^2 & -2B_\xi B_\eta & -2B_\xi B_\eta & B_\xi^2 - B_\eta^2 \\ 0 & 0 & -B_\xi^2 - B_\eta^2 & 0 \\ 0 & -B_\xi^2 - B_\eta^2 & 0 & 0 \\ -B_\xi^2 + B_\eta^2 & -2B_\xi B_\eta & -2B_\xi B_\eta & -2B_\eta^2 \end{bmatrix} (\nabla \delta^2 \bar{\mathbf{u}}) \quad (\text{A.49})$$

Adding (A.49) and (A.46) yields the final result which can be used

to determine \mathbf{K}_{uu}^{mag} as shown in (2.159)

$$\begin{aligned} \nabla_{\xi} \delta^1 \bar{\mathbf{u}} \mathbf{K}_{uu}^{mag} \nabla_{\xi} \delta^2 \bar{\mathbf{u}} &= \frac{V}{2\mu} (\nabla_{\xi} \delta^1 \bar{\mathbf{u}}) \begin{bmatrix} 2B_x^2 & 0 & 2B_x B_y & -B_x^2 - B_y^2 \\ 0 & 2B_x^2 & B_x^2 + B_y^2 & 2B_x B_y \\ 2B_x B_y & B_x^2 + B_y^2 & 2B_y^2 & 0 \\ -B_x^2 - B_y^2 & 2B_x B_y & 0 & 2B_y^2 \end{bmatrix} (\nabla_{\xi} \delta^2 \bar{\mathbf{u}}) \\ &\approx \frac{1}{2\mu} \int_{\Omega} \mathbf{B}_{2u}^T \mathbf{K}_{uu}^{mag} \mathbf{B}_{2u} \, d\Omega \end{aligned} \quad (\text{A.50})$$



Additional Measurements

During the operational measurements, other quantities related to the generator were measured. It was investigated, how the bearing monitoring could be improved. For that, the current output of the generator as well as vibration measurements on the static side of the bearings, were conducted.

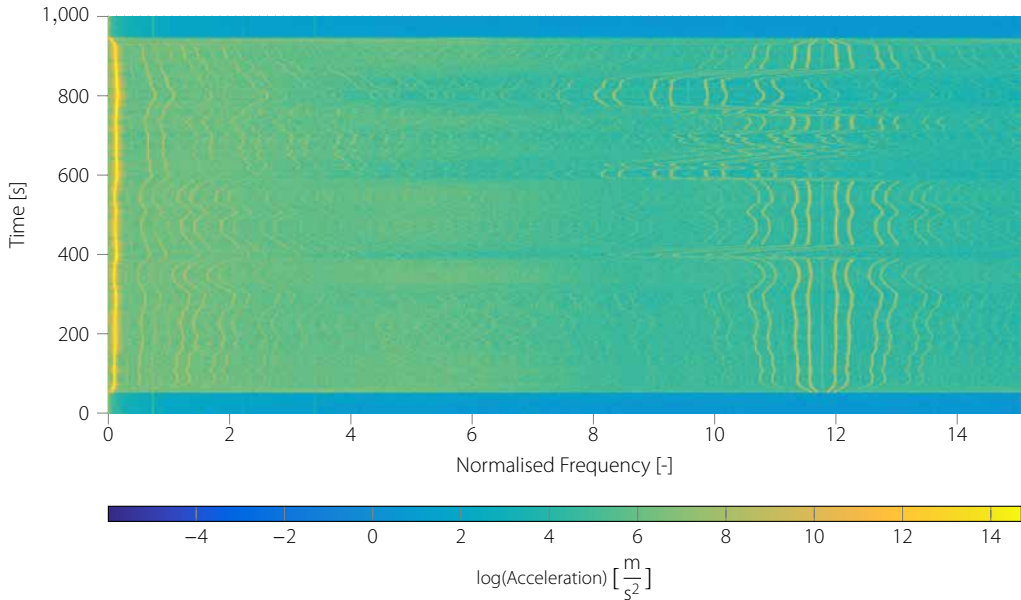


Figure B.1

Spectrogram of the current during the operation of the turbine

Fig. B.1 shows the spectrogram of one phase of the current, recorded during operation. At the beginning and end of the measurement, the turbine started up and shut down. The fundamental current frequency is clearly visible. At higher frequencies, the time harmonic of the frequency converter can be seen.

No structural frequencies are visible in the current measurements. The displacements of the structure are either so small that they play no role or the controller of the frequency converter reacts too fast. In either case, this measurement supports the theory that the two way coupling can be neglected for the XD-115.

Fig. B.2 shows the vibration measurement on the static side of the bearing. In the lower frequency range, the characteristic bearing frequencies, such as ball pass frequency, can be measured. It is also possible to measure the first mode at $\omega/\omega_{ref} = 1$. Therefore, it would be possible to conduct a structural monitoring of the rotor, with sensors that are placed on the stator.

In the higher frequency range, the vibrations induced by the frequency harmonic can be measured again. The switching frequen-

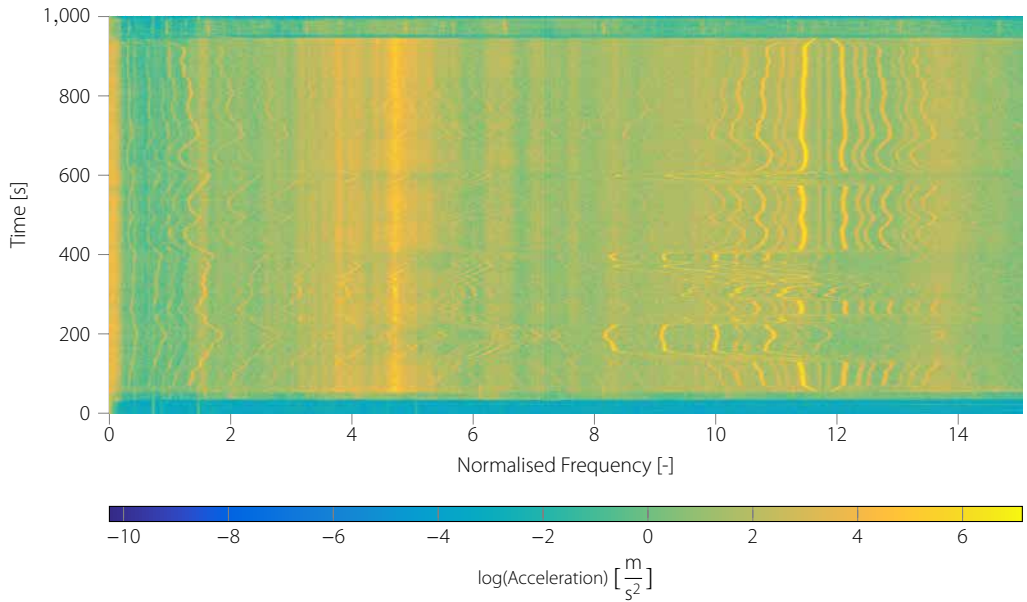


Figure B.2

Spectrogram of the bearing during the operation of the turbine

cies of the converter have thus an influence on the structure. If there was a global mode with a resonance frequency in that frequency range, this mode could get excited by the converter frequency.

Further research was done towards bearing monitoring in direct-drive wind turbine generators using current probes. This research however has not lead to significant results. The details of the research can be found in [142]



Magnetic Torque Harmonics

The analysis presented in this appendix is based on [64, 115]

In an electric machine, various sources for the space harmonics present in the stator and rotor fields exist. The various sources give the space harmonics unique properties, that have an influence on the torque ripple they create. This part of the appendix analyses the source of the harmonic content of torque ripple that does not originate from the interaction between the permanent magnets and the stator slotting.

Let us consider an electric machines with a homogenous air gap length $g(\varphi) = g_0$. The magneto motive fore for the rotor can be expanded as a Fourier series. Because the MMF of the rotor has roughly a square shape, only the odd terms of the Fourier series contribute to the total MMF

$$\mathcal{F}_{PM} = \sum_{k=1,3,5,\dots} c_k \sin(k\theta + \omega_m t) \quad (\text{C.1})$$

where c_k denotes the Fourier coefficient, ω_m the rotational velocity of the rotor and θ circumferential coordinate in a cylindrical coordinate system.

To generate a torque, the two harmonics in stator and rotor need to have the same order.

$$\int_0^{2\pi} \sin(k\theta) \sin(h\theta) = 0 \quad \text{for } h \neq k \quad (\text{C.2})$$

This integral describes if the product of stator field and rotor field interact and produce a torque. Because the rotor only has odd harmonics, only odd harmonics are of interest for the stator. All other harmonics will not produce a torque.

For the stator, the MMF is a combination of the current and the winding distribution

$$\mathcal{F}_M = n_k(\theta) i_a(t) + n_k(\theta) i_b(t) + n_k(\theta) i_c(t) \quad (\text{C.3})$$

where n_k , n_k and n_k denote the winding distributions of the phases a, b and c, respectively. i_a , i_b and i_c represent the coil currents of phase a,b and c respectively. The winding distribution can be expanded to a Fourier series again, yielding

$$\begin{aligned} n_k &= \sum_k n_k \sin(k\theta) \\ n_k &= \sum_k n_k \sin\left(k\left(\theta - \frac{2}{3}\pi\right)\right) \\ n_k &= \sum_k n_k \sin\left(k\left(\theta - \frac{4}{3}\pi\right)\right) \end{aligned} \quad (\text{C.4})$$

where n_k denotes the Fourier coefficient for the winding distribution. In this case, all coefficients can appear. In fact, for fractional windings even coefficients for value of k that are non integer are possible.

The coil current is influence by the switching frequency of the inverter and usually also carries some higher harmonics. In this case we assume for simplicity that the currents are ideal and can be expressed by

$$\begin{aligned} i_a(t) &= \hat{i}_k \sin(\omega_e t) \\ i_b(t) &= \hat{i}_k \sin(\omega_e t - \frac{2}{3}\pi) \\ i_c(t) &= \hat{i}_k \sin(\omega_e t - \frac{4}{3}\pi) \end{aligned} \quad (C.5)$$

Inserting (C.5) and (C.4) into (C.3) yields

$$\begin{aligned} \mathcal{F}_M &= \sum_k n_k \sin(k\theta) \hat{i}_k \sin(\omega_e t) \\ &+ n_k \sin(k(\theta - \frac{2}{3}\pi)) \hat{i}_k \sin(\omega_e t - \frac{2}{3}\pi) \\ &+ n_k \sin(k(\theta - \frac{4}{3}\pi)) \hat{i}_k \sin(\omega_e t - \frac{4}{3}\pi) \end{aligned} \quad (C.6)$$

Using the trigonometric identity $\sin(\theta) \sin(\varphi) = \frac{1}{2}(\cos(\theta - \varphi) - \cos(\theta + \varphi))$ yields

$$\begin{aligned} \mathcal{F}_M &= \sum_k n_k \hat{i}_k \frac{1}{2} (\cos(k\theta - \omega_e t) - \cos(k\theta + \omega_e t)) \\ &+ \sum_k n_k \hat{i}_k \frac{1}{2} (\cos(k\theta - \omega_e t - k\frac{2}{3}\pi + \frac{2}{3}\pi) - \cos(k\theta + \omega_e t - k\frac{2}{3}\pi - \frac{2}{3}\pi)) \\ &+ \sum_k n_k \hat{i}_k \frac{1}{2} (\cos(k\theta - \omega_e t - k\frac{4}{3}\pi + \frac{4}{3}\pi) - \cos(k\theta + \omega_e t - k\frac{4}{3}\pi - \frac{4}{3}\pi)) \\ &= \sum_k n_k \hat{i}_k \frac{1}{2} (\cos(k\theta - \omega_e t) - \cos(k\theta + \omega_e t)) \\ &+ \sum_k n_k \hat{i}_k \frac{1}{2} (\cos(k\theta - \omega_e t - (k-1)\frac{2}{3}\pi) - \cos(k\theta + \omega_e t - (k+1)\frac{2}{3}\pi)) \\ &+ \sum_k n_k \hat{i}_k \frac{1}{2} (\cos(k\theta - \omega_e t - (k-1)\frac{2}{3}\pi) - \cos(k\theta + \omega_e t - (k+1)\frac{4}{3}\pi)) \end{aligned} \quad (C.7)$$

The trigonometric identity

$$\cos(\alpha + \beta) = \cos(\alpha) \cos(\beta) - \sin(\alpha) \sin(\beta)$$

let us take the constant terms out of the trigonometric functions

$$\begin{aligned}
\mathcal{F}_M &= \sum_k n_k \hat{i}_k \frac{1}{2} [\cos(k\theta - \omega_e t) - \cos(k\theta + \omega_e t)] \\
&+ \cos(k\theta - \omega_e t) \cos\left(-\left(k-1\right)\frac{2}{3}\pi\right) - \sin(k\theta - \omega_e t) \sin\left(-\left(k-1\right)\frac{2}{3}\pi\right) \\
&- \cos(k\theta + \omega_e t) \cos\left(-\left(k+1\right)\frac{2}{3}\pi\right) + \sin(k\theta + \omega_e t) \sin\left(-\left(k+1\right)\frac{2}{3}\pi\right) \\
&+ \cos(k\theta - \omega_e t) \cos\left(-\left(k-1\right)\frac{4}{3}\pi\right) - \sin(k\theta - \omega_e t) \sin\left(-\left(k-1\right)\frac{4}{3}\pi\right) \\
&- \cos(k\theta + \omega_e t) \cos\left(-\left(k+1\right)\frac{4}{3}\pi\right) + \sin(k\theta + \omega_e t) \sin\left(-\left(k+1\right)\frac{4}{3}\pi\right)
\end{aligned} \tag{C.8}$$

At this point the equation is split up in three different parts for various k . For $k = 1, 7, 13, \dots$ the term $(k-1)\frac{2}{3}\pi$ a multiple of 2π and thus sine of these terms are zero and the cosine equal to one. The terms $\cos\left(-\left(k+1\right)\frac{2}{3}\pi\right)$ and $\cos\left(-\left(k+1\right)\frac{4}{3}\pi\right)$ are always -0.5 and the terms $\sin\left(-\left(k+1\right)\frac{2}{3}\pi\right)$ and $\sin\left(-\left(k+1\right)\frac{4}{3}\pi\right)$ have opposite pre-signs. That yields for $k = 1, 7, 13, \dots$:

$$\begin{aligned}
\mathcal{F}_{M,k=1,7,13,\dots} &= \sum_{k=1,7,13,\dots} n_k \hat{i}_k \frac{1}{2} [\cos(k\theta - \omega_e t) - \cos(k\theta + \omega_e t)] \\
&+ \cos(k\theta - \omega_e t) \\
&- \cos(k\theta + \omega_e t) \cos\left(-\left(k+1\right)\frac{2}{3}\pi\right) + \sin(k\theta + \omega_e t) \sin\left(-\left(k+1\right)\frac{2}{3}\pi\right) \\
&+ \cos(k\theta - \omega_e t) \\
&- \cos(k\theta + \omega_e t) \cos\left(-\left(k+1\right)\frac{4}{3}\pi\right) + \sin(k\theta + \omega_e t) \sin\left(-\left(k+1\right)\frac{4}{3}\pi\right) \\
&= \sum_{k=1,7,13,\dots} n_k \hat{i}_k \frac{1}{2} [3 \cos(k\theta - \omega_e t)]
\end{aligned} \tag{C.9}$$

For $k = 5, 11, 17, \dots$, the term $(k+1)\frac{2}{3}\pi$ is a multiple of 2π . The terms $\cos\left(-\left(k-1\right)\frac{2}{3}\pi\right)$ and $\cos\left(-\left(k-1\right)\frac{4}{3}\pi\right)$ are always -0.5 and the terms $\sin\left(-\left(k-1\right)\frac{2}{3}\pi\right)$ and $\sin\left(-\left(k-1\right)\frac{4}{3}\pi\right)$ have opposite pre-signs. That yields for $k = 5, 11, 17, \dots$:

$$\begin{aligned}
\mathcal{F}_{M,k=5,11,17,\dots} &= \sum_{k=5,11,17,\dots} n_k \hat{i}_k \frac{1}{2} [\cos(k\theta - \omega_e t) - \cos(k\theta + \omega_e t)] \\
&+ \cos(k\theta - \omega_e t) \cos\left(-\left(k-1\right)\frac{2}{3}\pi\right) - \sin(k\theta - \omega_e t) \sin\left(-\left(k-1\right)\frac{2}{3}\pi\right) \\
&- \cos(k\theta + \omega_e t) \\
&+ \cos(k\theta - \omega_e t) \cos\left(-\left(k-1\right)\frac{4}{3}\pi\right) - \sin(k\theta - \omega_e t) \sin\left(-\left(k-1\right)\frac{4}{3}\pi\right) \\
&- \cos(k\theta + \omega_e t) \\
&= \sum_{k=5,11,17,\dots} n_k \hat{i}_k \frac{1}{2} [-3 \cos(k\theta + \omega_e t)]
\end{aligned} \tag{C.10}$$

For $k = \{3, 9, 15, \dots\}$, the terms $\cos\left(-\left(k+1\right)\frac{2}{3}\pi\right)$, $\cos\left(-\left(k+1\right)\frac{4}{3}\pi\right)$,

$\cos(-(k-1)\frac{4}{3}\pi)$ and $\cos(-(k-1)\frac{2}{3}\pi)$ are all equal to -0.5 . The terms $\sin(-(k+1)\frac{2}{3}\pi)$ and $\sin(-(k-1)\frac{4}{3}\pi)$ are identical. The same is true for the terms $\sin(-(k-1)\frac{2}{3}\pi)$ and $\sin(-(k+1)\frac{4}{3}\pi)$. Considering all this, some simplifications can be applied.

$$\begin{aligned}
 \mathcal{F}_{M,k=3,9,15,\dots} &= \sum_{k=3,9,15,\dots} n_k \hat{i}_k \frac{1}{2} [\cos(k\theta - \omega_e t) - \cos(k\theta + \omega_e t)] \\
 &\quad - 0.5 \cos(k\theta - \omega_e t) \\
 &\quad + 0.5 \cos(k\theta + \omega_e t) \\
 &\quad - 0.5 \cos(k\theta - \omega_e t) \\
 &\quad + 0.5 \cos(k\theta + \omega_e t) \\
 &= 0
 \end{aligned} \tag{C.11}$$

Assembling (C.11), (C.10) and (C.9) yields

$$\begin{aligned}
 \mathcal{F}_M &= \sum_{k=1,7,13,\dots} n_k \hat{i}_k \frac{1}{2} [3 \cos(k\theta - \omega_e t)] \\
 &\quad + \sum_{k=5,11,17,\dots} n_k \hat{i}_k \frac{1}{2} [3 \cos(k\theta + \omega_e t)]
 \end{aligned} \tag{C.12}$$

for the total magneto motive force. (C.12) shows that the odd harmonics, which are not dividable by three travel either forward or backward around the stator. The rotation speed at which they travel is the electrical rotation speed, which is $\frac{n_{poles}}{2}$ higher than the mechanical rotation speed. Therefore they create a pulsating torque, which is zero when the two fields are aligned and highest when they are rotated by $\frac{2 \cdot 90^\circ}{n_{poles}}$. Because of the rotation of the rotor the pulsating frequency is either at $k-1$ times the electrical frequency or at $k+1$, depending on the order.

In this case, the rotation of the fundamental $k=1$ is in negative direction. The rotor will thus rotate in negative direction too. The 7th, 13th, 19th, ... harmonics will thus create a pulsating torque at 6, 10, 13 times $\frac{n_{poles}}{2} \omega_m$. The same is true for the 5th, 11th and 17th harmonic.

Curriculum Vitae

Michael Kirschneck was born on 9th of December 1984 in Hamburg. He completed his secondary education at the Gymnasium Eppendorf in Hamburg in 2004. Afterwards he did his civilian service at the 'Hauspflegestation Barmbek-Uhlenhorst', an outpatient nursery service. In 2005 he started studying mechanical engineering at the Technische Universität München with the specialisation Engineering Fundamentals and Thermo-Fluid Dynamics. He graduated in 2011, being awarded the degree of Diplom-Ingenieur.

Since October 2011 he has been working as a researcher at the Delft University of technology in a project together with XEMC-Darwind under the supervision of prof. dr. Daniel J. Rixen and the co-supervisors Henk Polinder and Ron A.J. van Ostayen. The results of this project are compiled in this thesis.

References

- [1] A. Abrahamsen et al. “Feasibility study of 5MW superconducting wind turbine generator”. *Physica C: Superconductivity* 471.21-22 (2011), pp. 1464–1469. DOI: [10.1016/j.physc.2011.05.217](https://doi.org/10.1016/j.physc.2011.05.217). 
- [2] A. Andreykiv and D. J. Rixen. “Numerical modelling of electromechanical coupling using fictitious domain and level set methods”. *International Journal for Numerical Methods in Engineering* 80.4 (2009), pp. 478–506. DOI: [10.1002/nme.2636](https://doi.org/10.1002/nme.2636). 
- [3] A. C. Antoulas and D. C. Sorensen. “Approximation of large-scale dynamical systems: An overview”. *Applied Mathematics and Computer Science* 11.5 (2001), pp. 1093–1122.
- [4] E. Balmès. “Frequency domain identification of structural dynamics using the pole/residue parametrization”. *Proceedings of the International Modal Analysis Conference*.
- [5] E. Balmès. “Integration of existing methods and user knowledge in a MIMO identification algorithm for structures with high modal densities”. *Proceedings of SPIE - The International Society for Optical Engineering*. 1, pp. 613–619. ISBN: 0912053410.
- [6] E. Balmès. *SDTools Vibration Software*. URL: <http://www.sdtools.com/>.
- [7] M. Balser. *Bayerns lange Leitung*. URL: <http://www.sueddeutsche.de/bayern/energiewende-bayerns-lange-leitung-1.2331870>.
- [8] M. C. C. BAMPTON and R. R. CRAIG, JR. “Coupling of substructures for dynamic analyses.” en. *AIAA Journal* 6.7 (1968), pp. 1313–1319. DOI: [10.2514/3.4741](https://doi.org/10.2514/3.4741). 
- [9] D. Bang et al. “Review of generator systems for direct-drive wind turbines”. *European Wind Energy Conference & Exhibition*, pp. 1–11. ISBN: 9781615671151.
- [10] A. van Beek. *Advanced engineering design : lifetime performance and reliability*. TU Delft, 2006, 499 p. ISBN: 9081040618.
- [11] A. Belahcen. “Magnetoelastic coupling in rotating electrical machines”. *IEEE Transactions on Magnetics* 41.5 (2005), pp. 1624–1627. DOI: [10.1109/TMAG.2005.846123](https://doi.org/10.1109/TMAG.2005.846123). 
- [12] A. Belahcen. “Magnetoelasticity, Magnetic Forces and Magnetostriction in Electrical Machines”. PhD thesis. Helsinki University of Technology, 2004, p. 115. ISBN: 9512271850.
- [13] A. Belahcen. “Vibrations of rotating electrical machines due to magnetomechanical coupling and magnetostriction”. *IEEE Transactions on Magnetics* 42.4 (2006), pp. 971–974. DOI: [10.1109/TMAG.2006.871469](https://doi.org/10.1109/TMAG.2006.871469). 
- [14] M. P. Bendsøe. “Optimal shape design as a material distribution problem”. *Structural Optimization* 1.4 (1989), pp. 193–202. DOI: [10.1007/BF01650949](https://doi.org/10.1007/BF01650949). 
- [15] N. Bianchi and S. Bolognani. “Design techniques for reducing the cogging torque in surface-mounted PM motors”. *IEEE Transactions on Industry Applications* 38.5 (2002), pp. 1259–1265. DOI: [10.1109/TIA.2002.802989](https://doi.org/10.1109/TIA.2002.802989). 
- [16] K. J. Binns, P. J. Lawrenson and C. Trowbridge. *The Analytical and Numerical Solution of Electric and Magnetic Fields*. John Wiley & Sons Ltd, 1993. ISBN: 0471924601.
- [17] A. Bossavit. “Edge-element computation of the force field in deformable bodies”. *IEEE Transactions on Magnetics* 28 (1992), pp. 1263–1266. DOI: [10.1109/20.123919](https://doi.org/10.1109/20.123919). 
- [18] G. E. P. Box and N. R. Draper. *Empirical model-building and response surfaces*. Wiley, 1987. ISBN: 0471810339.

- [19] A. Brandt and A. Linderholt. "A periodogram-based method for removing harmonics in operational modal analysis". *ISMA*.
- [20] R. Brincker, L. Zhang and P. Andersen. "Modal Identification from Ambient Responses using Frequency Domain Decomposition". *Proceedings of the International Modal Analysis Conference, IMAC XVIII*, pp. 625–630.
- [21] M. Bruggi and M. Verani. "A fully adaptive topology optimization algorithm with goal-oriented error control". *Computers and Structures* 89.15-16 (2011), pp. 1481–1493. DOI: [10.1016/j.compstruc.2011.05.003](https://doi.org/10.1016/j.compstruc.2011.05.003). 
- [22] H. B. Callen. *Thermodynamics and an Introduction to Thermostatistics*. Wiley, 1985. ISBN: 978-0471862567.
- [23] P. Campbell. "Comments on "Energy stored in permanent magnets"". *IEEE Transactions on Magnetics* 36.1 (2000), pp. 401–403. DOI: [10.1109/20.822554](https://doi.org/10.1109/20.822554). 
- [24] Chang-Hwan Im, Hyun-Kyo Jung and Yong-Joo Kim. "Hybrid genetic algorithm for electromagnetic topology optimization". English. *IEEE Transactions on Magnetics* 39.5 (2003), pp. 2163–2169. DOI: [10.1109/TMAG.2003.817094](https://doi.org/10.1109/TMAG.2003.817094). 
- [25] N. Chestney and G. D. Clercq. *Global nuclear decommissioning cost seen underestimated, may spiral*. URL: <http://www.reuters.com/article/2015/01/19/nuclear-decommissioning-idUSL6NoUV2BI20150119>.
- [26] J. S. Choi et al. "Rotor pole design of IPM motors for a sinusoidal air-gap flux density distribution". *Structural and Multidisciplinary Optimization* 46.3 (2012), pp. 445–455. DOI: [10.1007/s00158-012-0774-8](https://doi.org/10.1007/s00158-012-0774-8). 
- [27] J. Coulomb. "A methodology for the determination of global electromechanical quantities from a finite element analysis and its application to the evaluation of magnetic forces, torques and stiffness". *IEEE Transactions on Magnetics* 19.6 (1983), pp. 2514–2519. DOI: [10.1109/TMAG.1983.1062812](https://doi.org/10.1109/TMAG.1983.1062812). 
- [28] J. Coulomb and G. Meunier. "Finite element implementation of virtual work principle for magnetic or electric force and torque computation". *IEEE Transactions on Magnetics* 20.5 (1984), pp. 1894–1896. DOI: [10.1109/TMAG.1984.1063232](https://doi.org/10.1109/TMAG.1984.1063232). 
- [29] R. Craig, Jr. "Coupling of substructures for dynamic analyses - An overview". *41st Structures, Structural Dynamics, and Materials Conference and Exhibit*. Structures, Structural Dynamics, and Materials and Co-located Conferences. 
- [30] *The Philosopher's Tree: Michael Faraday's life and work in his own words*. Ed. by P. Day. Taylor & Francis, 1999. ISBN: 978-0750305716.
- [31] K. Delaere et al. "Coupling of Magnetic Analysis and Vibrational Modal Analysis using local Forces". *Proceedings of the Xth International Symposium on Theoretical Electrical Engineering*. 10, pp. 417–422.
- [32] K. Delaere et al. "Coupling of numerical magnetic and experimental vibration analysis for electrical machines". *3rd Chinese International Conference on Electrical Machines*, pp. 0–3.
- [33] E. Di Lorenzo et al. "Dynamic characterization of wind turbine gearboxes using Order-Based Modal Analysis". *ISMA*.
- [34] J. M. Dickens and A. Stroeve. "Modal truncation vectors for reduced dynamic substructure models". *AIAA/ASME/ASCE/AHS/ASC Structures, Structural Dynamics, and Materials Conference and Exhibit*, 41 st.
- [35] J. Donkers and A. Brand. *Offshore wind atlas of the Dutch part of the North Sea*. Tech. rep. EWEA, 2011, pp. 29–31.

- [36] L. Dorfmann and R. W. Ogden. *Nonlinear Theory of Electroelastic and Magnetoelastic Interactions*. Springer US, 2014. ISBN: 9781461495963.
- [37] M. R. Dubois and H. Polinder. “Study of TFPM machines with toothed rotor applied to direct-drive generators for wind turbines”. *Proceedings of the Nordic workshop on power and industrial electronics*.
- [38] O. Duque, M. Perez and D. Morinigo. “Detection of Bearing Faults in Cage Induction Motors Fed by Frequency Converter using Spectral Analysis of Line Current”. *IEEE International Conference on Electric Machines and Drives, 2005*. Pp. 17–22. ISBN: 0-7803-8987-5. 
- [39] R. Eberhart and J. Kennedy. “A new optimizer using particle swarm theory”. *MHS'95. Proceedings of the Sixth International Symposium on Micro Machine and Human Science*, pp. 39–43. ISBN: 0-7803-2676-8. 
- [40] M. S. Eldred, V. B. Venkayya and W. J. Anderson. “Mode tracking issues in structural optimization”. en. *AIAA Journal* 33.10 (1995), pp. 1926–1933. DOI: [10.2514/3.12747](https://doi.org/10.2514/3.12747). 
- [41] S. Engström et al. “Development of NewGen - a New Type of Direct-Drive Generator”. *European Wind Energy Conference*. Vol. 4, pp. 22–25.
- [42] EWEA. *The European offshore wind industry –key trends and statistics 2014*. Tech. rep. January. European Wind Energy Association, 2015.
- [43] EWEA. *Wind in our Sails - The coming of Europe's offshore wind energy industry*. Tech. rep. EWEA, 2011, p. 93.
- [44] C. Farhat et al. “Dimensional reduction of nonlinear finite element dynamic models with finite rotations and energy-based mesh sampling and weighting for computational efficiency”. *International Journal for Numerical Methods in Engineering* 98.9 (2014), pp. 625–662. DOI: [10.1002/nme.4668](https://doi.org/10.1002/nme.4668). 
- [45] S. Faulstich, B. Hahn and P. J. Tavner. “Wind turbine downtime and its importance for offshore deployment”. *Wind Energy* 14.3 (2011), pp. 327–337. DOI: [10.1002/we.421](https://doi.org/10.1002/we.421). 
- [46] A. E. Fitzgerald, C. Kingsley and S. D. Umans. *Electric Machinery*. 7th ed. McGraw-Hill Education, 2013, p. 704.
- [47] B. Flemisch et al. “Coupling scalar and vector potentials on nonmatching grids for eddy currents in a moving conductor”. *Journal of Computational and Applied Mathematics* 168.1-2 (2004), pp. 191–205. DOI: [10.1016/j.cam.2003.05.017](https://doi.org/10.1016/j.cam.2003.05.017). 
- [48] K. Fonteyn et al. “Simulated results and experimental verification of a novel magneto-mechanical coupled method”. *Electrical Machines and Systems (ICEMS)*, pp. 1743–1748.
- [49] E. Fröde and W. Fröde. *Windmühlen in Deutschland, Holland und Belgien. Energiespender und ästhetische Architektur*. Studio Dumont Buchverlag, 1981. ISBN: 3770112229.
- [50] W. Fu et al. “Magnetic Force Computation in Permanent Magnets Using a Local Energy Coordinate Derivative Method”. *IEEE Transactions on Magnetics* 40.2 (2004), pp. 683–686. DOI: [10.1109/TMAG.2004.824774](https://doi.org/10.1109/TMAG.2004.824774). 
- [51] M. Furlan, A. Cernigoj and M. Boltezar. “A coupled electromagnetic-mechanical-acoustic model of a DC electric motor”. *COMPEL - The international journal for computation and mathematics in electrical and electronic engineering* 22.4 (2003), pp. 1155–1165. DOI: [10.1108/03321640310483075](https://doi.org/10.1108/03321640310483075). 
- [52] M. Géradin and D. Rixen. *Mechanical Vibrations : Theory and Applications to Structural Dynamics*. 3rd ed. Wiley, 2015, p. 444. ISBN: 047197546X.

- [53] M. van der Giet et al. "Comparison of 2-D and 3-D Coupled Electromagnetic and Structure-Dynamic Simulation of Electrical Machines". *IEEE Transactions on Magnetics* 44.6 (2008), pp. 1594–1597. DOI: [10.1109/TMAG.2007.916121](https://doi.org/10.1109/TMAG.2007.916121). 
- [54] P Gipe. *Wind in power - 2014 European statistics*. Tech. rep. February. EWEA, 2015, p. 12.
- [55] R. Girgis and S. Verma. "Resonant Frequencies and Vibration Behaviour of Stators of Electrical Machines as Affected by Teeth, Windings, Frame and Laminations". *IEEE Transactions on Power Apparatus and Systems* PAS-98.4 (1979), pp. 1446–1455. DOI: [10.1109/TPAS.1979.319347](https://doi.org/10.1109/TPAS.1979.319347). 
- [56] C. Golovanov et al. "3D mesh connection techniques applied to movement simulation". *IEEE Transactions on Magnetics* 34.5 (1998), pp. 3359–3362. DOI: [10.1109/20.717790](https://doi.org/10.1109/20.717790). 
- [57] R. J. GUYAN. "Reduction of stiffness and mass matrices". en. *AIAA Journal* 3.2 (1965), pp. 380–380. DOI: [10.2514/3.2874](https://doi.org/10.2514/3.2874). 
- [58] E. Hau. *Wind Turbines*. Berlin, Heidelberg: Springer Berlin Heidelberg, 2013. ISBN: 978-3-642-27150-2. 
- [59] W. H. Hayt. *Engineering electromagnetics*. 5th. McGraw-Hill, 1989. ISBN: 0-07-027406-1.
- [60] O Heaviside. "On the Forces, Stresses, and Fluxes of Energy in the Electromagnetic Field". *Philosophical Transactions of the Royal Society of London* 183 (1892), pp. 423–480.
- [61] H. Helmholtz. *Über die auf das Innere magnetisch oder dielectrisch polarisirter Körper wirkenden Kräfte*. Barth Leipzig, 1881.
- [62] F. Henrotte and K. Hameyer. "Computation of electromagnetic force densities: Maxwell stress tensor vs. virtual work principle". *Journal of Computational and Applied Mathematics* 168.1-2 (2004), pp. 235–243. DOI: [10.1016/j.cam.2003.06.012](https://doi.org/10.1016/j.cam.2003.06.012). 
- [63] Hokyung Shim et al. "Topology Optimization for Compliance Reduction of Magnetomechanical Systems". *IEEE Transactions on Magnetics* 44.3 (2008), pp. 346–351. DOI: [10.1109/TMAG.2007.914670](https://doi.org/10.1109/TMAG.2007.914670). 
- [64] S. R. Holm, H. Polinder and J. a. Ferreira. "Analytical modeling of a permanent-magnet synchronous machine in a flywheel". *IEEE Transactions on Magnetics* 43.5 (2007), pp. 1955–1967. DOI: [10.1109/TMAG.2007.892791](https://doi.org/10.1109/TMAG.2007.892791). 
- [65] G. A. Holzapfel. *Nonlinear Solid Mechanics: A Continuum Approach for Engineering*. Wiley, 2000, p. 455. ISBN: 0471823198.
- [66] P. G. Huray. *Maxwell's Equation*. Wiley-IEEE Press, 2009, p. 312. ISBN: 978-0-470-54276-7.
- [67] W. C. HURTY. "Dynamic analysis of structural systems using component modes". en. *AIAA Journal* 3.4 (1965), pp. 678–685. DOI: [10.2514/3.2947](https://doi.org/10.2514/3.2947). 
- [68] W. Hurty. "Vibrations of Structural Systems by Component Mode Synthesis". eng. *Journal of the Engineering Mechanics Division* 86.4 (1960), pp. 51–70.
- [69] T. Ishikawa, P. Xie and N. Kurita. "Topology Optimization of Rotor Structure in Permanent Magnet Synchronous Motors Considering Ease of Manufacturing". *IEEJ Journal of Industry Applications* 4.4 (2015), pp. 469–475. DOI: [10.1541/ieejjia.4.469](https://doi.org/10.1541/ieejjia.4.469). 

- [70] R. Islam et al. “Permanent-Magnet Synchronous Motor Magnet Designs With Skewing for Torque Ripple and Cogging Torque Reduction”. English. *IEEE Transactions on Industry Applications* 45.1 (2009), pp. 152–160. DOI: [10.1109/TIA.2008.2009653](https://doi.org/10.1109/TIA.2008.2009653). 
- [71] N.-J. Jacobsen, P. Andersen and R. Brincker. “Using Enhanced Frequency Domain Decomposition as a Robust Technique to Harmonic Excitation in Operational Modal Analysis”. *ISMA*.
- [72] Jeonghoon Yoo and N. Kikuchi. “Topology optimization for reduction of vibration caused by magnetic harmonic excitation”. *IEEE Transactions on Magnetics* 38.6 (2002), pp. 3643–3649. DOI: [10.1109/TMAG.2002.804806](https://doi.org/10.1109/TMAG.2002.804806). 
- [73] M. Kaltenbacher. *Numerical Simulation of Mechatronic Sensors and Actuators*. Springer Verlag, 2007. ISBN: 978-3-540-71359-3.
- [74] G. Kerschen et al. “The Method of Proper Orthogonal Decomposition for Dynamical Characterization and Order Reduction of Mechanical Systems: An Overview”. *Nonlinear Dynamics* 41.1-3 (2005), pp. 147–169. DOI: [10.1007/s11071-005-2803-2](https://doi.org/10.1007/s11071-005-2803-2). 
- [75] T. S. Kim and Y. Y. Kim. “Mac-based mode-tracking in structural topology optimization”. *Computers & Structures* 74.3 (2000), pp. 375–383. DOI: [10.1016/S0045-7949\(99\)00056-5](https://doi.org/10.1016/S0045-7949(99)00056-5). 
- [76] F. Klinger and L. Müller. “State of the Art and new Technologies of Direct-Drive Wind Turbines”. *IRENEC*.
- [77] K. Komezsa et al. “Comparative computation of forces and torques of electromagnetic devices by means of different formulae”. *IEEE Transactions on Magnetics* 30.5 (1994), pp. 3475–3478. DOI: [10.1109/20.312687](https://doi.org/10.1109/20.312687). 
- [78] F. von König. *Windenergie in praktischer nutzung: räder, rotoren, mühlen, windkraftwerke*. Udo Pfriemer, 1978. ISBN: 3-7906-0077-6.
- [79] D. J. Korteweg. “Ueber die Veränderung der Form und des Volumens dielectricischer Körper unter Einwirkung electricischer Kräfte”. *Annalen der Physik und Chemie* 245.1 (1880), pp. 48–61. DOI: [10.1002/andp.18792450103](https://doi.org/10.1002/andp.18792450103). 
- [80] C. Kost. *Levelized Cost of Electricity Renewable Energy Technologies*. Tech. rep. November. Fraunhofer Institute for Solar Energy Systems ISE, 2013.
- [81] D. Kostopoulos, H. Polinder and A. van den Brink. “High Temperature Superconducting generators for direct drive wind turbines: A review”. *Proc. Eur. Wind Energy Assoc. Conf*, pp. 1–10. ISBN: 9781627482912.
- [82] B. Lalanne and M. Touratier. “Aeroelastic Vibrations and Stability in Cyclic Symmetric Domains”. *International Journal of Rotating Machinery* 6.6 (2000), pp. 445–452. DOI: [10.1155/S1023621X00000403](https://doi.org/10.1155/S1023621X00000403). 
- [83] E Lantz et al. “The Past and Future Cost of Wind Energy Preprint”. *World Renewable Energy Forum*. August.
- [84] B. S. Lazarov and O. Sigmund. “Filters in topology optimization based on Helmholtz-type differential equations”. *International Journal for Numerical Methods in Engineering* 86.6 (2011), pp. 765–781. DOI: [10.1002/nme.3072](https://doi.org/10.1002/nme.3072). 
- [85] A. Lazarus, B. Prabel and D. Combescure. “A 3D finite element model for the vibration analysis of asymmetric rotating machines”. *Journal of Sound and Vibration* 329.18 (2010), pp. 3780–3797. DOI: [10.1016/j.jsv.2010.03.029](https://doi.org/10.1016/j.jsv.2010.03.029). 

- [86] J. Le Besnerais et al. "Characterization and Reduction of Audible Magnetic Noise Due to PWM Supply in Induction Machines". *IEEE Transactions on Industrial Electronics* 57.4 (2010), pp. 1288–1295. DOI: [10.1109/TIE.2009.2029529](https://doi.org/10.1109/TIE.2009.2029529). 
- [87] C.-W. Lee et al. "Modal analysis of periodically time-varying linear rotor systems". *Journal of Sound and Vibration* 303.3-5 (2007), pp. 553–574. DOI: [10.1016/j.jsv.2007.01.041](https://doi.org/10.1016/j.jsv.2007.01.041). 
- [88] J. Lee and N. Kikuchi. "Structural Topology Optimization of Electrical Machinery to Maximize Stiffness With Body Force Distribution". *IEEE Transactions on Magnetics* 46.10 (2010), pp. 3790–3794. DOI: [10.1109/TMAG.2010.2052365](https://doi.org/10.1109/TMAG.2010.2052365). 
- [89] T. H. Lee. "Adjoint Method for Design Sensitivity Analysis of Multiple Eigenvalues and Associated Eigenvectors". *AIAA Journal* 45.8 (2007), pp. 1998–2004. DOI: [10.2514/1.25347](https://doi.org/10.2514/1.25347). 
- [90] T. H. Lee. "An Adjoint Variable Method for Structural Design Sensitivity Analysis of a Distinct Eigenvalue Problem". *KSME International Journal* 13.6 (1999), pp. 470–476. 
- [91] J. Leuridan et al. "High Resolution Order Tracking Using Kalman Tracking Filters - Theory and Applications". *SAE Transactions: Journal of Passenger Cars*, p. 291. 
- [92] H. Lovatt and P. Walterson. "Energy stored in permanent magnets". *IEEE Transactions on Magnetics* 35.1 (1999), pp. 505–507. DOI: [10.1109/20.737473](https://doi.org/10.1109/20.737473). 
- [93] R. H. MacNeal. "A hybrid method of component mode synthesis". *Computers & Structures* 1.4 (1971), pp. 581–601. DOI: [10.1016/0045-7949\(71\)90031-9](https://doi.org/10.1016/0045-7949(71)90031-9). 
- [94] N. M. M. Maia and J. M. M. Silva. *Theoretical and Experimental Modal Analysis*. Research Studies Press, 1997. ISBN: 0863802087. 
- [95] M. Mair et al. "Numerical and experimental investigation of the structural characteristics of stator core stacks". *COMPEL - The international journal for computation and mathematics in electrical and electronic engineering* 32.5 (2013), pp. 1643–1664. DOI: [10.1108/COMPEL-04-2013-0122](https://doi.org/10.1108/COMPEL-04-2013-0122). 
- [96] Y. Marechal et al. "A general purpose tool for restoring inter-element continuity". *IEEE Transactions on Magnetics* 28.2 (1992), pp. 1728–1731. DOI: [10.1109/20.124037](https://doi.org/10.1109/20.124037). 
- [97] J. Martinez, A. Belahcen and J. Detoni. "A 2D magnetic and 3D mechanical coupled finite element model for the study of the dynamic vibrations in the stator of induction motors". *Mechanical Systems and Signal Processing* 66-67 (2016), pp. 640–656. DOI: [10.1016/j.ymssp.2015.06.014](https://doi.org/10.1016/j.ymssp.2015.06.014). 
- [98] K. Maute, S. Schwarz and E. Ramm. "Adaptive topology optimization of elastoplastic structures". *Structural Optimization* 15.2 (1998), pp. 81–91. DOI: [10.1007/BF01278493](https://doi.org/10.1007/BF01278493). 
- [99] J. C. Maxwell and J. C. Maxwell. "A Dynamical Theory of the Electromagnetic Field". *Philosophical Transactions of the Royal Society of London* 155 (1865), pp. 459–512. 
- [100] W. Miller et al. "Recent development in aluminium alloys for the automotive industry". *Materials Science and Engineering: A* 280.1 (2000), pp. 37–49. DOI: [10.1016/S0921-5093\(99\)00653-X](https://doi.org/10.1016/S0921-5093(99)00653-X). 
- [101] P. Mongeau. "High Torque Density Propulsion Motors". *Naval Engineers Journal* 117.4 (2005), pp. 53–57. DOI: [10.1111/j.1559-3584.2005.tb00384.x](https://doi.org/10.1111/j.1559-3584.2005.tb00384.x). 
- [102] F. C. Moon. *Applied Dynamics: With Applications to Multibody and Mechatronic Systems*. Wiley, 1998. ISBN: 0-471-13828-2. 

- [103] K. Motte et al. “Operational Modal Analysis in the Presence of Harmonic Excitations: A Review”. *Proceedings of the International Modal Analysis Conference*.
- [104] M. Mueller, A. Zavvos and A. McDonald. “Optimisation tools for large permanent magnet generators for direct drive wind turbines”. *IET Renewable Power Generation* 7.2 (2013), pp. 163–171. DOI: [10.1049/iet-rpg.2012.0135](https://doi.org/10.1049/iet-rpg.2012.0135). 
- [105] W. Muller. “Comparison of different methods of force calculation”. *IEEE Transactions on Magnetics* 26.2 (1990), pp. 1058–1061. DOI: [10.1109/20.106503](https://doi.org/10.1109/20.106503). 
- [106] J. A. Nelder and R. Mead. “A Simplex Method for Function Minimization”. *The Computer Journal* 7.4 (1965), pp. 308–313. DOI: [10.1093/comjnl/7.4.308](https://doi.org/10.1093/comjnl/7.4.308). 
- [107] I. Nishiguchi, A. Kameari and K. Haseyama. “On the local force computation of deformable bodies in magnetic field”. *IEEE Transactions on Magnetics* 35.3 (1999), pp. 1650–1653. DOI: [10.1109/20.767323](https://doi.org/10.1109/20.767323). 
- [108] S. Oh, S. Min and J. P. Hong. “Air gap flux density waveform design of surface-mounted permanent magnet motor considering magnet shape and magnetization direction”. *IEEE Transactions on Magnetics* 49.5 (2013), pp. 2393–2396. DOI: [10.1109/TMAG.2013.2246142](https://doi.org/10.1109/TMAG.2013.2246142). 
- [109] P. van Overschee and B. de Moor. *Subspace Identification for Linear Systems: Theory - Implementation - Applications*. Springer, 2011, p. 272. ISBN: 1461380618.
- [110] M. Ozbek. “Optical Monitoring and Operational Modal Analysis of Large Wind Turbines”. PhD thesis. TU Delft, 2013, p. 178.
- [111] E. Pedersen and K. Persson Waye. “Perception and annoyance due to wind turbine noise—a dose–response relationship”. *The Journal of the Acoustical Society of America* 116.6 (2004), p. 3460. DOI: [10.1121/1.1815091](https://doi.org/10.1121/1.1815091). 
- [112] P. Pellerey, V. Lanfranchi and G. Friedrich. “Coupled Numerical Simulation Between Electromagnetic and Structural Models. Influence of the Supply Harmonics for Synchronous Machine Vibrations”. *IEEE Transactions on Magnetics* 48.2 (2012), pp. 983–986. DOI: [10.1109/TMAG.2011.2175714](https://doi.org/10.1109/TMAG.2011.2175714). 
- [113] V. Piefort. “Finite Element Modelling of Piezoelectric Active Structures”. PhD thesis. Free University of Brussels, 2001, p. 154.
- [114] M. Pirnat, G. Čepon and M. Boltežar. “Introduction of the linear contact model in the dynamic model of laminated structure dynamics: An experimental and numerical identification”. *Mechanism and Machine Theory* 64 (2013), pp. 144–154. DOI: [10.1016/j.mechmachtheory.2013.02.003](https://doi.org/10.1016/j.mechmachtheory.2013.02.003). 
- [115] H. Polinder and M. J. Hoeijmakers. “Analytic calculation of the magnetic field in PM machines”. *Industry Applications Conference, 1997. Thirty-Second IAS Annual Meeting, IAS '97, Conference Record of the 1997 IEEE*. Vol. 1, 35–41 vol.1. ISBN: 0-7803-4067-1. 
- [116] H. Polinder. “Overview of and Trends in Wind Turbine Generator Systems”. *IEEE Power Engineering Society General Meeting*, pp. 1–8.
- [117] H. Polinder et al. “Trends in Wind Turbine Generator Systems”. *IEEE Journal of Emerging and Selected Topics in Power Electronics* 1.3 (2013), pp. 174–185. DOI: [10.1109/JESTPE.2013.2280428](https://doi.org/10.1109/JESTPE.2013.2280428). 
- [118] J. H. J. Potgieter. “Optimal topology and critical evaluation of slip synchronous permanent magnet wind generator”. PhD thesis. Stellenbosch University, 2014.
- [119] M. J. D. Powell. *The BOBYQA algorithm for bound constrained optimization without derivatives*. Tech. rep. Department of Applied Mathematics and Theoretical Physics, 2009.

- [120] A Preumont. *Mechatronics Dynamics of Electromechanical and Piezoelectric Systems*. 1st ed. Springer Netherlands, 2006, p. 208. ISBN: 9781402046957.
- [121] A. Rabl and J. Spadaro. *Externalities of Energy: Extension of accounting framework and Policy Applications*. Tech. rep. August 2005. ARMINES/Ecole des Mines de Paris, 2005.
- [122] C. Rainieri and G. Fabbrocino. *Operational Modal Analysis of Civil Engineering Structures*. New York, NY: Springer New York, 2014. ISBN: 978-1-4939-0766-3. 
- [123] Z. Ren. “Comparison of different force calculation methods in 3D finite element modelling”. *IEEE Transactions on Magnetics* 30.5 (1994), pp. 3471–3474. DOI: [10.1109/20.312686](https://doi.org/10.1109/20.312686). 
- [124] Z. Ren and A. Razek. “A strong coupled model for analysing dynamic behaviours of non-linear electromechanical systems”. *Magnetics, IEEE Transactions on* 30.5 (1994), pp. 3252–3255. DOI: [10.1109/20.312631](https://doi.org/10.1109/20.312631). 
- [125] Z. Ren and A. Razek. “Local force computation in deformable bodies using edge elements”. *Magnetics, IEEE Transactions on* 28.2 (1992), pp. 1212–1215. DOI: [10.1109/20.123904](https://doi.org/10.1109/20.123904). 
- [126] Z. Ren et al. “Simulation of an Electromagnetic Actuator by a Coupled Magneto-Mechanical Modeling”. *COMPEL - The international journal for computation and mathematics in electrical and electronic engineering* 14.4 (1995), pp. 203–206.
- [127] D. J. Rixen and R. F. Lohman. “Efficient computation of eigenmodes of quasi-cyclic structures”. *Proceedings of the International Modal Analysis Conference*, pp. 1–13.
- [128] D. Rixen. “Generalized mode acceleration methods and modal truncation augmentation”. *Structures, Structural Dynamics and Material Conference and Exhibit*. Vol. 1300.
- [129] D. Rixen. “High order static correction modes for component mode synthesis”. *Fifth World Congress on Computational Mechanics*.
- [130] D. J. Rixen. “A dual Craig–Bampton method for dynamic substructuring”. *Journal of Computational and Applied Mathematics* 168.1-2 (2004), pp. 383–391. DOI: [10.1016/j.cam.2003.12.014](https://doi.org/10.1016/j.cam.2003.12.014). 
- [131] V. Rochus, D. J. Rixen and J.-C. Golinval. “Monolithic modelling of electro-mechanical coupling in micro-structures”. *International Journal for Numerical Methods in Engineering* 65.4 (2006), pp. 461–493. DOI: [10.1002/nme.1450](https://doi.org/10.1002/nme.1450). 
- [132] S. Rubin. “Improved Component-Mode Representation for Structural Dynamic Analysis”. en. *AIAA Journal* 13.8 (1975), pp. 995–1006. DOI: [10.2514/3.60497](https://doi.org/10.2514/3.60497). 
- [133] N. Sadowski et al. “Finite element torque calculation in electrical machines while considering the movement”. *IEEE Transactions on Magnetics* 28 (1992), pp. 1410–1413. DOI: [10.1109/20.123957](https://doi.org/10.1109/20.123957). 
- [134] A. Saito et al. “Efficient forced vibration reanalysis method for rotating electric machines”. *Journal of Sound and Vibration* 334 (2015), pp. 388–403. DOI: [10.1016/j.jsv.2014.09.004](https://doi.org/10.1016/j.jsv.2014.09.004). 
- [135] R. Sanchez Grandia et al. “General Formulation for Magnetic Forces in Linear Materials and Permanent Magnets”. *IEEE Transactions on Magnetics* 44.9 (2008), pp. 2134–2140. DOI: [10.1109/TMAG.2008.2000493](https://doi.org/10.1109/TMAG.2008.2000493). 
- [136] G Shrestha. “Structural flexibility of large direct drive generators for wind turbines”. PhD thesis. Tu Delft, 2013. ISBN: 9789088919992.

- [137] G. Shrestha, H. Polinder and J. Ferreira. “Scaling laws for direct drive generators in wind turbines”. 2009 *IEEE International Electric Machines and Drives Conference*, pp. 797–803. ISBN: 978-1-4244-4251-5. 
- [138] G. Shrestha et al. “Structural Flexibility: A Solution for Weight Reduction of Large Direct-Drive Wind-Turbine Generators”. *IEEE Transactions on Energy Conversion* 25.3 (2010), pp. 732–740. DOI: [10.1109/TEC.2010.2048713](https://doi.org/10.1109/TEC.2010.2048713). 
- [139] O. Sigmund. “Morphology-based black and white filters for topology optimization”. English. *Structural and Multidisciplinary Optimization* 33.4-5 (2007), pp. 401–424. DOI: [10.1007/s00158-006-0087-x](https://doi.org/10.1007/s00158-006-0087-x). 
- [140] R. K. Singal, K. Williams and S. P. Verma. “The effect of windings, frame and impregnation upon the resonant frequencies and vibrational behavior of an electrical machine stator”. *Experimental Mechanics* 30.3 (1990), pp. 270–280. DOI: [10.1007/BF02322822](https://doi.org/10.1007/BF02322822). 
- [141] R. Singal, K. Williams and S. Verma. “Vibration behaviour of stators of electrical machines, part II: Experimental study”. *Journal of Sound and Vibration* 115.1 (1987), pp. 13–23. DOI: [10.1016/0022-460X\(87\)90489-5](https://doi.org/10.1016/0022-460X(87)90489-5). 
- [142] D. Smet. “Improvement and Adaptation of Bearing Monitoring System”. Master Thesis. TU Delft, 2014.
- [143] E. Spooner et al. “Lightweight ironless-stator PM generators for direct-drive wind turbines”. *IEE Proceedings - Electric Power Applications* 152.1 (2005), p. 17. DOI: [10.1049/ip-epa:20041084](https://doi.org/10.1049/ip-epa:20041084). 
- [144] R. Stainko. “An adaptive multilevel approach to the minimal compliance problem in topology optimization”. *Communications in Numerical Methods in Engineering* 22.2 (2006), pp. 109–118. DOI: [10.1002/cnm.800](https://doi.org/10.1002/cnm.800). 
- [145] J. N. Stander, G. Venter and M. J. Kamper. “Review of direct-drive radial flux wind turbine generator mechanical design”. *Wind Energy* 15, July 2011 (2012), pp. 459–472. DOI: [10.1002/we](https://doi.org/10.1002/we). 
- [146] Stephan Hannot. “Modeling Strategies for Electro - Mechanical Microsystems with Uncertainty Quantification door”. PhD thesis. TU Delft, 2010. ISBN: 9789090256801.
- [147] R. Strahan. “Energy conversion by nonlinear permanent magnet machines”. *IEE Proceedings - Electric Power Applications* 145.3 (1998), p. 193. DOI: [10.1049/ip-epa:19981863](https://doi.org/10.1049/ip-epa:19981863). 
- [148] J. A. Stratton. *Electromagnetic Theory*. McGraw Hill Book Company, 1941, p. 648.
- [149] K. Svanberg. “The method of moving asymptotes – a new method for structural optimization”. *International Journal for Numerical Methods in Engineering* 24.2 (1987), pp. 359–373. DOI: [10.1002/nme.1620240207](https://doi.org/10.1002/nme.1620240207). 
- [150] D. Tcherniak. “Topology optimization of resonating structures using SIMP method”. *International Journal for Numerical Methods in Engineering* 54.11 (2002), pp. 1605–1622. DOI: [10.1002/nme.484](https://doi.org/10.1002/nme.484). 
- [151] H. Tiersten. “Hamilton’s principle for linear piezoelectric media”. *Proceedings of the IEEE* 55.8 (1967), pp. 1523–1524. DOI: [10.1109/PROC.1967.5887](https://doi.org/10.1109/PROC.1967.5887). 
- [152] P. Tiso, R. Dedden and D. Rixen. “A Modified Discrete Empirical Interpolation Method for Reducing Non-Linear Structural Finite Element Models”. *9th International Conference on Multibody Systems, Nonlinear Dynamics, and Control*. ISBN: 978-0-7918-5597-3. 

- [153] D. Torregrossa et al. "Multiphysics Finite-Element Modeling for Vibration and Acoustic Analysis of Permanent Magnet Synchronous Machine". *IEEE Transactions on Energy Conversion* 26.2 (2011), pp. 490–500. DOI: [10.1109/TEC.2010.2080681](https://doi.org/10.1109/TEC.2010.2080681). 
- [154] University of Massachusetts Amherst. *Wind Energy Center Alumni and the Early Wind Industry*. URL: <http://www.umass.edu/windenergy/about/history/alumni>.
- [155] M. Valavi, A. Nysveen and R. Nilssen. "Effects of loading on radial magnetic forces in low-speed permanent magnet machine with concentrated windings". *2014 International Conference on Electrical Machines (ICEM)*, pp. 1128–1132. ISBN: 978-1-4799-4389-0. 
- [156] M. Valavi et al. "Influence of Pole and Slot Combinations on Magnetic Forces and Vibration in Low-Speed PM Wind Generators". English. *IEEE Transactions on Magnetics* 50.5 (2014), pp. 1–11. DOI: [10.1109/TMAG.2013.2293124](https://doi.org/10.1109/TMAG.2013.2293124). 
- [157] M. Valavi et al. "Slot Harmonic Effect on Magnetic Forces and Vibration in Low-Speed Permanent-Magnet Machine With Concentrated Windings". English. *IEEE Transactions on Industry Applications* 50.5 (2014), pp. 3304–3313. DOI: [10.1109/TIA.2014.2309717](https://doi.org/10.1109/TIA.2014.2309717). 
- [158] P. L. C. van der Valk and D. J. Rixen. "An Effective Method for Assembling Impulse Response Functions to Linear and Non-linear Finite Element Models". *Proceedings of the International Modal Analysis Conference*. Conference Proceedings of the Society for Experimental Mechanics Series, pp. 123–135. ISBN: 978-1-4614-2421-5. 
- [159] N. Van Dijk. "Pushing the Boundaries: Level-set Methods and Geometrical Non-linearities in Structural Topology Optimization". en. PhD thesis. Delft University of Technology, 2012. ISBN: doi:10.4233/uuid:4d9aa813-6d51-4a01-83f8-bb8ed6bcc274. DOI: [10.4233/uuid:4d9aa813-6d51-4a01-83f8-bb8ed6bcc274](https://doi.org/10.4233/uuid:4d9aa813-6d51-4a01-83f8-bb8ed6bcc274). 
- [160] A. Verbart. "Topology Optimization with Stress Constraints". en. PhD thesis. 2015. ISBN: urn:isbn:9789462597396. DOI: [10.4233/uuid:ee24b186-5db6-4c57-aa50-3b736110ff2a](https://doi.org/10.4233/uuid:ee24b186-5db6-4c57-aa50-3b736110ff2a). 
- [161] S. Verma, R. Singal and K. Williams. "Vibration behaviour of stators of electrical machines, part I: Theoretical study". *Journal of Sound and Vibration* 115.1 (1987), pp. 1–12. DOI: [10.1016/0022-460X\(87\)90488-3](https://doi.org/10.1016/0022-460X(87)90488-3). 
- [162] S. Verma, K. Williams and R. Singal. "Vibrations of long and short laminated stators of electrical machines Part I: Theory, experimental models, procedure and set-up". *Journal of Sound and Vibration* 129.1 (1989), pp. 1–13. DOI: [10.1016/0022-460X\(89\)90531-2](https://doi.org/10.1016/0022-460X(89)90531-2). 
- [163] W. Voigt. *Lehrbuch der Kristallphysik*. Wiesbaden: Vieweg+Teubner Verlag, 1966. ISBN: 978-3-663-15316-0. 
- [164] S. N. Voormeeren, P. L. C. Van Der Valk and D. J. Rixen. "Generalized Methodology for Assembly and Reduction of Component Models for Dynamic Substructuring". *AIAA Journal* 49.5 (2011), pp. 1010–1020. DOI: [10.2514/1.J050724](https://doi.org/10.2514/1.J050724). 
- [165] S. N. Voormeeren. "Dynamic Substructuring Methodologies for Integrated Dynamic Analysis of Wind Turbines door". PhD thesis. TU Delft, 2012. ISBN: 9789491104107.
- [166] H. Wang and K. Williams. "Effects of Laminations on the Vibrational Behaviour of Electrical Machine Stators". *Journal of Sound and Vibration* 202.5 (1997), pp. 703–715.

- [167] M. Y. Wang, X. Wang and D. Guo. “A level set method for structural topology optimization”. *Computer Methods in Applied Mechanics and Engineering* 192.1-2 (2003), pp. 227–246. DOI: [10.1016/S0045-7825\(02\)00559-5](https://doi.org/10.1016/S0045-7825(02)00559-5). 
- [168] H. Weh and H. May. “Achievable force densities for permanent magnet excited machines in new configurations”. *Proc. Int. Conf. on Electrical Machines*, pp. 1107–1111.
- [169] B. Weilharter et al. “Experimental investigation of the vibration behaviour of a laminated stack with winding”. *IECON 2013 - 39th Annual Conference of the IEEE Industrial Electronics Society*, pp. 2816–2820. ISBN: 978-1-4799-0224-8. 
- [170] F. Wein. “Topology Optimization of Smart Piezoelectric Transducers”. PhD thesis. University of Erlangen, 2011.
- [171] M. F. While. “Rolling Element Bearing Vibration Transfer Characteristics : Effect of Stiffness”. *Journal of Applied Mechanics* 46.September 1979 (2013), pp. 677–684.
- [172] Wikipedia. *Wikipedia.com - Lists of offshore wind farms by country*. URL: http://en.wikipedia.org/wiki/Lists_of_offshore_wind_farms_by_country.
- [173] H. H. Woodson and J. R. Melcher. *Electromechanical Dynamics Part I: Discrete Systems*. Wiley, 1968. ISBN: 0471959855.
- [174] XEMC-Darwind. *XEMC-Darwind Web page*. URL: <http://www.darwind.nl/Wind-turbines/XD115-5MW>.
- [175] A. Zavvos et al. *Structural comparison of permanent magnet direct drive generator topologies for 5MW wind turbines*. 
- [176] A. Zavvos. “Structural Optimisation of Permanent Magnet Direct Drive Generators for 5MW Wind Turbines”. PhD thesis. The University of Edinburgh, 2013.
- [177] O. C. Zienkiewicz, R. L. Taylor and J. Z. Zhu. *The Finite Element Method: Its Basis and Fundamentals*. Vol. 1. The Finite Element Method. Elsevier Butterworth-Heinemann, 2005, p. 733. ISBN: 0750663200.